Computational methods for Light Sheet Fluorescence Microscopy: towards a quantitative analysis of AVE migration in the mouse

Holly Hathrell

Lincoln College

University of Oxford

A thesis submitted for the degree of

Doctor of Philosophy

Trinity 2020

Contents

Acknowledgements

I would like to thank my supervisors, Professor Shankar Srinivas and Dr Matthew Stower who, together with our collaborator Dr Felix Zhou, have guided me and this project. Your patience and encouragement have been invaluable.

In addition, my colleagues in the Srinivas lab, in particular Dr Richard Tyser, Dr Chris Royer, Dr Tomoko Watanabe, Dr Shifaan Thowfeequ, Dr Satish Arcot Jayaram, and Jonathan Godwin for their eternal good humour and friendship.

Likewise, to my friends in Oxford and elsewhere who have provided endless distraction and entertainment, shared congratulations and commiserations, and whose company I have enjoyed in just about every pub in Oxford.

I thank Prof Elizabeth Robertson, Prof Vicente Grau, Siu Lun Yeung, Dr Jochen Kursawe, and Dr Jens Rittscher for their advice, along with the team at Micron Oxford. I am also grateful to Dr Phillip Keller and Dr Kate McDole, who were wonderful hosts at Janelia Research Campus early in this project.

I extend my gratitude to Wellcome for funding me and to those members of my department, Physiology, Anatomy, and Genetics, who aided in the project and my personal development. I also thank the good people of Lincoln College, who provided me with a friendly and welcoming community during my time in Oxford.

Most importantly, I would like to thank my parents, Alison and Kim Hathrell, and my grandma Jean Parker, who have been an ever constant source of love, support, and inspiration.

Declaration

The project has been an interdisciplinary collaboration between myself, Dr Matthew Stower (Srinivas Lab, Dep. Physiology, Anatomy and Genetics, University of Oxford) and Dr Felix Zhou (Ludwig Cancer Institute, University of Oxford).

All the biological datasets, as outlined in the methods section, were cultured and imaged by Dr Stower. Dr Satish Arcot Jayaram and Jonathan Godwin (University of Oxford) also provided help with the mouse lines.

Dr Zhou was brought onto the project initially in January 2017 and then increased his participation in January 2018. As such, the methods for the data processing framework in Chapter 2 were initially developed by myself, and then steadily improved with a back and forth between myself and Dr Zhou, the final product of which is shown. This process primarily involved me using the tools to find appropriate parameters and process the bulk of the dataset, and discussing improvements required with Dr Zhou, who implemented the changes into the code.

In Chapter 3, Dr Stower and I provided ground truth and manually analysed data for the cell segmentation and tracking. I built the initial CNN for automating segmentation, which was developed into its final version by Dr Zhou, who additionally completed the MOSES analysis and produced many of the plots and graphs in the Chapter, with contributions discussed in place.

Work on the automated tracking was done in developmental collaboration with Siu Lun Yeung (Dep. of Electrical Eng. & Electronics, University of Liverpool) and Dr Zhou, again with myself and Dr Stower providing the manual reference data and guiding requirements.

Manual analysis in Chapter 4 was carried out by myself, with additional inputs for specific sections by Dr Stower and Dr Zhou, also labelled in place.

Computational supervision for the initial part of the project (Oct 2016 – Sep 2017) was by Dr Jens Rittscher (Institute of Biomedical Engineering, University of Oxford) before the computational collaboration was taken over by Dr Zhou.

Main supervision for the biological aspects of the project was provided by Dr Shankar Srinivas, with additional supervision by Dr Stower throughout the full length of the project (Oct 2015 – April 2020).

None of the work presented in this thesis has been accepted or submitted for any degree, diploma or certificate or other qualification in this University or elsewhere. This thesis does not exceed the 50,000 words as recommended by the Medical Sciences Division.

Holly Hathrell, June 2020.

Abstract

Collective migration in epithelial tissues is required for many developmental processes, wound healing, and cancer, and is conserved across vertebrates. It is a process that has been difficult to study for 3D epithelia *in vivo* as the large timelapse datasets required present significant computational challenges for quantitative analysis. An important example of collective migration in an epithelial context is the migration of Anterior Visceral Endoderm (AVE) cells in the mouse embryo. From E5.5, this subgroup of cells in the visceral endoderm monolayer migrate from the distal tip, specifying the anterior-posterior axis by patterning the underlying epiblast which will later give rise to the embryonic lineage. AVE induction and migration have yet to be fully characterised and understood, and provide an attractive *in vivo* system to study the biological function of collective migration due to the relatively small cell numbers at this stage and the experimental accessibility of the visceral endoderm tissue. In this thesis, a new computational framework is developed to analyse and extract quantitative information from light sheet fluorescence microscopy (LSFM) 3D timelapse datasets of E5.5 mouse embryos during AVE migration. The proposed framework initially isolates the migratory cell movement, and secondly extracts the apical surface data to simplify the 3D volume to a 2D characterisation problem. Applying this computational framework on LSFM datasets from 3 fluorescent reporter mouse lines, I demonstrate the first comprehensive tracking of individual cells and cell divisions in the entire visceral endoderm, the first study of cell division angles, and the movement of cells in the underlying epiblast. Altogether these results reveal a model of AVE migration as an active process that drives large-scale tissue deformation and changes in morphology independent of cell proliferation in the VE, and presents evidence that suggests the A-P axis could be pre-defined.

List of abbreviations

aa	amino acid
a-Epi-VE	anterior Epi-VE
AJ	Adherens junctions
AR	Aspect Ratio
AVE	Anterior Visceral Endoderm
BDV	Big Data Viewer
BM	Basement Membrane
CNN	Convolutional Neural Network
DIC	Differential Interference Contrast microscopy
dpc	days post-coitum
DSLM	Digital Scanned Laser lightsheet fluorescence microscopy
E	Embryo day
ECM	Extracellular matrix
EMT	Epithelial-to-mesenchymal transition
EPC	Ectoplacental cone
Epi	Epiblast
Epi-VE	Visceral Endoderm overlying the Epiblast
ExE	Extraembryonic Endoderm
ExE-VE	Visceral Endoderm overlying the Extraembronic Endoderm
ICM	Inner Cell Mass
LSFM	Light Sheet Fluorescence Microscopy
mins	minutes
MIP	Maximum Intensity Projection
MOSES	Motion Sensing Superpixels
MVRA	Multiview-Reconstruction Application
p-Epi-VE	posterior Epi-VE
p-SMAD	phosphorylated SMAD
PIV	Particle Image Velocimetry
ROI	Region of Interest
SiMView/MuViSPIM	Simultaneous Multiview Light-Sheet Microscopy
stdev	standard deviation
SVM	Support Vector Machine
TJ	Tight junctions
tp	time point
VE	Visceral Endoderm
VET	Visceral Endoderm Thickening

Chapter 1: Introduction

Embryonic development is a complex process involving specification, growth, and shape change, which requires precise spatiotemporal coordination of cell morphology and migration. Epithelia are an example of tissues which undergo collective movement, and contribute to shape changes in a range of contexts, not limited to development. Understanding the contribution of individual cell behaviour to this collective movement requires continuous observation with timelapse microscopy. One critical epithelial process which is yet to be fully characterised is the migration of the Anterior Visceral Endoderm (AVE) cells in the mouse embryo, which specifies the anterior-posterior (A-P) axis at E5.5 dpc (days post-coitum) by patterning the underlying epiblast. The mouse Visceral Endoderm (VE) is a useful *in vivo* model for studying how collective cell movements contribute to development in a mammalian system, and has the advantage of having a relatively small number of cells easily accessible for live imaging. The following chapter first provides an overview of mouse development from fertilisation to gastrulation, and second covers the subject of this thesis, the Anterior Visceral Endoderm (AVE), in more detail.

1.1 Mouse embryogenesis: pre-implantation to gastrulation

1.1.1 Pre-implantation

Initially, the cells of the mouse embryo divide inside the Zona Pellucida without growth, dependent on inherited maternal factors (Li, Zheng, & Dean, 2010). The first differences in morphology and transcription appear after 3 cleavage events, when the blastomeres compact and polarise, leaving the outer edges with microvilli and the inner surfaces smooth (Johnson & Ziomek, 1981). The next cleavage events leave larger outer cells enclosing smaller inner cells by the 16 cell stage (Sutherland, Speed, & Calarco, 1990). The trophectoderm is the first differential pathway specified, and goes on to form the embryonic portion of the placenta. The trophectoderm is formed almost

exclusively from the larger outer cells, whereas the inner cells remain pluripotent, accounting for about 75% of the makeup of the Inner Cell Mass (ICM), the outer cells also contributing in some cases (Fleming, 1987; Watanabe, Biggins, Tannan, & Srinivas, 2014). At the 8 cell stage *Oct4* and *Cdx2* are co-expressed throughout the cells, but by the 16 cell stage reciprocal negative inhibition leads to exclusive expression of *Cdx2*, concurrent with *Tead4* (Niwa et al., 2005; Yagi et al., 2007) in the trophectoderm fated cells. *Oct4* (Niwa et al., 2005), *Sox2* (Avilion et al., 2003) and *Nanog* (Mitsui et al., 2003) are restricted to the ICM fated cells by E3.5.

While the cells of the 16 stage morula are obtaining their fates, the outer trophectoderm cells begin to pump fluid into the embryo, forming a cavity called the blastocoel, and displacing the ICM to a clump on one side of the (now called) blastocyst by E3.5 (reviewed in Rossant and Tam, 2009; Takaoka and Hamada, 2012). Lineage tracing confirms cells at this stage are already dividing into distinct populations of epiblast and primitive endoderm (Plusa, Piliszek, Frankenberg, Artus, & Hadjantonakis, 2008). Through cell sorting and apoptosis (Plusa et al., 2008), the primitive endoderm cells expressing *Gata6* (Chazaud & Rossant, 2006) line the boundary between the *Nanog* (Mitsui et al., 2003) and *Sall4* (Zhang et al., 2006) expressing inner epiblast.

The primitive endoderm goes onto become the extra-embryonic membranes, including the visceral endoderm (VE) (Gardner & Rossant, 1979), whereas the remaining ICM cells go on to form the primitive ectoderm or epiblast, continuing the embryonic line.

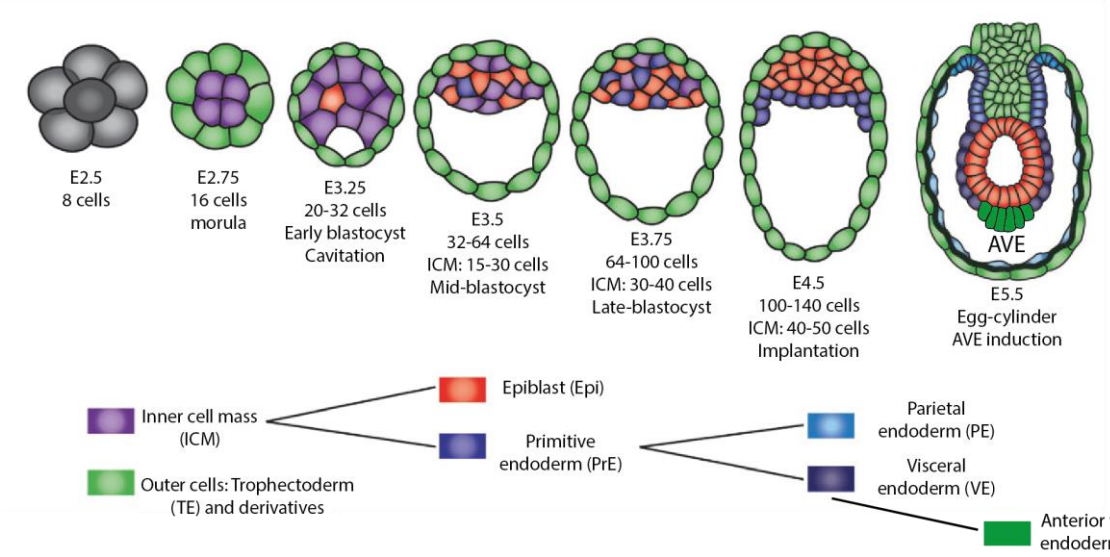

Figure 1-1: Early mouse development, from the 8-cell stage to AVE induction in early implantation (adapted from Bassalert, Valverde-Estrella and Chazaud, 2018).

1.1.2 Implantation

At E4.5 the blastocyst is made up of the three cells types: trophectoderm, primitive endoderm and epiblast. It is released from the Zona Pellucida and undergoes implantation into the uterine wall, then expands in size and change of shape over the next day.

The blastocyst first adheres to the uterine epithelium, before the trophectoderm cells not in contact with the epiblast give rise to giant, primary trophoblast cells and invade the uterine wall. After implantation the mouse blastocyst undergoes a dramatic transformation distinct to murine and rodent embryos. Whereas the chick or human embryo forms a flat disc of layered epiblast and hypoblast, the mouse instead forms an egg cylinder, an elongated structure of extraembryonic tissues encircling the epiblast.

After adhesion to the uterine epithelium, the giant trophectoderm cells envelop the blastocyst, driven by FGF signalling from the epiblast (Goldin & Papaioannou, 2003; Tanaka, Kunath, Hadjantonakis, Nagy, & Rossant, 1998). The trophectoderm cells linking the epiblast and the

uterine wall continue to undergo normal cell division, pushing the epiblast below further into the cavity, and forming the ectoplacental cone (EPC) and the extra-embryonic ectoderm (ExE). These tissues link the epiblast to the uterine wall and will both contribute to the placenta.

The primitive endoderm cells split into two layers. The first of these, the parietal endoderm, divides and migrates to cover the inner region of what was the blastocyst cavity in a monolayer. The epiblast within grows and cavitates, forming a pseudo-stratified cylindrical epithelium. Pluripotency is maintained in the epiblast by the OCT4-SOX2 and NANOG-SALL4 transcription factor complexes, suppression of genes by polycomb proteins, and Nodal signalling (reviewed in Tam and Loebel, 2007).

The primitive endoderm cells covering the epiblast and ExE are known as the Visceral Endoderm (VE). The VE cells, separated from the epiblast by the basal membrane, are tightly intertwined with cell signalling pathways from the epiblast and ExE and go on to have a vital effect on anterior-posterior axis formation. It was thought that the VE cells, like the parietal endoderm, were completely extraembryonic, contributing to the visceral yolk sac. However, live imaging of genetically labelled cells has shown the VE mixing with epiblast cells and small numbers of VE cells being incorporated into the gut tube (Kwon, Viotti, & Hadjantonakis, 2008). This was not specific to the AVE cells, whose ultimate fate is still unknown. The combined growth of the different tissues results in a 2.5x increase in blastocyst length by E5.0 to form the egg-cylinder (Aitana Perea-Gomez et al., 2007).

It is from within the VE cells that a sub-population, the Anterior Visceral Endoderm, arise. The process by which this group of cells migrate and inhibit primitive streak formation to the posterior of the embryo is discussed in Section 1.2 *The Anterior Visceral Endoderm.*

1.1.3 Gastrulation

Gastrulation establishes the basic body plan of the embryo, through Epithelial-to-Mesenchymal transition (EMT) and ingression of the pluripotent epiblast cells into the primitive streak where they begin to differentiate until they commit to their future lineages. The primitive streak begins to form around E6.5 with prior asymmetric expression of characteristic posterior markers *Brachyury* and *Wnt3*, and shown by a thickening of cells in the proximal epiblast, as epiblast cells converge towards the posterior and ingress towards the basal membrane. This thickening elongates over 12-24 hours down to the distal tip. The ingressed cells spread out laterally forming a coherent layer of prospective mesoderm between the epiblast and the VE, separated on both sides by its own basement membrane.

At the distal tip, the node and slightly more anterior notochord are formed, whereas the anterior epiblast becomes the prospective neuroectoderm. Somite formation begins at the anterior (now rostral) at E7.5, followed by the neural folds at E8.0. The most posterior converging epiblast cells give rise to the first lineage from the primitive streak: the extraembryonic mesoderm tissues which will form the visceral yolk sac, amnion and chorion, which completely surround the embryo by E9.5. The lateral epiblast cells form the cardiac, lateral plate and paraxial mesoderm. The last lineage to arise from the anterior epiblast, the definitive endoderm, largely replaces the VE, and becomes internalised to form the gut and hindgut. For more detailed information see the reviews by Rivera-Pérez and Hadjantonakis, 2015; and Wolpert and Tickle, 2011, p109-113.

1.2 The Anterior Visceral Endoderm

Anterior Visceral Endoderm (AVE) migration is the underlying process that occurs after implantation leading to gastrulation. The AVE is a distinct subset of cells in the epithelial VE monolayer which are essential for patterning the epiblast correctly to induce the formation of the anterior-posterior axis pre-gastrulation. The cells induce at the distal tip at E5.5 when the embryo

is in the post-implantation, egg-cylinder stage (see Figure 1-2A). At this stage the embryos are made up of three distinct cell populations; the inner epiblast and more proximal Extra-embryonic Ectoderm (ExE) are covered by a single contiguous monolayer of VE, which can be subdivided into ExE-VE (the VE overlying the ExE) and Epi-VE (the VE overlying the epiblast). Additionally, the ectoplacental cone (EPC) remains to varying degrees, in the most proximal position.

At the distal tip, AVE cells undergo characteristic changes in morphology (Kimura et al., 2000; Rivera-Pérez, Mager, & Magnuson, 2003) then migrate coherently over 4-5 hours to the boundary between the epiblast and the ExE (Srinivas, Rodriguez, Clements, Smith, & Beddington, 2004; Trichas et al., 2011), and restrict primitive streak formation to the posterior (opposite) side of the embryo by E6.5 (Kimura et al., 2000). Mutations causing arrest or over-migration of these cells can result in lethal embryonic defects, most often during gastrulation (reviewed in Stower and Srinivas, 2014).

Many questions remain unanswered in this system due to the difficulties in studying migration dynamics in delicate live embryos. So far evidence has been collected with relatively low time resolution, limited volume information, or fixed samples. The mechanism driving migration is unknown, and several models exist both for the induction of the AVE cells and the determination of their direction of motion. The latter is particularly interesting as it relates to the first overt radial symmetry breaking event in the mouse embryo.

In the following review, I describe the current knowledge surrounding AVE induction, function, and mode of migration. In this review ‘AVE’ is used to describe the subset of cells which induce at the distal tip of the E5.5 embryo (often referred to in the literature as the Distal Visceral Endoderm or DVE) and which then migrate to the anterior location. When the anterior location is referred to, it will be termed the ‘anterior VE’ or simply ‘anterior’.

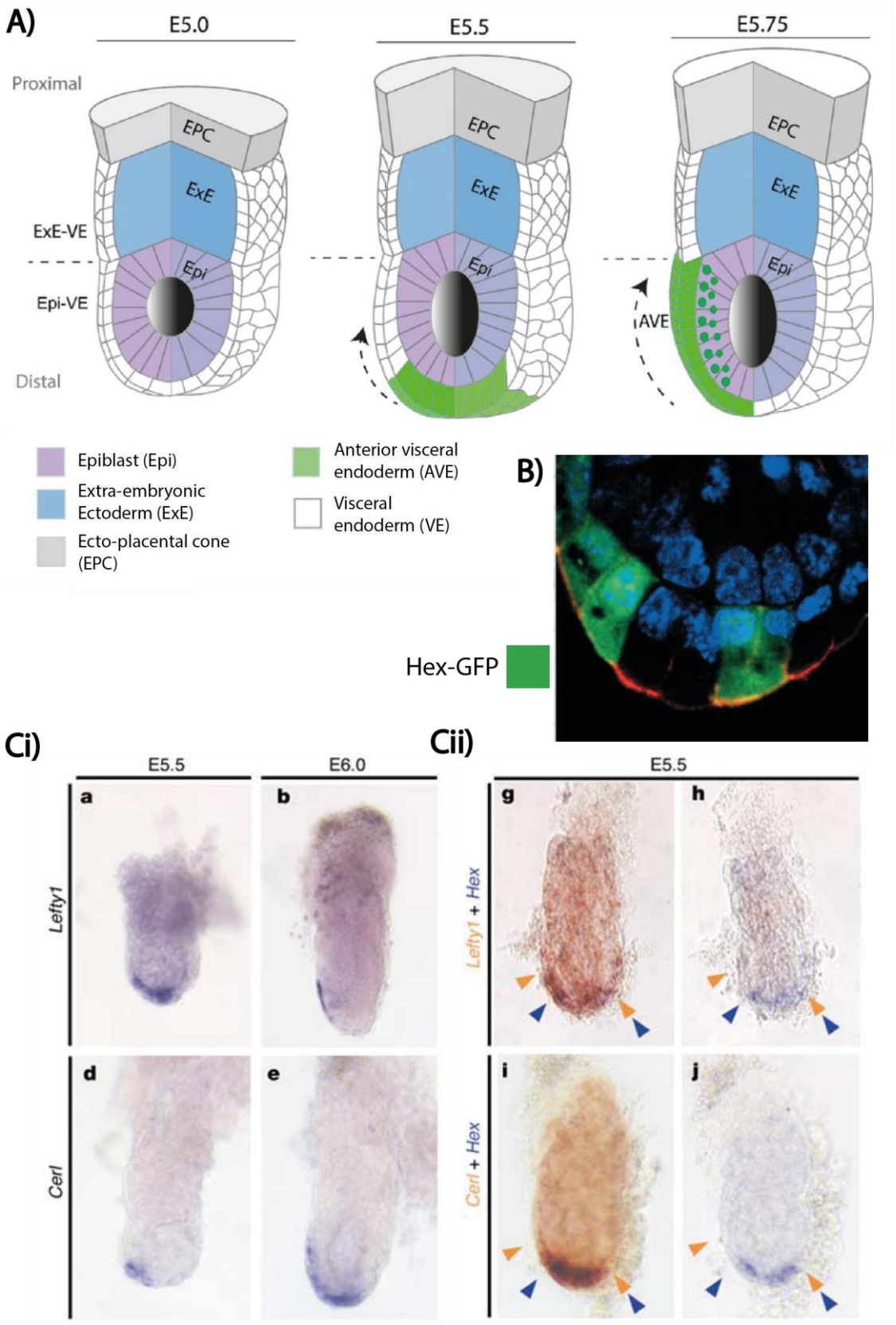
A)
E5.0
E5.5
E5.75
Proximal
EPC
ExE
ExE-VE
Epi
Epi-VE
Distal
AVE
Epiblast (Epi)
Extra-embryonic Ectoderm (ExE)
Ecto-placental cone (EPC)
Anterior visceral endoderm (AVE)
Visceral endoderm (VE)
B)
Hex-GFP
Ci)
E5.5
E6.0
a
b
Lefty1
d
e
Cerl
Cii)
E5.5
g
h
Lefty1 + Hex
i
j
Cerl + Hex

Figure 1-2

Figure 1-2: Identification of the Anterior Visceral Endoderm. A) The AVE induces at the distal tip of E5.5 embryos, before migrating towards the anterior and patterning the underlying epiblast (adapted from Stower and Srinivas, 2018). B) Hex-GFP positive AVE cells show columnar morphology and salt and pepper expression (adapted from Srinivas et al., 2004). Ci) Lefty and Cer1 expression are also used to mark AVE cell, and Cii) predate Hex expression (adapted from Yamamoto et al., 2004).

1.3 Induction of the AVE

1.3.1 The discovery of the AVE

The AVE was first discovered through the expression pattern of divergent homeobox gene *Hesx1*, and was shown to play an essential role in the formation of the rostral neural structures of the mouse embryo (Harrison, Dunwoodie, Arkell, Lehrach, & Beddington, 1995; P. Thomas & Beddington, 1996).

Hesx1 was first identified from a cDNA library screen from the E7.5 embryo (Harrison et al., 1995). Lineage tracing showed the expression pattern of *Hesx1* was restricted to the anterior VE at E6.5 (P. Thomas & Beddington, 1996). Microsurgical removal of the *Hesx1* expressing region (later to become known as AVE) caused a corresponding absence of forebrain marker *Hesx1* in the anterior epiblast 24 hours later, an effect which was more pronounced the earlier the cells were removed (P. Thomas & Beddington, 1996). This introduced the notion of patterning between the VE and epiblast tissues, and has led to one definition of AVE cells as a signalling centre required for neural development (Stower & Srinivas, 2014).

1.3.2 Asymmetric Gene expression in the pre streak embryo

After the discovery of the AVE through *Hesx1* expression, additional genetic markers were shown to be expressed asymmetrically prior to the induction of rostral or mesodermal character and the induction of the primitive streak.

The cytokine *Cerberus-like* or *Cer1* is named for its ability to induce ectopic head formation in *Xenopus* (Bouwmeester, Kim, Sasai, Lu, & De Robertis, 1996). It is expressed at the distal tip and anterior of the E5.5 mouse embryo, with exclusive anterior expression by the early streak stage (Belo et al., 1997). *Lefty1*, a TGF-β superfamily member, also expresses on the anterior side pre-streak at E6.0 (Meno et al., 1996) and at the distal tip around E5.5 (Yamamoto et al., 2004). It is present in the Parietal Endoderm at E4.5, but downregulated after implantation before resuming expression at the distal tip (Mesnard, Guzman-Ayala, & Constam, 2006).

Hex (*HHex, Hematopoietically Expressed Homeobox*), encodes a member of the homeobox family of transcription factors. *Hex* is present in the primitive endoderm cells of the E4.5 blastocyst. A day later, expression of *Hex* is limited to the distal tip of the VE cells, before localising anteriorly by E6.0. Lineage tracing by labelling these VE cells at the distal tip with DiI demonstrated the transient gene expression was due to the *Hex-GFP* positive cells migrating in a coordinated manner from the distal tip to the anterior (P. Q. Thomas, Brown, & Beddington, 1998).

1.3.3 Identifying AVE cells: genetic markers and morphology

Mice transgenic for a *Hex-GFP* reporter (Rodriguez, Casey, Harland, Smith, & Beddington, 2001) have proven very useful and become the canonical method for identifying AVE cells. 8.0kb of the *Hex* promoter sequence encompassing the AVE enhancer drives GFP expression in the AVE cells, separate to the endogenous *Hex* locus (see Section 2.2.1 *Mouse strains, husbandry, and embryo collection*). Several markers such as *Hex*, *Cer1* and *Lefty1* have been proposed to uniquely mark AVE cells (Figure 1-2). However, they do not have identical expressions to mark the AVE. *Cer1* and *Hex* show salt and pepper expression (Figure 1-2B) (Isabelle Migeotte, Omelchenko, Hall, & Anderson, 2010; Srinivas et al., 2004; Takaoka, Yamamoto, & Hamada, 2011) and the anterior shift of *Lefty1* and *Cer1* expression predates that of *Hex* (Figure 1-2Cii), suggesting a bias to the anterior directing the AVE (Yamamoto et al., 2004). Their expression a day earlier than *Nodal* and *Brachyury*, which

mark the primitive streak, is the first overt sign of radial symmetry breaking, although questions remain as to whether the anterior shift direction is predetermined at an earlier stage.

The cells expressing these AVE markers show different morphology compared to the Epi-VE as a whole. The AVE cells are thicker, with fewer microvilli and large oval nuclei in cells (Kimura et al., 2000). Detailed morphological and lineage analysis using the *Hex-GFP* transgenic mice showed that the *Hex*-expressing AVE cells at the distal tip were tall, slanted, and more columnar than their Epi-VE counterparts at E5.5, but remained a monolayer (Rivera-Pérez et al., 2003). This VE Thickening (VET) became a visual landmark used primarily alongside *Hex* to identify AVE cells, although as yet no functional impact of the change in cell shape has been identified. By E5.75, these thicker, *Hex-GFP* positive cells move to form a crescent shape across the anterior side of the embryo, along the boundary overlaying the epiblast and ExE (Rivera-Pérez et al., 2003).

Lefty1, *Hex* and *Cer1* are all absent or downregulated when the ExE is formed between E5.0 and E5.25, suggesting there is no induction of the AVE cells prior to E5.5 (Mesnard et al., 2006). Whereas *Lefty1* and *Cer1* have been shown to be *Nodal* antagonists (Belo et al., 2000; Chen & Shen, 2004; Sakuma et al., 2002), no role has been identified for the *Hex* gene during A-P axis formation, with mutants gastrulating normally (Dattani et al., 1998; Juan Pedro Martinez-Barbera, Rodriguez, & Beddington, 2000), although there is indication they may be required further downstream in the expansion of the forebrain region (J P Martinez-Barbera & Beddington, 2001).

1.3.4 Nodal signalling in the pre-gastrulation embryo

Nodal, a cytokine of the TGF-β family of secreted growth factors, is implicated in a number of processes involving the AVE. *Nodal* is known to be present throughout the epiblast and VE at the time of AVE induction, and is later localised to the posterior prior to primitive streak formation, along with *Brachyury* (Wilkinson, Bhatt, & Herrmann, 1990). It is required in the epiblast for the primitive streak formation, and, like *Hesx1*, in the VE for the formation of anterior rostral structures (Rodriguez, Srinivas, Clements, Smith, & Beddington, 2005; Varlet, Collignon, & Robertson, 1997).

Mice homozygous mutant for *Nodal* arrest at gastrulation, failing to specify an AVE (Brennan et al., 2001) or initiate the primitive streak (Conlon et al., 1994). The mutants lose expression of key posterior markers *Brachyury*, *Wnt*, *Eomes* and *Fgf-8* (Brennan et al., 2001) and also lack *Cripto*, and *Otx2* in the VE, both of which result in a migration arrest (Brennan et al., 2001; Ding et al., 1998).

Nodal is initially expressed as an uncleaved proprotein in the proximal epiblast and is regulated by a proximal epiblast enhancer (Norris and Robertson, 1999; Vincent2003). This signal is required for maintenance of the ExE, and also spreads throughout the epiblast independent of *Smad2* (Brennan2001). The pro-NODAL signal from the epiblast activates subtilisin-like proprotein convertases (SPCs) FURIN and PACE4 in the ExE, via activin receptors, which cleave the proprotein into mature NODAL (Beck et al., 2002; Constam & Robertson, 1999). Both the proprotein and mature NODAL activate BMP4, which induces a positive feedback loop by activating *Wnt3*, which re-stimulates the *Nodal* locus in the epiblast via the SMAD-FOXH1 auto-regulatory enhancer (Brennan, Norris, & Robertson, 2002; Saijoh et al., 2000). WNT3 also then induces mesoderm marker *Brachyury* in the epiblast.

SMAD2-mediated *Nodal* is required for anterior character, which acts by restricting the SMAD2-independent posterior character. In the absence of *Smad2*, *Nodal* expression remains in the distal region and the epiblast gains a proximal character, with an expansion in *Fgf8* domains. No distinct AVE is apparent, and the VE appears uniformly thickened in both extra and embryonic regions (Waldrip, Bikoff, Hoodless, Wrana, & Robertson, 1998).

Mature NODAL and co-receptor CRIPTO also stimulate the phosphorylation of MAPK p38, which in turn strengthens NODAL by phosphorylating the SMAD2 linker region, enhancing the levels of SMAD2 activation in the VE (Clements, Pernaute, Vella, & Rodriguez, 2011; Yamamoto et al., 2009). However, P-SMAD2 is still apparent in the AVE of *Nodal* null embryos, suggesting the SMAD2 activation is mediated by another TGF-β family member. ACTIVIN inhibited embryos maintained levels of p-SMAD2 in the epiblast, but not in the VE, suggesting it also contributes to SMAD2

activation in AVE (Yamamoto et al., 2009). Once activated, SMAD2 binds to co-SMAD4 and moves into the nucleus where it transcribes target genes (Chu, Dunn, Anderson, Oxburgh, & Robertson, 2004). Inhibiting p38 causes a loss of AVE markers *Lim1*, *Hex*, *Dkk1*, and *Lefty1/2*, whereas *Bmp2* and *Hex* expression could still be observed, suggesting that p38 is directly regulating the expression of a subset of AVE genes. It also causes the AVE in E5.5 embryos to assume an ExE-VE identity (Clements et al., 2011).

1.3.5 Theory 1: Repressive signals from the ExE block Nodal in the DVE before induction

There are two main theories concerning the induction of AVE cells at the distal tip. The first theory of AVE induction concerns an antagonistic relationship between BMP-SMAD1 and NODAL/ACTIVIN-SMAD2: NODAL signals from the epiblast induce the transition of VE to AVE cells, but repressive BMP signals from the ExE restrict this induction to the distal tip (Figure 1-3A).

BMP and NODAL are both secreted ligands of the TGF-β superfamily known to act via SMAD proteins, which transmit signals from the type I/II receptors on the cell surface to the nucleus. They share extracellular components such as ActR2A and ActR2B and intracellular components including SMAD4, but whereas NODAL/ACTIVIN acts via R-SMADs SMAD2/3, BMP signalling is mediated by R-SMADs SMAD1/5/8. A shortage of a shared component could lead to a competitive and therefore antagonist relationship.

Whereas AVE cells require the NODAL/ACTIVIN-SMAD2 signalling, p-SMAD1 signalling is absent from the distal tip at the time of induction (Yamamoto et al., 2009). It has been suggested BMP signals from the ExE block the induction of the AVE, as removing the ExE caused a loss of p-SMAD1 in the VE and ectopic AVE induction, whereas transplanting ExE adjacent to the distal tip inhibited AVE induction (Rodriguez et al., 2005).

The ectopic phenotype was replicated by culturing E5.2 embryos with NOGGIN, which down regulates p-SMAD1, whereas embryos cultured with BMP4 lost expression of AVE markers *Hex*, *Cer1* and *Lefty1*, with p-SMAD1 remaining present throughout the VE (Mesnard et al., 2006; Yamamoto et al., 2009). ActR2A and ActR2B, not SMAD4, were found to be the limiting components shared by the competing pathways (Yamamoto et al., 2009).

The minimum length of the embryo required for the induction was 180µm, with a distance of over 70µm between the ExE and distal tip (Mesnard et al., 2006). This requirement was not reached by *Nodal* mutants which show a shortened egg cylinder, due to decreased proliferation (Brennan et al., 2001; Hiramatsu et al., 2013; Mesnard et al., 2006). Additionally, *Nodal* signalling was essential even in cases where the repressive signal from the ExE was removed, providing further evidence for the need for *Nodal* to induce the AVE (Mesnard et al., 2006).

Once the AVE has induced, the characteristic markers *Cer1* and *Lefty1* are then thought to antagonise *Nodal*, restricting its expression to the posterior of the embryo as the AVE migrates to the prospective anterior (Yamamoto et al., 2004).

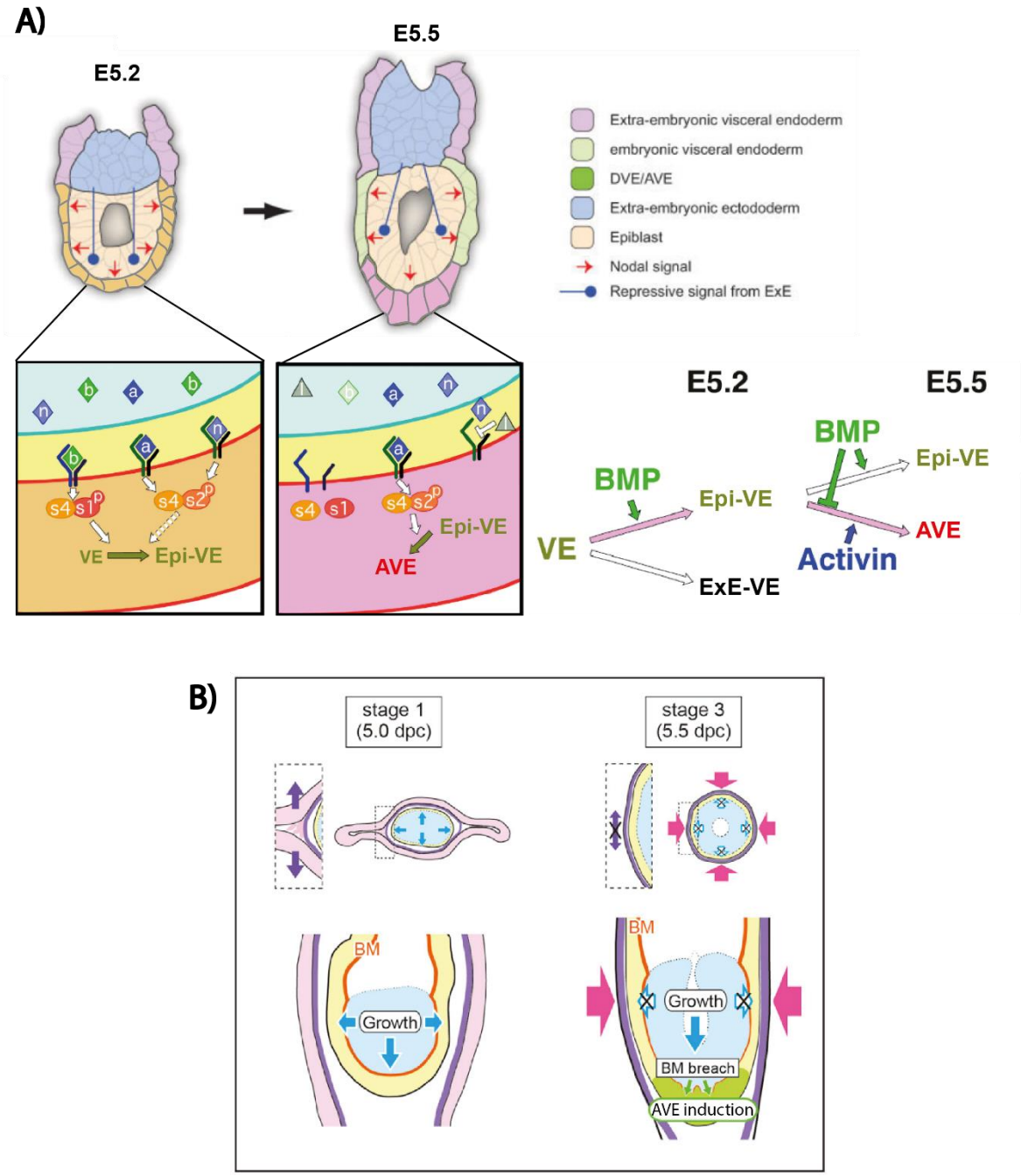

Figure 1-3: Possible modes of AVE induction. A) The first theory of induction suggests the AVE is induced by Nodal/Activin-SMAD2 signalling, when the distal tip is sufficiently far from the repressive BMP-SMAD1 signals from the epiblast. a, ACTIVIN; b, BMP; l, LEFTY1; n, NODAL; $s1^p$, phosphorylated SMAD1/5; $s2^p$, phosphorylated SMAD2/3; s4, SMAD4. Broken arrows indicate an unknown mechanism. (Adapted from Srinivas, 2006; Yamamoto et al., 2009). B) The second theory suggests the AVE is made up of epiblast cells which have transmigrated into the VE at the distal tip. The breach in the basement membrane (BM) is thought to be as a result of the uterine constriction (adapted from Hiramatsu et al., 2013).

1.3.6 Theory 2: Transmigration from the epiblast

The second theory of AVE induction suggests that the mechanical constraint of the uterine wall on the egg cylinder causes cell transmigration from the epiblast to the VE (Figure 1-3B). The transmigrated cells then become and further induce other AVE cells in the VE layer (Hiramatsu et al., 2013; Matsuo & Hiramatsu, 2017).

Hiramatsu *et al.*, 2013 cultured embryos in 90µm wide microcavities engineered to simulate a constraining yolk sac. This resulted in an increase in length of the egg cylinder compared to those cultured in wider (180µm), non-restrictive cavities. The shorter embryos failed to show characteristic AVE markers *Cer1* and *Hex*: with an average length of 138.1 ± 9.7µm it is likely they were not long enough for the distal tip to escape the repressive BMP signals from the ExE. Additionally, embryos from the restrictive cavities which induced AVE successfully (192.8 ± 15.7µm) showed a breach of the basement membrane at the distal tip, and less COLLAGEN4 correlated with positive expression of *Cer1* in VE cells.

They then used a transgenic *Sox2-Cre* line crossed to the Rosa26R$^{lacZ/+}$ reporter to label the epiblast cells. They saw an average of 3.2 ± 0.84 β-gal positive cells in the VE of the embryos cultured in the narrow cavity which they interpreted to have transmigrated from the epiblast to the VE. While the number of cells was small, and thought not to be entirely responsible for the AVE cell population, it was suggested they bring with them diffusible or cell surface factors which influence the adjacent cells in the VE (Hiramatsu et al., 2013; Matsuo & Hiramatsu, 2017).

The theory of transmigration is not necessarily incompatible with the first theory of induction, which suggests that the AVE is induced via NODAL signalling, once the embryo has grown enough to carry the cells at the tip beyond the competitive BMP4-SMAD1 signals from the ExE tissue. Hiramatsu et al. only found evidence of transmigration in egg cylinders which had reached approximately 180µm in length, and suggests that mechanical tension from the uterine tissues becomes large enough to break the basement membrane at that point.

However, while the case for antagonistic BMP4/NODAL signalling is well established, there is evidence to contradict transmigration being responsible for AVE induction. The AVE induces normally in embryos cultured without constraints in direct opposition to the theory. Although transmigration has been observed in timelapse in another study using the *Sox2-Cre* line, a small number of cells were found throughout the VE at various developmental stages, not limited to the distal tip (Bedzhov et al., 2015). Bedzhov et al.'s timelapse imaging had only a 30min resolution, and did not capture the process of a cell breaking through the basement membrane. Additionally, transmigration has not been observed in timelapse with 3 or 5min resolution (Shioi et al., 2017). Capturing the transmigration itself would prove lineage, without which the alternative explanation of ectopic expression of the *Sox2-Cre* in the VE remains a possibility.

1.4 Migration in the AVE

DiI labelling studies first revealed that VE cells at the distal tip at E5.5 moved to the anterior side of the embryo by E5.75 (P. Q. Thomas et al., 1998), before spreading laterally to form a crescent across the boundary (Rivera-Pérez et al., 2003). Mutations in genes such as *Otx2* and *Cripto* induce AVE cells at the distal tip, characterised by the expression of markers *Hex*, *Cer1*, and columnar morphology, but show no migration and ectopic posterior markers *Brachyury* and *Fgf8* (Ding et al., 1998; Kimura et al., 2000; A. Perea-Gomez et al., 2001). Migration, as well as induction, of the AVE is therefore critical for correct positioning of the posterior streak. Here, I review AVE migration, and the theories concerning what causes the AVE to move, and to do so in a coordinated, directed manner.

1.4.1 Theory 1: Migration is driven by asymmetric proliferation

One proposed mode of migration suggests *Nodal* not only induces the AVE but also drives migration by increasing cell proliferation in the posterior VE, whereas *Lefty1* and *Cer1*, acting as *Nodal*

antagonists, repress the corresponding proliferation in the anterior (Yamamoto et al., 2004) (Figure 1-4B).

Although reduced levels of *Nodal* still induce the AVE, they result in an incorrectly positioned A-P axis and thickened cells near the distal tip indicating migration arrest (Norris, Brennan, Bikoff, & Robertson, 2002), suggesting it has a further part to play in the migration of the cells.

Hex-GFP positive AVE cells at the distal tip will migrate towards the more anteriorly-located *Nodal* antagonists *Lefty1* and *Cer1* (Yamamoto et al., 2004). However individual knockouts of these genes do not prevent gastrulation (Belo et al., 2000; Meno et al., 1998). Compound mutants result in correct positioning of the streak in 30% of cases, with the other 70% showing more severe defects such as aberrant accumulation of AVE cells in the anterior and ectopic streak formation (Aitana Perea-Gomez et al., 2002).

Embryos undergoing migration were seen to show regional differences in proliferation corresponding to the gradient of *Nodal* expression, with lower *Nodal* in the anterior Epi-VE corresponding to reduced proliferation compared to the posterior (Yamamoto et al., 2004). Thus the asymmetric expression domains of antagonists *Lefty1* and *Cer1*, tilted towards the prospective anterior prior to migration, were thought to act as a directional signal to 'nudge' the AVE cells towards the anterior (Yamamoto et al., 2004). Another timelapse study also suggested that the cell divisions in the posterior Epi-VE coordinate with the migration of the AVE cells, showing that perturbing cell cycle progression using an FGF inhibitor pre-implantation affected migration (Antonica, Orietti, Mort, & Zernicka-Goetz, 2019). However, several papers have found no evidence of asymmetric rates of proliferation in the VE (Shioi et al., 2017; Stuckey et al., 2011). Furthermore, two mutants resulting in migration arrest, *Otx2* (A. Perea-Gomez et al., 2001) and *Pten* (Bloomekatz, Grego-Bessa, Migeotte, & Anderson, 2012), do not show abnormal proliferation suggesting that asymmetric proliferation rates alone cannot drive migration.

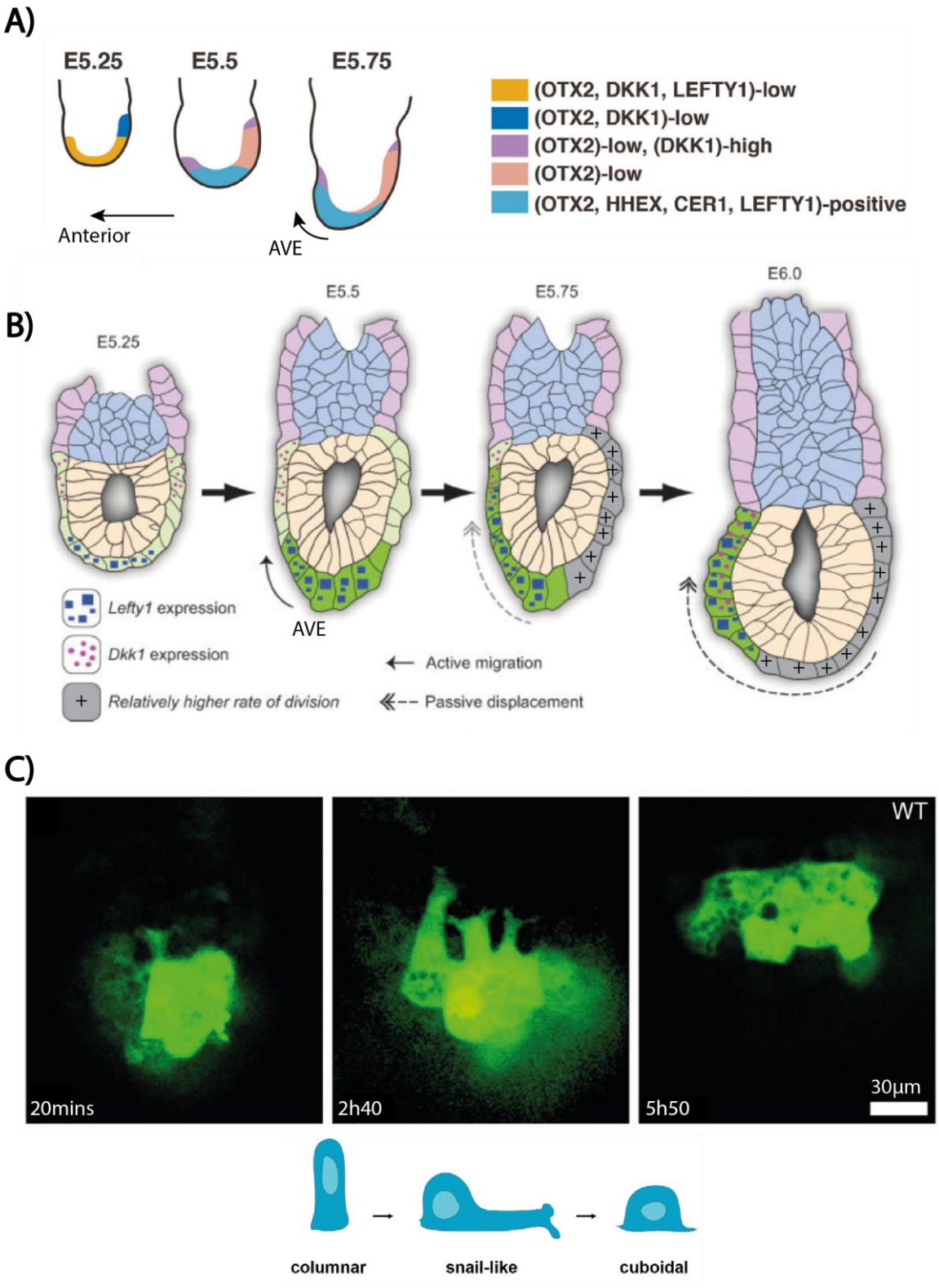
A)
E5.25
E5.5
E5.75
(OTX2, DKK1, LEFTY1)-low
(OTX2, DKK1)-low
(OTX2)-low, (DKK1)-high
(OTX2)-low
(OTX2, HHEX, CER1, LEFTY1)-positive
Anterior
AVE
B)
E5.25
E5.5
E5.75
E6.0
AVE
Lefty1 expression
Dkk1 expression
Relatively higher rate of division
Active migration
Passive displacement
C)
WT
20mins
2h40
5h50
30µm
columnar
snail-like
cuboidal

Figure 1-4

Figure 1-4: Possible modes of AVE migration. A) The shifting locations of expression patterns during AVE migration. At E5.5, expression of Dkk1 shifts anteriorly, in the direction of AVE migration (adapted from Hoshino et al. 2005). B) Cells in the AVE migrate actively towards DKK1. An alternative explanation is a relatively higher rate of division in the posterior cells, which either directs the AVE towards the anterior initially, or further drives migration (adapted from Srinivas et al. 2006). C) Timelapse confocal imaging has captured long cellular protrusions extending from the AVE, suggestive of active migration. The cells exhibit snail-like morphology, beginning columnar, extending the protrusion during migration, and finishing cuboidal (adapted from Migeotte et al. 2010).

1.4.2 Theory 2: The A-P axis is already pre-defined before AVE migration

There is some evidence to indicate the A-P axis is already in place before AVE migration. Previous studies have shown a correlation between the asymmetric tilt of ectoplacental cone (EPC) and the position of the primitive streak on the posterior of the mouse embryo (Gardner, Meredith, & Altman, 1992; Smith, 1985). Smith recorded asymmetry of the mouse blastocyst at implantation, with the ICM-polar trophectoderm complex tilted at an angle relative to the proximal-distal axis. They suggested the axis persisted as the A-P axis to later stages via the tilt of the EPC, with the direction in which the cone is tilted towards, the posterior, and away from, the anterior. A later study investigated the hypothesis during primitive streak formation, taking measurements of EPC angle in embryos at E6.5 (Gardner et al., 1992). However, although the tilt of EPC was found to lie roughly along the A-P axis, it was equally likely to be tilted towards the anterior as the posterior.

Another study has shown that the eccentricity of the embryo predates AVE migration, with the E5.0 embryo showing a distinct bilateral asymmetry (Mesnard, Filipe, Belo, & Zernicka-Goetz, 2004). This asymmetry almost disappears during AVE migration, before reappearing and becoming more pronounced by E6.5 (Mesnard et al., 2004). However, complicating the picture, it has also been shown that the AVE and thus A-P axis is aligned with the short axis during migration and later at around E6.0, before aligning to the long axis again by primitive streak formation at E6.5 (Mesnard

et al., 2004; Aitana Perea-Gomez et al., 2004). The mechanism for this change in A-P axis orientation from the short to the long axis is not clear, although it is speculated it may be due to preferential proliferation, or that the shape of the underlying epiblast cells could affect the rotation of the cavity and thus the surrounding tissues (Mesnard et al., 2004; Aitana Perea-Gomez et al., 2004).

There is also speculation that the columnar morphology of migrating AVE cells is linked to the change in aspect ratio of the epiblast, as epiblast cells underneath the VET region appear compressed, but it was not known whether this was a consequence of or a driving factor in AVE migration (Rivera-Pérez et al., 2003).

The change in aspect ratio from E6.0 to E6.5 occurs in embryos cultured *in vitro*, and so is unlikely to depend on uterine signals (Mesnard et al., 2004). However, this does not rule out the possibility that such signals could have laid out the A-P axis much earlier at the blastocyst stage and subsequently carried forwards as suggested by Smith, 1985.

1.4.3 Theory 3: The AVE migrates due to attractive and repulsive signals from Dkk1-Wnt signalling

While AVE cells will migrate towards ectopically expressed *Lefty1* and *Cer1*, and away from *Nodal*, the lack of complete arrest of the *Lefty1* and *Cer1* double mutants suggests other factors may be involved in directing migration (Aitana Perea-Gomez et al., 2002). One candidate for this is *dikkopf1* (*Dkk1*), a secreted antagonist of WNT in the canonical pathway, and in WNT-PCP signalling. *Dkk1* is expressed asymmetrically in the anterior and more proximal posterior at E5.5, which is suggested to provide an attractive directional cue to the AVE (Hoshino, Shioi, & Aizawa, 2015; Kimura-Yoshida et al., 2005) (Figure 1-4A and B).

Otx2 is a paired homeobox gene expressed throughout the epiblast and in the induced AVE of E5.5 embryos, largely colocalising with *Hex* at E6.5. (Hoshino et al., 2015; Kimura-Yoshida et al., 2005). It is essential for the migration of the AVE, but does not affect proliferation (A. Perea-Gomez et al.,

2001). *Dkk1* is absent in *Otx2*$^{-/-}$ mutants, and insertion of *Dkk1* cDNA into the *Otx2* locus can rescue the migration, but not expression of all the absent genes required for correct forebrain induction (Kimura-Yoshida et al., 2005). Although expressing *Dkk1* in the AVE cells in this manner does not conclusively show DKK1 acting as a morphogen, Kimura-Yoshida *et al.* also showed the AVE in WT embryos migrates in the direction of embedded DKK1 soaked beads (in addition to presumably endogenous expression), even altering migration direction when embedded after its initiation; the same test with a WNT3 bead was shown to repel AVE cells.

DKK1 is thought to block the inhibitory action of WNT by binding to its co-receptors in *Xenopus*. This allows the phosphorylation of β-CATENIN which then degrades instead of translocating to the nucleus for the transcription of target genes (Mao *et al.*, 2002; reviewed in Logan and Nusse, 2004). Migration in mouse also requires β-CATENIN, with deficient embryos arresting at the distal tip (Huelsken et al., 2000). Kimura-Yoshida *et al.*, also found that β-CATENIN was specifically diminished in the WT AVE from E5.75, but was uniform in the *Otx2* mutant. They showed a β-CATENIN soaked bead did not change the pattern of nuclear localisation, but a DKK1 bead dramatically reduced its expression on that side, and suggested the same mechanism described in *Xenopus* also applies to the mouse.

However, embryos mutant for *Dkk1* correctly express *Otx2* and still migrate, confirming *Dkk1's* position downstream of *Otx2*, but complicating the picture for inhibiting β-CATENIN mediated transcription as a sole requirement for migration (Mukhopadhyay et al., 2001). The AVE will also migrate towards ectopically expressed *Lefty1* and *Cer1*, so it is possible the combination of multiple asymmetric chemoattractants show redundancy (Yamamoto et al., 2004). It remains unclear whether *Wnt* alone is capable of repelling the AVE from the posterior in the absence of *Dkk1*; *Wnt* is found throughout the VE at E5.5 with no reported asymmetry, but after migration is confined to the posterior (Ferrer-Vaquer et al., 2010). A further role for *Otx2* upstream from *Wnt* would explain

the requirement of *Otx2* for migration, and the ability of the cells to still migrate when rescued by attractant *Dkk1*.

1.4.4 Theory 4: AVE cells migrate actively

As opposed to the theory of AVE cells being passively driven by increased posterior proliferation, the fourth theory, compatible with the notion of a chemoattractant, involves cells actively migrating by sending out long protrusions and using them to 'pull' themselves towards to the anterior (Figure 1-4C).

Time-lapse confocal imaging of the *Hex-GFP* reporter line confirmed the coordinated cell movement of AVE cells from the distal tip to the anterior of the embryo, over 4-5 hours, before coming to an abrupt halt at the boundary and spreading laterally into a crescent shape (Isabelle Migeotte et al., 2010; Srinivas et al., 2004; Trichas et al., 2011). At no point did the migrating cells lose contact with the basement membrane, with Tight Junction (TJ) markers ZO-1 and PAR3, Adherens Junction (AJ) marker E-CADHERIN consistently present including in migrating cells (Isabelle Migeotte et al., 2010; Trichas et al., 2011).

Importantly, the temporal imaging showed AVE cells continuously changing shape and projecting filopodial processes several cell diameters in length, and lasting 1-2.5 hours, in the direction of motion (Isabelle Migeotte et al., 2010; Omelchenko et al., 2014; Srinivas et al., 2004). The presence of these protrusions in the direction of motion suggests an active migration, possibly in response to an extracellular cue (Srinivas et al., 2004).

The protrusions have been shown to be mediated by WAVE complex components NAP1 and RAC1 (Isabelle Migeotte et al., 2010; Rakeman & Anderson, 2006) (Figure 1-5A). For AVE cells in the VE to migrate and undergo intercalation events with the surrounding cells, they must be able to restructure the actin cytoskeleton in order to break cell-cell (TJ and AJ) and cell-basement membrane connections, and form new ones.

The ARP2/3 complex is the main regulator of actin polymerisation to reshape the cytoskeleton, recently shown to mediate active migration via protrusions in mouse gut epithelial cells (Krndija et al., 2019). ARP2/3 is guided by the Rho-family of small GTPases, in response to extracellular signals (reviewed by Bompard and Caron, 2004), a rearrangement in part mediated by the WASP family of proteins, of which the 5 protein complex WAVE is a member (Bompard & Caron, 2004). Once localised to the cell membranes, Rho-GTPases drive the WAVE complex to polymerize monomeric actin into actin filaments, leading the cell to send out basal protrusions in the direction of migration (Isabelle Migeotte et al., 2010). It is has been proposed that such protrusions might carry E-CADHERIN to form new AJ forming and pulling the cell in that direction (Stower & Srinivas, 2014).

NAP1 is a regulatory subunit of the WAVE complex, mediated by small GTPase RAC1. Approximately half of NAP1 mutants show migration impairment, with 25% duplicating the AP body axis and the embryos arresting at mid gestation (Rakeman & Anderson, 2006). VE deleted *Rac1* mutants also show arrest, resulting in a ring of ectopic posterior markers in the ExE region, and a tight constriction around the boundary; the cells instead bunch at the distal tip, some forming a pear shape and losing contact with the basal membrane (Isabelle Migeotte et al., 2010).

In contrast to the long-lasting protrusions shown by the WT embryos, the *Rac1* mutant embryos had only a couple of AVE cells which sent out short, and transient (20-30mins) protrusions, with no neighbour exchange in the VE (Isabelle Migeotte et al., 2010). Additionally, although F-actin was present in strong cortical rings in both WT and mutant *Rac1*-deleted VE, the migrating WT AVE had weaker apical F-actin, suspected to be due to dynamic rearrangements (Isabelle Migeotte et al., 2010). Together, these studies showed F-actin organisation was dependent on RAC1 to inform cell shape changes, and RAC1 acting upstream of NAP1 to direct the AVE migration. Additionally, a member of the Rho family, *β-pix*, has been shown to regulate the spatial organisation of RAC1, with its deletion showing disrupted collective migration, and more laterally directed and branching protrusions (Omelchenko et al., 2014) (Figure 1-5B).

The protrusions are impossible to distinguish from the fluorescent signal in most AVE cells marked by *Hex-GFP*, making them difficult to measure and fully characterise except on the leading and trailing cells. The transient structures have also proved difficult to fix and very thin, making them difficult to visualise in other lines, leaving questions remaining as to the exact nature and function of the protrusions, whether they do transport E-CADHERIN, whether they are present in other cells in the Epi-VE, and whether they are responding to a chemoattractant such as *Dkk1* (Stower & Srinivas, 2014).

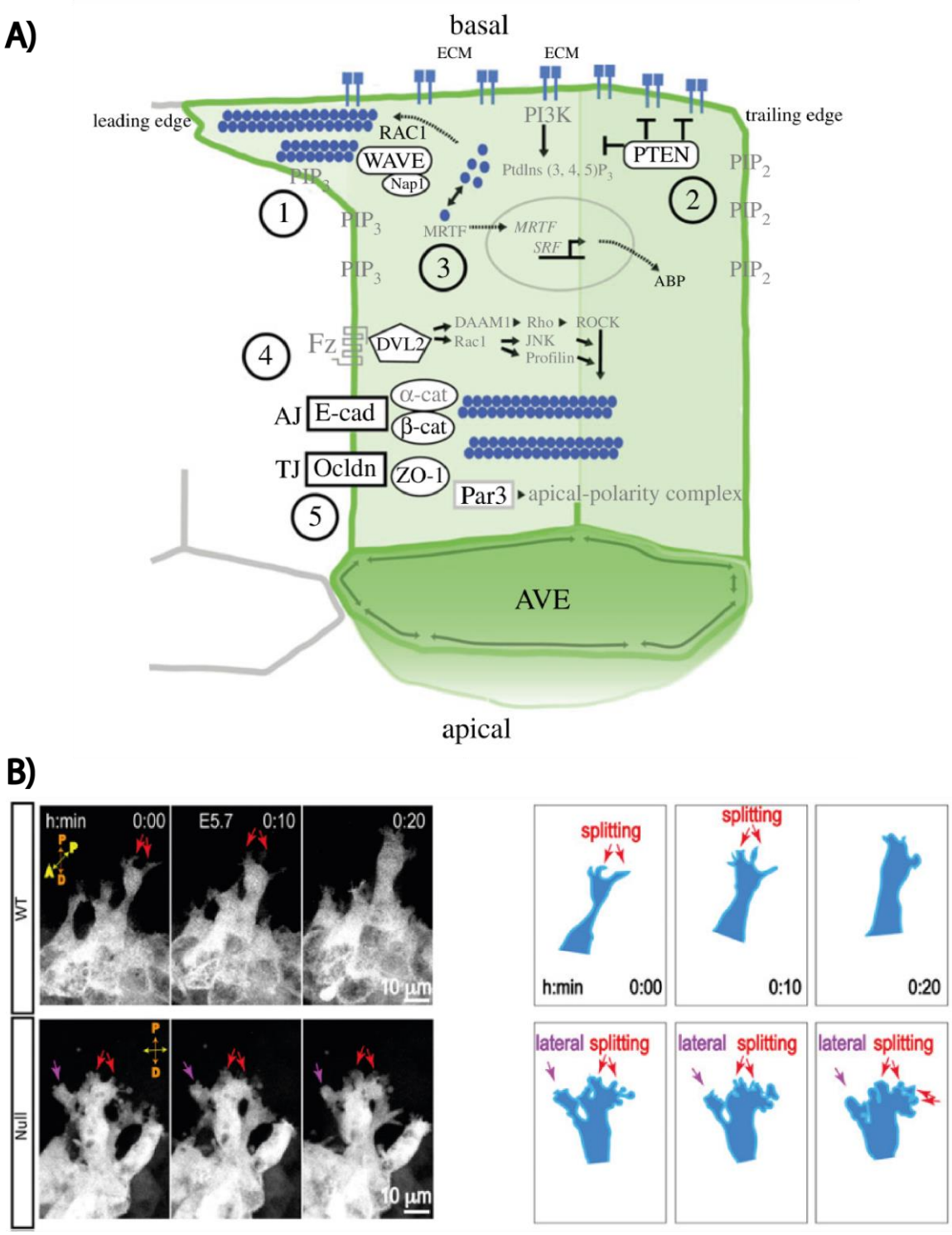

Figure 1-5: Cellular protrusions are mediated by members of the WAVE complex. A) Protrusions have been shown to be mediated by WAVE complex components NAP1 and RAC1, which direct F-actin organisation. PTEN is also required for protrusions by forming correct F-actin foci (adapted from Stower and Srinivas, 2014). B) ϐ-pix deletion causes lateral branching of cellular protrusions, by disrupting the spatial localisation of RAC1, resulting in a loss of directed migration (adapted from Omelchenko et al., 2014).

1.4.4.1 Pten is required for protrusions by forming correct F-actin foci

Another mutant showing the ectopic posterior markers around the embryos circumference is *Pten*, a regulator of phosphoinositides (PtdIns). PIP_3 acts to anchor signalling proteins to the plasma membrane and cannot bind when converted to PIP_2 by PTEN (Manning & Cantley, 2007) (Figure 1-5A). A number of studies have shown PTEN directing migration of cells by creating a gradient of PtdInds, with higher levels of PTEN and thus lower levels of PIP_3 in the trailing edge (for a review in *Dictyostelium discoideum* and mammalian neutrophils, see Cai and Devreotes, 2011). Without PIP_3 a cell will fail to form connections between the cell integrins and laminar of the basement membrane.

The AVE in *Pten* null mutants does not arrest completely, instead showing some movement, but in random directions at around 60% of their normal distance (Bloomekatz et al., 2012). The WT phenotype was still observed in embryos with conditional epiblast *Pten* deletions, suggesting the requirement for *Pten* was in the VE alone. There were no changes in proliferation compared to the WT (a canonical role for PTEN); instead mutants showed high levels of PIP_3 membrane localisation throughout the VE and ectopic expression of F-actin to the middle of the apical surface of VE cells, suggesting *Pten* is required for coherent migration via correct organisation of actin (Bloomekatz et al., 2012).

Although there was no indication of differences in PIP_3 between WT AVE and VE cells, the lack of PIP_3 localised to the membrane across the VE suggests a general permissiveness to migration, as the cells will fail to form such strong connections to the basal lamina, and may yet be shown to work in partnership with RAC1 to promote new protrusions by organising the F-actin network.

1.4.5 PCP signalling mediated by Nodal causes a non-permissive ExE-VE

Hex-GFP negative cells at the leading edge of migration undergo an extreme shape change at the approximate location of the boundary overlying the epiblast, becoming highly elongated laterally,

as if hitting an invisible barrier and being compressed by the AVE behind (Trichas et al., 2011). Although the VE forms a single epithelial sheet with no observable difference in TJ or AJ (Isabelle Migeotte et al., 2010), the Epi-VE and ExE-VE show differences in morphology and behaviour. It is not yet understood why the cells of the AVE come to such an abrupt a halt at the boundary, but evidence suggests it may be due to a lack of permissiveness of the ExE-VE tissue, in effect forming a physical barrier by preventing further intercalation events (Trichas et al., 2011).

The ExE-VE is more cuboidal than the squamous cells of the Epi-VE (excluding the induced AVE), and are shown by electron microscopy to have more microvilli, pinocytotic profiles and lysosomal granules than Epi-VE, suggesting it is a more absorptive tissue (Batten & Haar, 1979). Whereas cells throughout the Epi-VE undergo extensive neighbour exchange and intercalation during migration, the cells in the ExE-VE remain largely static and regular in shape with a roughly hexagonal apical surface in a low energy honeycomb formation (Trichas et al., 2011, 2012)

F-actin and MYOSIN-IIA localisation are identical to each other and differ between the ExE-VE and Epi-VE (Figure 1-6A). The Epi-VE shows F-actin in cortical rings before and during AVE migration, whereas the ExE-VE initially confines F-actin to cortical rings prior to migration, then additionally enriches the apical cortex and forming an 'apical shroud' (Trichas et al., 2011). Trichas et al. showed the membrane localisation of F-actin was affected in embryos overexpressing a membrane tethered C-fragment of *Celsr1*, a homologue of the *Drosophila* flamingo and disruptor of PCP-dependent DVL2. In zebrafish, this a core component of the non-canonical PCP pathway acts via translocation to the plasma membrane by the FRIZZLED ligand (Carreira-Barbosa et al., 2009). *Dvl2* was downregulated where F-actin signal was strong; it was enriched to the plasma membrane in the Epi-VE, but excluded from the membrane of the ExE-VE (Trichas et al., 2011)

Trichas et al. also suggested a role for *Nodal* in both Epi and ExE-VE tissues. In *Nodal* inhibited and null mutants *Dvl2* failed to enrich to the Epi-VE membrane but was abnormally persistent in the ExE-VE, whereas the F-actin shroud was lost (Trichas et al., 2011). In contrast, the *Lefty1* mutant

(where *Nodal* is overexpressed) shows ectopic membrane localisation in the ExE-VE and is characterised by an overmigration phenotype. This suggests PCP signalling mediated by *Nodal* is responsible for the differences in permissiveness exhibited by the tissues, and thus the lateral spread of the AVE at the boundary (Trichas et al., 2011) (Figure 1-6B).

However, the presence of asymmetric chemoattractants such as *Dkk1*, *Lefty1* and *Cer1* in the posterior Epi-VE means that a chemical basis for the pause of cells at the boundary cannot be ruled out: it is not clear that cells in the anterior attracted to ectopic DKK1 in the ExE-VE would not migrate beyond the boundary. It is also not clear whether protrusions are only extended towards the epiblast, in which AVE cells may have no driving force to propel them past the boundary.

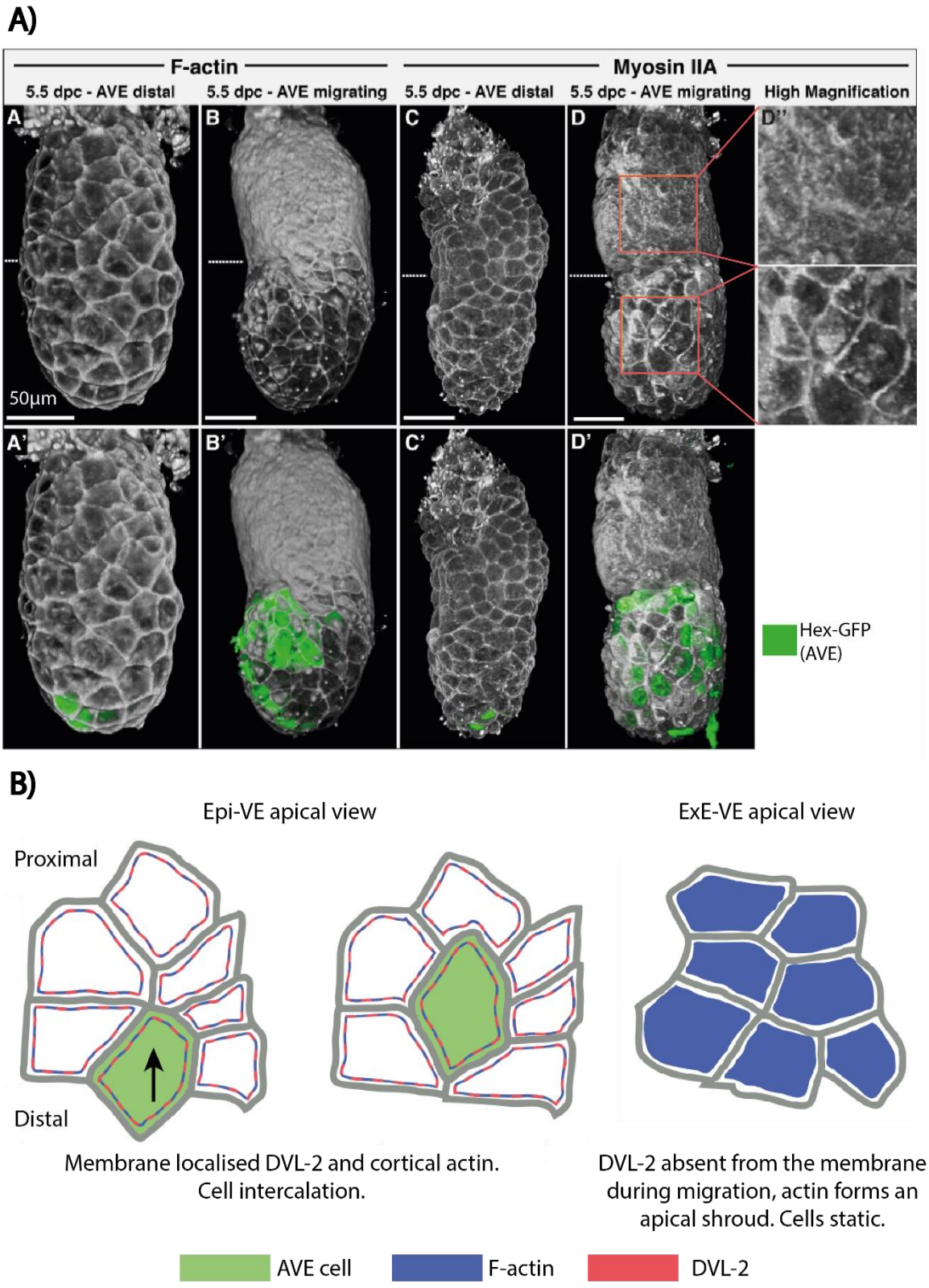
A)
F-actin
Myosin IIA
5.5 dpc - AVE distal
5.5 dpc - AVE migrating
5.5 dpc - AVE distal
5.5 dpc - AVE migrating
High Magnification
A
B
C
D
D''
50µm
A'
B'
C'
D'
Hex-GFP (AVE)
B)
Epi-VE apical view
ExE-VE apical view
Proximal
Distal
Membrane localised DVL-2 and cortical actin. Cell intercalation.
DVL-2 absent from the membrane during migration, actin forms an apical shroud. Cells static.
AVE cell
F-actin
DVL-2

Figure 1-6

Figure 1-6: PCP signalling mediated by Nodal causes a non-permissive ExE-VE. A) F-actin and MYOSIN-IIA localisation when the AVE is induced at the distal tip at E5.5, and when the AVE is migration at E5.5 (adapted from Trichas et al., 2011). B) It is proposed that Epi-VE cells with membrane localisation of DVL2 and cortical actin are permissive to cell intercalation events, whereas ExE-VE cells with DVL2 absent from the membrane during migration are static (adapted from Stower and Srinivas, 2014).

1.4.6 Mediators of PCP signalling are also required for large scale tissue reorganisation in the chick

The mouse AVE is thought to be homologous to the chick hypoblast. The hypoblast shares extraembryonic fate, expression of several molecular markers (*Otx2*, *HNF3β*, *Gsc*, and *Cer1*, but not *Lefty1*), induction of markers *Otx2* and *Sox3* in the epiblast, and characteristic anterior movements around the time of gastrulation (Foley, Skromne, & Stern, 2000).

There is evidence to suggest that the chick hypoblast directs epiblast cell movement. Prior to the primitive streak formation, ≈100,000 cells in the chick epiblast move in bilateral symmetric whirls (Gräper, 1929; Wetzel, 1929). Timelapse microscopy has shown that these rotational movements are characterised by medio-lateral cell intercalation events, driven by localised Wnt-PCP signalling mediators *Vangl2*, *Flamingo* and *Prickle*, which are induced in the epiblast by FGF secreted by the hypoblast (Rozbicki et al., 2015; Voiculescu, Bertocchini, Wolpert, Keller, & Stern, 2007) (Figure 1-7A).

Despite the genetic similarity between the chick hypoblast and the mouse VE, the cell movements in the chick epiblast bear closer relation to those in the mouse VE during AVE migration. In the chick epiblast, cells move coherently in the central domain, extending long (although bilateral) protrusions and seeming to undergo active migration, before a passive lateral movement with smaller protrusions (Voiculescu et al., 2007). Improved 3D timelapse imaging has shown that these whirling movements may also describe the wider pattern of movement in the mouse (Shioi et al.,

2017; Takaoka et al., 2011), where *Flamingo* homologue *Celsr1* and *Prickle* homologue *Testin* are present (Crompton, Du Roure, & Rodriguez, 2007) (Figure 1-7B). However, the 3D nature of the mouse egg-cylinder has prevented full visualisation of the epithelial sheet.

In the mouse epiblast, the interaction of *Prickle* homologue *mpk1*, and *Vangl2*, is essential for apical-basal polarity and also caused an arrest of AVE cells at the distal tip (Tao et al., 2009). Fixed chimeric studies have also demonstrated that movement occurs and suggest that it is not random, but that cells sort based on aligning *Nodal* gradients between the epiblast and Epi-VE (Lu & Robertson, 2004). To date no studies have be able to track cells in the epiblast during timelapse earlier than E6.5 in the posterior, where the cells haves been shown to display limited movement with no large scale cell rearrangements (Williams, Burdsal, Periasamy, Lewandoski, & Sutherland, 2012); as such it is not known whether the cells mirror the rotational movements seen in the mouse VE and chick epiblast.

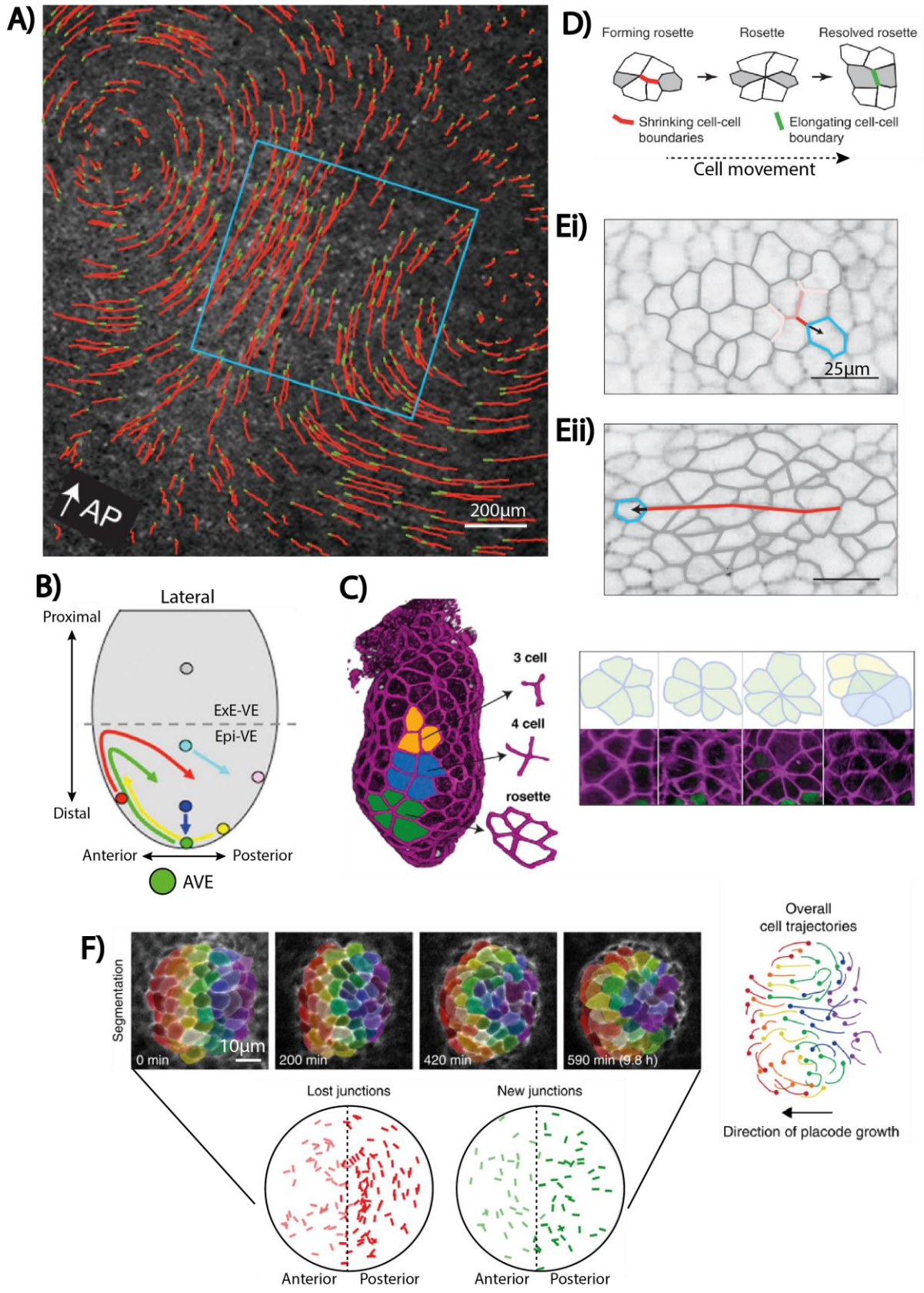
A)
AP
200µm
D)
Forming rosette
Rosette
Resolved rosette
Shrinking cell-cell boundaries
Elongating cell-cell boundary
Cell movement
Ei)
25µm
Eii)
B)
Lateral
Proximal
ExE-VE
Epi-VE
Distal
Anterior
Posterior
AVE
C)
3 cell
4 cell
rosette
F)
Segmentation
0 min
10µm
200 min
420 min
590 min (9.8 h)
Lost junctions
New junctions
Anterior
Posterior
Anterior
Posterior
Overall cell trajectories
Direction of placode growth

Figure 1-7

Figure 1-7: PCP-dependent Rosettes in the Epi-VE are indicative of wider F-actin/MYOSIN-IIA apical junction remodelling. A) Cells in the chick epiblast move in bilateral whirls, shown here midway through primitive streak formation Rozbicki et al., 2015. B) Similar rotational movements have been seen in the mouse during AVE migration (adapted from Shioi et al.,,2017). C) Rosette structures have been identified in the mouse during AVE migration (adapted from Trichas et al., 2012). D) Diagram of the polarised orientation of rosette formation and resolution in Drosophila germ band extension (adapted from Lienkamp et al., 2012). Ei) Randomly aligned cells outside sickle region. Eii) Asymmetric cells inside the sickle region with aligned junctions primed for force propagation along the red line (adapted from Rozbicki et al., 2015). F) Hair follicles in the mouse show similar PCP-dependent rotations, with mediated by polarised loss and gain of junctions (adapted from Cetera et al., 2018).

1.4.7 PCP-dependent Rosettes in the Epi-VE are indicative of wider F-actin/MYOSIN-IIA apical junction remodelling

As the first wave of AVE cells push through the VE tissue towards the boundary, the surrounding cells undergo cell intercalation events and neighbour exchange, becoming less orderly in comparison to the regular honeycomb formation of the ExE-VE (Trichas et al., 2011). In addition to the severe elongation of cells at the boundary, another sign of disruption to the tissue equilibrium was the formation of multi-cellular rosettes: 5 or more cells meeting at a central point Figure 1-7C.

15min interval timelapse imaging showed rosettes were formed, predominantly in the Epi-VE, by cell intercalation rather than division or apoptosis (Trichas et al., 2011). Transgenic embryos with disrupted PCP signalling showed greatly reduced rosette formation, altered epithelial packing, and abnormally dispersed AVE migration (Trichas et al., 2012). This phenotype was emulated in mathematical simulations when rosette formation was prevented, suggesting that rosettes, while not responsible for driving migration, are necessary for it to remain coherent (Trichas et al., 2012).

These unlikely structures are also observed to be oriented by non-canonical Wnt and planar PCP signalling in *Xenopus* kidney tubule elongation (Lienkamp et al., 2012). In *Xenopus*, MYOSIN-

mediated shrinking of cell boundaries led to the formation of rosettes, which resolved at a perpendicular angle, narrowing the tissue (Lienkamp et al., 2012).

Coordinated shortening of mediolateral junctions are also essential for driving germ band extension in *Drosophila*. This action is driven by polarised action of non-muscle MYOSIN-II aligning across multiple cells and contracting to create rosettes, which then resolve perpendicular to formation, narrowing and elongating the tissue (Blankenship, Backovic, Sanny, Weitz, & Zallen, 2006) (Figure 1-7D). However, mutations in core PCP components *Frizzled* and *Dishevelled* do not affect germband extension in *Drosophila* (Zallen & Wieschaus, 2004). The involvement of the PCP pathway has been shown in *Drosophila* wing and eye formation, where the pathway is credited with regulating the polarity of cells along a tissue axis, and is thought to be generally conserved across vertebrates (reviewed in Seifert and Mlodzik, 2007).

A detailed LSFM study of global cell rearrangement in the chick, as in the mouse hair follicle, showed sequential contraction of apical junctions inside the sickle region (precursor to the streak when the most contraction occurs). The junctions contracted in the direction of motion leading to large scale force propagation and rotational cell movements during streak formation (Rozbicki et al., 2015) (Figure 1-7E). Rozbicki et al. showed that this motion was correlated with active MYOSIN-II cables in the apical cell junctions spanning 2-8 cells, and with cell shape indicative of coordinated junctional remodelling. However, the sequential nature of the contractions during streak formation was at odds with the simultaneous nature seen *Drosophila*, where the rosette structures were also clearer (Blankenship et al., 2006).

A similar PCP-dependent rotational pattern of cell rearrangement has been seen in hair follicle development in mice, with polarising cells in the placode (developing follicle) moving in a rotational manner highly reminiscent of the chick (Cetera, Leybova, Joyce, & Devenport, 2018) (Figure 1-7F). As cells migrated, intercellular junctions perpendicular to the direction of migration were lost, whereas more in the direction of motion were created, allowing cells to slide easily past their

neighbours. *Celsr1* localisation correlated closely with the lost junctions, suggesting PCP signalling played an active part in neighbour exchange by contracting those junctions in the way of the advancing cells into a vertex, and allowing them to be easily remodelled (Cetera et al., 2018). Cetera et al. also showed that *Vangl1* and *Vangl2* were required for correct rotational migration, showing further similarity in the pathway to AVE migration, and that MYOSIN-II mediated by RHO KINASE was acting downstream of PCP to remodel the apical junctions.

Rosettes in the mouse AVE were not seen to be formed by convergent-extension movements (Trichas et al., 2012), but may instead be a consequence of the disruptive nature of AVE migration across the sheet, causing junctional rearrangement and cell shape changes in the permissive Epi-VE. However, limitations in the field of view and time resolution of live imaging have so far been unable to place dynamic rosette formation and resolution in the context of the epithelial sheet during mouse AVE migration.

1.5 Summary

There remain many unanswered questions regarding AVE migration, not least the mechanism of AVE cell movement and the relative contributions of chemoattractants and mechanical forces.

Evidence supporting the suggestion that relatively increased proliferation in the posterior drives migration is mixed and can be tested with higher spatial and temporal resolution microscopy, but this visualisation has not been available until now. Theories of a chemoattractant such as *Dkk1*, or combination of redundant chemoattractants require careful time controlled genetic intervention to elucidate. Such a chemoattractant is likely to be required for active migration, but although PTEN and WAVE-mediated protrusions have been visualised in WT embryos, they are not necessarily indicative of a chemoattractant. Until these questions can be answered, the possibility of the A-P axis being specified prior to AVE migration remains.

Evidence further suggests that non-canonical PCP signalling is responsible for reducing the permissiveness of the ExE-VE, causing the AVE to stop and move laterally at the boundary, and the role of canonical *Wnt* in apical basal polarity. Finally, the relationship between AVE and the underlying epiblast is unknown: the AVE is known to pattern the epiblast by restricting posterior markers, but it is not known whether the AVE additionally influences the movement of epiblast cells. Likewise, whether the epiblast exerts any influence on the induction or migration of AVE cells, beyond a known requirement for proliferation.

1.6 Aims

While this thesis does not use genetic intervention to elucidate molecular mechanisms, it shows high resolution timelapse imaging coupled with a new data processing framework can provide insight into the likely modes of AVE induction and migration. In light of the above summaries, this thesis can be divided into three main themes for study, each requiring the investigation of a number of unanswered questions:

1. How is cell migratory behaviour coordinated in the context of the epithelial VE in wild-type embryos?

- What are the relative contributions of cell movements, cell rearrangements, cell division and cell shape change?
- Is there any correlation between the movement of the VE outer layer and the underlying epiblast during AVE migration?

2. Are there any regional differences in VE behaviour: anterior vs posterior?

- If so, do these asymmetries contribute to the direction of AVE migration?

1.7 Overview of thesis chapters

The next chapter reviews the recent developments in timelapse imaging to study AVE migration, and introduces the Light Sheet Fluorescence Microscopy datasets we have acquired, with the challenges it presents for quantitative analysis. The development of a computational framework to address these challenges is then discussed at length, including the spatiotemporal registration of the datasets and simplification of the quantitative analysis by projecting the VE apical layer from 3D to 2D.

Chapter 3 introduces further tools for analysis of the projected epithelial sheet for holistic analysis of global motion and cell shape changes, in addition to manual tracking and single cell annotation. This provides insights into the collective migration, tissue deformation, and cell intercalation. I further describe ongoing work on a convolutional neural network to automate cell segmentation and cell tracking.

Chapter 4 focuses on possible asymmetries during and prior to migration, looking at the tilt of the ectoplacental cone, eccentricity of the epiblast, rates of proliferation and the angle of cell division to shed light on the possible modes of AVE induction and migration.

The final chapter discusses previously unanswered questions introduced in this Introduction in light of the results.

Chapter 2: Light Sheet Fluorescence Microscopy Methods

2.1 Light Sheet Fluorescence Microscopy: advantages to studying AVE migration

It is clear from live widefield imaging that AVE cells migrate collectively, covering the ≈100µm distance to the ExE-VE in 4-5 hours (Srinivas et al., 2004), however, the mechanism driving AVE movement remains poorly understood. Confocal timelapse imaging studies of AVE migration in mice suffer from limited time and axial resolution (Hoshino et al., 2015; Omelchenko et al., 2014; Shioi et al., 2017; Trichas et al., 2011). Additionally, few papers other than Shioi et al. 2017 use a marker for non-AVE cells other than brightfield differential interference (DIC) microscopy, which Trichas et al. 2011 found is extremely hard to use to track cells on a cylindrical surface.

The most recent and comprehensive attempt at AVE cell tracking used live confocal microscopy with frames acquired every 3 or 10mins and 3 or 5µm z intervals (Shioi et al., 2017), an example of which is shown in Figure 2-1A. However their analysis does not fully take into account the nuances of 3D motion analysis.

A random sample of up to 244 cell nuclei from 3 *R26-H2B-GFP* mice were manually tracked, and another subset of cells across 17 *R26-PHA7-GFP* embryos were used to measure changes in apical size (Shioi et al., 2017). The *R26-PHA7-GFP* line (Shioi et al., 2017) uses PLEKHA7, a zonula adherens component, to mark cell membranes (Meng, Mushika, Ichii, & Takeichi, 2008). However, it is not clear from the paper how Shioi et al. tracked cells nor how measurements were carried out. Cells were chosen at random from regions across 3 embryos. From my own comprehensive manual counts discussed in later chapters, this covers approximately only one third of the cells in the VE. Cell movements are described qualitatively in terms of relative positions, but from the videos provided it appears no registration or other video stabilisation were conducted to enable artefact-

free measurements. The imaging appears to have taken place from only one view angle, with only one side of the embryo being analysed. The reported 'apical size' measurement from which conclusions regarding apical constriction were drawn appears to be the maximum cell length along the proximal-distal axis: a 1D measurement of a 2D concept. This limitation was no doubt caused by the lack of depth resolution required for volumetric imaging, leaving the 2D views incapable of making accurate area measurements of surfaces at different angles to the frontal plane.

The processing of frames is likely similar to those employed by Omelchenko *et al.* 2014 which is shown in Figure 2-1B. They describe manual temporal alignment of confocal images using MetaMorph (Molecular Devices), and rotation fixing using MetaMorph and Adobe Photoshop (Adobe Systems), and manual tracking of cell nuclei using a mixture of MetaMorph and Manual Tracking (ImageJ). They observe and manually track cell protrusions from a maximum of 109 cells from 6 independent experiments. Z-stacks appear to have been flattened using a maximum intensity projection and the tracking is 2D, with no accounting for volume or 3D distortions. They also employ Particle Image Velocimetry to track movement, but with the limitations of registration noted above.

Improved imaging capabilities are required to capture the full dynamics of migration with a greater and more comprehensive time resolution than that currently reported in confocal studies, in order to begin to understand the mechanisms underlying migration and its effect on the entire epithelial sheet.

Light Sheet Fluorescence Microscopy (LSFM) is particularly useful for live timelapse acquisitions of whole volumes (reviewed in Wan, McDole and Keller, 2019). It uses spatially selective optical sectioning to construct 3D volumes. Unlike the confocal microscope which illuminates pointwise and consequently imparts a high phototoxic load the longer a sample is imaged, LSFM illuminates whole sections in plane reducing the acquisition time and phototoxic load on the sample (Keller & Stelzer, 2008) (Figure 2-1C). LSFM has been used very successfully in timelapse studies of whole-

mount samples including early zebrafish development (Amat et al., 2014; Keller, Schmidt, Wittbrodt, & Stelzer, 2008), the zebrafish heart (Heemskerk & Streichan, 2015; Royer et al., 2016; Weber & Huisken, 2015), and in *Drosophila* (Amat et al., 2014; Heemskerk & Streichan, 2015; Royer et al., 2016; Tomer, Khairy, Amat, & Keller, 2012). Custom inverted lightsheets have been used to image mice from zygote to blastocyst (Strnad et al., 2016), *C. elegans* (Wu et al., 2011) and the chick during primitive streak formation (Rozbicki et al., 2015), but with the inverted configuration, LSFM loses the ability to rotate samples for higher-resolution multiple angle acquisition.

Two-photon light scanning microscopy was combined with nuclear H2B-GFP nuclear marker for lineage tracing experiments in the 8-32 stage mouse (McDole, Xiong, Iglesias, & Zheng, 2011). The study of Interkinetic Nuclear-like Migration (INM-like) in the epiblast of the E5.5 mouse and INM in the E6.5 epiblast has been made possible using a Digital Scanned Lightsheet Microscopy (DSLM), which scans the laser beam in-plane instead of illuminating a whole 2D plane, an earlier approach which imparts a higher peak laser power onto the specimen, and causes defects after 3 hours of imaging with frame acquisition every 1.5mins (Ichikawa et al., 2013, see also Keller and Stelzer, 2008).

Most recently, custom built Simultaneous Multiview (SiMView or MuVi-SPIM) LSFMs combined with software designed to overcome movement and changes in scale and morphology not typically seen in the zebrafish or *Drosophila* (Royer et al., 2016; Udan, Piazza, Hsu, Hadjantonakis, & Dickinson, 2014) have allowed the imaging of pre-gastrulation embryos (Amat et al., 2014; McDole et al., 2018) (Figure 2-1D).

The Ziess Z1 microscope (Figure 2-1E) was the first commercially available LSFM, widening access to lightsheet technology for lab groups without the resources to build custom microscopes. It enables full 3D imaging of semi-transparent embryos approximately 100μm in width with single angle acquisition, and can imaging samples from multiple angles to overcome limited penetration depth due to light scattering.

Unlike the SiMView LSFM (Krzic, Gunther, Saunders, Streichan, & Hufnagel, 2012; Tomer et al., 2012), the Ziess Z1 has only one detection and two illumination arms. To capture multiple views, the sample itself is rotated, leading to slower imaging times and the potential for small positional differences as the culturing sample shifts during acquisition. Nevertheless, mouse embryos have been cultured successfully in the Z1 with 5 acquisition angles, sufficient to capture a whole volume from the E6.5 embryo and enabling a 24 hour study of the yolk sac (Udan et al., 2014). Furthermore, very little difference was reported in performance between a custom SiMView LSFM and the Ziess Z1 when using nuclei tracking for lineage tracing in *Drosophila*, although the individual Z1 angle acquisitions were not fused in order to avoid artefacts, and only the ventral angle analysed for cell dynamics (Amat et al., 2014).

The E5.5 embryo is more delicate than that of the E6.5 embryo, and challenging to imaging live for extended periods. They are difficult to culture and mount, more susceptible to phototoxicity, and exhibit dimmer fluorescence than in later stages. Advances made in the Srinivas group now make the culture of delicate E5.5 mouse embryos inside a Ziess Z1 LSFM possible for around 15 hours. The smaller size of the mouse at E5.5 enables full volume capture with only two acquisition angles, and does not require software developed for custom set ups to automatically refocus and scale the imaging plane (Royer et al., 2016). The accessibility of the outer VE, coupled with the variety of mutants (reviewed by Stower and Srinivas, 2014) and number of fluorescent lines available lend this system to the first comprehensive timelapse study of AVE cell migration within the entire epithelial layer, and the epiblast beneath.

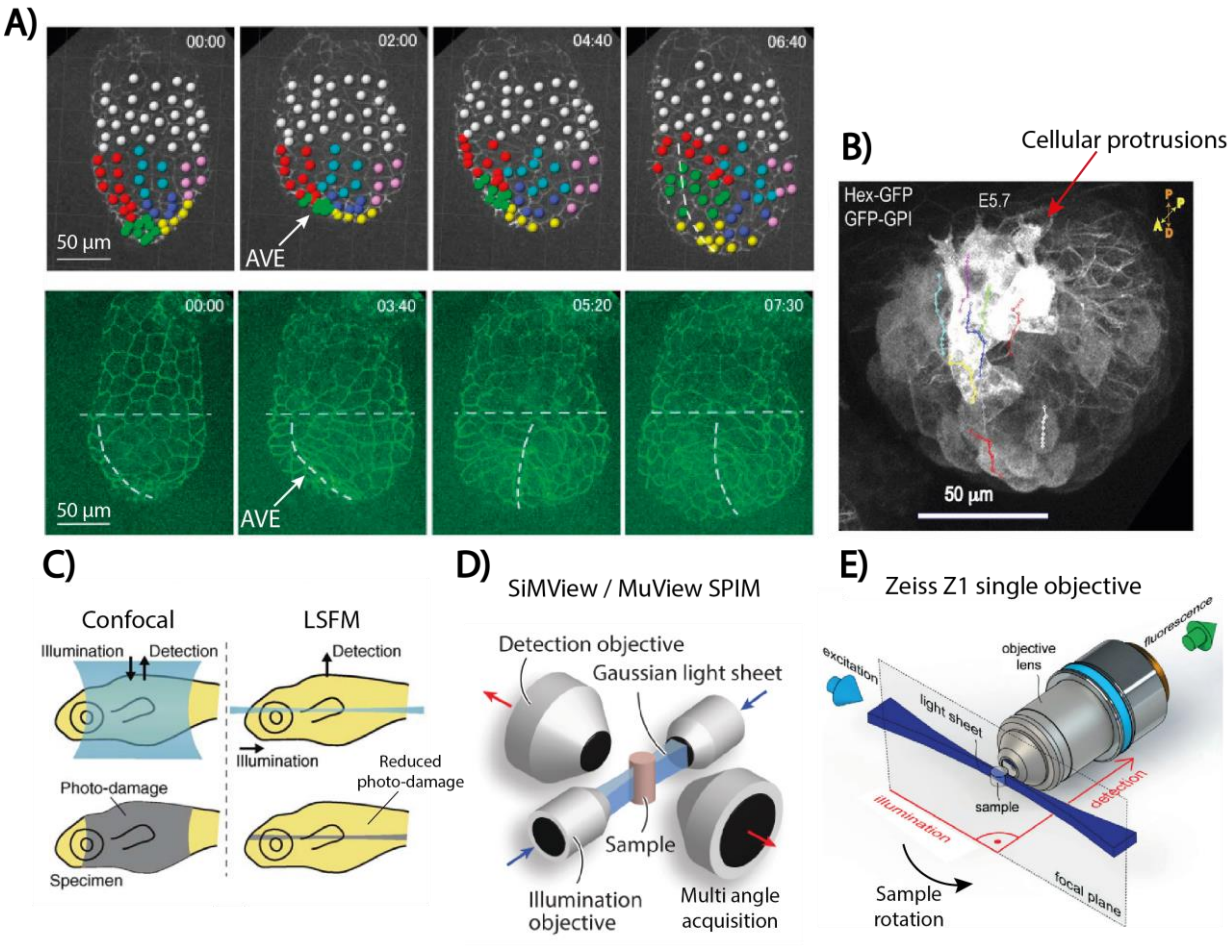

Figure 2-1: Current methods for timelapse imaging. A) Image of manually tracking nuclei (coloured dots) and R26-PHA7-GFP membrane fluorescence line (adapted from Shioi et al., 2017). E5.5 embryos were imaged for 24hours, with no temporal registration, leaving them to drift and rotate. Membrane analysis was carried out from a narrow field of view which employed a 1D vertical measurement of apical size (dotted lines) not accounting for 3D surface curvature. B) Manual tracking of 8 cells over confocal timelapse of Hex-GFP positive cells (adapted from Omelchenko et al., 2014). Z-stacks appear to have been flattened by maximum intensity projection for 2D tracking. C) LSFM optical sectioning reduces photodamage when compared with a confocal microscope (adapted from Keller and Stelzer, 2008). D) SiMView/MuVi-SPIM schematic showing the use of two objectives to capture opposing views simultaneously (adapted from Wan, McDole and Keller, 2019). E) Schematic of the Zeiss Z1 LSFM, with a sample which rotates in-place to capture different angles with one objective (adapted from Selchow and Huisken, 2013).

2.2 Method: culture and imaging of mouse embryos

2.2.1 Mouse strains, husbandry, and embryo collection

Animal work and LSFM imaging was carried out by Dr Matthew Stower under project licenses 30/3420 and PCB8EF1B4, according to Home Office regulations.

The Lifeact construct originates from a pCAG vector, with a cytomegalovirus (CMV) enhancer, chicken-β-actin promoter, chimeric intron and 17aa actin binding peptide-GFP sequence, and polyadenylation tail (Riedl et al., 2010) (Figure 2-2A). *Lifeact* transgenic mice from a C57BL/6 background were maintained on a 12h light, 12h dark cycle. Noon on the day of finding a vaginal plug was designated 0.5 days post conception (dpc). Embryos of the appropriate stage were dissected in M2 medium (Sigma) with fine forceps and tungsten needles.

The *Gt(ROSA)26Sor*$^{tm4(ACTB\text{-}tdTomato,\text{-}GFP)Luo}$ line (referred to as '*mTmG'*) is described by Muzumdar et al. 2007. Membrane targeted tdtomato is expressed until it is removed by Cre recombinase mediated recombination enabling expression of membrane targeted GFP (Figure 2-2B).

The *Hex-GFP* line has a transgene of 8.0kb of the *Hex* (*Hematopoietically Expressed Homeobox*) promoter sequence, with 4.2kb upstream and 3.8kb downstream of the ATG of Exon1 (Rodriguez et al., 2001) driving GFP expression (Figure 2-2C). This includes the enhancer required for expression in AVE cells at E5.5 (P. Q. Thomas et al., 1998).

The *mTmG* line was crossed into the *Hex-GFP* by Dr Satish Arcot Jayaram to create a stable double homozygous line. For experiments the *mTmG ; Hex-GFP* stud males were crossed with CD1 females.

The *Ttr-Cre* line (obtained from Dr AK Hadjantonakis) was maintained in a CD1 background. *Transthyretin* (*Ttr*) is expressed in the VE in pre-streak embryos (Mesnard et al., 2006). The *Ttr-Cre* line consists of a 3kb of the *Ttr* promoter driving *Cre* recombinase expression between Exon2 (Kwon

& Hadjantonakis, 2009) (Figure 2-2D). For experiments *Ttr-Cre* stud males were crossed with *mTmG* females.

2.2.2 Embryo culture and light sheet microscopy

The embryo culture was carried out as described in Trichas et al. 2011. Culture media consisted of 50% knockout serum media replacement (Fischer) and 50% CMRL (Invitrogen) supplemented with L- glutamine, equilibrated at 37°C and 5% CO2 for at least 2h prior to use. For imaging with the Ziess Z1, a cylinder of 2% agarose 1xPBS, was first drawn up into to a glass capillary and a cavity was created using a 150µm diameter wire. Once the agarose had set the wire was removed and the sample embryo placed into the lumen of the cavity, and kept submerged in the culture medium. The capillaries were mounted in the Z1 microscope chamber, filled with 25ml of culture medium and maintained at 37°C and 5% C02 (example set up in Figure 2-2E). It is possible to culture and image a maximum of two embryos as a time: these embryos have the same litter identifier.

Example embryos from each line are shown in Figure 2-2F. Ubiquitously expressed *Lifeact-GFP* was excited at 488 nm. For live samples a 2µm-interval z-stack volume was acquired with 63 x (1 NA) objective, every 5mins over a period of up to 10 hours. Angles were acquired using dual-side illumination, at (0°, 180°), or in one case (0°,140°), with a voxel size of 0.185 x 0.185 x 2.0µm.

The 2-colour *mTmG ; Ttr-Cre* and *mTmG ; Hex-GFP* embryos were imaged using a similar method, but at intervals every 10mins using the 561nm laser for RFP and 488nm laser for GFP. Laser power for the 488 nm laser (Coherent, 135 µW ± 228 nW) was set at 2% for single channel imaging, or 1.5% in combination with the 561 nm laser (Coherent, 106.9 µW ± 248 nW) set at 1.5%.

The Zeiss Z1 has a default x-y resolution of 0.1815µm, and user set z resolution of 2.0µm. Acquisition parameters were chosen to balance y-z spatial resolution and a temporal resolution capable of capturing cell divisions, with the increased phototoxic load from a long timelapse and multiple angle acquisition.

2.3 Mouse lines and fluorescence: advantages and disadvantages

Each of the three mouse lines in our dataset has specific uses, but come with significant challenges we must overcome in order to extract quantitative information from them.

We use the *mTmG ; Hex-GFP* embryos to specifically mark the AVE cells in the VE layer. The GFP-labelled (green) AVE cells migrate against the ubiquitously expressed membrane-targeted tdTomato-labelled (red) background. To analyse the context of the migration in the entire sheet, we also use the *Lifeact-GFP* F-actin marker to delineate cell membranes (shown in greyscale throughout), and the *mTmG ; Ttr-Cre* embryos which separately mark the (GFP expressing) VE from the (tdTomato expressing) epiblast and ExE, allowing computational removal of the VE layer. The *mT* background localises fluorescent proteins to the Epi and ExE membranes, giving a strong and consistent signal in both tissues. However, low level tdTomato expression in the VE leads to problems exclusively visualising the inner tissues.

The fluorescent reporter labelling comes with several caveats. The *Ttr-Cre* signal is widespread in the VE but not fully penetrant, and *Hex* likewise only expresses in a subgroup of AVE cells (Srinivas et al., 2004). The fluorescent reporter may not capture fast temporal events as there may be a lag of around 14-60mins in expression of the GFP signal as the protein is transcribed and translated, and folds (Iizuka, Yamagishi-Shirasaki, & Funatsu, 2011; Nomura, Tanaka, Poellinger, Higashino, & Kinjo, 2001). Additionally, GFP is not rapidly degraded, so the signal will remain after the gene has stopped producing the protein. The membrane targeted GFP and tdTomato from the *mTmG* embryos tends to accumulate in a thick layer in the apical region of VE cells giving a shrouding effect. The cytoplasmic GFP in the *Hex-GFP* embryos has a similar problem. This means that although membrane fluorescence in the epiblast cells, which have a much smaller apical surface, remains very clear, neither the *mTmG ; Hex-GFP* nor the *mTmG ; Ttr-Cre* embryos enable delineation of cell boundaries in the VE or AVE.

The *Lifeact-GFP* line does enable visualisation of the subcortical actin network and can be used to delineate cell boundaries in the VE and epiblast regions. Embryos from this line can be used to extract cell specific data such as cell shape and area, in addition to enabling the number of cells to be counted and the movement of each cell to be tracked.

However, F-actin is also expressed on the apical surface of VE cells leading to difficulties in delineation. This is particularly prevalent in the ExE-VE during AVE migration when F-actin and Myosin-IIA are enriched to the apical cortex (Trichas et al., 2011). The F-actin GFP signal is also inhomogeneous, both over small areas, and throughout the embryo, with brighter junctions, light scatter at greater depths, and brighter membranes orthogonal to the focal panes and dimmer membranes *en-face* due to their alignment versus the anisotropic point spread function of the laser (see Mosaliganti et al., 2012). Imaging at three angles instead of two would help address the latter problem, but at the cost of temporal resolution due to a greater phototoxic load. Finally, expression is particularly dim in the ExE, despite phalloidin staining suggesting that F-actin expression is homogeneous in fixed samples. The inhomogeneity of F-actin therefore prevents its use as a quantitative measure of tissue stress.

These factors effecting intensity discount the use of threshold based techniques to identify membranes. Background or apical signal in one area may be brighter than the membrane fluorescence in another. As opposed to photobleaching, common when imaging fixed samples using a confocal microscope, under LSFM the fluorescence in each embryo increases in brightness as the embryos age, leading to the need to balance the available grey levels in the dimmer earlier timepoints without saturating the later timepoints.

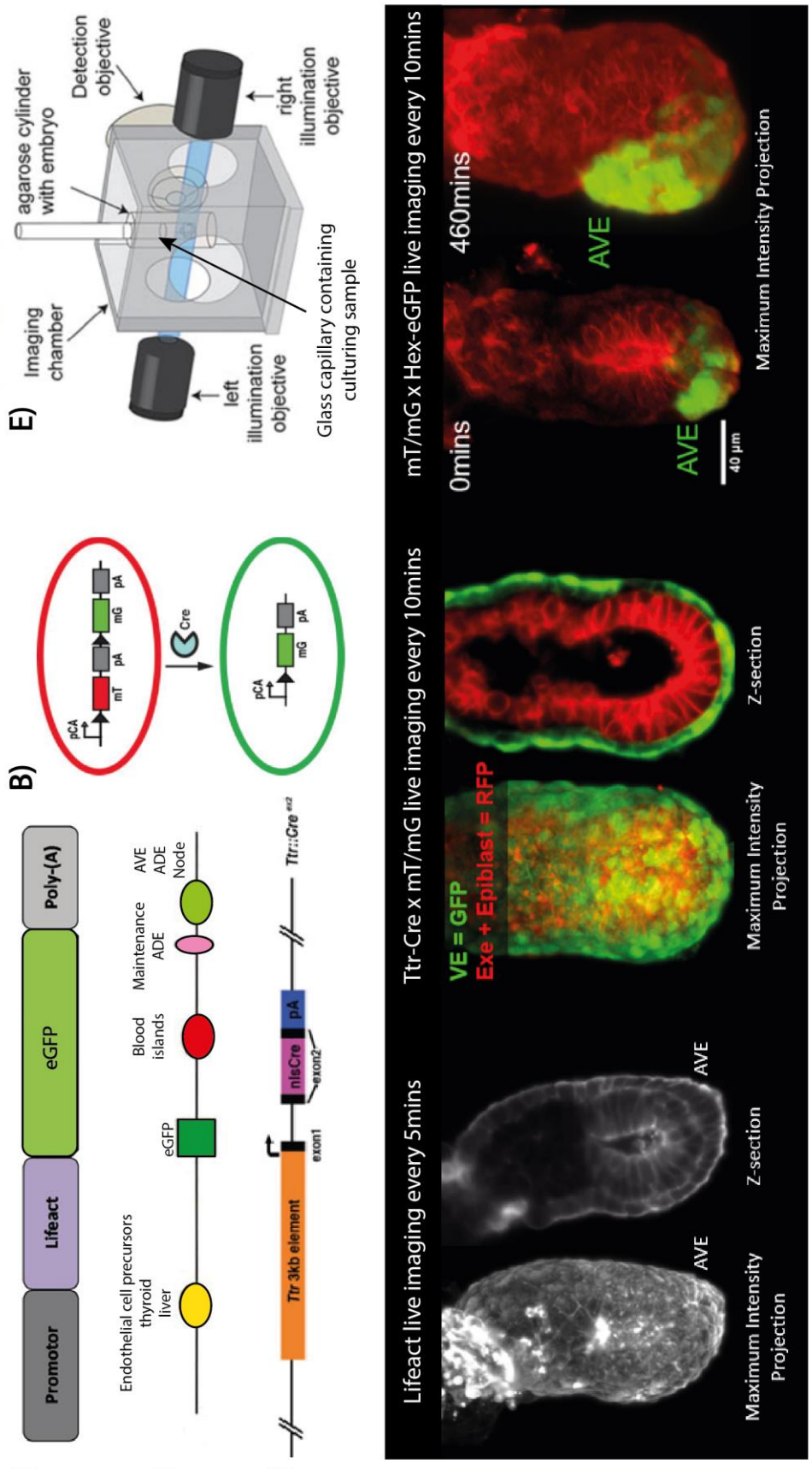
A)
Promotor
Lifeact
eGFP
Poly-(A)
C)
Endothelial cell precursors
thyroid
liver
eGFP
Blood islands
Maintenance ADE
AVE ADE Node
D)
Ttr 3kb element
exon1
nlsCre
pA
exon2
Ttr::Cre
B)
pCA
mT
pA
mG
pA
Cre
pCA
mG
pA
E)
agarose cylinder with embryo
Detection objective
right illumination objective
Imaging chamber
left illumination objective
Glass capillary containing culturing sample
F)
Lifeact live imaging every 5mins
Maximum Intensity Projection
AVE
Z-section
AVE
Ttr-Cre x mT/mG live imaging every 10mins
VE = GFP
Exe + Epiblast = RFP
Maximum Intensity Projection
Z-section
mT/mG x Hex-eGFP live imaging every 10mins
0mins
460mins
AVE
AVE
40 µm
Maximum Intensity Projection

Figure 2-2: The mouse lines acquired for this dataset. A) The Lifeact construct (adapted from Reidl et al., 2010). B) Schematic of the mTmG construct before (red circle) and after (green circle) Cre-mediated recombination (adapted from Muzumdar et al., 2007). C) The Hex construct is a copy of the Hex promoter driving GFP and is inserted randomly into the genome as a transgene (adapted from Rodriguez et al., 2001). D) The Ttr-Cre construct consists of 3kb of the Ttr promoter driving Cre recombinase expression between Exon2 (adapted from Kwon and Hadjantonakis, 2009). E) The Ziess Z1 imaging chamber. A sample is placed within the chamber, cultured inside an exposed hollow column of agarose within a glass capillary (adapted from Udan et al., 2014). F) Examples of Lifeact, mTmG ; Ttr-Cre and mTmG ; Hex-GFP embryos in this dataset.

2.4 Existing computational tools for analysing LSFM datasets

Despite the optical advantages of LSFM, there are practical challenges that need to be overcome. A single timeseries output from the Zeiss Z1 is very large with initial 16bit datasets of up to 0.5 TB. Such datasets require large amounts of computing space and RAM to store and process. The Ziess .czi imaging format may require conversion to a more common imaging format such as TIFF (.tif) for use with other software. The two angles necessary to capture high quality data on both sides of an opaque sample require subsequent stitching using spatial registration. The live embryos rotate, drift, and grow during acquisition, coupling the movement of cell migration with those of the embryo as a whole. Direct measurement of cell motion without correction is therefore susceptible to over- or under-estimation. Even once these additional movements are accounted for through spatiotemporal registration, the dataset is still 3D. Visualisation, cell segmentation and tracking of 3D datasets is extremely time consuming to do manually, with a single volumetric timepoint taking around 24 hours to hand outline. With AVE migration occurring over 4-5 hours (Srinivas et al., 2004), or 60-100 timepoints at 5min resolution, the manual extraction of quantitative information from complete LSFM datasets is extraordinarily impractical.

Development of software for the analysis of 3D LSFM datasets has focussed on *Drosophila* datasets which possess very good signal-to-noise ratios (Amat et al., 2014; Heemskerk & Streichan, 2015;

Royer et al., 2016; Tomer et al., 2012). Existing automatic segmentation and tracking methods have largely used nuclei which are spatially well separated and not marked in this dataset. Automatic methods have rarely been applied to mice and manual methods remain the norm to annotate timelapse imaging of AVE migration (Omelchenko et al., 2014; Shioi et al., 2017; Trichas et al., 2011). The section below introduces and discusses my attempts to use published software to analyse the acquired mouse LSFM datasets.

2.4.1 Registration and pre-processing

The Zeiss Z1 Zen software has two modes of registration: registering dual fusion of the left and right illumination, and registering angles. The mean dual angle fusion was found to work well, with no additional artefacts detected, and was used throughout imaging. The main barrier to using the Zen software was registration of multiple acquisition angles. This is carried out through an interactive registration module, but involves manually moving each acquisition angle to overlay the other. The requirement to manually register views for all the timepoints of a drifting and rotating embryo individually was highly impractical over a timelapse.

A few other commercial and open source tools are commonly used for analysing LSFM or confocal timelapse data. A useful tool for visualising timelapse data is Volocity (Improvision). However, Volocity often crashes while attempting to process large timelapse datasets. Another option is Imaris (Bitplane), frequently used for 3D manual segmentation, where volume, surface area and intensity data can be found (Watanabe et al., 2014). It also has manual nuclei tracking capabilities (Ichikawa et al., 2013; Shioi et al., 2017; Udan et al., 2014). Although Imaris can be used to track these volumes over time by giving cells specific IDs, the manual process is cumbersome and only practical for use in a small number of cells, and there is no built in capacity for linking mother and daughter tracks after cell divisions.

Several ImageJ plug-ins have already been mentioned, such as Manual Tracking (Cordelières, 2005) alongside the standard visualisation tools. Another ImageJ plug-in designed with LSFM datasets in

mind is BigDataViewer (BDV) (Pietzsch, Saalfeld, Preibisch, & Tomancak, 2015), which I found was the most useful tool for visualisation of the image stacks. The Ziess Z1 .czi files are very large, and difficult to load and explore in established image processing software. BDV excels in loading virtual slices of a dataset in any 3D orientation, optimising scaling, partial loading, and caching of data utilising its HDF5 format. It also works directly with .czi formatted data before translating it into the more efficient .hdf5 format.

In early versions of my data-processing framework, the LSFM dataset was registered using the Multiview Reconstruction Application (MVRA) (Preibisch et al., 2014; Preibisch, Saalfeld, Schindelin, & Tomancak, 2010) integrated with BigDataViewer. MVRA was originally built to register datasets using fiduciary, fluorescent beads as a guide, but while attempting registration with embryos cultured with beads, I found patches of particular brightness at junctions were able to act as references points instead of physical beads (shown in Figure 2-3A). However, the program again required a manual rotation and then translation to seed the registration of two angles, which could then be applied to all embryos, taking a number of hours and usually being run overnight. However, options for merging registered angles did not allow weighting the good and bad data from the two angles, which had to be done in an additional step involving custom written code. The timelapse registration was also difficult to apply successfully to this dataset, often failing in several places over the long timelapse.

Neither BDV nor MVRA have the facility for volume or surface viewing, a key requirement for easily tracking cells in the VE. Another plug in, ImageJ 3D Viewer (Schmid, Schindelin, Cardona, Longair, & Heisenberg, 2010) was found to be useful for volume imaging, as discussed in Section 4.2 *The ectoplacental cone tilt relative to the A-P axis clusters into two groups at E5.5*.

2.4.2 Cell segmentation and tracking

Existing automated tracking methods have predominantly been developed for nuclear markers. It is typically easier to track nuclei than it is to segment and track cell boundaries from membrane

markers. Nuclei are thicker, more compact, and more consistent in shape and marker expression (Mosaliganti et al., 2012). One such program, Tracking with Gaussian Mixture Models (TGMM) has demonstrated success in large scale nuclei tracking in *Drosophila*, zebrafish, and mouse, with an automated, semi-automated, or manual approach, including in the automatic detection of cell divisions (Amat et al., 2014). More recently Massive Multiview Tracker (MaMuT) has integrated ImageJ tracking plugins such as TGMM and the single particle tracker, TrackMate (Tinevez et al., 2017), with registration and visualisation plugins BDV and MVRA, and has been used to investigate limb development in the crustacean *Parhyale hawaiensis* (Wolff et al., 2018). Earlier approaches include Modular Interactive Nuclear Segmentation (MINS) for nuclei tracking in confocal-imaged mouse blastocysts (Lou, Kang, Xenopoulos, Muñoz-Descalzo, & Hadjantonakis, 2014).

However, tracking nuclei alone does not give information on cell shape or size which are also vital to the understanding of epithelial sheet mechanics in the context of AVE migration. Many membrane segmentation methods use the nuclei as 'seeds' to provide additional information for watershed algorithms run on the cell membrane fluorescence. Such a combined approach has been applied to zebrafish (Zanella *et al.*, 2010; BioEmergences: Faure *et al.*, 2016) and *Drosophila* (RACE: Stegmaier *et al.*, 2016).

In mouse, the most comprehensive reference for single cell gastrulation to date employed a long SiMView timelapse from E6.5 to E8.5 with general and lineage specific nuclear markers, combined with MaMuT and TGMM tracking (updated to include a machine learning based division detection algorithm and supplemented with statistical vector flow analysis) (McDole et al., 2018). The study used the *CAG-TAG* mouse line, which uses HISTONE 2B-GFP to label nuclei, and membrane targeted tdTomato (Trichas, Begbie, & Srinivas, 2008). Unfortunately the signal of both fluorophores is very weak at E5.5 (unlike at E6.5) and the membrane targeted tdTomato also has the same problem of shrouding in the VE as our *mTmG* embryos, hence its absence in our dataset.

However, the nuclei of mouse at E5.5-6.5 are also large relative to the cell and it is questionable if crossing a *H2B-RFP* line with the *Lifeact-GFP* would provide suitable seeds to aid watershed algorithms, as can be seen in the data from Shioi et al. 2017. Attempts to automatically track H2B-GFP tagged nuclei in E6.25 mice embryos imaged using SiMView LSFM showed success over a 2 hour period, but were noted to be "exceptionally challenging" compared to gastrulating *Drosophila* or zebrafish embryos due to the "crowded cells, low temporal sampling, low image contrast and specimen rotation over time", despite capturing and fusing data from 4 angles using bidirectional illumination (Amat et al., 2014). Even capturing just 2 angles, imaging a *H2B-GFP* line in younger embryos would require greater laser power and 4 volumes per time point to capture the additional channel, more than doubling the photo-toxic load on the embryo and potentially causing developmental defects.

For our *Lifeact* dataset, we were left only with the option of membrane fluorescence segmentation. A few existing programs have shown success in membrane segmentation. The most recent of these, Real-time Accurate Cell-shape Extractor (RACE) (Stegmaier et al., 2016) has been successfully combined with TGMM (Amat et al., 2014) to segment cells in 3D in *Drosophila*, zebrafish and E6.5 *CAG-TAG1* mice, with nuclear GFP and membrane-localized tdTomato. This combination was shown to outperform other programs such as the plant cell segmentation software, MARS (Fernandez et al., 2010), the zebrafish somite formation segmentation software, ACME (Mosaliganti et al., 2012), the *Drosophila* segmentation, EDGE4D (Khan, Wang, Wieschaus, & Kaschube, 2014) and overcomes the key difficulty noted by Khan *et al.* in applying methods developed for different systems to a new one. However, the RACE segmentation was applied primarily to fixed SiMView and confocal images, and only applied to timelapse data of the inherently high signal-to-noise *Drosophila* embryo.

Although the performance of RACE in published data used both nuclear and membrane segmentation, the use of nuclei is not mandatory, inverted membranes can also act as watershed

seeds for segmentation. Attempts to simplify the approach and segment z stacks of embryos using XPIWIT (Bartschat et al. 2016, kindly provided by Dr Johannes Stegmaier), a wrapper for the Insight Toolkit (McCormick, Liu, Jomier, Marion, & Ibanez, 2014; Yoo et al., 2002) including elements of RACE, were unsuccessful. This included a noble attempt by Dr Stegmaier, who noted the especially low signal-to-noise ratio in the early embryo. Further attempts to segment the best data on the VE apical surface, enhanced using a maximum intensity projection of the top 5 z-stacks, also lead to either under- or over-segmentation (Figure 2-3B). I hypothesized the failure was because XPIWIT includes a binary threshold which is problematic for the embryo data with inhomogeneous fluorescence, including embryo images where concentrated 'pools' of actin hamper attempts to seed the watershed algorithm using the inverted fluorescent signal.

Additional attempts to segment the dataset using tensor voting as employed by Automated Cell Morphology Extractor (ACME) (Mosaliganti et al., 2012) and the first machine learning software approach Interactive Learning and Segmentation Toolkit (ilastik) (Sommer, Straehle, Kothe, & Hamprecht, 2011), were also unsuccessful due to the low signal-to-noise and F-actin inhomogeneity.

As it became clear that the existing methods for both registration and membrane segmentation were unsuitable for this difficult dataset, we decided to adopt a different approach, which involved writing custom software. This data processing framework is described in the next section.

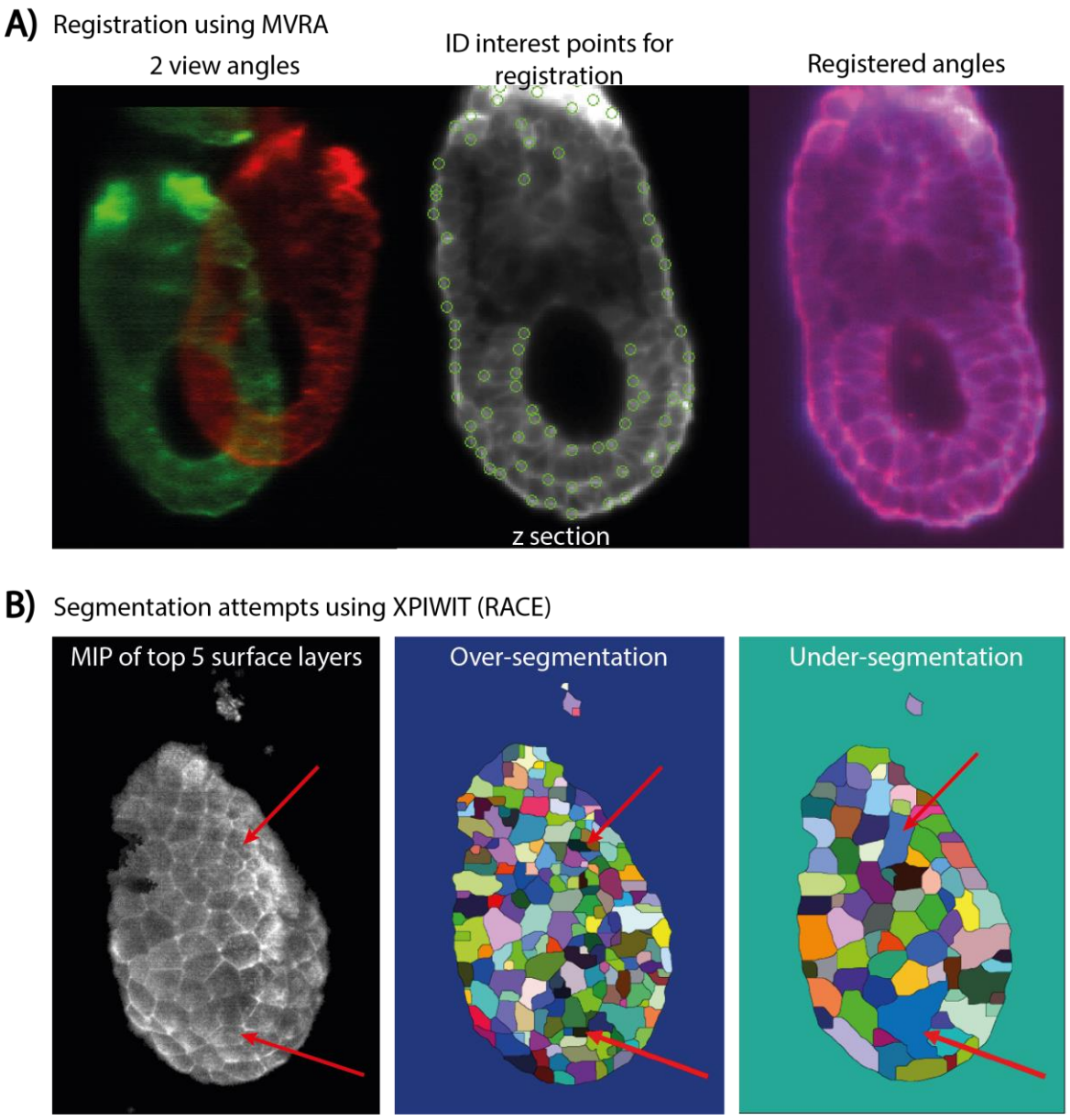

Figure 2-3: Early attempts to register and segment the Lifeact dataset using existing software. A) Registering angles in Big Data Viewer: bright intensity at junctions could be used as interest points (green circles) instead of florescent beads. By comparing the pattern of interest points between the 2 data-sets they were registered automatically. B) Attempts to use XPIWIT, to segment 2D z-stacks of the LSFM data were unsuccessful due the low signal-to-noise ratio. Improving the surface data by performing a maximum intensity projections (MIP) of the top 5 z-stacks improved the signal-to-noise ratio, but still showed over and under-segmentation using XPIWIT (red arrows).

2.5 Overview of the data processing framework

LSFM allows the imaging of whole 3D volumes of delicate E5.5 mouse embryos for up to 15 hours, in order to view AVE migration with a high time resolution. However, to work with the very large datasets, it is necessary to register them in both space and time to capture high quality volume data throughout the embryo, remove artefactual movements, and isolate relative cell movement. Any large scale quantitative analysis also needs to be automated to practically capture full stages of development. Existing automated methods have shown success for large datasets of LSFM *Drosophila* and zebrafish images and fixed mouse datasets as early as E6.25 for which both membrane and nuclei are clearly labelled (with nuclei acting as seeds for segmentation). However, these solutions adapt poorly to automatically segment live LSFM E5.5 mouse imaging datasets. In order to effectively address the many remaining questions about the AVE, myself and Dr Felix Zhou worked closely to develop a new data processing framework which addresses these challenges.

Figure 2-4A summarises the proposed data processing framework which is discussed in this chapter, co-developed by myself and Dr Felix Zhou. The LSFM embryos are first 3D registered in space and time to create an invariant 3D coordinate system as a pre-processing step. Then, noting the fact that the VE remains as a monolayer throughout migration, we simplify the 3D analysis problem to a more tractable 2D problem by projecting the 3D surface onto a 2D plane through surface reparametrization.

In Chapter 3 I will show how this 2D projection enables easier manual annotations and the use of an alternative superpixel based tracking method, similar to existing vector flow methods that proved extremely useful for extracting quantitative information about collective epithelial movement. With this bespoke framework, we conduct the first comprehensive examination of AVE migration in the mouse and demonstrate the benefits of greater spatiotemporal resolution in the quantitative analysis of a complex, dynamic system. I then further discuss ongoing work to automate the segmentation and tracking of cells in the 2D projections using the *Lifeact* membrane

fluorescence. This is an alternative data-driven approach to the traditional seeded watershed algorithms: a convolutional neural network to artificially enhance the membranes in the unwrapped 2D video (discussed in detail in Section 3.5 *Developing tools for automated single cell analysis*). This combined registration, projection and CNN segmentation approach enables the extraction of key biological information such as 3D cell area, shape, and individual cell dynamics.

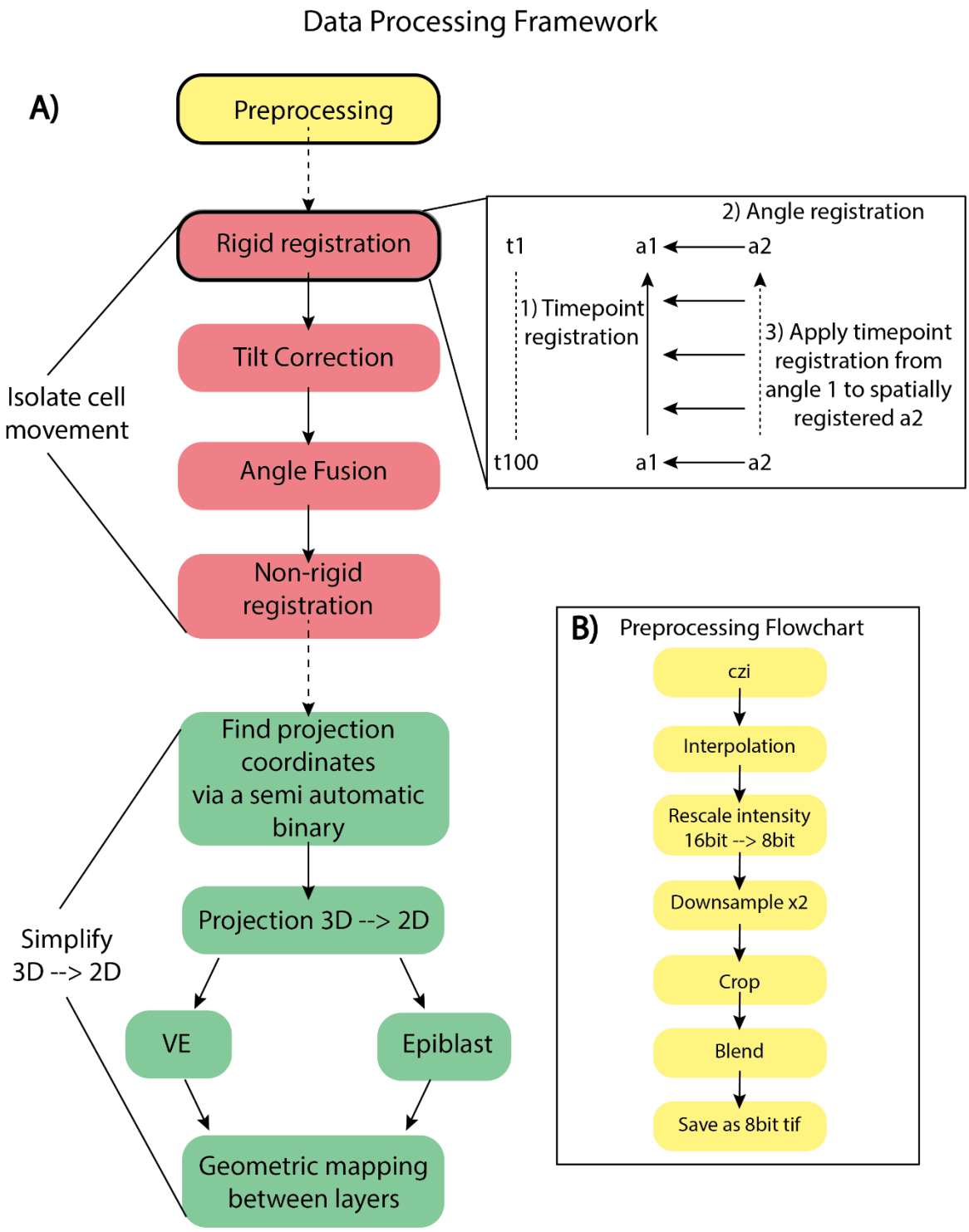

Figure 2-4: Summary of the steps in the data processing framework. A) The flowchart shows the complete framework, from preprocessing through to the rigid spatial and temporal registration and fusion of angles, and the non-rigid registration which completes the isolation of relative cell movement and simplifies the next stage. Lastly, layers of the VE and epiblast are projected onto a 2D surface where they can be more easily analysed. B) Highlights the prepocessing steps which transform the Zeiss Z1 raw output into a more workable format and size.

2.6 Preprocessing raw image data

Several preprocessing steps were developed and implemented to reduce the initial data size for easier analysis: 16bit to 8bit conversion, bounding box cropping and volumetric downsizing. A summary flowchart can be seen in Figure 2-4B.

The first step of the framework processes the raw image data from the Zeiss Z1 into a more standard imaging format for subsequent analysis. The raw LSFM dataset is 16bit and in the custom Ziess .czi format. While some programs such as MVRA and BigDataViewer can directly use these .czi files, the .tif format is more widely accepted by most biological imaging software. The size of a raw .czi dataset is approximately 0.5-1TB. This is very difficult to store and requires several hours to transfer over standard USB3.0 connections. Furthermore, processing the full size 16bit images resulted in memory errors on a computer with 16GB RAM.

In order to reduce the size of the dataset, images were converted from a 16bit .czi to an 8bit .tif format and downsampled by a factor of 2 (after interpolation).

The conversion from 16bit to 8bit comes at the expense of reduced resolution in the lower intensity grey levels. However, the conversion is justified as the 16bit datasets make very little use of the full range of available greyscale levels. A common intensity range chosen was 240-2500 from the 0-65535 available, which balanced the range of grey levels available while not saturating extremely bright patches of actin typically appearing at junctions, in dividing cells and in the EPC.

Of the three fluorescent reporter mouse lines, the *Lifeact* embryos in particular increased in intensity as the embryo aged, in which case the available grey levels earlier in the timelapse were sacrificed for those later on. Rescaling all the timepoints by the same levels allows relative comparison of the intensity of the same embryo over the timelapse. Appropriate intensity levels were identified using maximum intensity projections of first and last timepoints (of each view) in

ImageJ, using the original .czi files. The implementation for two colour frames uses separate rescale ranges for each channel.

Raw acquired datasets possess voxel anisotropy in z-direction due to the default Zeiss Z1 x-y resolution and the user set z resolution chosen to minimise phototoxicity when capturing a long timelapse. The initial voxel anisotropy ratio of acquired images was approximately 11, or (0.1815 : 0.1815 : 2.0) µm in (x,y,z). In order to facilitate spatiotemporal registration and visualisation, voxels were interpolated to be isotropic (0.1815 : 0.1815 : 0.1815) µm. This interpolation does not add new information, but is merely a linear gradient of the information in the original stacks. The interpolation increases the size of the dataset by the anisotropy factor of roughly 11 (2.0/0.1815).

To further reduce data size, raw images were cropped based on a rough binary threshold segmentation to create a bounding box. A parameter choice allowed for manually expanding the cropping bounding box boundaries, with a larger border allowing for changes in embryo orientation and shape during the downstream spatiotemporal registration stage. For the two colour embryos, the cropping needed to be the same for each channel in order to keep both channels in the same coordinate space, so a particular channel was specified as a reference to find the cropping parameters. For the two colour lines, this reference was the tdTomato (red) channel or occasionally the GFP from the *Ttr-Cre* embryos (green) if the embryo had a large EPC. The registration was robust to the different fluorescence expressions.

Downsampling a volume image by a factor N in all three spatial dimensions decreases its size by a factor of N^3. A downsampling factor of 2 in each dimension, or a decrease in size by a factor of 8, leading to a roughly corresponding decrease in processing time was chosen to make the dataset more computationally tractable. This downsampling decreases the real spatial resolution in x-y, from 0.1815µm to 0.3630µm. A cell in the E5.5 embryo is on the order of 10µm in diameter, giving more than enough resolution to still identify cellular shape, area, and observe individual cell divisions.

Additional preprocessing steps involve inverting the raw image (some embryos were imaged upside down) and an option to perform a moving average blend to reduce the appearance of striations, an artefact of the 2D plane imaging.

The final output is a cropped, interpolated embryo, with a spatial voxel resolution of 0.3630µm in x-y-z, and a size of approximately 200MB per 8bit .tif file of a video frame, or 30-45GB for a timelapse with two separate acquisition angles per timepoint.

2.7 Registration

Following the initial preprocessing steps, the dataset needs to be spatiotemporally registered. As imaging has evolved from 2D to capturing 3D volume and 4D timeseries data, so too have techniques for image registration. Image registration is particularly prevalent in the field of medical imaging, where it is routine practice to compare images taken using multiple modalities (e.g. CT, MRI, PET) and between patients by creating reference 'atlases' of organ data (reviewed in Oliveira and Tavares 2014).

Methods for registering images taken either at different angles (multi-view spatial) or at different times (spatiotemporal) loosely fall into two basic categories based on methodology; intensity based and feature based. In feature based registration, key features in the images such as anatomical structures are identified and may involve image segmentation.

Once key features have been identified, an iterative registration process minimises a computed 'cost' based on the combined distance or overlap of the key features between images. If a new transformation is found which reduces the cost (increases similarity), the search is updated and restarted from the more similar point, until the cost is minimised. The same process occurs for

intensity based registration, only the features used for matching involve the raw intensity of all the pixels or voxels instead of select sparse features.

Registration methods are also classified as either rigid or non-rigid (Figure 2-5A). Rigid registration encompasses linear geometric transformations such as translation, rotation, and scale, which effect the entire embryo equally, preserving its shape (treating it as a rigid body), whereas non-rigid registration encompasses local non-linear transformations such as warping which modify the shape of either the whole embryo or a small section of it.

The main challenge of registering live LSFM E5.5 embryos to study AVE migration is isolating the relative cell migration from additional captured motion components such as embryo drift, rotation, growth and cell morphodynamics.

As detailed in the methods Section 2.2.2 *Embryo culture and light sheet microscopy*, embryos are cultured live in hollow capillaries allowing them to grow without constriction similar to the way they would *in vivo*. This also allows them to drift and rotate in space. Occasionally the sample had to be reset when extreme drift causes the embryo to move out of the frame, resulting in two time series that required stitching. As the embryo rotates, the best quality in-focus sections rotate too. Typically the embryos show significant growth between E5.25 and E5.75, including changes in morphology and relative proportions. All of the above increase the difficulty of the registration problem.

Here, I outline the novel process we developed by creatively adapting existing registration principles to successfully isolate cell movement due to migration, by matching size, orientation, and shape across the time series.

2.7.1 Rigid spatiotemporal registration

To register both angles (multi-view spatial) and timepoints (spatiotemporal), the same general rigid registration method was used, albeit with different degrees of freedom in the linear transformations applied globally to the entire embryo.

2.7.1.1 Intensity-based registration

Due to a lack of well-defined and permanent key structures in the embryo, we use intensity-based rigid registration. Raw intensity values vary substantially between angles and timepoints, therefore for a cost function we use the correlation difference based on the pattern of voxel intensities in a spatial neighbourhood of individual voxels in the image. Specifically, we adapt the MATLAB implementation of Matte's mutual information metric (Mattes, Haynor, Vesselle, Lewellyn, & Eubank, 2001; Rahunathan, Stredney, Schmalbrock, & Clymer, 2005). This local pattern matching approach is more robust than the alternative cost of minimizing the mean squared error of individual voxel intensities.

Using the similarity of membrane intensity as a feature for matching, we did not require the addition of fluorescent beads in the support matrix (e.g. agarose) unlike in Preibisch et al. 2010. During early attempts to register datasets cultured with beads using MVRA, I realised the Gaussian intensity based registration method employed by MVRA was successfully registering embryos using the membrane intensity alone, primarily using bright junctions as bead 'substitutes', information which we carried forwards. Not having to use beads simplified the culturing process, removed the risk of shadowing effects, and allowed for more tightly cropped images.

2.7.1.2 Degrees of freedom of spatial transformations

Whilst in theory the registration algorithm should successfully recover the correct spatial transformation regardless of the degrees of freedom, in practice the registration is more robust to small and inconsistent errors and converges faster if the correct degree of freedom is pre-specified.

As such, the spatial alignment (Figure 2-5C) of two angles uses only a translation in (x,y,z) space, given that the rotation between the two angles is known from the acquisition setup. This approach was also taken by Rauzi *et al.* 2015. This reasonably assumes that embryo rotation and growth is negligible in the ~30seconds between the imaging angles (20s to image the volume, 10s to reset). If an error remains, it is necessarily a small systematic one, rather than an inconsistent error introduced by the registration process. The automatic spatial registration is well within the manual registration of a researcher, and compared similarly to results from MVRA. The algorithm relies on a minimal overlap of cellular detail between the two angle views. The more similar in shape the area to match, the more successful the final stitching will be.

Temporal alignment (Figure 2-5F) instead uses a similarity transform registration: one that permits global translation, rotation, and scaling. Translation compensates for the drift of the embryo and rotation for the rotations around and towards the embryonic long axis. Importantly, scaling the embryo removes the components of cell movement due to growth. Inclusion of shear (a non-rigid transformation) at this stage was found to be inefficient. The repetitive local similarity of cells can result in a lot of sub-optimal minima destabilising the registration algorithm when finding globally suitable shear parameters. Instead, any shear effects together with potential changes in embryonic morphology are removed during a following non-rigid shape matching stage (described in Section 2.10.3 *Non-Rigid shape matching*).

By using a rigid similarity transformation we isolate only the components of relative cell movement caused by migration and cell shape change. All the transformations are reversible, and the different translational, rotational, and scaling components can be isolated. This ensures we can still retrieve accurate quantification data for e.g. apical cell area, when conducting analysis on the registered embryo.

The temporal registration is particularly difficult when the embryo rotates significantly, due to one side of the embryo moving in or out of focus as the time series progresses. Combining this with

embryo shape change and changes in cell shape and position, I found the best way to register the timepoints was to use a temporally close frame as reference, instead of attempting to match to one global reference frame. Implementing a pairwise registration whereby frames were matched to previously registered timepoints in sequence from the first frame i.e. matching tp2 to tp1, tp3 to registered tp2 etc. was consistently more successful as the appearance between consecutive timepoints was very similar.

However, matching to the immediate previous frame was not precise enough to correct for small cumulative differences in location in the embryo between timepoints, resulting in steady drift, particularly in the out of focus y-z direction. To address this, a hybrid scheme was adopted whereby the reference frame would be switched every 10 frames, that is matching tp2-10 to tp1, tp11-20 to the registered tp10, tp21-30 to registered tp20, and so on.

The temporal registration worked most consistently on a single angle, potentially due to the rotational asymmetry created by the light scatter constraining the possible rotation estimation, making it easier to find a consistent optima despite the locally repetitive cell appearance. The asymmetry effectively creates a prior that functions in a similar manner to the initial 'guess' or pre-registration manual translation or rotation often implemented, and which was required by MVRA. The optimal registration parameters from registering a single angle was directly applied to the second spatially registered angle view to create a fully registered two angle dataset.

2.7.1.3 Multiscale optimisation

A key challenge in registration is to avoid finding local instead of global minima. A good optimiser will converge quickly to the global optimal transformation without getting caught in a local loop. We minimise the effects of local minima in our registration by using multiscale registration implemented through downsampling spatial pyramids (Figure 2-5E). The image registration is first solved at the lowest resolution (highest downsampling) first where the basic embryo shape is salient to provide an initial solution. This initial solution is then used to seed the next level up, and

refined using the higher resolution data. Such a progressive low-to-high resolution approach takes into account the differences in cell shape and movement, which can be quite significant between timepoints during migration, whilst ensuring computational efficiency. We further improve the speed of registration by restricting the downsampling factor to 16, 8, or 4 at the cost of only marginal performance gains at higher image resolutions of 2x and original size.

The typical default parameters we chose for spatial registration was (1250,1250,100) iterations, and for temporal (750,750,100) iterations at downsampling scales of [16,8,4]. This scaling approach led to an improvement in speed from 8+ hours to around 2 hours for a 100 frame timelapse, with a greater chance of finding a successful registration.

An additional stage of registration uses a non-rigid registration to predominantly match the outer edge of the registered embryo across different timepoints to create a shape-invariant 3D reference volume. In development we found this dramatically reduced the amount of manual annotation required to project the embryo. This registration is described in the Section 2.10.3 *Non-Rigid shape matching*.

2.8 Tilt correction and stitching of multiple angle views

The two spatially-aligned and temporally registered angle views need to be merged in order to create one embryo containing good quality data on both sides of the embryo. However, in order to keep the best in-focus data after merging we found it was necessary to correct for the off-axis tilt of the embryo first, making them as upright as possible (Figure 2-5B). 'Upright' in this case does not mean the 'most extremal point along the long y-axis', but refers to the alignment of the embryos across the dataset by the distal-proximal axis.

Upright alignment was efficiently carried out manually. Most embryos were dissected with the ectoplacental cone intact, and depending on where the columnar AVE were located, the most

extreme downwards tip of the embryo was often not the most proximal. Thus recognition of features such as the shape of the epiblast and cavity, and stage of migration was required.

Upright alignment should be carried out consistently for each timepoint. Exploiting the developed spatiotemporal registration, alignment could be applied either by tilt correcting the initial frame in the timelapse before temporal registration, or applied to all registered frames. Although applying the transformation to a single timepoint is more time-saving, in practice application post-registration was found to show better results as the recognisable morphological features changed over time.

Once spatiotemporally registered and upright aligned, the two angles were then fused smoothly using a custom sigmoidal blending scheme, with a specified depth parameter marking roughly half way through the embryo (Figure 2-5D). This depth parameter was usually manually specified to avoid the same problems in asymmetry mentioned above.

2.9 Special cases

The usual processing order was to spatially register all angle 2's to angle 1's, temporally register the angle 1's, apply the registration transforms to spatiotemporally register angle 2's, tilt correct all registered angles by the same tilt angle, and merge individual angle views (Figure 2-4).

In cases where the cylindrical rotation was extreme (up to 90°), or the embryo also rotated significantly against the long y-axis (which was less likely in a confined space), it was necessary to change the order of operations in order to keep the best data from each angle when the embryos were merged. In these cases, one side of the embryo would 'angularly drift' from being entirely good quality to entirely scattered during temporal registration. If these volumes were temporally registered before being merged, by the time the full rotation had taken place there would be a timepoint containing the worst halves of the embryo instead of all containing the best.

In such cases, the embryo angles were first spatially registered and tilt corrected. The temporal registration transformation was then found using single angle views but was not applied until after both angle views had all been merged. The merging in this case did not use a single z-slice parameter, since timepoints have yet to be corrected by registration. Instead, the central join point at every timepoint was individually found by calculating the centre of mass. This is not a perfect solution, as the centre of mass is effected by the ectoplacental cone, but works well enough in practice to avoid manually specifying a central join point for each time frame.

Finally I did not consider cases where the rotation was so extreme that the embryo becomes more horizontal rather than vertical. This was not a case that occurred during collection of this dataset, as the capillaries in which the embryos were cultured were too narrow for this to happen. If this was the case, light scatter would likely be too extreme to capture good data throughout the depth (or in this case length) of the embryo.

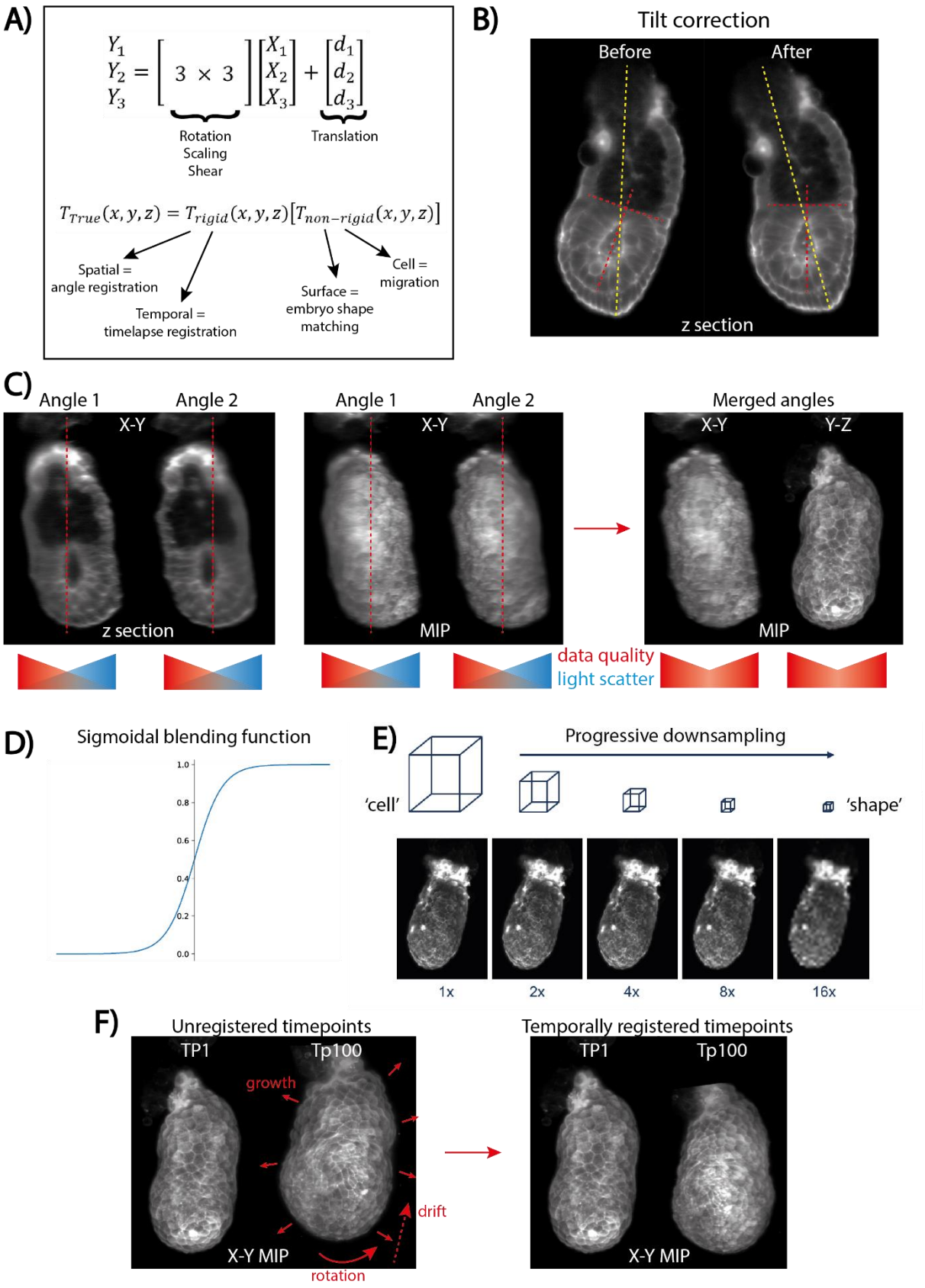
A)
$\begin{bmatrix} Y_1 \\ Y_2 \\ Y_3 \end{bmatrix} = \underbrace{\begin{bmatrix} 3 \times 3 \end{bmatrix}}_{\text{Rotation Scaling Shear}} \begin{bmatrix} X_1 \\ X_2 \\ X_3 \end{bmatrix} + \underbrace{\begin{bmatrix} d_1 \\ d_2 \\ d_3 \end{bmatrix}}_{\text{Translation}}$
$T_{True}(x,y,z) = T_{rigid}(x,y,z)[T_{non-rigid}(x,y,z)]$
Spatial = angle registration
Temporal = timelapse registration
Surface = embryo shape matching
Cell = migration
B)
Tilt correction
Before
After
z section
C)
Angle 1
Angle 2
X-Y
z section
Angle 1
Angle 2
X-Y
MIP
Merged angles
X-Y
Y-Z
MIP
data quality
light scatter
D)
Sigmoidal blending function
1.0
0.8
0.6
0.4
0.2
0.0
E)
Progressive downsampling
'cell'
'shape'
1x
2x
4x
8x
16x
F)
Unregistered timepoints
TP1
Tp100
growth
drift
rotation
X-Y MIP
Temporally registered timepoints
TP1
Tp100
X-Y MIP

Figure 2-5

Figure 2-5: Spatial and temporal registration. A) The registration problem which includes both rigid (spatial and temporal) and non-rigid (surface and cell) movements. B) Embryos were manually tilt corrected using cues such as the boundary between the epiblast and the ExE, as the EPC and columnar morphology of the AVE cells which complicates automation. C) Spatial registration of the two angle acquisitions to create a single volume timepoint that fuses the best quality data in each angle view. D) The spatially registered angles are fused using a sigmoidal blending function. E) Multiscale registration implemented by progressive downsampling the frames optimised registration and improved speed (fig. by Dr Felix Zhou). F) The temporal registration scales, rotates and translates the timepoints to remove components of motion due to drift, rotation and growth. 'MIP' is maximum intensity projection.

2.10 Projecting the VE and the epiblast

2.10.1 Simplifying 3D to 2D

Full 3D analysis of the embryos is unintuitive and highly computationally demanding. As the VE maintains a 3D monolayer during migration, it is more natural to simplify the motion analysis of VE cells from 3D to 2D, by projecting the apical surface onto a 2D plane. This allows visualisation of the entire epithelial sheet at once, and makes cell segmentation and tracking far simpler than in 3D. The projection inherently assumes a consistent cell depth, and does not take volume into account. However, it does account for the 3D nature of the embryo in a way that measurements of apical area from a maximum intensity projection are unable to do (Shioi et al., 2017; Trichas et al., 2011). From observing the data in stacks I have judged these assumptions sufficiently reasonable to provide representative measurements of biological cell behaviour.

The projection approach of 3D to 2D has previously been taken to analyse *Drosophila* gastrulation (Heemskerk & Streichan, 2015; Krzic et al., 2012; Rauzi et al., 2015) and zebrafish hearts (Heemskerk & Streichan, 2015). In Rauzi et al. 2015 *Drosophila* were imaged in a MuVi-SPIM LSFM with 4 angles, and registered using beads according to a method established by Krzic et al. (Krzic et

al., 2012; Rauzi et al., 2015). The regular shape of a gastrulating *Drosophila* which does not change shape temporally enabled a straight forward cylindrical projection of the embryo, with a maximum radial projection providing depth. This was the method I used for my early, proof-of-principle projections of the mouse embryo, obtaining a similar projection of a *Drosophila* embryo to that of Rauzi et al. (Figure 2-6E).

Heemskerk et al. developed the projection idea further to include the *Drosophila* poles, the areas which have the most curvature and thus are the most distorted during cylindrical projection, using an azimuthal equidistant projection to preserve distance from the pole (Heemskerk & Streichan, 2015). The authors also extended this to the more arbitrarily shaped zebrafish heart by organising the surface points into a triangular mesh, and choosing an appropriate algorithm to parameterise the mesh based on its particular shape.

The *Drosophila* lends itself to this analysis: it has well delineated, homogenous nuclei and undergoes no cell division or neighbour intercalation during gastrulation (Rauzi et al., 2015). However, the methods developed by Rauzi and Heemskerk do not need to take into account the shape change in either the embryos or the cells themselves during AVE migration in the mouse. While Heemskerk et al. did develop a method to project less regular shapes, this involved the creation of multiple 2D projections or 'maps' which had to be further linked or 'charted' if temporal data was used. To utilise this method, the surface must not overlap or have holes. Critically the initial creation of a suitable surface mesh for projection was not sufficiently addressed as the authors assume such a regular, sufficiently smooth surface segmentation has already been obtained.

In the next section I will describe the developmental steps that led to a more robust and widely applicable method for finding and projecting the surface of mouse embryos, using an additional shape matching registration step to create a temporally invariant surface across the timelapse, before performing a single geodesic projection.

2.10.2 Finding the surface coordinates to project

The problem of 3D surface projecting over time in mouse embryos is very difficult due to the potentially large morphological changes that occur over the timelapse.

The first step in projecting the apical surface of the VE is to identify the relevant coordinates to project. This involves segmenting the embryo to identify the bounding 3D surface. For the automatic embryo segmentation I initially used a mixture of morphological operations to separate the embryo from the background. Rescaling the embryo from 16bit to 8bit using a minimum intensity threshold above 0 in the pre-processing stage already reduces most of the background noise. Noting this, I used Otsu thresholding or a fixed specified intensity threshold together with a series of opening and closing 3D operations to produce a binary volume that captures the embryo surface. To enable a clear outline of the cells, the final surface coordinates were then cut in beyond the apical surface to view perpendicular membranes and avoid apical shrouding.

To project the entire timelapse one can either segment all timepoints or, if shape variation is not significant, project using the surface coordinates found from a reference timepoint. It became clear during early unwrapping attempts that the automated embryo segmentation was not sufficiently accurate to overcome inconsistencies between embryos. For example, failures arose in sections where cell blebbing has occurred (a cell dying and moving out of the embryo), or where a part of the membrane was particularly dim and had left a 'keyhole' missing. Regional differences in VE cell height also resulted in some cells presenting a more apical shroud of actin, or in some cases even cutting into the epiblast layer beneath. This cutting-in was especially prevalent in regions undergoing more drastic changes in morphology, such as the distal tip, or with the compacted AVE cells at the boundary. The problem was even more pronounced when trying to project the epiblast, especially in the area around the boundary, where the VE is considerably thicker in that small region.

In practice most of the embryos underwent some manual corrections, particularly to compensate for morphological changes requiring additional erosion at the distal tip. To save time, for embryos where the automatic segmentations were largely successful, their binaries were manually edited in ImageJ using the brush tool to edit the 2D stacks, and then fed back into the data processing framework. After manual corrections, the binary was downsampled, smoothed, and reupsampled to give a smooth surface whose contour provides the surface coordinates for unwrapping.

The use of morphological operations to automatically find the surface of each timepoint individually was time consuming, taking around 25mins per timepoint. Additionally, once it became apparent that manually corrections taking around an hour per timepoint would be required, I realised it would not be possible or realistic to apply these corrections consistently to each timepoint. Instead we introduced a further registration step: non-rigid shape matching. This step, applied to the spatially merged and temporally registered data, warps the outer surface of the embryo to closely match the surface of a reference timepoint, and is described in more detail in the next section.

The proposed shape matching allows a greatly simplified process for unwrapping the surface over time. Now only coordinates from a single reference timepoint are required; the same coordinates can be applied to every shape matched timepoint. Thus the segmentation and manual correction of only 1 binary image as opposed to e.g. 100 is required, and ensures temporal consistency between all timepoints.

In summary, finding the single reference timepoint coordinates was therefore done in either an automated, semi-automated, or manual fashion with semi-automated most often applied. This approach incorporates time saving aspects and allows for enough precision to project the correct embryo depth despite irregularities across timepoints. The projection method is outlined in Figure 2-6.

2.10.3 Non-Rigid shape matching

To match the outer embryo shape over time to the shape at a reference timepoint, non-rigid registration that allows for local warping was used (Figure 2-6A). One such implementation is Thirion's DEMONS algorithm (Thirion, 1998) which can use local smoothing to ensure biologically plausible deformation (diffeomorphism) (Vercauteren, Pennec, Perchant, & Ayache, 2009) and whose code is readily available in MATLAB.

In order to ensure warping of the outer shape with minimal impact to individual cells, the DEMONS algorithm was only applied to downsampled volumetric images where the embryo-level detail of the outer edge of the embryo and the inner cavity were apparent, but not the cellular detail. Matching cellular level details would introduce severe biologically significant artefacts in cell shape and remove AVE cell migration entirely from the timelapse data.

It was easy to allow very extreme warping to exactly match the outer embryo shape, however, this propagates to the internal cell shapes. Therefore, I tested the regularization parameter in the optimization objective of demons to find a balance between keeping the cell shape realistic while matching the outer surface as closely as possible. As with the temporal registration, I found a moving reference frame of ten timepoints most consistently offered a closely shape-matched result.

As the DEMONS non-rigid shape matching emphasises the outer shape of embryo, and not the cellular details, the basal membrane does still shift between timepoints. This presents a difficulty in creating the epiblast binary. This is also most prevalent if the first timepoint is at E5.5, when the AVE presents as very columnar cells at the distal tip. As such for the *mTmG ; Ttr-Cre* embryos, I tried to mask off the VE layer and register the epiblast separately, but without full penetrance and a distinct basal membrane to match to, the algorithm was less successful, and I returned to the original method without masking.

2.10.4 Surface projection method

The surface projection development began initially with a cylindrical projection, as used by Rauzi et al. 2015 and shown in Figure 2-6E. However, this method of projection does not capture the curvature of the embryo, severely misrepresenting the cellular area when embryo shape departs from a cylinder. Thus, instead of projecting by (Y,θ), where Y is the distance along the long axis to which the embryo is aligned, and θ the radial angle, we project using (S,θ), where S is the geodesic distance along the curved embryo surface from a fixed specified reference coordinate (here the distal most surface point along the long embryo axis through the embryo's centroid), shown in Figure 2-6F. This method ensures the embryo surface is faithfully unwrapped with respect to its 3D curvature. It is referred to as the 'Cartesian geodesic projection'.

To compute the geodesic distance and smooth the surface coordinates, splines are fit vertically along the surface of embryo, and radially around θ. These build up a 2D grid which better takes into account the shape and curvature of the surface compared to a cylindrical projection. We specify the projection surface to be defined by the maximum length/width in the S and θ directions, and then interpolate the points to give an even surface. Crucially, any coordinate on the 2D projection maps back to a coordinate on the 3D surface, which can be further extrapolated back to undo all previous spatiotemporal registrations to give accurate shape and size information.

Like Heemskerk et al. (Heemskerk & Streichan, 2015), we create polar projections of the embryo to better highlight the motion at the distal tip which is otherwise highly distorted in the geodesic planar projection. The distal tip is the most important region to study AVE induction and the onset of migration, but despite this, it has not been visualised in this manner previously. Unlike Heemskerk et al. our polar geodesic parametrization projects the whole embryo as opposed to just one half. This is achieved by converting the Cartesian geodesic projection parametrised by (S,θ) to its equivalent polar coordinates, (S cosθ , S sinθ). The projection perspective is of one from below the specified reference point, looking up at the distal tip of the embryo.

2.10.5 Projecting the epiblast and geometric mapping between layers

The method for finding the surface coordinates is readily extended to project any depth into the embryo, in particular, the basal epiblast layer. The epiblast coordinates were found by further automatically eroding the apical surface binary, and then refining the binary manually. Manual annotations were required for the epiblast and ExE regions as the VE changes thickness, being more columnar in the ExE-VE, in addition to the particular columnar morphology of the AVE cells.

While the VE monolayer can be simplified to a 2D problem for cell tracking, the epiblast undergoes interkinetic nuclear-like migration, with cells rounding up and moving to the apical surface (cavity) to divide, before reintegrating into the main body of the epiblast. As such, unwrapping an epiblast layer at any particular depth will show cells disappearing and reappearing as they move out of plane to divide. This makes automating individual cell tracking a very difficult problem, and hard to accomplish manually. Reintegrating daughter cells have no unique fluorescent identifiers, and may have lost the characteristic features of the mother used to identify the same cell between frames, such as shape and size. The epiblast is also considerably mobile at E5.5, such that it is difficult to isolate migration trends by eye. However, we can still use a 2D projection for long-time superpixel tracking to analyse the global motion behaviour at this VE-Epi interface which does not require information on individual cells, as I show later in Section 3.4 *Characterisation of VE migration in the WT embryo.*

2.10.6 Geometric mapping between layers

In order to compare the cell movement between the smaller epiblast and the larger VE surface, the two 2D unwrapped layers must be made the same size in alignment with their corresponding 3D coordinates. Thanks to the geodesic projection approach we developed which effectively 'flattens' the curvature of both surfaces, alignment of the two surfaces is equivalent to an easy proportional remapping and does not require further sophisticated registration techniques. The proportional remapping can be explained as follows: if the length from the pole along two splines at different

depths on the surface is divided into e.g. 1000 equal steps, the corresponding pixels in each layer are those at the same step number in each layer. Thus a pixel 80% or 800 steps of the way up the inner spline will correspond to one 80% or 800 steps up the outer spline.

In practice the proportional remapping is achieved by upsampling the projected epiblast to the same image dimensions as the VE. Whilst downsampling is also valid, this option decreases the resolution of the VE unnecessarily.

It should be noted whilst there is no absolute way to map two arbitrary 3D surfaces without additional constraints, here this method gives the most biologically most plausible solution by taking advantage of the similar curvatures and proportionality between layers in the same embryo. Compared to using nearest neighbour alignment, there are no areas where the inner surface is concave where the outer surface is convex or areas which have been multiply-mapped. After surface alignment, we can now use the 2D Cartesian and polar projections to compare movement in the VE layer directly with movement in the epiblast below.

Examples of the registration process for one embryo can be found in Supplementary Videos 1A-4B, with descriptions found in Appendix 6.1 *Supplementary video descriptions*.

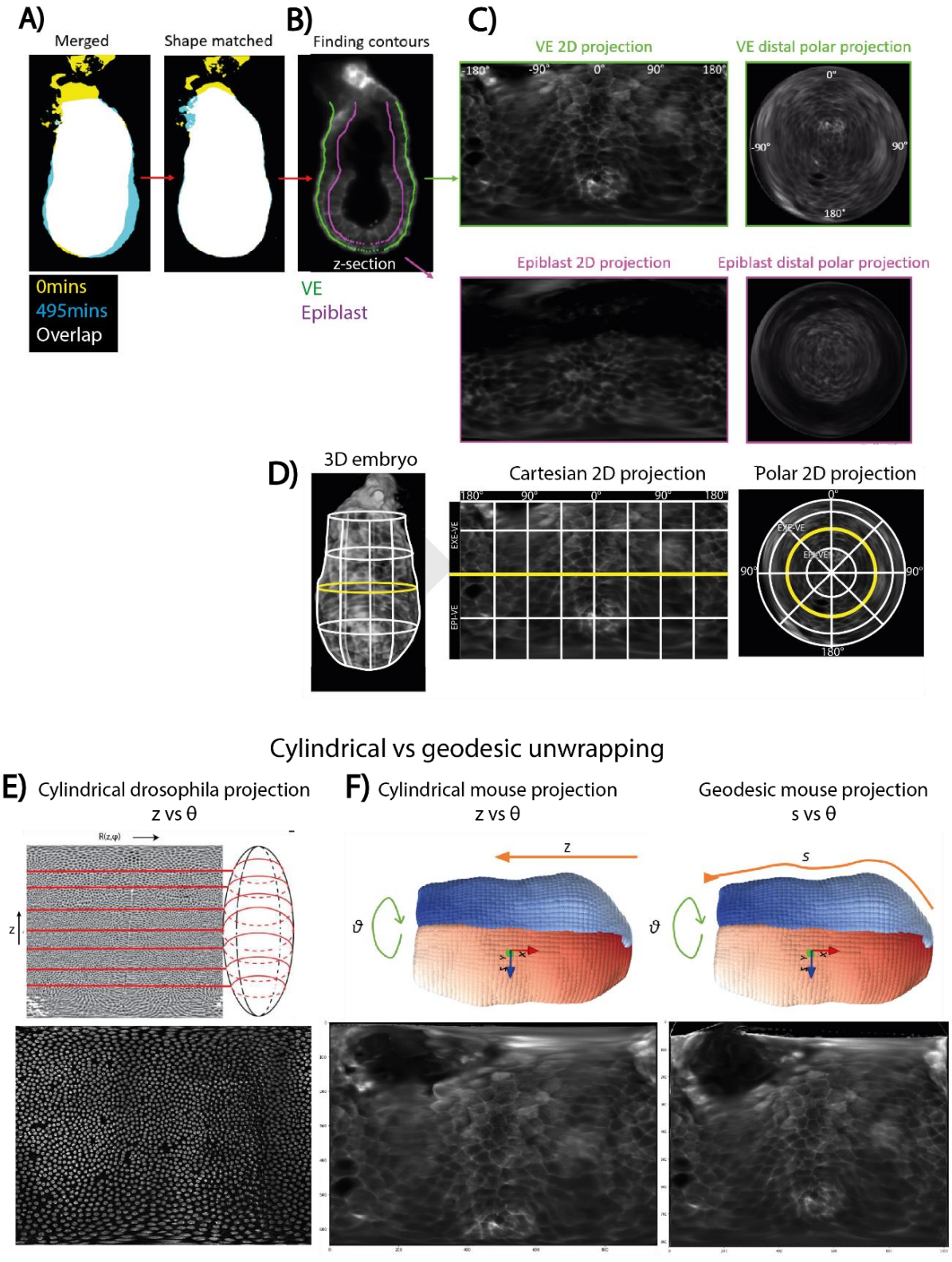
A)
Merged
Shape matched
0mins
495mins
Overlap
B)
Finding contours
z-section
VE
Epiblast
C)
VE 2D projection
VE distal polar projection
Epiblast 2D projection
Epiblast distal polar projection
D)
3D embryo
Cartesian 2D projection
Polar 2D projection
Cylindrical vs geodesic unwrapping
E) Cylindrical drosophila projection
z vs θ
F) Cylindrical mouse projection
z vs θ
Geodesic mouse projection
s vs θ

Figure 2-6

Figure 2-6: Simplifying the problem from 3D to 2D by projecting the surface. A) Non-rigid registration matches the outer surface of the embryo (tp1 in yellow, last tp in blue, overlap in white). B) A combination of morphological operations and manual annotations produces a binary volume for both the VE (green) and the epiblast (purple), from which contours give the coordinates to project. C) The coordinates are projected onto Cartesian and polar maps. The areas around the distal tip which show most distortion in the Cartesian projection show the least distortion in the polar. This is summarised in D) with grid lines in white and the boundary in yellow (image. by Dr Felix Zhou).
E) shows the cylindrical Cartesian unwrapping method (adapted from Rauzi et al., 2015) on a Drosophila embryo, compared with my own unwrapping of a Drosophila using an early version of the projection code which employed Rauzi et al.'s cylindrical method. F) Comparison of the cylindrical and geodesic projection methods. The geodesic method minimises distortion by following the curve of the embryo's surface, and allows easy mapping of the VE and epiblast (image by Dr Felix Zhou).

2.11 Discussion

In this methods chapter I have outlined the fluorescence mouse lines and LSFM culturing, and discussed the advantages and disadvantaged of such an approach. I have examined existing software for analysing LSFM datasets, and concluded none were able to address all the challenges involved in automatically registering, segmenting or tracking our mouse embryo dataset. I then described at length a custom framework developed for this purpose. While much is discussed in place, there a few points of additional note.

The entire framework takes around 24 hours to process a 100TP timelapse of two angles from start to finish (which has been downsampled by a factor of two in the initial preprocessing stage). Only a minority of that time involved manual input: most is left to computer processing time. No special equipment, such as parallel or cluster computing, was used in the development or implementation of the framework. Although a desktop with 64GB RAM is useful, I carried out most of the work using a Dell XPS 15 9560 laptop, with an Intel Core i7-7700HQ 2.8GHz CPU, and 16GB of RAM.

With more computing power and storage, it would be possible to process and analyse the dataset without having to downsample by a factor of two. However, the current level of resolution is more than enough for our purpose, and features of particular interest can still be examined on the original raw dataset. With the power of hindsight, I would in future temporally register embryos backwards where they are larger, from the last timepoint to the first. Currently by registering to the first frame, in later analysis stages I have found this has led to the constricted AVE cells in later timepoints appearing frustratingly small and difficult to delineate when performing manual analysis. Performing the registration temporally backwards would fix the minimum size of the image in the final frame for guaranteed resolution.

Having both Cartesian and polar projections enables a comprehensive study of the entire epithelial sheet at once, without excessive warping in any one region. This massively increased the ability to do manual analysis in addition to simplifying the problem of automating analysis. The embryo no longer needs to be visualised using maximum intensity projections, being rotated and reprojected multiple times for each timepoint, or imaged with only a small frame of reference visible (as in Trichas et al. 2011; Shioi et al. 2017). Furthermore, the isolation of the components of cellular movements from the drifting, rotation, and growth components of the global embryo allows for a more comprehensive analysis of motion to be undertaken.

Nearly all of the questions relating to cell movements and divisions can be addressed by viewing only the apical surface of the VE. However, one downside of projecting a single depth as used here is that cellular protrusions visible in 3D opacity renderings or maximum intensity projections of the *mTmG ; Hex-GFP* embryos are missed. This is because these protrusions lie on the basal layer. When projected at a single depth the basal layer appears very dynamic, as a constantly moving dense sheet of actin, making it impossible to delineate cells or protrusions. 3D Sections further show that these protrusions are very thin, and thus would be difficult to capture consistently across the time series without finding coordinates to project for each timepoint individually manually. To capture

this, maximum projection across multiple depths can be implemented. This would not help the problem of identifying *Hex-GFP* positive protrusions underneath the fluorescence of *Hex-GFP* positive cells, but would enable them to be followed from around the edges of the *Hex-GFP* positive group.

The method of registration does not require identification of keypoint features. Instead, we have shown successful registration even when the intensity profiles of the different fluorescence lines varies from membrane to largely shrouded apical fluorescence, and the strength of intensity varying substantially over time. This suggests the developed registration framework could be immediately employed to register other biological datasets, with potentially more than two angles, such as *Drosophila* or zebrafish, or adaptable to larger organs such as mouse hearts. In principle, as long as the imaging metadata is known (voxel size etc.), and there is sufficient overlap shared between image angles and similarity in the dataset between successive timepoints, the developed registration should be robust across different systems. The ability to register at multiple spatial resolutions, and to different reference timepoints (or a moving timepoint) makes the framework highly versatile. The 3D to 2D projection can equally be applied to simpler shapes such as *Drosophila* and zebrafish, and adapted to nuclear fluorescence as has been shown using an earlier version of the code. It has been successful when tried on confocal mouse data including to unwrap the apical epiblast (cavity facing) layer.

The variability and unpredictability of the age of embryos across and within litters leads to large fluorescence variation across time and adds to the difficulty of capturing the process of AVE migration. A particular challenge for analysis is that as the orientation of the embryo with respect to the objective is not known before migration is underway, the lateral sections perpendicular to the objective show the most scattering after stitching. This means, even after processing and projecting, we are left with an inhomogeneous dataset of embryos at different stages, showing significant variability in morphology and migration. McDole et al. 2018 developed TARDIS, a

method using feature extraction to compare statistics over multiple embryos. Here, due to the geodesic projections flattening the embryo curvature, proportional remapping as with VE and Epi alignment allows easy direct comparison of statistics across multiple embryos without additional processing.

However, since we have simplified the embryo into two 2D layers, the depth and volume of cells were not assayed directly. This is a limitation of our approach in regard to epiblast divisions and the transition between squamous and columnar cells. To be able to carry out analysis in full 3D would require additional segmentation and tracking tools, which are discussed in the next chapter.

The final output of the framework is a selection of folders containing the output of the different processing steps, including the transformations to go between them. The combined size of these folders is 80-200GB depending on the number of channels and timepoints, and is less than half the size of the original .czi files.

2.12 Summary

The E5.5 mouse embryo represents unique challenges for image analysis, due to the large size of its nuclei, low photo-toxic load, presence of cell divisions, and changes in morphology. Although numerous tools have been developed primarily for the processing and analysis of *Drosophila* data, some of which have been successfully applied to the mouse, developing our own processing framework by combining and extending existing ideas has enabled us far more control over the dataset. Our framework uses spatial and temporal registrations to separate the components of cell movement due to drift, rotation, and growth, isolating those due to relative cell movement and simplifying the analysis. An additional non-rigid registration step using the DEMONS algorithm dramatically reduced the time taken to create binaries and find projection coordinates by semi-automated and manual methods. Projecting the 3D embryo into 2D simplified the motion analysis problem, and through a geometric spline approach we minimised unrealistic warping and enabled

easy comparison between the VE and epiblast layers. Notably, all of the geometric transformations are reversible, allowing the original biological sizes, shapes, and velocities to be measured from annotation of the final 2D projections. The framework output is significantly more manageable to store and analyse than the original Ziess .czi files. This framework has enabled the full manual tracking of all the cells in the VE for the first time, allowed comparisons between datasets, analysis of asymmetries in embryo shape and rates of proliferation in different regions, as discussed in the next chapters.

Chapter 3: How is migratory behaviour coordinated tissue-wide in the VE?

3.1 Introduction

Extracting quantitative information from large datasets manually is difficult and time consuming. In this chapter I describe the tools we have used and developed for analysing the 2D projected timelapse datasets. The tools investigated for use early in this project, and other manual and automatic approaches for segmenting and tracking LSFM datasets have been discussed in Chapter 2; for further review, see (Meijering, Dzyubachyk, & Smal, 2012). Previous tracking attempts in the E5.5 mouse have been limited to following random selections of cell nuclei from different regions of the VE, up to about a third of the cells in 3 embryos (Shioi et al., 2017). Here, I instead describe a collaborative approach to attempt cell segmentation and tracking in all the cells of the VE.

Methods used to analyse motion in large datasets can be placed into two categories: those that carry out large cell population based analysis and those that extract information on single cells. The first of these categories includes optical flow methods and superpixel analysis, which give overall trends in the data without the need to segment and track individual cells. This approach is popular for use in epithelial sheets, including would healing (see Masuzzo, Van Troys, Ampe, & Martens, 2016 for a review), and has previously been used to study *Hex-GFP* positive AVE cells (Omelchenko et al., 2014) and the chick epiblast (Rozbicki et al., 2015) in the form of Particle Image Velocimetry (PIV).

I describe the use of a superpixel tracking algorithm, Motion Sensing Superpixels (MOSES), developed by one of our collaborators Dr Felix Zhou prior to this project (F. Y. Zhou et al., 2019). Dr Zhou created a classifier based on the extracted patterns of movement of Hex-GFP marked AVE cell to identify patterns of movement in unmarked embryos, and used it to automatically stage the

embryos. This staging was compared to manual staging also based on addition geometric features, and used to create a reference for analysis. The superpixel tracking was also used to identify characteristic migratory movement ~~across embryos~~, and investigate wider tissue deformation across the epithelial sheet.

The second category of motion analysis involves extracting quantitative information from individual cells. Manually segmenting and tracking single cells in large 3D datasets such as this one can take days for a single timepoint, making it highly impractical to extract large scale quantitative information such as changing cell shape over time and the tracking of neighbour interactions or cell divisions. The superpixel tracking results were thus validated on manual annotations from an exemplar embryo, which was also used to investigate migration on a cellular level and show the first complete tracking of cells in the entire VE using the 2D projection. Manual annotations of cellular protrusions and cell tracking in sagittal sections of the 3D data also showed further evidence for active migration.

The ability to extract this information automatically would allow full use of this dataset, and provide a level of individual analysis that superpixel tracking alone cannot provide. Later in this chapter I describe the development of a Convolutional Neural Network to automatically segment the *Lifeact* timelapse dataset in order to extract quantitative single-cell information. Lastly, I describe ongoing development of semi-automated tracking applied to the output of the CNN segmentation. These developments add to our initial LSFM processing pipeline allowing automated analysis of AVE migration for the first time.

3.2 Motion Sensing Superpixels: a tool to study tissue wide cellular dynamics

Motion Sensing Superpixels (MOSES) is a systematic motion analysis framework used to study cell population dynamics (F. Y. Zhou et al., 2019). It quantitatively captures cellular motion in timelapse microscopy videos, robust to the changing image quality in our LSFM dataset, as fluorescence

intensity brightens over time, and can be applied to both the membrane fluorescence of the *Lifeact* data and more apical fluorescence of the *mTmG ; Ttr-Cre and mTmG ; Hex-GFP* embryos.

The 2D geodesic surface projections results in two projection layers, VE and epiblast. MOSES works by seeding the projection with a predefined number of regular regions-of-interest (ROIs) or superpixels (that are larger than a single image pixel). The centroid positions of each superpixel are then updated between frames, using the average displacement of the motion vectors inside the superpixel, computed by optical flow, here using deepflow (Weinzaepfel, Revaud, Harchaoui, & Schmid, 2013). The centroids from each frame are then linked to form a superpixel track. In an additional step, each track is filtered and linked to neighbouring tracks, creating a dynamic mesh enabling measurement of the local collective dynamics. The method is shown in Figure 3-1A.

MOSES analysis was specifically used to study tissue wide cellular dynamics, as discussed later in this chapter. It was also used to study the correlation between the tissue movement in VE and epiblast cell layers. First, I describe how we applied MOSES to create a classifier from *Hex-GFP* labelled embryos to identify characteristic AVE cell movement, and use this to automatically stage all the embryos in our dataset, including those without the *Hex-GFP* marker, for comparative analysis.

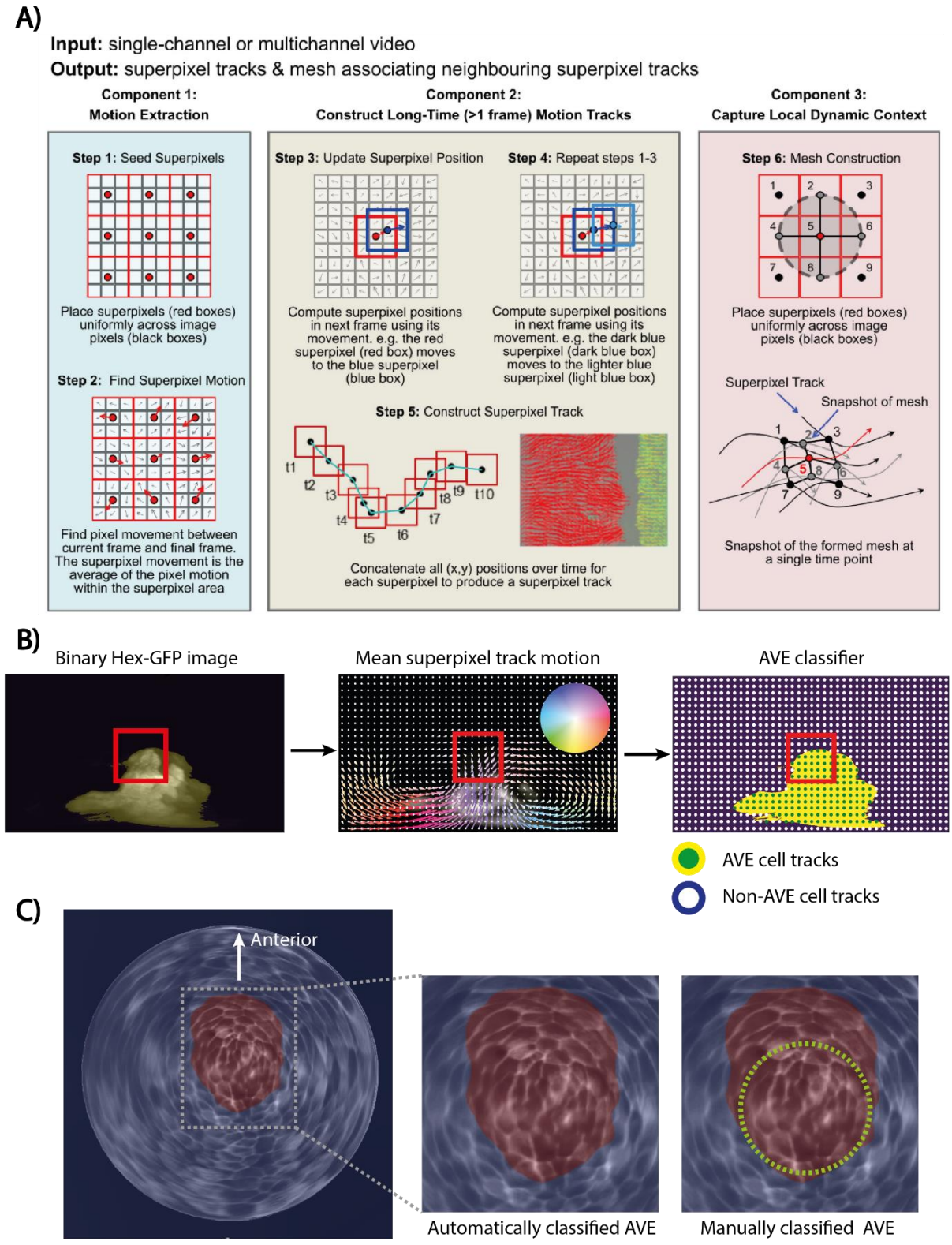
A)
Input: single-channel or multichannel video
Output: superpixel tracks & mesh associating neighbouring superpixel tracks
Component 1: Motion Extraction
Component 2: Construct Long-Time (>1 frame) Motion Tracks
Component 3: Capture Local Dynamic Context
Step 1: Seed Superpixels
Place superpixels (red boxes) uniformly across image pixels (black boxes)
Step 2: Find Superpixel Motion
Find pixel movement between current frame and final frame. The superpixel movement is the average of the pixel motion within the superpixel area
Step 3: Update Superpixel Position
Compute superpixel positions in next frame using its movement. e.g. the red superpixel (red box) moves to the blue superpixel (blue box)
Step 4: Repeat steps 1-3
Compute superpixel positions in next frame using its movement. e.g. the dark blue superpixel (dark blue box) moves to the lighter blue superpixel (light blue box)
Step 5: Construct Superpixel Track
t1
t2
t3
t4
t5
t6
t7
t8
t9
t10
Concatenate all (x,y) positions over time for each superpixel to produce a superpixel track
Step 6: Mesh Construction
Place superpixels (red boxes) uniformly across image pixels (black boxes)
Superpixel Track
Snapshot of mesh
Snapshot of the formed mesh at a single time point
B)
Binary Hex-GFP image
Mean superpixel track motion
AVE classifier
AVE cell tracks
Non-AVE cell tracks
C)
Anterior
Automatically classified AVE
Manually classified AVE

Figure 3-1

Figure 3-1: Motion Sensing Superpixels. A) MOSES has three components. The first divides the image frames into a set number superpixels, and finds the average of the motion vectors inside the superpixel area. These are then used to construct tracks in the second component, by updating the cell centroid position between frames and linking them across the timelapse. The third component connects neighbouring tracks to form a mesh, which allows measurement of the local collective dynamics. Adapted from Zhou et al., 2019. B) A support vector machine classifier trained on the Hex-GFP dataset learns to classify pixels as either AVE or non-AVE (images by Dr Felix Zhou and Dr Matthew Stower). C) The classifier then shows how pixels belonging to the Hex-GFP marked AVE cells identified in B) are moving on average of the timelapse. The yellow dotted circle shows the approximate manually identified AVE region.

3.3 Staging embryos

3.3.1 Manual staging

Staging the dataset was necessary to allow comparison between embryos captured at different stages of AVE migration. As a degree of subjectivity is involved, particularly in those embryos with no *Hex-GFP* expression to identify the AVE, this was first attempted by myself and Dr Matthew Stower independently to help control for researcher-researcher variation.

We divided the embryos into 3 stages: Pre-migration, Migration to the boundary, and Post-migration. The post-migration stage does not describe the end of migration, but instead the movement after the leading edge of the AVE cells reaches the boundary between the Epi-VE and ExE-VE. This is characterised by the leading edge spreading laterally, whilst trailing cells continued to migrate proximally up the Epi-VE anterior. This manual staging required the polar projection to accurately determine when the initial migratory movements took place, and the Cartesian projections to see with certainty where the boundary between the Epi-VE and ExE-VE fell.

Comparing our results from staging the initial 20 embryos, we had an exact match staging 9, a close match (<5 frames out) in 6, and differed (≥5 frames out) in 5. For those embryos where the staging

was a close match, we chose the middle value between our estimates. For those where we differed, we looked through again together to discuss and resolve the differences. For 4/5 of the embryos the difference was due to defining the point where migrating cells reached the boundary. This was not always clearly defined, as the migrating cells often pause for several frames, requiring the overlay of the epiblast to determine if they have reached the boundary. For these embryos, we took the earlier values as consensus. For the 1 other embryo, the difference in opinion was at the initiation of movement. In this case, the cells at the tip underwent spreading in all directions, making assignment of a beginning of directionality more difficult.

The consensus results from manually staging 23 embryos are shown in Table 3-1. The staging showed we had 9 embryos capturing pre-migration (of which 8 covered the initiation of migration), 20 during migration, and 18 post migration.

3.3.2 Creating a classifier for unmarked AVE cells using *Hex* datasets

It is not clear if there are migratory characteristics of the AVE cells which set them conclusively apart from the rest of the VE, which we observe to also undergo significant movement, particularly in the region surrounding the AVE cells (Shioi et al., 2017). The change in cell morphology at the distal tip from squamous to columnar is well known (Kimura et al., 2000; Rivera-Pérez et al., 2003) and is clearly seen in the *Hex-GFP* dataset. However, genetic markers of the AVE: *Hex*, *Lefty1*, *Cer1*, show salt and pepper expression, and not all the cells in the AVE region express *Hex-GFP* equally (Isabelle Migeotte et al., 2010; Srinivas et al., 2004; Takaoka et al., 2011).

Using the extracted superpixel tracks from MOSES on the 9 *mTmG ; Hex-GFP* embryos, Dr Felix Zhou trained a classifier to identify AVE cell migration, which we then applied to the other unlabelled datasets to identify regions exhibiting AVE-like movement.

To best capture the relevant AVE migration, MOSES was applied to shorter *Hex-GFP* embryo video segments containing only AVE migration. To construct robust velocity features for training, the

mean velocity of each superpixel is combined with that of its k-nearest neighbour superpixels, to create a velocity feature matrix that captures neighbouring motion information (Figure 3-1B). Using the constructed velocity feature matrix a support vector machine (SVM) classifier (Cortes & Vapnik, 1995) was then trained to classify each superpixel track as either 0 – not AVE associated, or 1 – AVE associated. After training, the classifier could be applied to unseen *Lifeact* embryos without a specific AVE marker using only the MOSES extracted tracks.

Creating a motion classifier based on the expression pattern of the 9 *Hex-GFP* embryos gave a more robust outcome than the salt and pepper *Hex* signal alone. The classifier was able to extrapolate the motion behaviour of positively expressing *Hex* cells to include additional *Hex* negative cells that exhibit the migratory characteristics of the AVE.

The cells which were covered by AVE-classified superpixels included those that would be classified as AVE manually, by dint of their small apical surface area, initial distal location, and directed movement towards the anterior boundary (Figure 3-1C). The classifier appears to positively identify cells proximal to the AVE, which do not show the characteristic small apical surface. This is because the AVE classifier is identifying all superpixels that capture the AVE migration at some point in time, not the instantaneous cell population for which further post-processing is required.

3.3.3 Automatic staging using the AVE Classifier

Using the AVE classifier built from the patterns of directional movement in *Hex-GFP* positive embryos, Dr Felix Zhou was also able to automatically stage the embryos, an unbiased approach which could then be compared to the manual staging (shown in Table 3-1).

The plots in Figure 3-2 and continued in Figure 3-3 show the cumulative distance moved by the AVE in the direction of average superpixel track velocity. As can be seen, the AVE showed persistent directional movement during the migration phase. However, this motion was not smooth, with plateaus and rapid movement in embryos such as L871_Emb1, L871_Emb2, and L924. This was also

noted during the manual staging when some embryos seemed to show short bursts of rapid migration.

The results of the automatic staging were largely similar to the manual, however, they differed in one significant way. The manual staging defined the period of migration ending when the leading edge of the AVE cells reached the Epi-ExE boundary. This positional information was not considered in the automatic staging, which was based on movement alone. The period of migration in the automatic staging was therefore seen on average to be shorter than in the manual staging, as the classifier picked up the initial, more motile 'ramp' phase, and classified the second period of 'plateau' movement as 'post-migration', despite cells not having reached the boundary. A good example of this is in L871_Emb2, which showed a long pause mid-way through migration (Figure 3-2). In a minority of embryos, the automatic staging gave a longer migration phase for the same reason. In these cases there was no discernible change in movement when cells reached the boundary, such as in L455_Emb2 and L848 (Figure 3-2).

Re-examining the case when the two researchers disagreed on the initiation of migration (L455_Emb2), we can see the cause of confusion reflected in the cumulative plot (Figure 3-2). Instead of a flat plateau pre-migration, we see a slow linear movement of cells at the distal tip. Re-examining the data, we saw this was due to a spreading of cells at the distal tip, not just in the direction of the anterior, which may be due to the inducing AVE cells becoming more columnar.

There was a large degree of variation in time taken for the AVE cells to migrate, in both manually and automatically staged embryos. Unfortunately, of the 23 embryos in the dataset, only 6 embryos captured all three pre-migration, migration, and post-migration phases, according to the manual staging. These embryos had an average migration period of 267mins and a standard deviation (stdev) of 159mins (4.45h, stdev 2.65h). The automatic staging had the same 6 embryos capturing all stages, plus another 5 giving 11 total. They had an average migration period of 258mins and stdev 77mins (4.3h, stdev 1.28h), not too dissimilar.

However, it is worth noting the timelapse is less likely to capture all three phases for embryos which undergo longer migration. Including the timelapses not yet finished, the range in the manually staged migration phase was 70mins to 580mins, and the automatic 140mins to 400mins, with some unfinished embryos potentially migrating for longer. Many unfinished embryos were around the 5hour (300m) mark by the end of the timelapse. The average migration from the distal tip to the boundary is thus probably towards the longer end of the 4-5hours originally reported (Srinivas et al., 2004), with individual embryos potentially exceeding this, and closer to the 6hours suggested by (Rivera-Pérez et al., 2003).

Embryo	Line	Interval	Agreed final staging (tp)			MOSES staging (tp)		
			Pre-migration	Migration to Boundary	Post-Boundary	Pre-migration	Migration to Boundary	Post-Boundary
401	LA	5min		1-37	38-100		1-38	39-100
455-E2	LA	5min	1-45	46-59	60-90	1-41	42-69	70-90
455-E3	LA	5min	1-41	42-102	103-111	1-23	24-103	104-111
491	LA	5min		1-50	51-100	1-11	12-45	46-100
505	LA	5min	1-39	40-74	75-110	1-38	39-93	94-110
864	LA	5min	1-30	31-70	71-115	1-22	23-70	71-115
871_E1	LA	5min	1-10	11-66		1-11	12-66	
871_E2	LA	5min		1-66			1-22	23-66
917	LA	5min		1-37	38-120		1-39	40-120
921	HTMG	10min		1-33		1-6	7-23	23-33
922	HTMG	10min		1-50	51-70		1-35	36-70
924	HTMG	10min	1-13	14-71	72-97	1-31	32-55	56-97
926	HTMG	10min			1-45		1-32	33-45
927	HTMG	10min		1-30	31-42	1-21	22-42	
928_E1	HTMG	10min		1-46	47-94	1-12	13-40	41-94
928_E2	HTMG	10min	1-10	11-37	38-53	1-8	9-34	35-53
930	HTMG	10min	1-27	28-60		1-27	28-57	58-60
932	HTMG	10min		1-40	41-77	1-5	6-42	43-77
848	TTR-MTMG	10min		1-24	25-30		1-30	25-30
860	TTR-MTMG	10min		1-30	31-35		1-27	28-35
905	TTR-MTMG	10min			1-30			1-30
910	TTR-MTMG	10min		1-22	23-36		1-17	18-36
945	TTR-MTMG	10min	1-27			1-27		

Table 3-1: The LSFM dataset with manual staging agreed by two researchers based on migration and location of the AVE cells, and the MOSES automatic staging based on the movement of superpixels alone. LA=Lifeact, HTMG = mTmG ; Hex-GFP, TTR-MTMG = mTmG ; Ttr-Cre.

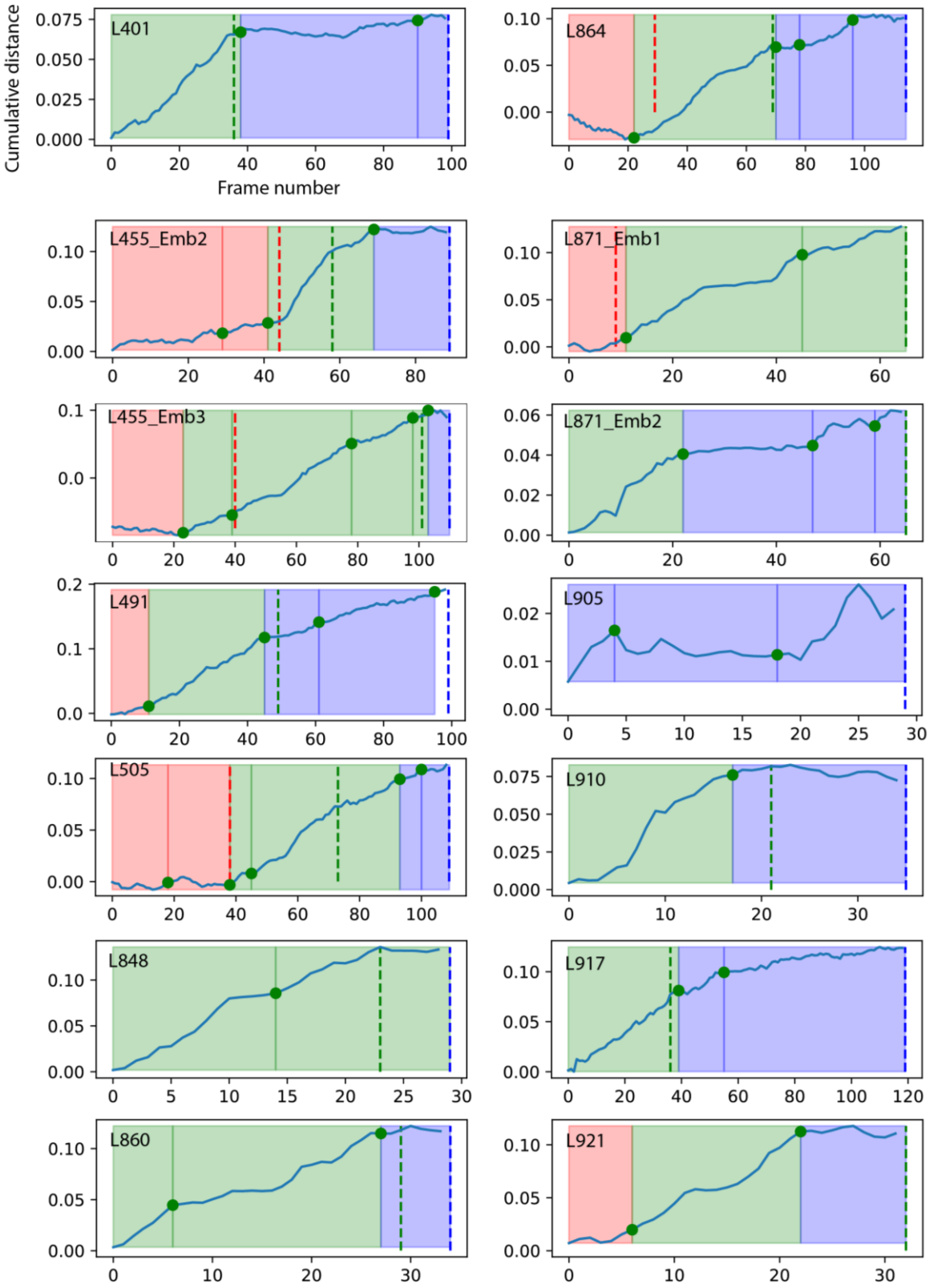

Figure 3-2: See Figure 3-3 for description.

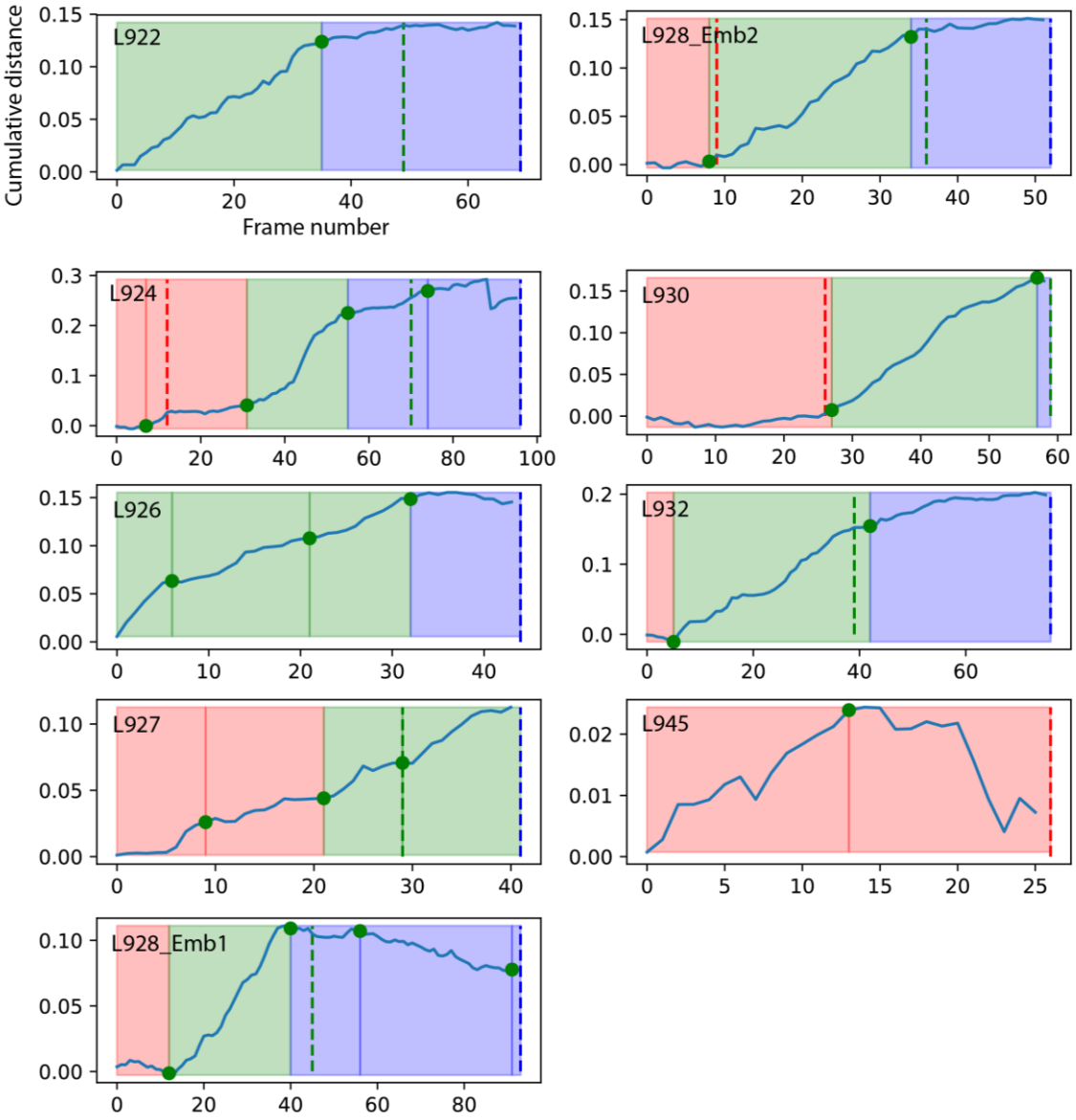

Figure 3-3: A continuation of Figure 3-2.

Figure 3-2 and 3-3: The cumulative distance moved by the AVE in the average direction. Frame number is displayed on the x-axis. The background colours show the automatic staging, with red showing pre-migration, green migration and blue post-migration. The solid lines and dots correspond to changing motion signatures which are candidates for different phases. A threshold determined where the stages are applied. The dotted lines in corresponding colours show the manual staging. The plots have been normalised and are directly comparable in the y-axis. A linear upwards line shows the AVE moving at a steady speed, whereas an upwards curve would show an increasing speed, and a flat line denotes no movement. Plots were made by Dr Felix Zhou.

3.4 Characterisation of VE migration in the WT embryo

The 2D projections of the registered data allow all the cells in the epithelial sheet to be seen at once, which vastly simplifies the tracking of cells. In order to provide an exemplar embryo to validate the computation framework in combination with the MOSES superpixel tracking approach, I used Volocity (Improvision) to manually track all the cells one *Lifeact* embryo (L491) 2D Cartesian projection, and the Epi-VE cells in the polar projection. I was able to track approximately one cell over the 100 frames every 4-5 minutes, or around 13 cells per hour, giving a total time of 23 hours for the planar and 9 hours for the polar projection. However, the work was taxing for long stretches, requiring frequent breaks, and had to be spread over 8 working days.

Cells in the AVE region near the boundary were particularly difficult to track manually, as they are smaller and much more densely packed relative to the cell around them. In a number of cases, cell tracks ended when the cell became either too elongated or too small to delineate from those around it, or disappeared from view as the embryo buckled at the boundary.

Using a GUI developed by Siu Lun Yeung, I was able to use these manual tracks to identify where individual cells in each region of the embryo were migrating to, or had originated from. I did this for embryo L491 in the Cartesian projection for ExE-VE and Epi-VE cells (Figure 3-4), and the polar projection, for the Epi-VE (Figure 3-5). The timelapse data for this embryo comprises 495mins (100 timepoints at 5 min intervals) including the period where the AVE migrates to the boundary.

By tracking the cells in the 2D projection manually, it could be seen that they appeared to move in a coordinated manner. Cells which began next to each other largely ended up in close proximity, including daughter cells. The movement of AVE cells, manually identified by a smaller apical surface area, was characterised by a directed proximal motion. Upon reaching the boundary, the cells paused and spread slightly laterally (Figure 3-4 and Figure 3-5).

In comparison to the Epi-VE, there was very little movement of cells in the ExE-VE. This embryo (L491) had a posterior ExE partially obscured by the EPC. However, cells in the posterior boundary region showed movement towards the distal tip (Figure 3-4, yellow panel).

Cells which began in the posterior Epi-VE underwent greater movement towards the distal tip, and those that started more distally contributed to the future anterior (Figure 3-4 and Figure 3-5). However, much of the contribution to the future anterior was from the lateral Epi-VE cells, which moved in roughly symmetric whirling motions. The lateral cells near the Epi-ExE boundary are displaced more laterally and distally forming the top of these whirls, but did not contribute to the anterior in the 495min timeframe.

The cells which began proximal to the AVE, in the anterior-boundary region, exhibited interesting behaviour (Figure 3-4 and Figure 3-5). As the AVE migrated behind them, they moved both laterally and proximally towards the boundary, fanning out in a symmetric manner.

Figure 3-6 shows the Epi-VE tracks in the polar plots, with a track length of 10 frames (the timelapse can also be viewed in Supplementary Video 5). The automatic staging put the post-migration phase for this embryo at tp46 (225mins). With a 10-frame lag, the difference between the motion signatures of each stage is clear comparing the frames at tp30 (145mins) and tp60 (295mins). The migration phase showed a stronger, directional motion corresponding to an active migration of those cells. The post-migration timepoints showed less directed movement, across broader regions of the epithelial sheet.

The tracks were not symmetrical throughout the timelapse, beginning with stronger rotational movement on the left of the frame, and the direction of the AVE migration slightly rightwards. During the course of migration, the right rotation grew stronger, and the direction of migration shifted back centrally. The cells showed distinctly left-biased movement after the leading cells had reached the boundary, in the ‘post-migration’ phase.

The length of tracks indicates how far a cell has moved in the previous 10 frames, and although there is warping in the projection (the closer to the circumference, the longer tracks will appear), the AVE region consistently appeared to be the most motile during migration, with cells in the posterior showing less movement in comparison.

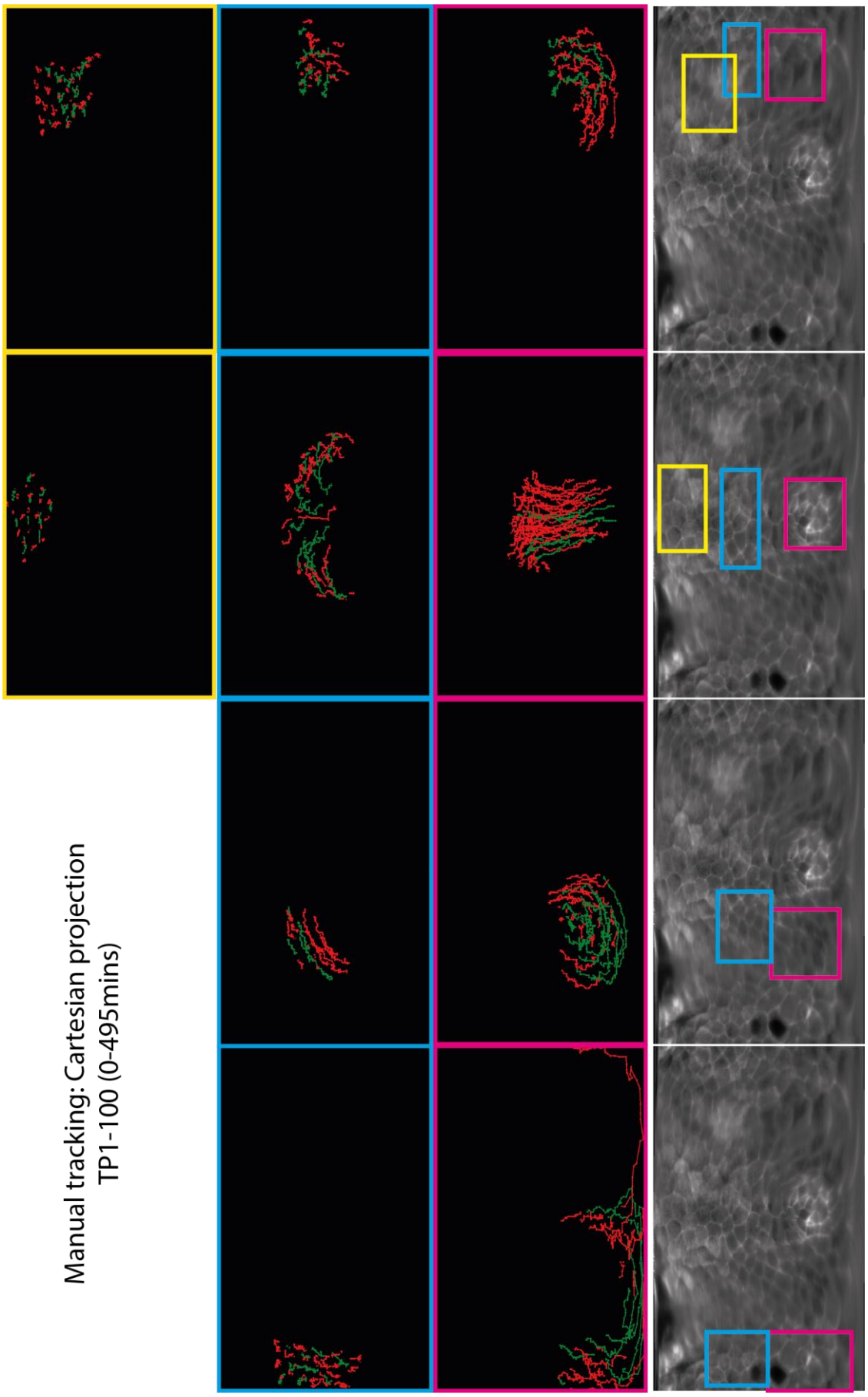
Manual tracking: Cartesian projection
TP1-100 (0-495mins)

Figure 3-4: Manual tracks from different starting areas, on the Cartesian projection of L491. The pink boxes correspond to tracks in the Epi-VE region, blue to those in the boundary region, and yellow to those in the ExE-VE. This embryo had the ectoplacental cone in the posterior region, so samples were not taken from there. Green tracks show mother or undivided cells, and the red tracks show daughter cells.

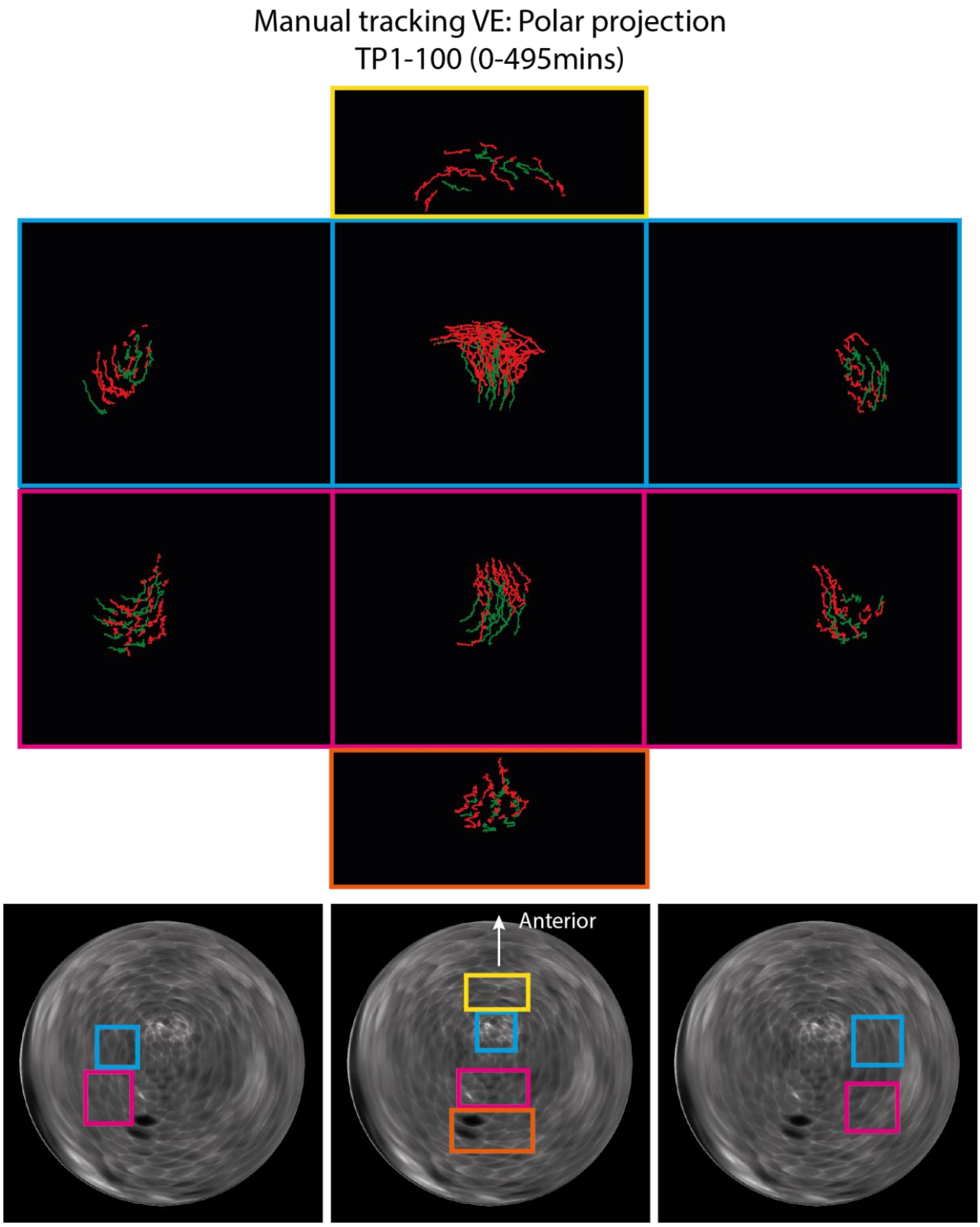

Figure 3-5: Manual tracks from different starting areas, displayed on the Polar projection of L491. The orange shows the posterior-boundary Epi-VE cells, pink boxes correspond to tracks in the more distal and lateral posterior Epi-VE regions, blue to those in the more distal and lateral anterior Epi-VE regions (including the AVE in the central panel), and yellow to those in the anterior-boundary region. Green tracks show mother or undivided cells, and the red cells show daughter cells.

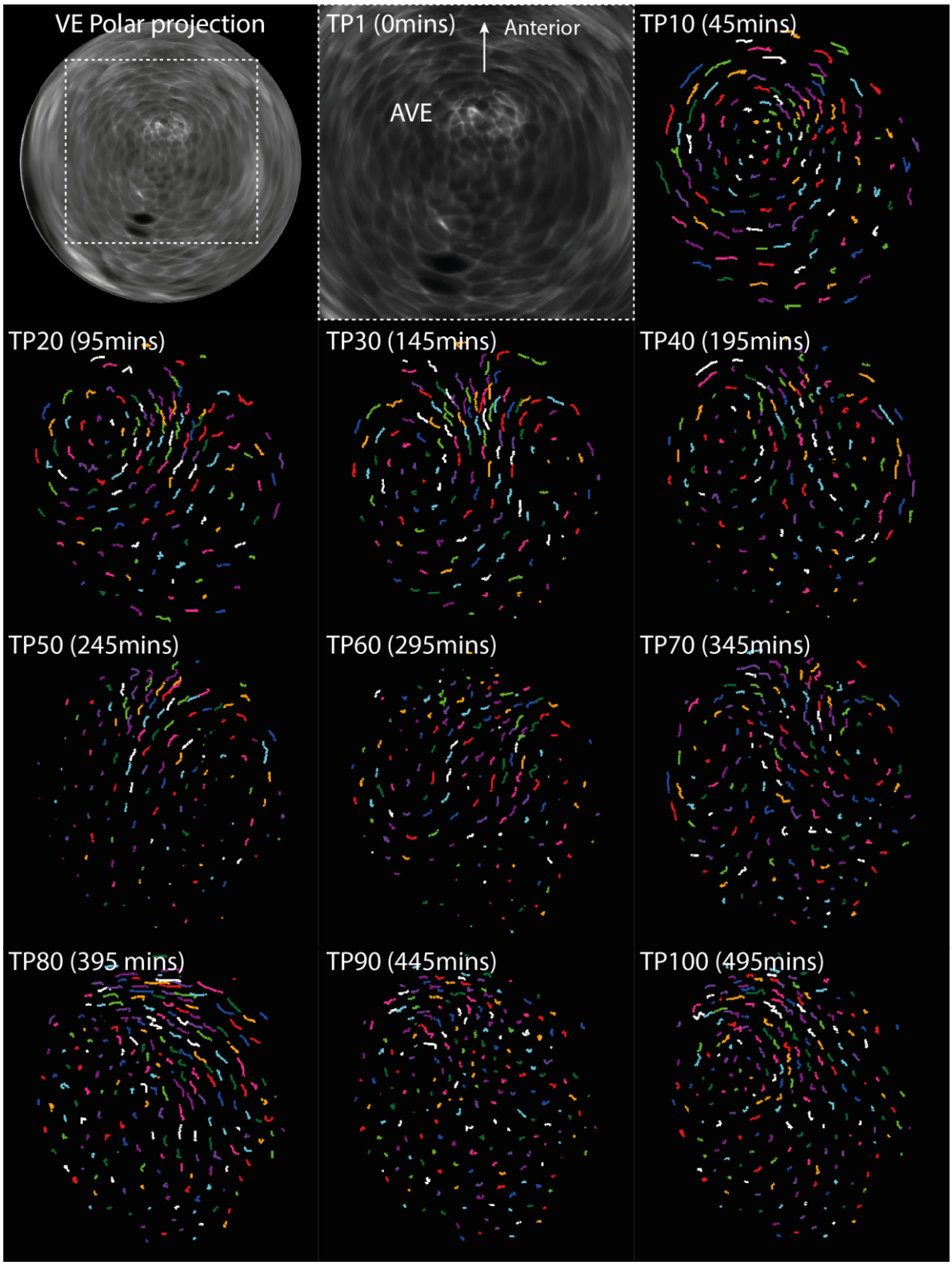

Figure 3-6: Manual tracks of the polar projection of L491. Track length covers movement for the previous ten frames. TP30 is fully in the migration phase according to the manual staging, and TP60 and onwards are fully post-migration. Different colours show tracks from different cells.

3.4.1 AVE migration is characterised by rotational movements of the lateral VE

While manual tracking gives single cell resolution, it is laborious and impossible to apply to the 14/23 embryos in our dataset which do not have the *Lifeact* F-actin marker to delineate cell membranes. With an exemplar embryo to validate patterns of movement, automated MOSES superpixel tracking can be used to give valuable insights into the entire dataset.

The automatic staging using MOSES identified migration as a persistent, directional motion. However, it is important to note that MOSES cannot distinguish between superpixel motion caused by cell shape changes and superpixel motion due to cell movement. To validate the approach, we applied MOSES to the same embryo used for exemplar manual tracking (L491), shown in Figure 3-7A. As the motion characteristics from manually tracking embryo L491 matched those from the MOSES analysis, this suggested that MOSES was picking up the cell motion signature of the VE, and could therefore be uses as a holistic approach to cell tracking and tissue deformation.

Using the frames identified by the automatic staging, we can show motion tracks for the all of the embryos without the need to do individual cell tracking. This enabled the motion to be discerned in the *mTmG ; Ttr-Cre* and *Hex-GFP* lines, which do not delineate cells as the clearly as the *Lifeact* line. The MOSES superpixel tracking showed the same patterns of whirling motion to the manual tracks (Figure 3-7A and B). A representative sample from N=21 embryos with a migratory phase is shown in Figure 3-7A.

A consistent pattern of movement emerged for the migration phase. The tracks in Figure 3-7A show that AVE migration was characterised over time by rotational, whirling movements, to varying degrees. Movement towards the future anterior was not limited to the posterior Epi-VE, but also involved cells in the lateral Epi-VE regions as the AVE cells migrate. The rotational movements were confined to the Epi-VE, with the ExE-VE reasonably static, although some movement did occur in the proximal and lateral directions near the anterior boundary.

In order to identify consistent motion characteristics, we aligned and averaged the *Lifeact* embryos, combining the tracks on the polar projection and dividing them into spatial regions for analysis (Figure 3-7C). The regional grid was aligned such that region 1 was centred on the distal AVE, as defined by the median MOSES direction from the AVE classifier. The inner two rings are in the Epi-VE, whereas the outer two rings are in the ExE-VE. The regions show the migratory fate of the cells which began the stage in that location, and so are 'moving' with the tracks, as opposed to 'static'.

The rotational pattern of movement was apparent in the average plot. Reversing the 3D to 2D projection and transformations enabled quantification of the average cell speed. This quantification showed the cells which began at the distal anterior were most motile, but cells both in front and behind also showed considerable movement (Figure 3-7C). The most motile cells are likely those often characterised as 'leading edge', being at the anterior of the AVE cluster. Whereas the group in the posterior distal tip also likely correspond to AVE cells, the cells in front likely correspond to the non-AVE proximal cells, which are misplaced during AVE migration. Cells in the ExE-VE showed very little movement overall.

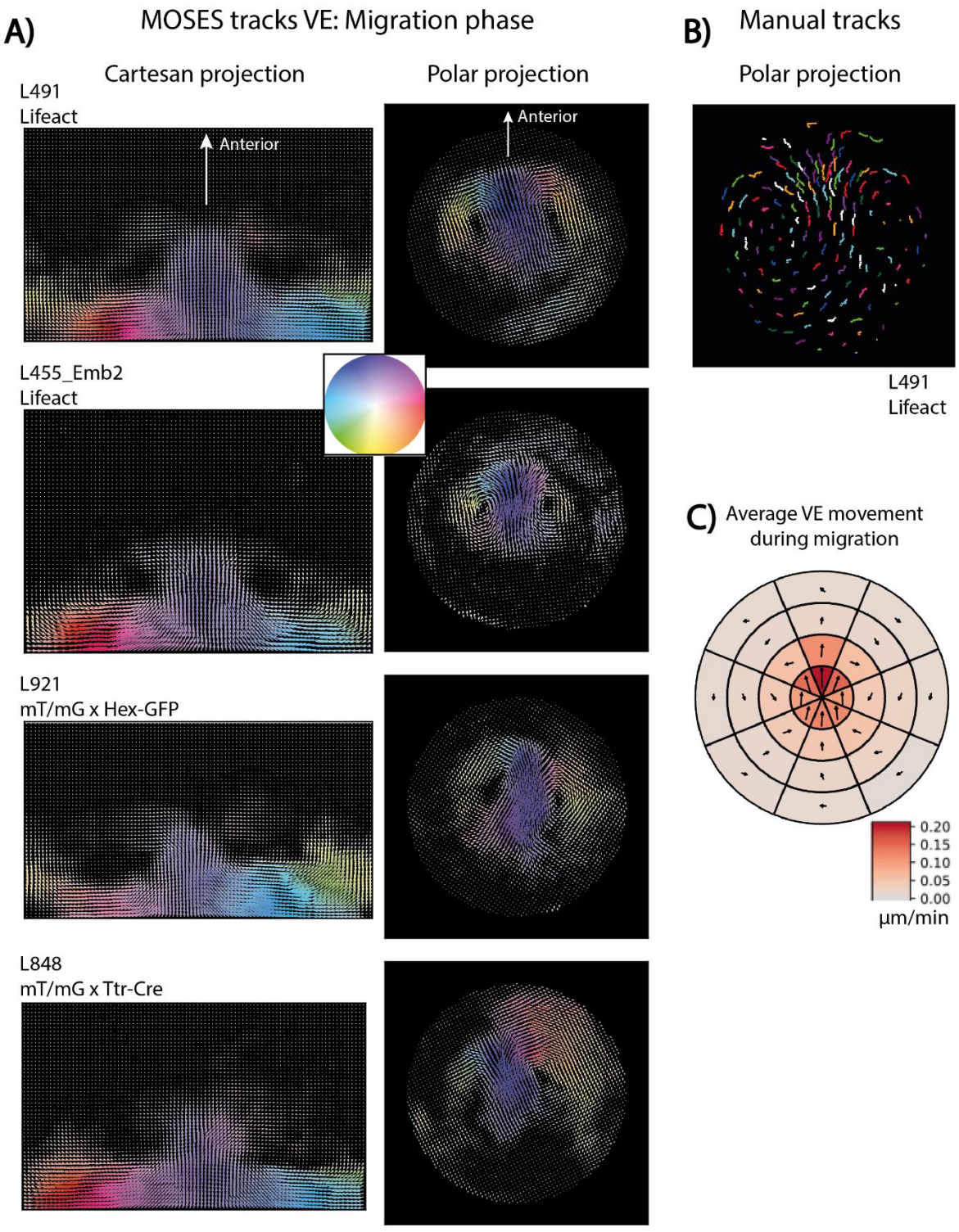
A)
MOSES tracks VE: Migration phase
Cartesan projection
Polar projection
L491
Lifeact
Anterior
Anterior
L455_Emb2
Lifeact
L921
mT/mG x Hex-GFP
L848
mT/mG x Ttr-Cre
B)
Manual tracks
Polar projection
L491
Lifeact
C)
Average VE movement
during migration
0.20
0.15
0.10
0.05
0.00
µm/min

Figure 3-7

Figure 3-7: The VE during migration. A) MOSES superpixel tracks showed characteristic whirling motion throughout the Epi-VE across the dataset, with a representative sample shown. The AVE is centred in the Cartesian projections, and the anterior is roughly upwards in the polar plots. The colour wheel corresponds to the directions of superpixel motion. Note that the movement is in each figure is plotted on a relative, not global scale, and so plots are not directly comparable. B) The MOSES motion corresponded to the manual tracks, validating the automated approach. C) The average motion, divided into regions relative to the direction of AVE migration, showed the most motile (red) regions were the anterior distal, followed by the posterior distal, and also the anterior Epi-VE. There was very little movement in the ExE-VE (pale outer two rings). MOSES plots and the average plot were created by Dr Felix Zhou.

3.4.2 AVE cells migrate via sheet deformation, not cell intercalation

Automated superpixel and manual cell centroid tracking have shown that cells migrate in a coordinated manner. However, they do not give detailed information about changes in individual cell morphology. In order to visualise cell morphology and neighbour intercalation events accurately, I tracked and outlined cells in the Cartesian projection of the same exemplar *Lifeact* embryo using Adobe Illustrator (Adobe Systems). I annotated three timepoints of the timelapse: 0mins (TP1), 120mins (TP25), and 245mins (TP50), as AVE migration occurred (Figure 3-8, with the raw Cartesian projection shown in Supplementary Video 6A).

The AVE cells are located centrally in the projection, unmarked in the *Lifeact* data but recognisable by their characteristic directed movement and small apical surface area. I coloured the annotated cells according to their position along the proximal-distal axis in the first frame, in order to clearly show the change in neighbours across the timelapse. The AVE cells began asymmetrically located towards the anterior in the first frame, and the leading cells reached the boundary by 245mins.

Viewing the cells across the sheet it was clear that, rather than the AVE moving via extensive cell intercalation and neighbour exchange, the majority of cells across the VE instead maintained contact with their initial neighbours despite the disruptive movement taking place. Although the

known presence of long cellular protrusions in the AVE of migrating embryos suggests active migration, individual cells did not move independently past those in the surrounding tissue. Instead, the behaviour of the Epi-VE was more like that of a sheet only loosely connected to the layer below, with adhesion between neighbouring cells stronger than adhesion to the basal laminar. This gave rise to general sheet deformation as migration occurred (Figure 3-8).

The MOSES superpixel tracks can be linked to create a 'dynamic-mesh' which deforms to reflect relative differences in local velocity across the epithelial sheet. This deformation can be used as a proxy for cell/tissue shape change. The Cartesian deformation mesh for the annotated embryo (L491) is shown in Figure 3-8 and Supplementary Video 6B, with the polar deformation mesh in Supplementary Video 6C. A representative sample of the other embryos is shown in Figure 3-9A. The deformation also illustrates the moving regions used to average the movement across different embryo, which is shown in Figure 3-9B and Supplementary Video 6D.

The cells proximal to the AVE showed the most interesting behaviour (Figure 3-8), as they also moved in a coordinated manner, pushed proximally by the AVE behind. Initially some of the movement was limited as the cells were compressed between the AVE and the boundary, which has the appearance of being non-permissive. The cells subsequently elongated in both lateral directions, moving proximally while maintaining contact with the same initial neighbours. Inevitably, the neighbours were also pulled out of shape as the AVE region moved past them, with chains of neighbours previously sitting on the same horizontal level now forming a stretched curve around the AVE group.

Although neighbour exchanges did occur, they involved only small changes in connections to neighbouring cells, as junctional rearrangements rather than cell-cell rearrangements or intercalation events (Figure 3-8). These tended to occur in the regions which undergo the most deformation: those above and lateral to the AVE.

The key events which did allow reorganisation of cells and pronounced neighbour exchange were cell divisions, when the cells underwent characteristic rounding and fission. Although daughters remained largely connected to the same neighbours, this could give rise to a neighbour exchange as the cells nearby were jostled to accommodate the new cell intercalating in between. In Figure 3-8 I have shown the dividing cells in a darker shade of the same colour, with dividing cells often intercalating into the next horizontal layer.

In the annotated embryo, I identified only one cell which underwent a more extensive intercalation without a cell division: that of the most central red-annotated cell which already appeared elongated in the first frame (further highlighted in Figure 3-10A). This cell lost contact with its initial neighbours very early after the first frame, and can be seen as a more rounded cell in the next image. It later moved again, now as a lateral cell which appeared to slide down the top of the cell below. This is evident in joining the orange and white layer of cells near the boundary in the second image. However, this exceptional behaviour did not appear to be due to stress, as other cells were more elongated as the AVE nears the boundary, but show no similar 'loose' movement.

I identified this behaviour in another 2 *Lifeact* embryos, giving a total of 3/9: one with 1 cell, and another with 2 cells showing 'loose connections', in the lateral or directly in front of the AVE region, shown in Figure 3-10B and C. In both of these embryos the loose cell was in close proximity to forming rosette structures. In Figure 3-10B the loose cell (red) began as part of a rosette of 6 cells, before being displaced laterally and leaving a 5 cell rosette. In Figure 3-10C a series of shortening events occurred in the proximal cells as they were displaced. The cells formed transient rosettes, first involving the two green cells in the figure, then 70mins later, the green cells loosely shifted to the left, and the rosette ends up shifted to the cells above. It is important to remember that by annotating cells on the 2D projection, only a single depth is visible, and cells showing small junctional rearrangements may remain connected to the same neighbours at another point across their volume. However, the distances moved make this unlikely for the 'loose' cells.

When the cells proximal to the AVE reached the non-permissive ExE, the tension was either released by cells buckling into the boundary as they were compressed (in which case they disappeared from the projection), or as they divided. Divisions in both the proximal-AVE cells and the ExE-VE cells near the boundary caused localised jumps in movement.

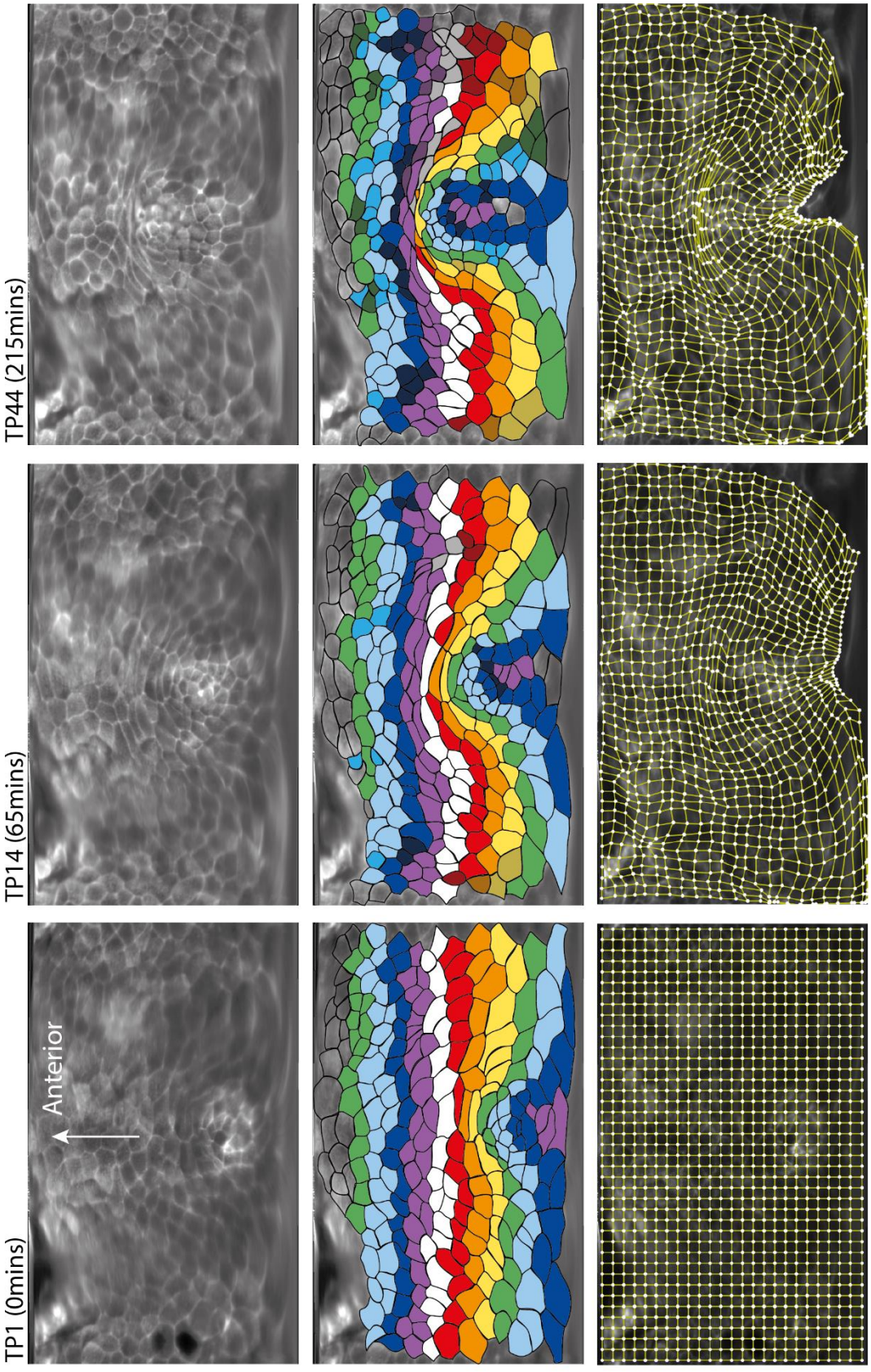
L491
Projection (AVE central)
Annotation
MOSES deformation mesh
TP1 (0mins)
TP14 (65mins)
TP44 (215mins)
Anterior

Figure 3-8: Tissue deformation during AVE migration in L491. The top row shows the raw Cartesian projection. The middle row shows the manual annotations. Cells are coloured according to their initial horizontal location, and keep the same colour throughout the timelapse. Cells which have divided are shown in a darker shade of their original colour. The ExE-VE sits roughly under and above the purple annotations in the middle of the images. The bottom row show the corresponding MOSES mesh deformation (images by Dr Felix Zhou). The AVE cells are located centrally in all images, denoted by their small apical surface area. The central red cells above the AVE region are further highlighted in Figure 3-10A, as the only cells in this timelapse which underwent extensive neighbour exchange without a cell division.

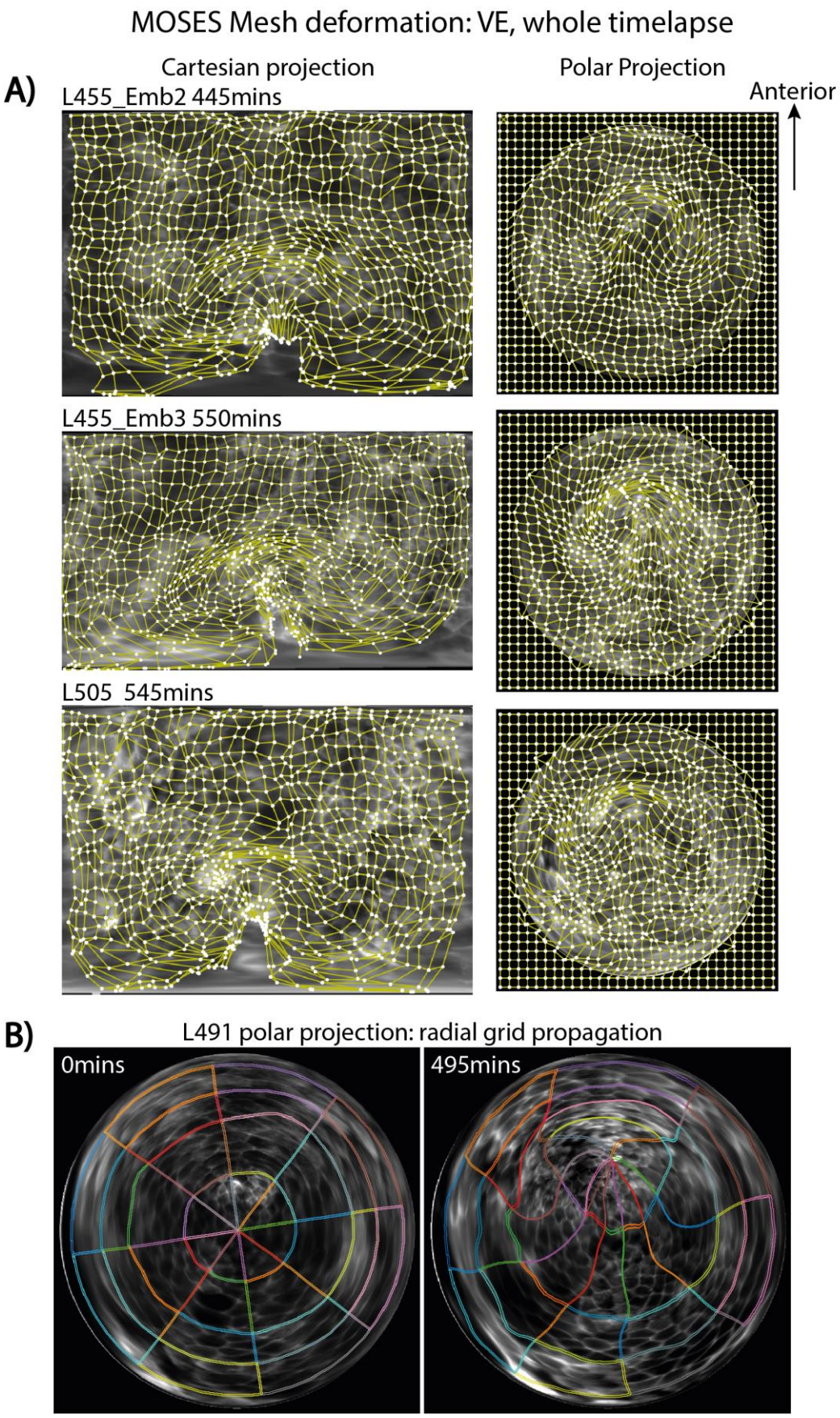
MOSES Mesh deformation: VE, whole timelapse
A)
Cartesian projection
Polar Projection
Anterior
L455_Emb2 445mins
L455_Emb3 550mins
L505 545mins
B)
L491 polar projection: radial grid propagation
0mins
495mins

Figure 3-9

Figure 3-9: Tissue deformation during migration. A) 3 of the 21 embryos are shown as a representative sample of deformation in the MOSES mesh over the course of a timelapse. B) This deformation can be used to illustrate the moving regions used to create the average analysis. Plots by Dr Felix Zhou.

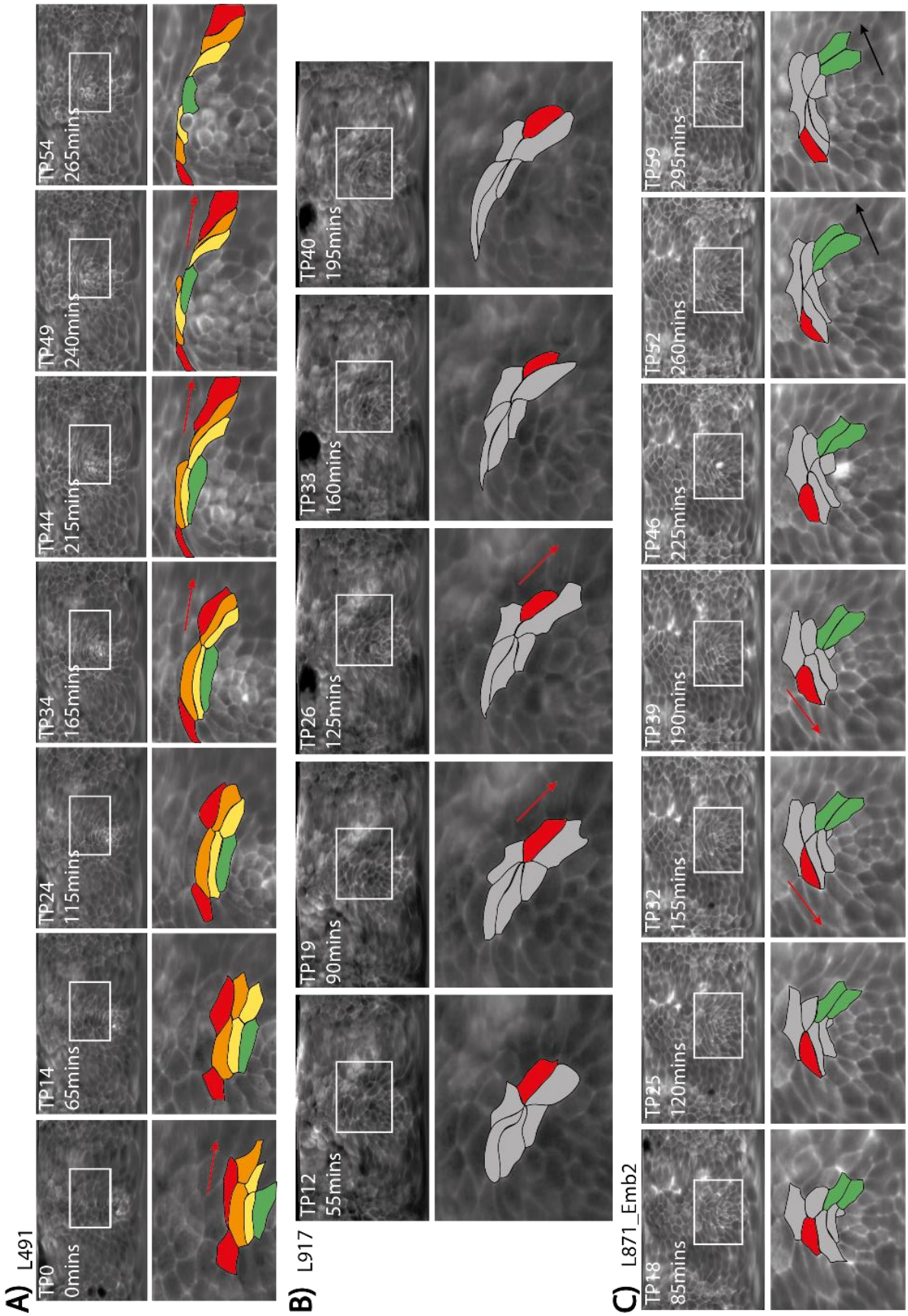
A) L491
TP0 0mins
TP14 65mins
TP24 115mins
TP34 165mins
TP44 215mins
TP49 240mins
TP54 265mins
B) L917
TP12 55mins
TP19 90mins
TP26 125mins
TP33 160mins
TP40 195mins
C) L871_Emb2
TP18 85mins
TP25 120mins
TP32 155mins
TP39 190mins
TP46 225mins
TP52 260mins
TP59 295mins

Figure 3-10: Cells with loose connections. A) Highlights the cells shown in Figure 3-8 using the same colour scheme. The red elongated cell is the only cell identified in embryo L491 which underwent extensive intercalation, losing contact with its initial pre-migration neighbour and being displaced to the right (red arrows). The embryo underwent buckling and it is not clear from annotating the projection if the orange and yellows calls also lost contact, or if contacts are hidden behind other cells. B) and C) both correspond to forming rosette structures in other embryos. In B) the red cell is displaced laterally from a rosette formation proximal to the migrating AVE cells. In C) cell junctions shortened in the proximal cells causing the formation of transient rosette structure involving the green cells. The red cell was then displaced laterally, and the green cells later exchanged neighbours and were displaced to the right (black arrow) excluded from the new rosette structure. Timepoints correspond to 5min time resolution.

3.4.3 Cellular protrusions suggest active migration

There are several published timelapse studies of protrusions using the *Hex-GFP* line, which suggest the AVE cells actively migrate (I. Migeotte, Grego-Bessa, & Anderson, 2011; Omelchenko et al., 2014; Srinivas et al., 2004; Trichas et al., 2011). Migeotte et al. have described the transition of *Hex-GFP* positive cells from columnar to cuboidal via a 'snail-like' morphology with highly elongated lamella splitting at their ends into smaller, 'horn-like' bifurcations. The protrusions were up to 2.5x the length of the cell body lasting up to 3 hours, and would extend, partially retract, and extend again in 'probing' like behaviour (7 protrusions over 5 embryos). Much shorter protrusions were also seen at the trailing edge of the AVE group.

Omelchenko et al. 2014 have produced the highest time resolution videos of the protrusions with frames captured every 1 or 2 minutes using a confocal microscope, and flattened using a maximum intensity projection before manual annotations. One key advantage of their study was the use of a GFP-GPI line to express GFP in the epiblast in addition to the *Hex* positive AVE cells, enabling the protrusions to be seen in context as they move along the basal lamina. Their videos showed a movement reminiscent of the horn-like bifurcations crawling along the extra cellular matrix (ECM). Looking in section, they noted that protrusions ran underneath proximal cells, and suggested this

could lead to competition for attachment to the ECM and cell displacement. The external clues directing the protrusions were not clear. Although the protrusions reached proximally towards the ExE region at slightly different angles, this changed for individual cells after retraction. Migeotte et al. noted the bifurcating nature of the protrusions was indicative of chemotaxis. They also found a degree of heterogeneity in the *Hex-GFP* expression (utilising it to be able to visualise the protrusions) and found velocities of individual cells also differed, being slightly higher further behind the leading edge and indicative of a push-pull mode of collective migration.

It has been suggested that the cellular protrusions could facilitate the formation of new cell contacts by carrying adherens junction component E-CADHERIN to new sites (Stower & Srinivas, 2014), but this has not been experimentally proven during AVE migration. E-CADHERIN is thought to link the actin cytoskeleton to adherens junctions via α-CATENIN and β-CATENIN, which facilitates mechanical coupling and the transmission of tensile forces (Martin, 2010; and reviewed in Desai *et al.*, 2013).

I was able to use the *Lifeact* line to view cellular protrusions, without needing the *Hex-GFP* fluorescence, in order to make qualitative observations to better understand how they may be causing active migration.

One of the key advantages of a spatiotemporally registered video dataset is the relative ease of following protrusions in a single section of the timelapse. To follow protrusions I created 4D hyperstacks in ImageJ to scroll through the timepoints and z stacks. I rotated the hyperstacks aligning them such that the AVE migration direction faced left of the stack. Due to the anisotropic acquisition of the z-stacks, the thin protrusions were only distinguishable in those embryos which were imaged with the AVE lateral to the objective (4/9). Of these 4, I followed a long (several cell lengths) protrusion in L455_Emb2 (Figure 3-11) and L864 (Figure 3-12) and a smaller protrusion in L871_Emb1 and L505, of which, L505 is shown as a representative example in Figure 3-13 with snapshots every 10mins. The two embryos with a long protrusion are shown every 50mins. In L505

I was able to follow all the cells in section, including the first timepoint for reference. Only a few protrusions were identified, as the thin nature of the protrusions made it hard to see those that were not directly perpendicular in the rotation of the stack. However, they still provide an opportunity to gain further insight into AVE cell movement.

I observed the cellular protrusions extending from cells in the leading edge of the AVE as seen previously (Isabelle Migeotte et al., 2010; Omelchenko et al., 2014). The cells I characterise as leading edge showed columnarity, and were located on the anterior side of the distal tip. The observed protrusions appear at least 50mins (10 frames) prior to the start of any directed movement. As previously described by Omelchenko et al., these long protrusions pushed underneath the cells in front, intercalating between the VE and the basal lamina. In the 5min resolution timelapse video of L864 and L455_Emb2, it is also possible to see occasional bursts of brighter actin on the basal lamina as the protrusions work their way up the proximal anterior.

The protrusions continue reaching proximally until they reach the epiblast boundary. When this happens, there is a brighter burst of actin, followed by a collective movement of the AVE cells as the protrusions contracts, which is propagated through the rest of the tissue. This results in bunching of the cells proximal to the leading edge. In embryos L455_Emb2 and L871_Emb1, the epiblast cells at the boundary appear to be pulled downwards by the protrusion. Rapid, collective movement following contraction is especially pronounced in L455_Emb2, which undergoes a very short migration phase of only 70mins according to the manual staging, during which the protrusion contracts.

The propagation of movement from anterior to posterior is shown in the angle and height of the VE cells. In 4/4 embryos, cells stretch very thin in the proximal region and around the distal tip, lengthening towards the anterior. With the greater time resolution of L505 in Figure 3-13, we can see that the posterior cells at 295mins have become more slanted towards the anterior, led by the apical surface, before lengthening later in the timelapse (data not shown).

In summary, I have used the registered *Lifeact* data to follow protrusions during and prior to migration. The apparent latching and pulling behaviour of the protrusions suggest an active process, and may explain the irregular velocity signature of the cells identified by the MOSES superpixel tracking.

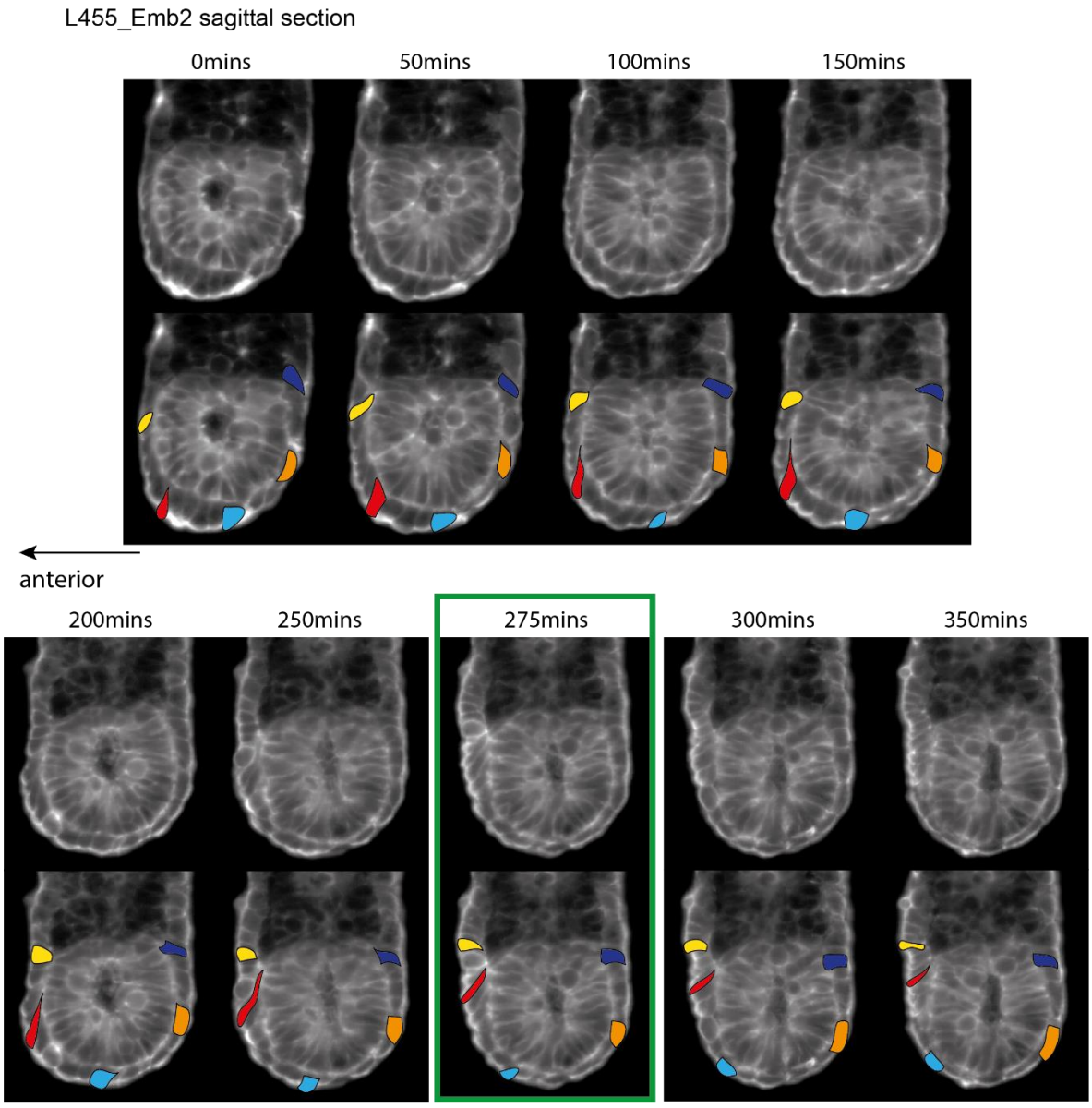

Figure 3-11: Protrusions in the sagittal section of L455_Emb2. Timepoints have a 5min resolution, and frames are shown 50mins apart, with the exception of at 275mins, which is 25mins apart. The green box around 275mins denotes this frame is from the migration phase. Anterior is to the left. The protrusion (red cell) reaches proximally underneath the cells in front before it latches onto the boundary, shown with a bright burst of actin, and the epiblast cells appear to pulled downwards (250mins). A quick, collective movement follows as the protrusion contracts. This is propogated through the VE, and results in cells bunching proximal to the protrusion.

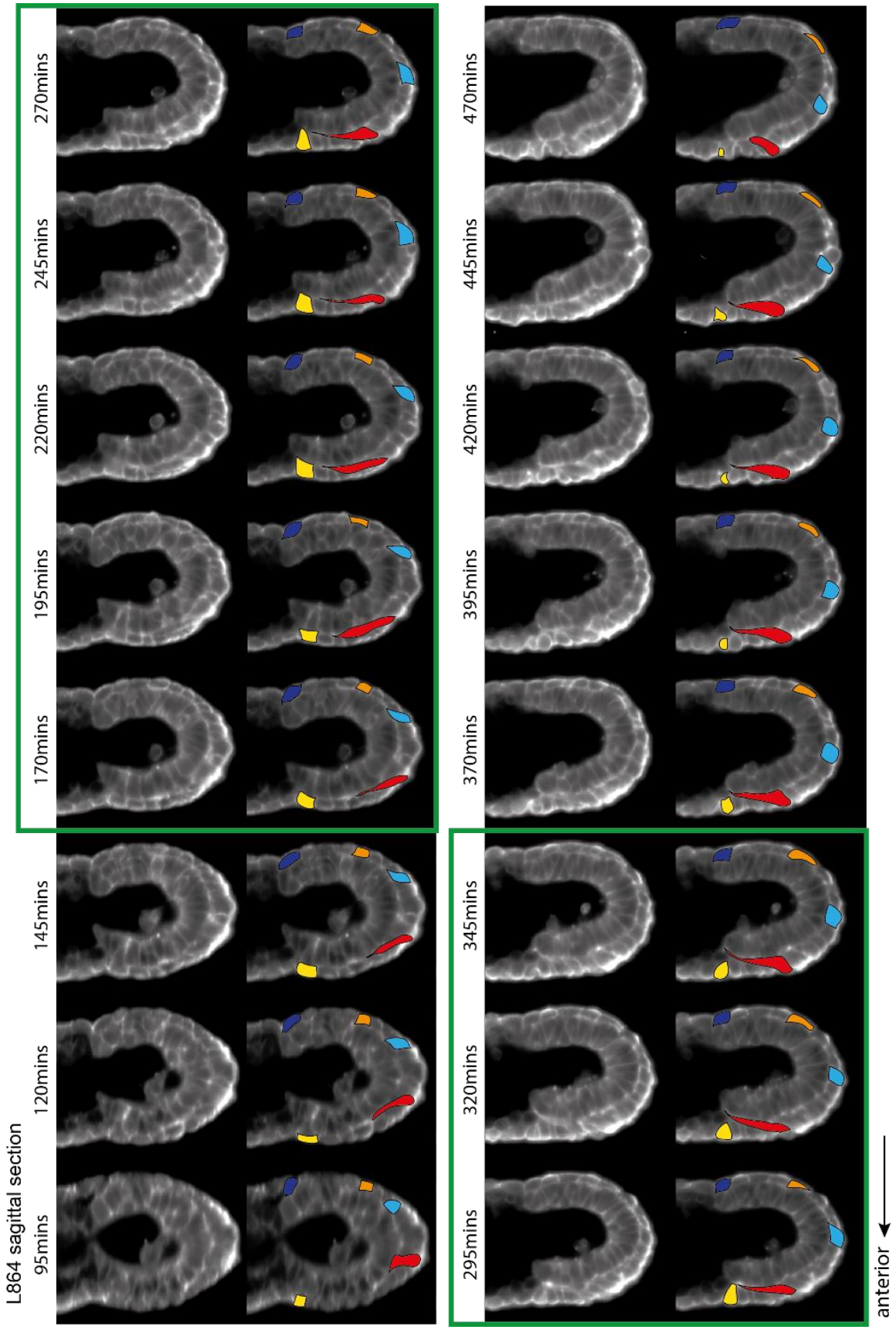
L864 sagittal section
95mins
120mins
145mins
170mins
195mins
220mins
245mins
270mins
295mins
320mins
345mins
370mins
395mins
420mins
445mins
470mins
anterior

Figure 3-12: Protrusions in the sagittal section of L864. Frames are shown 50mins apart. The green box denotes timepoints in the migration phase. The protrusion is shown in the red cell. Anterior is to the left. Cells in the posterior (right, orange) were stretched towards the anterior as the AVE migrate, becoming very thin.

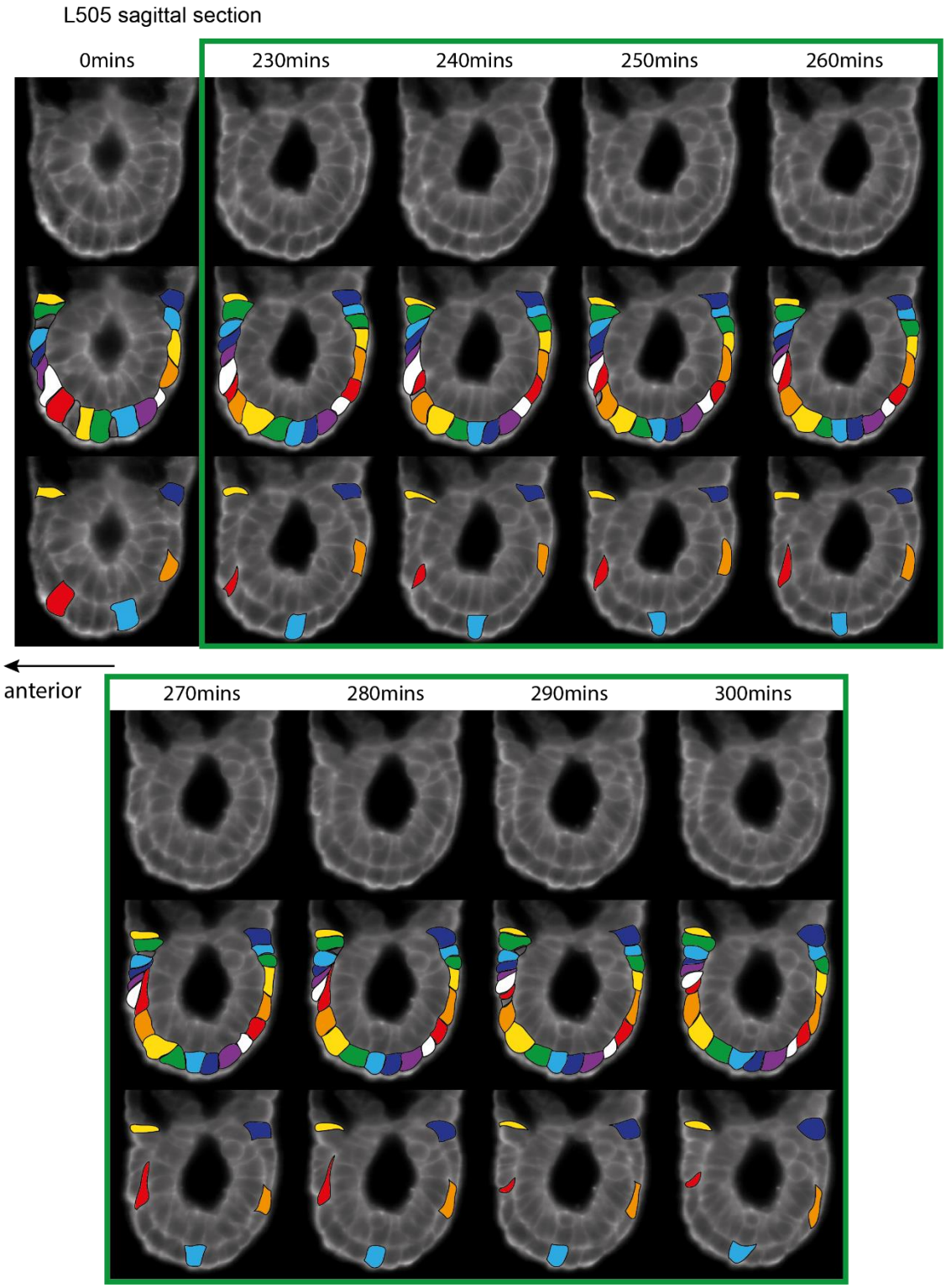

Figure 3-13: Protrusions in the sagittal section of L505. Frames are shown 10mins apart. The green box denotes timepoints in the migration phase. The protrusion is shown in the red cell. The anterior is to the left. The increased time resolution in this figure shows the slanting of cells in the posterior (right, orange) led by the apical surface as AVE migration propogates movement across the VE. The posterior cells later went on to stretch thinly towards the AVE.

3.4.4 Epi-VE cells move into the ab-embryonic half of the embryo during migration

One advantage of this LSFM dataset and the 2D projections is the ability to see all of the cells in the epithelial sheet, not just the *Hex-GFP* positive cells. This allowed us to address the temporal behaviour of the Epi-VE cells proximal to the migrating AVE. Looking at both the epiblast and VE layers overlaid, it was also possible to see the position of the boundary relative to the migrating cells (Figure 3-14 and Figure 3-15).

Interestingly, cells located in the anterior Epi-VE region before migration were pushed past the epiblast boundary in 7/9 *Lifeact* embryos. In those where this was not observed, the embryo appeared too early (L871) or had a small epiblast (L505). I confirmed this in sagittal sections using 4D hyperstacks, with L455_Emb2 (Figure 3-11), L864 (Figure 3-12) and L871_Emb1 (not shown) showing several cells beginning in the Epi-VE being pushed into the anatomical ExE-VE region. Their lack of contact with the epiblast was confirmed in 3D by scrolling through the stacks, in addition to using the overlay projections. In L871_Emb1 the most proximal Epi-VE cell was 3 cells above the boundary by the end of the timelapse. It appears more pronounced in the overlays with later embryos, with many embryos showing multiple cell layers of separation.

Rivera-Perez et al. noticed that a few of the *Hex* expressing cells in the largest embryos did cross the boundary, but not by more than one row of cells (Rivera-Pérez et al., 2003). I found 2/7 cases of this occurring in the *Hex-GFP* embryos which had captured post-migration, shown in Figure 3-16.

Additionally, I analysed if *Hex-GFP* positive cells were showing elongation due to squashing at the boundary, or if this was confined to cells proximal to the AVE. In 1/9 embryos (Figure 3-16) cells with strong *Hex-GFP* expression showed distinct elongation. In another 5/9 embryos, cells with weak, proximal *Hex-GFP* expression showed elongation and lateral movement (Figure 3-16 and Figure 3-17).

It is unclear whether the cells that express the *Hex-GFP* reporter at low levels are 'true' migratory AVE cells extending cellular protrusions, as they sit proximal to cells with strong AVE signal and

which also show characteristic small apical surface area. The Cartesian projection of L928_Emb2 captures a cellular protrusion showing strong *Hex-GFP* expression, reaching from behind the weakly expressing cells (Figure 3-17). AVE cells may have been exposed to a gradient of *Hex*-inducing signal. Cells which migrate behind the strongly expression 'leading edge' also exhibit low levels of *Hex-GFP* expression, although the reduced intensity may be partially due to the lag time for making GFP protein.

There were also two instances in the section analysis where ExE-VE cells moved distally into the Epi-VE region: shown by the dark blue cell in L455_Emb2 (Figure 3-11) and also apparent from the overlay of L917 (data not shown). It is likely the lengthening of cells in the posterior is dampening any movement in the posterior, but denotes that the ExE-VE is also not confined to its anatomical location during migration.

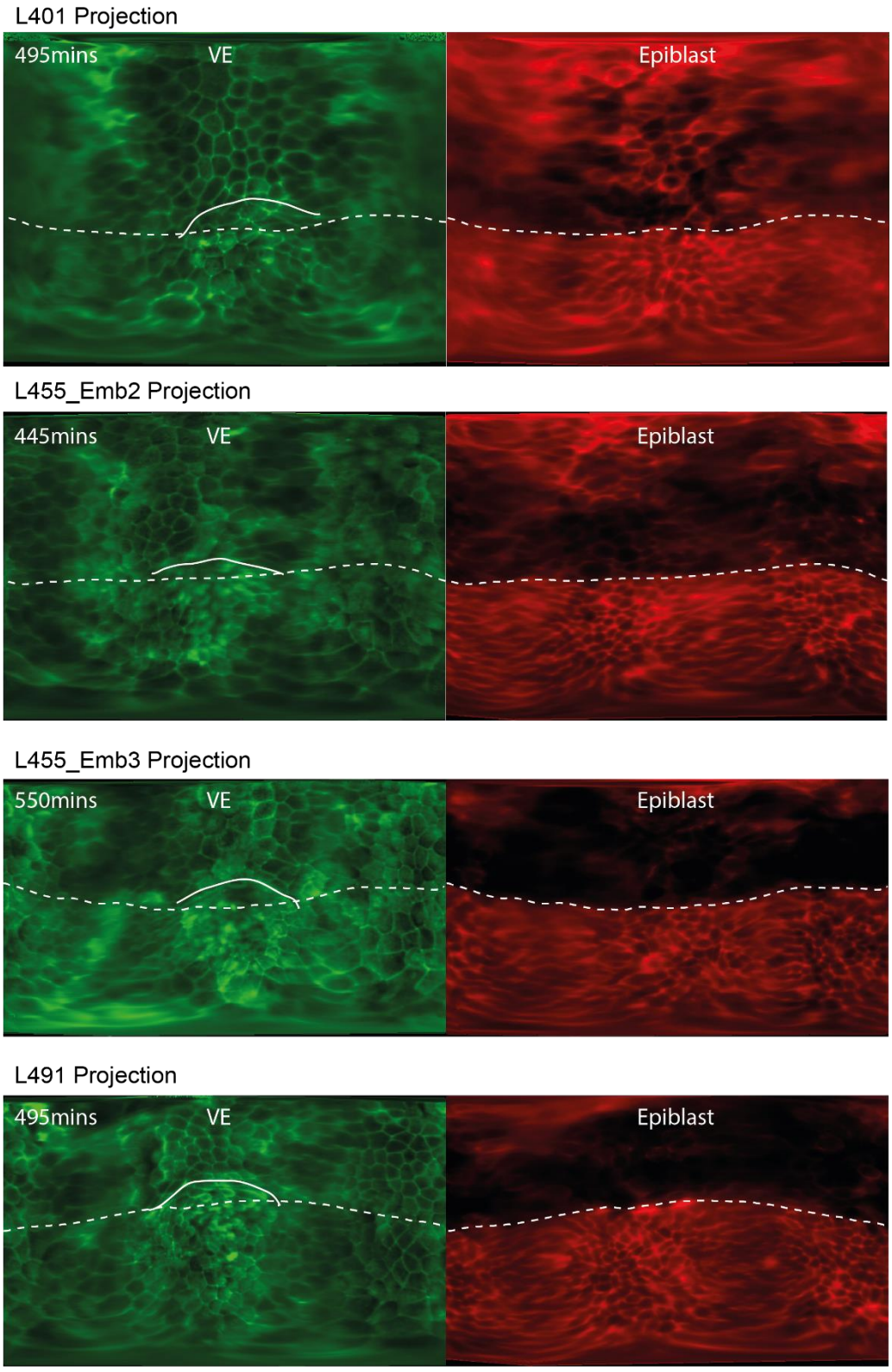

Figure 3-14: In 7/9 Lifeact embryos, Epi-VE proximal to the AVE were pushed beyond the boundary into the ExE region. The dotted line shows the epiblast boundary, whereas the white line shows the location of the cells proximal to the AVE which began the timelapse in the Epi-VE region.

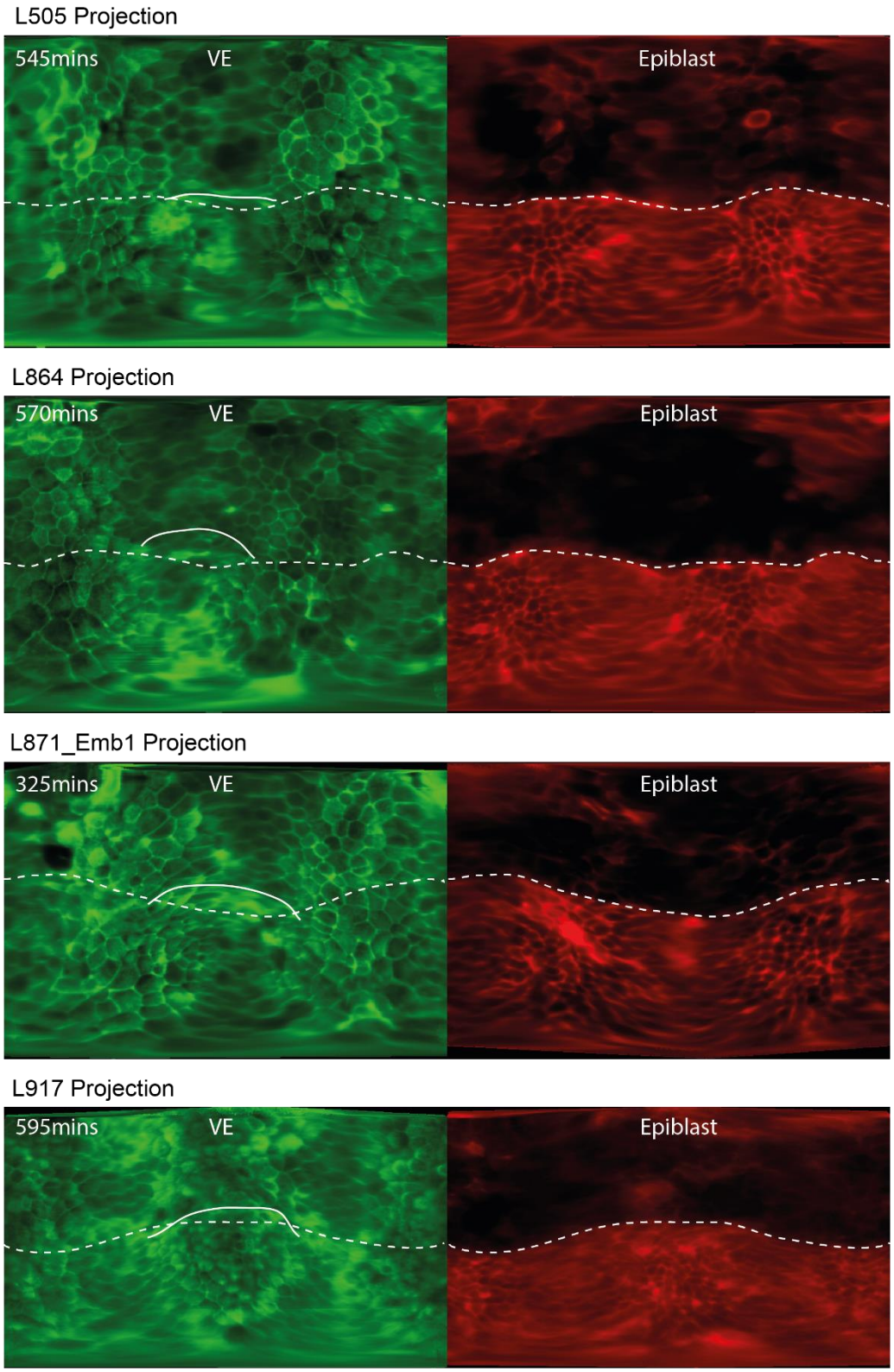

Figure 3-15: A continuation of Figure 3-14. Epi-VE cells in L505 did not migrate past the boundary.

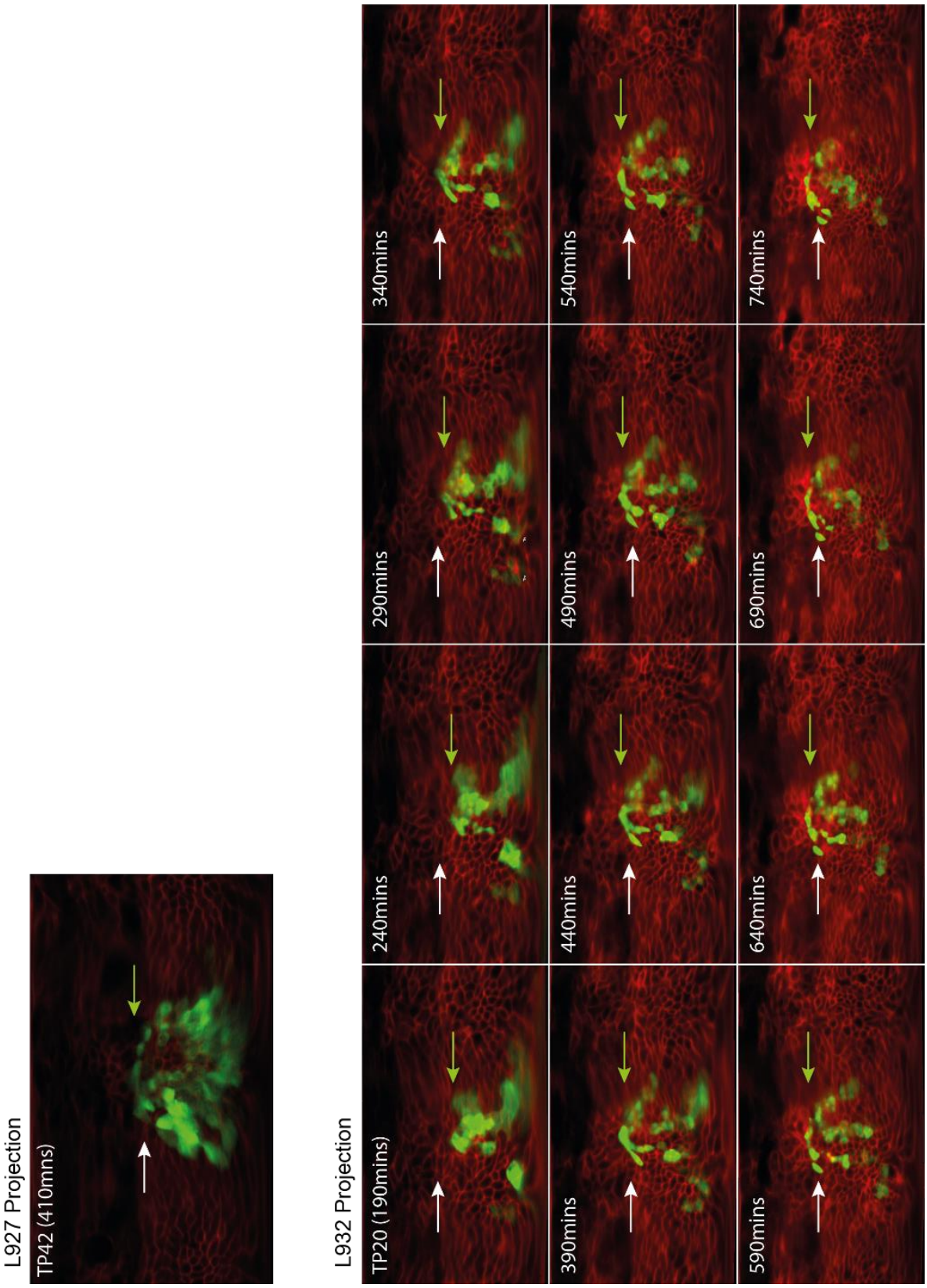
L927 Projection
TP42 (410mns)
L932 Projection
TP20 (190mins)
240mins
290mins
340mins
390mins
440mins
490mins
540mins
590mins
640mins
690mins
740mins

Figure 3-16: Hex-GFP positive cells (green and green arrow) migrate past the epiblast-ExE boundary (white arrow) in 2/7 post migration embryos. L927 also shows elongation of weakly Hex-GFP positive proximal cells. L932 shows elongation of strongly expression Hex-GFP cells near the boundary as they move laterally, at 340mins and 390mins (1/9 embryos to show this).

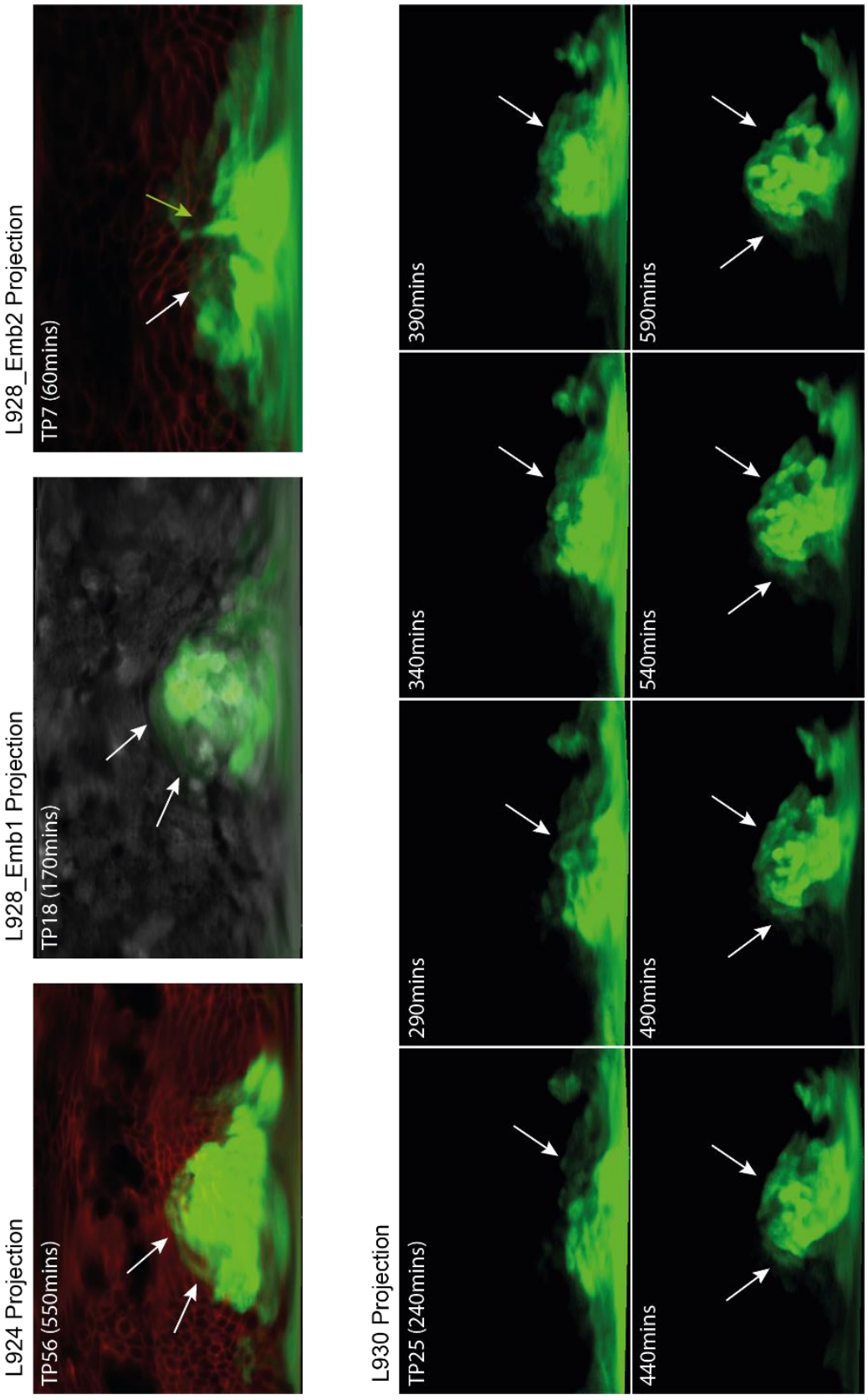
L924 Projection
TP56 (550mins)
L928_Emb1 Projection
TP18 (170mins)
L928_Emb2 Projection
TP7 (60mins)
L930 Projection
TP25 (240mins)
290mins
340mins
390mins
440mins
490mins
540mins
590mins

Figure 3-17: In 5/9 embryos, cells with weak, proximal Hex-GFP expression (white arrows) showed elongation and lateral movement (L927 is shown in Figure 3-16). L928 captures a protrusion showing strong Hex-GFP expression (green arrow), reaching from begin the weakly expressing proximal cells.

3.4.5 Post-migration left-right bias

The automatic staging identified a post-migration phase in 19 embryos, defined as the phase following persistent directional motion. Of these, 17 had a substantial number of timepoints in post-migration. Whereas the average movement during the migration phase of the *Lifeact* embryos was towards the anterior, the average movement vectors in post-migration showed an apparent bias towards the left of embryo when looking proximally from below the distal tip (Figure 3-18A).

This average result does not show the variation of individual embryos, and so Dr Matthew Stower and I independently validated a presence of an asymmetric post-migration bias in the individual embryos. I identified 8/17 embryos to have a left-leaning post-migration bias, 6/17 embryos to have a right bias, and 3/17 to have no apparent bias. Dr Stower identified 10/17 embryos with a left bias, 6/17 with a right bias, and 1/17 with no bias. We agreed in 13/17 embryos, and for the remaining 4/17 embryos one researcher identified a bias where the other gave a result of 'no bias'. In no cases did one researcher give a left bias and the other a right for the same embryo. A sample of each category is shown in Figure 3-18B.

Our manual validation does not quantify the strength of the bias, as the plots we based our analysis on show relative motion. The average movement plot is calculated using comparable absolute motion for the *Lifeact* embryos alone. However, it does confirm that the majority of the embryos (13/17 agreed) have an asymmetric left-leaning or right-leaning bias in the direction of AVE movement in the post-migration phase.

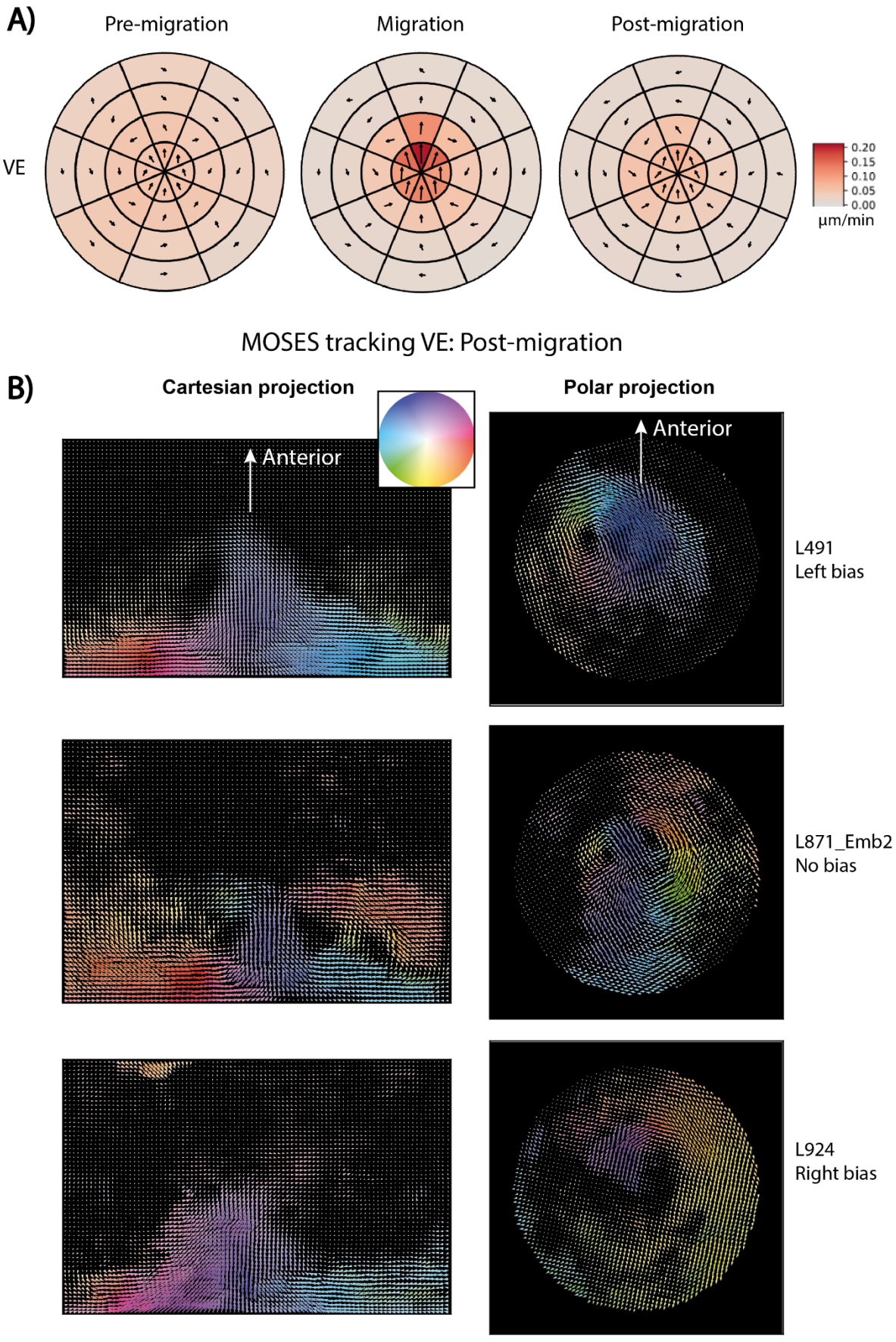
A)
Pre-migration
Migration
Post-migration
VE
0.20
0.15
0.10
0.05
0.00
µm/min
MOSES tracking VE: Post-migration
B)
Cartesian projection
Polar projection
Anterior
Anterior
L491
Left bias
L871_Emb2
No bias
L924
Right bias

Figure 3-18

Figure 3-18: Movement in the VE in the post-migration phase. A) Aligned average polar plots showed a leftwards bias in the direction of movement in the post-migration phase. The inner two layers show Epi-VE and the outer two layers show ExE-VE. The anterior is central and vertically upwards on the plots. B) This movement was validated manually, with examples showing embryos with left bias, no bias, and right bias. The colour wheel corresponds to the directions of superpixel motion. Note that the direction of AVE migration in the polar plots in B) is roughly upwards, but embryos were not completely aligned as they are in A). Plots were created by Dr Felix Zhou.

3.4.6 Is there coordinated movement between the VE and the epiblast?

We also applied MOSES as described previously to create tracks and deformation maps of the epiblast layer underneath the VE, in order to see whether or not there was coordinated movement between the VE and the epiblast cells.

Whereas the AVE in the VE layer showed a clear, directed movement towards the anterior accompanied by lateral rotations across embryos, the epiblast did not show such pronounced coordinated global movement during AVE migration. The cell movement at the interface was instead characterised by localised flows with no overall symmetry or directional persistence, and no apparent similarity between embryos, as shown with a representative sample in Figure 3-19 (the raw Cartesian projection for the epiblast is shown in Supplementary Video 7). Movement was primarily confined to the epiblast, with the ExE static.

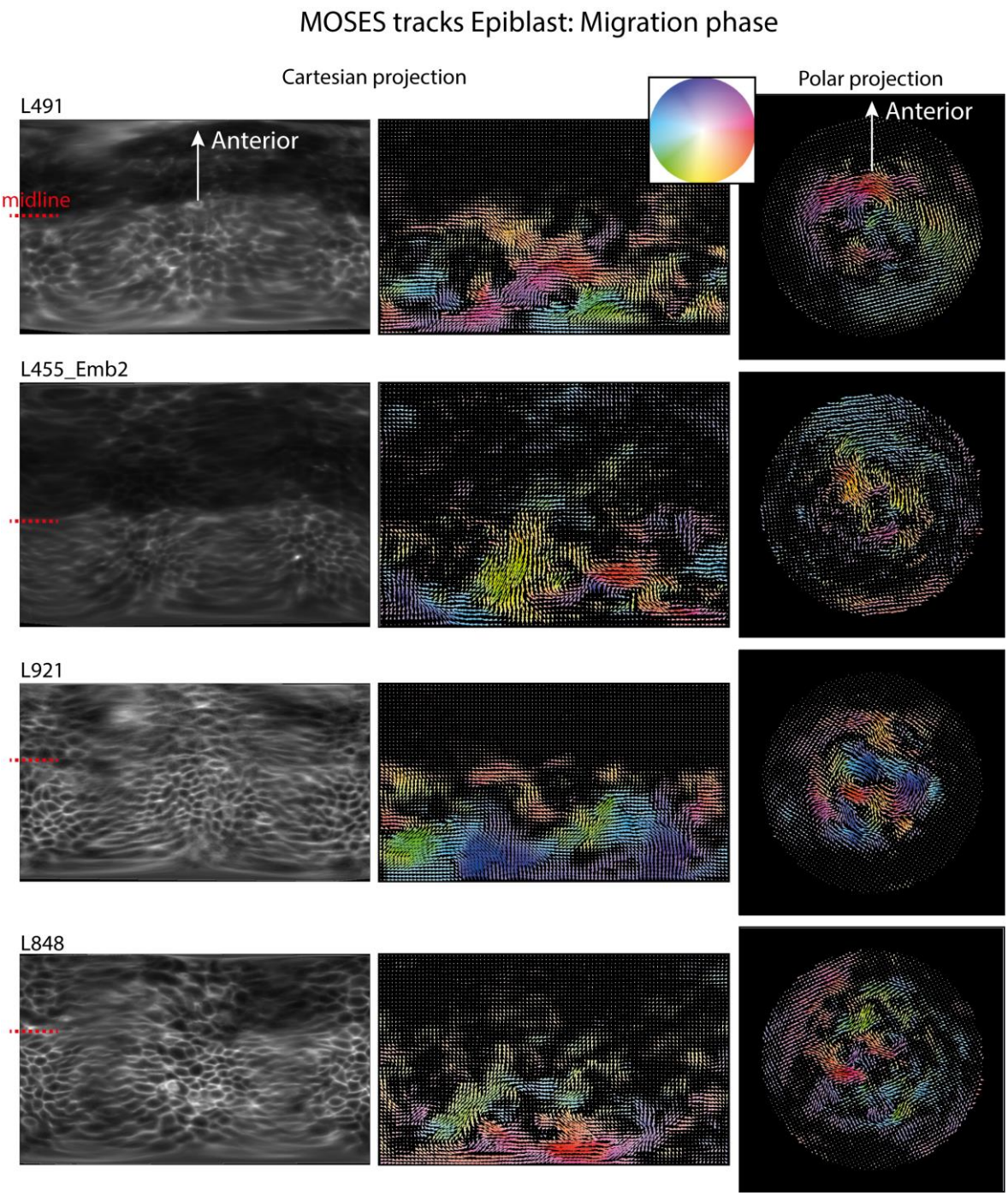

Figure 3-19: Cell movement in the epiblast and ExE. Unlike movement in the VE, there was no symmetry or global direction to cells in the epiblast. They instead moved in localised flows, which did not show correspondence between embryos. The boundary position is indicated with a red dotted line.

3.5 Developing tools for automated single cell analysis

Superpixel analysis does not provide quantitative information on individual cell morphologies. Although the process of manually annotating and tracking cells in the timelapse datasets has been simplified by the 2D projections, it is still incredibly time consuming and impractical for large datasets. The section below describes ongoing work on automatic cell segmentation and tracking, in collaboration with Dr Felix Zhou and Siu Lun Yeung, which aims to overcome this challenge.

Convolutional Neural Networks (CNNs) are a type of machine learning algorithm loosely inspired by the organisation of neurons in the animal visual cortex, traditionally used for computer vision tasks such as handwriting (LeCun, Bottou, Bengio, & Haffner, 1998), traffic (Ciregan, Meier, & Schmidhuber, 2012), or facial recognition (Lawrence, Giles, Tsoi, & Back, 1997). Recent developments in computer vision and machine learning have demonstrated how deep learning architectures (Long, Shelhamer, & Darrell, 2015) can be applied to address image segmentation problems involving poor signal-to-noise ratios and large datasets. They are being increasingly used for biological applications such as cell categorisation in differential interference contrast microscopy data (Ronneberger, Fischer, & Brox, 2015), and can be extended to learn temporal dependences by treating 2D + time imaging as volumetric imaging (Tran, Bourdev, Fergus, Torresani, & Paluri, 2015). Importantly, these methods are scalable to new datasets and computationally efficient by exploiting GPU processing.

The commonly used supervised learning approach in these methods attempts to train a CNN to 'learn' characteristic features from manually annotated or categorised training datasets, and to apply the trained CNN to predict the same information for unseen data.

In the following section, I outline a CNN based approach to better resolve the membrane fluorescence in the 3D dataset. After further refinement and post-processing, the enhanced image subsequently enables individual cell segmentation, succeeding where traditional threshold and watershed based methods have failed. This provides a fast, automated alternative to manual

annotation that makes the extraction of quantitative information from the entire VE monolayer practical for the first time.

I then describe the ongoing development of an automatic tracking algorithm by Siu Lun Yeung, applied to track the output of the CNN segmentation. I describe the process by which Dr Matthew Stower and I manually tracked cells to create a reference dataset and the curation process which supplemented the automatic results.

3.5.1 Convolutional neural network for cell segmentation

I began work on a CNN that used a standard U-Net type architecture (Ronneberger et al., 2015) to enhance cell membranes. I used Adobe Photoshop to outline cell membranes in all the 2D z-slices of one embryo timepoint. This took a total of 24 hours of manual outlining, highlighting the unfeasibility of manual curation of a complete data-set of 100 timepoints and multiple embryos. The slices and corresponding outlines were then split into 256x256 pixel patches to construct the training set. I computationally increased the size of the training dataset using data augmentation methods that mimic plausible experimental noise: adding Gaussian noise, rotating, flipping, and elastically warping the images, transforming one pair of images to 324 patch pairs, for a total training dataset of 42416 patches. Additionally, I tried to give the network 3D spatial context by providing as input 3 sequential z-slice images containing the z-1, z, and z+1 slices akin to an RGB image on which to predict the central z image**.** This original architecture is shown in Figure 3-20A.

Outlining the embryo manually was not easy in the image patches, as there were places where the membrane fluorescence was not clear enough to be certain of the outline. The 'ground truth' data used to train the CNN should more appropriately be referred to as 'reference data' in this case, as there is still a level of subjectivity involved. In order to evaluate the effect of this ambiguity, and to see if the CNN output was accurate enough for use on unseen data, I used the following criteria: if the result of the CNN prediction was within the variation of two researchers, its results were deemed accurate enough to be substituted for manual outlining. In theory the CNN should be

robust to infrequent mistakes or uncertainty in a minority of the training data, and propagate the results of the majority of more certain outlines, thus being more reliably accurate than an individual researcher.

To test this, Dr Matthew Stower also manually annotated the same embryo, which I used as a separate training dataset. The outlined data can be compared in Figure 3-20B, where we have each manually outlined the epiblast and VE layers, using two angles of unmerged data (the registration pipeline was not yet complete at this point). The two annotations are shown in red and green, with the overlapping portions in yellow.

We compared the results of our two original annotations using the Adjusted Random Score (ARS: a measure of the similarity above random success), and compared them to the outputs of the CNN trained individually on each training set. The higher ARS for the CNN predicted outlines show training convergence and that results were more similar than the original manual outlines (0.5-0.7 compared to 0.2-0.45). The latter is also clear from the increased overlap of the two predictions. The trained models gave a highly convergent prediction on an unseen embryo of slightly higher imaging quality, varying around 0.9 (Figure 3-20C). These results provide proof of principle that a CNN is more robust than manual outlines, and is not only a valid but a preferred option to enhance cell outlines in the difficult datasets.

However, the quality of the prediction output for the higher quality embryo was still insufficient for automatic segmentation using XPIWIT (Figure 3-20C), its watershed algorithm struggling to separate cells where membranes were not completely joined after binarisation.

After simplifying the problem from 3D to 2D using projections, Dr Felix Zhou took over work on the CNN and extended it to include several additional features to enable direct cell segmentation. The new CNN retains the basic U-Net architecture, but the convolutional filters have been changed from 2D to 3D. This enables explicit integration of temporal information from slices t-1, t, t+1, in a

bidirectional manner and is more efficient than strictly sequential networks such as recurrent neural networks.

The input and output are both 3 timepoint (channel) images. For a video containing a total of T timepoints, the final prediction at timepoint t is an average of the associated outputs when input images are created at t-1, t, t+1 where timepoint t is the last, middle and first image channel respectively. For each timepoint 3 predictions are output, which can be seen in Figure 3-21. The first is a probability map of the cells (inversion of the membrane prediction). The second predicts the distance from the predicted cell centroid in the x-direction each pixel belongs to. The third is the same for the y-direction. Combining the second and third outputs, the network has effectively learned the distance transform in a traditionally watershed, direct from the data itself (Bai & Urtasun, 2017).

The loss function for training has also been modified, using softmax loss instead of binary cross entropy to create the cell probability map. The loss function for the second and third outputs uses L2 Euclidean losses, with an uncertainty weighting scheme to automatically improve training (Kendall, Gal, & Cipolla, 2018).

Training images are also augmented in real time as opposed to in a preprocessing step, with the full size images used for training instead of patches. Due to the repetitive nature of epithelial cell structures, full size image training was found to be more successfully than training on smaller patches which had a tendency to over-enhance the output.

Having learnt the distance transform for a watershed segmentation, we propagate a seeded grid of (x,y) points to 'vote' for the predicted valley bottom i.e. the cell membranes. The individual valleys corresponding to the individual cell centroids are then identified by thresholding on the number of points that voted for it. Tracing back to the starting position of individual pixels which voted for a particular valley retrieves the individual cell segmentation. This integrated approach was more reliable than membrane enhancement followed by a traditional watershed.

The final outputs are individual cell segmentation maps, which contain information about cell shape and centroid position in individual timepoints, but are not linked across timepoints.

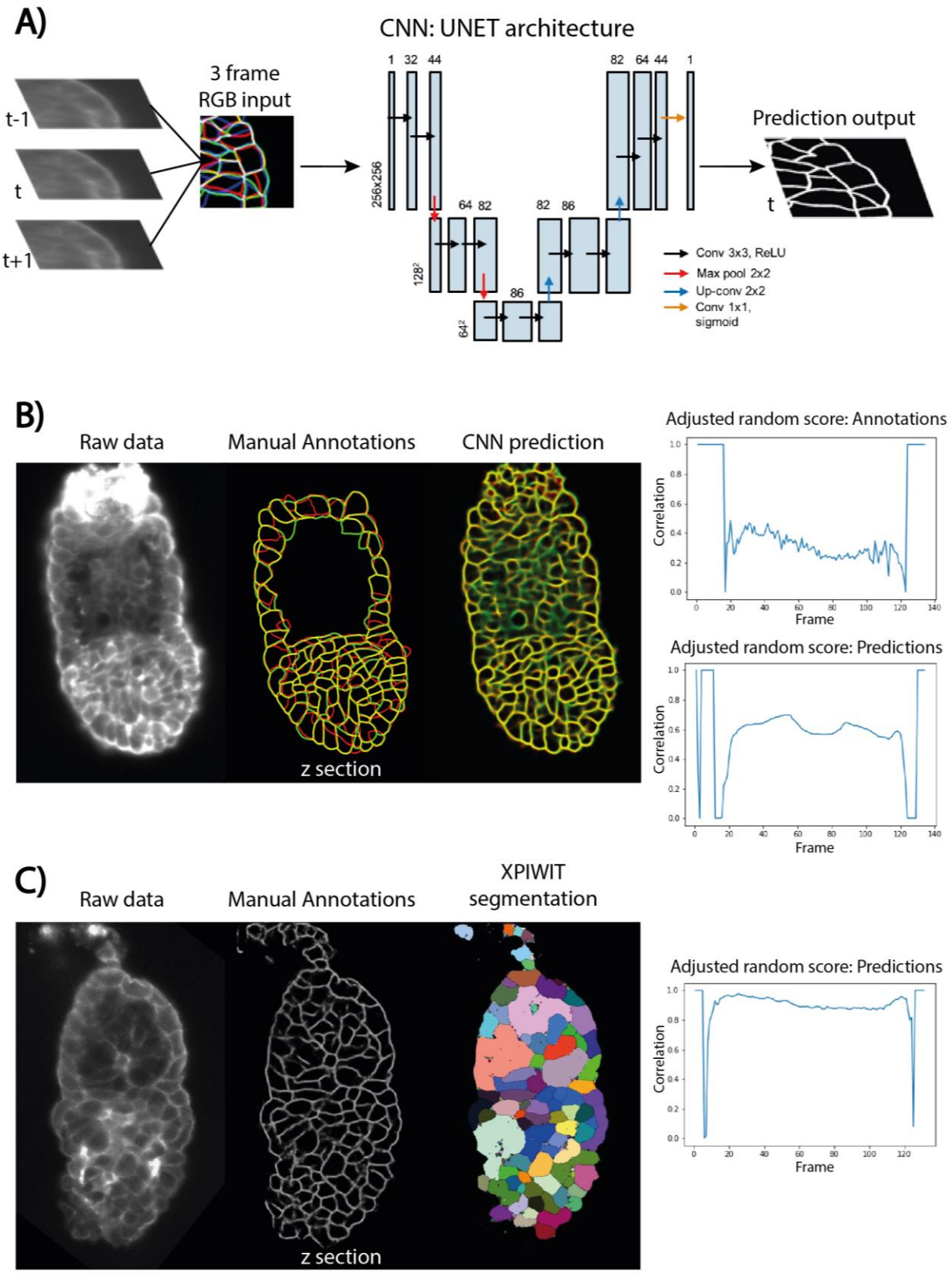
A)
CNN: UNET architecture
3 frame RGB input
t-1
t
t+1
1 32 44
82 64 44 1
256x256
64 82
82 86
128²
86
64²
Prediction output
t
Conv 3x3, ReLU
Max pool 2x2
Up-conv 2x2
Conv 1x1, sigmoid
B)
Raw data
Manual Annotations
CNN prediction
z section
Adjusted random score: Annotations
Correlation
Frame
Adjusted random score: Predictions
Correlation
Frame
C)
Raw data
Manual Annotations
XPIWIT segmentation
z section
Adjusted random score: Predictions
Correlation
Frame

Figure 3-20

Figure 3-20: Enhancing cell membranes using a convolutional neural network. A) The original U-Net architecture of my CNN, which predicted the middle of three spatial frames. B) The predictions of the network, trained on individual cells annotations from two researchers, were more similar than the original annotations. This is shown by the adjusted random score overlap measure, and yellow overlap in the image. C) The adjusted random score was also high on unseen data of better quality, but this prediction was still not complete enough for segmentation by XPIWIT.

3.5.2 Ground truth manual cell segmentation to train the CNN

A ground truth dataset was required to train and test the accuracy of the revised CNN. The manual cell segmentation was carried out using VGG Image Annotator (Dutta & Zisserman, 2019), developed by the Visual Geometry Group at the University of Oxford for annotation to train neural networks. The annotations used a polygon tool to outline the cells by marking the cell membrane. No tracking or linking of cells between cells was involved at this step.

I annotated 75 frames of *Lifeact* data, with 2 sets of 5 frames from 6 embryos, and 3 sets from another, L491. The sets of 5 were spread across the time series with an earlier and a later set from each embryo shown to be necessary after initially training with mostly mid to late frames. This training dataset consisted of over 14000 individual cell annotations, and 98 divisions, taking approximately an hour per frame or 75 hours work, spread over three working weeks. The use of a Wacom graphics drawing tablet and pen greatly sped up the process and provided greater precision than using a mouse or trackpad.

As I had found with the 3D membrane outline, it was quickly apparent that there were areas, especially around the laterally imaged sections and the densely packed AVE in later timepoints, where a best guess was required. There were some areas where it was unclear if I was seeing one cell or two, and it was necessary to look forwards or backwards and follow the cell up to 15 frames to where it appeared more clearly, or was seen to divide, in order to be sure.

The output of the CNN trained on this dataset is shown in Figure 3-21, and the membrane probability map for L491 is shown in Supplementary Video 8.

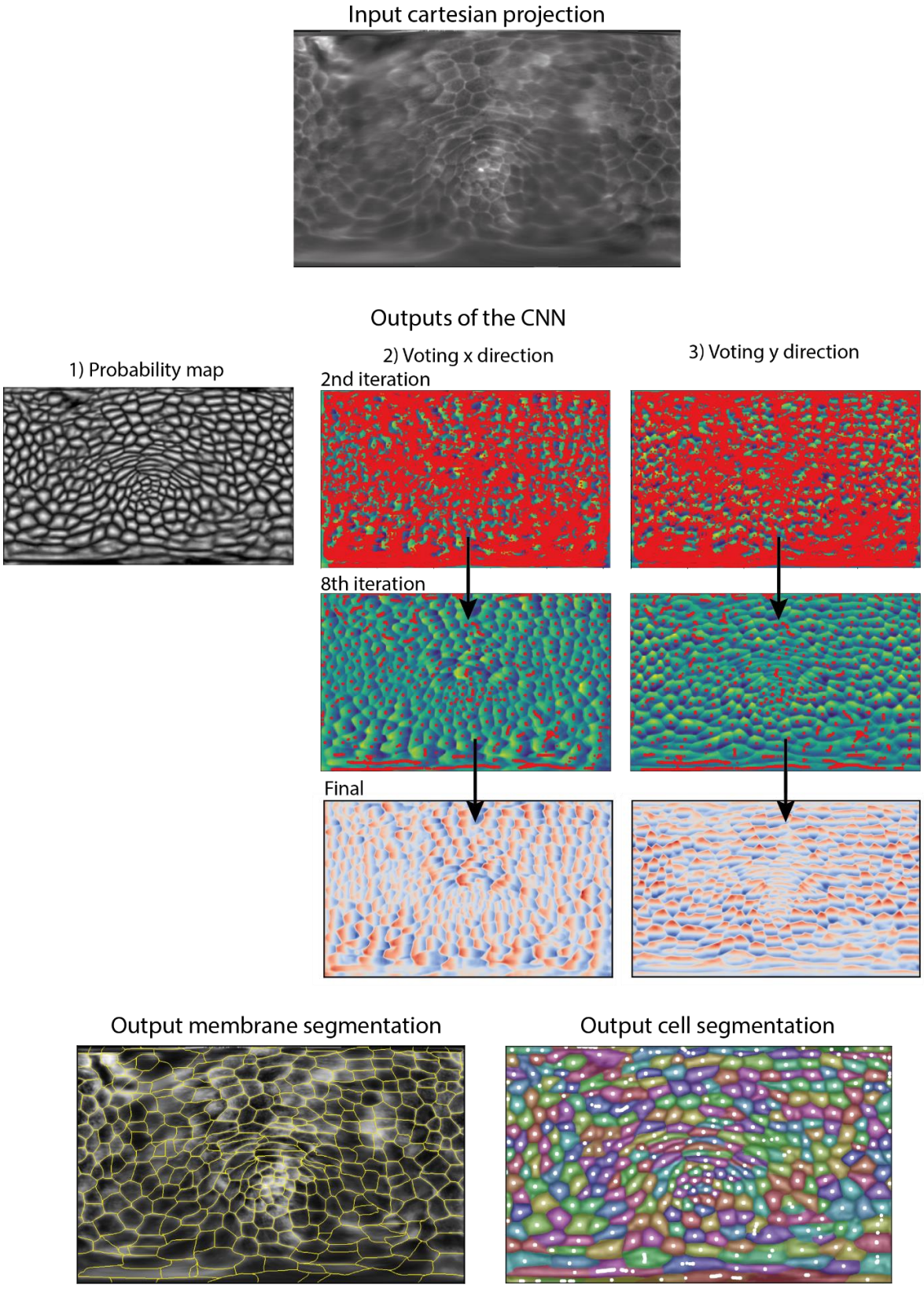
Input cartesian projection
Outputs of the CNN
1) Probability map
2) Voting x direction
2nd iteration
3) Voting y direction
8th iteration
Final
Output membrane segmentation
Output cell segmentation

Figure 3-21

Figure 3-21: The CNN: inputs and outputs. The CNN accepts the 2D projection timelapse as input, and uses this to create three initial outputs: 1) a probability map of the cell membranes; 2) a voting map containing the Euclidean distance of each pixel to its nearest membrane in the x-direction; 3) the same in y. The iterations of pixels voting for their nearest membrane performs the function of a watershed, which is used to further delineate the cell membranes. The final outputs are membrane and cell segmentation maps, containing cell shape and centroid information. CNN output images by Dr Felix Zhou.

3.5.3 Automating cell tracking

While the CNN segments the 2D projections using temporal context, it does not follow cells between frames and link them into tracks. The divisions in the embryo occur infrequently in the context of the projection, and are too sparse to collect a sufficiently large dataset to train a sufficiently sensitive CNN method to identify them. Instead, a 2D tracking algorithm applied to the CNN segmentation was developed by Siu Lun Yeung, with additional help from Dr Felix Zhou.

The CNN segmentation provides information on cell centroid and shape which can be used for tracking. Published tracking algorithms often exploit a predictive method to help identify the spatial location in the next frame to look for a match. Constant velocity models that predict the expected movement are commonly used in the tracking of people and rigid body objects (see Bar-Shalom, Li, and Kirubarajan 2002). However cells in an epithelium such as the non-AVE VE are fairly static, exhibiting very little directed movement on a cellular scale. Instead the cellular morphology or appearance can exhibit large changes in response to their neighbours. As such with the cell in frame t+1 in largely the same spatial location as in t, the effectiveness of centroid prediction algorithms were limited. However, this lends itself to a gating approach based on particular shape statistics such as area which shows greater success combined with nearest neighbour optimisation (Bar-Shalom, Daum, & Huang, 2009).

When trying to link cells across frames, the nearest neighbour optimisation first attempts to assign the cells in a frame to all the cells in the previous frame whilst minimising the overall displacement. Gating is used as an additional step to eliminate unlikely associations: a cell is only assigned in time, t+1 if it sits within the original cell area of the previous frame t (as a fitted circle centred on the centroid). The cells are closely packed and even in the AVE they do not move that far between frames. If no cell falls within this area, instead of ending the track, the track is updated for a maximum of 5 consecutive frames using the average displacement of cells in its local area. Frame by frame new cells that are found are assigned to a track. Additionally, if a new track is less than 5 frames long, it is assumed to be an incorrect segmentation and removed.

The added difficulty with this dataset, which does not have to be accounted for by algorithms tracking cells in gastrulating *Drosophila*, is continuing to follow cells which undergo cell division events. Using the method above, if a cell divides, the track of the mother cell will continue unbroken with one of the daughters while the second daughter forms a new track.

If the segmentation was perfect, and we assume cells do not leave the plane of view, you would expect tracks to never terminate, and every case where a new cell appears to be attributable to a cell division. Thus if two cells were found in the space of a previous cell, they would be assigned as daughters of that mother. However, despite extensive work on the CNN, the limitations of the data are such that there are inevitably still areas of under- and over-segmentation which are indistinguishable from cell divisions.

Over-segmentation leads to multiple cells being mistaken for one cell, which results in tracks terminating prematurely. These cells can reappear later as they are re-resolved, in which case they could be mistaken for a cell division or a new track. Over-segmentation can also cause true mother cells to appear as two daughters. The converse occurs with under-segmentation: a cell is split up into multiple ‘cells’, which can be mistaken for cell divisions, and the false tracks are terminated when the cell is segmented correctly and one of the errant cell disappears.

With this in mind, a method must seek to both maximise the number of true positive cells found (reducing over-segmentation), while minimising the number of false positive cells (reducing under-segmentation). The former would require less stringent rubrics, whereas the latter would require more stringent rubrics, hence the difficulty in accomplishing both.

A compromise was reached involving manual curation of the cell divisions. Siu Lun Yeung developed a GUI for manually curating the automatic division events. The detection algorithm uses an elliptical instead of a circular area to maximise the number of true positive events found. This uses the assumption that cells will divide roughly along their long axis, and detects 96% of the events compared to the manual annotations. It also finds many false positives, which are then removed in the manual curation step using the GUI, a step which takes around 2 hours for 100 timepoints.

The corrected divisions are then used to annotate the tracks found in the first initial step: daughter tracks are assigned to a mother, and where the track of a daughter has previously been combined with the mother to create a long track, it was separated and reassigned.

False positive tracks are also removed in a manual curation step, which should be much faster than creating new tracks. As the fully manual tracking takes around 8 working days to complete, reducing this to a day or so with manual curation steps, including running both the CNN and tracking (each a matter of minutes), is worthwhile, particularly as the number of embryos increases.

3.5.4 Ground truth for cell tracking

In order to determine the accuracy of the tracking algorithm, it was necessary to create a reference dataset. This was the manual tracking of L491 described at length in this Chapter. As with the CNN training data, we were interested in the variation between the annotations of two researchers, as it was not always easy to clearly delineate cells. Dr Matthew Stower also independently manual tracked the cells in the L491 embryo Cartesian and polar projections, using the same method.

The tracks from both researchers are shown in (Figure 3-22A), and the corresponding polar projection in Figure 3-22B. The manual tracking was very similar, as shown by the number of tracks per frame and track length distribution comparisons for the Cartesian projection in Figure 3-22C. Tracks were matched if they fell most often within 20 pixels (approximately half a cell diameter). The small difference in cell number was mostly due to the tracking being carried out independently: Researcher 1 did not track cells at the edge of the image, whereas Researcher 2 did include them. The precision values comparing Researcher 1 to Researcher 2 varied between 0.92 and 0.96 over time, and recall between 0.87-0.93.

The cell division angles for the same embryo (L491) are also mapped in Figure 3-22D. The number of cell divisions identified by Researcher 1 in the Cartesian view was 198, with 199 for Researcher 2. With a 2 frame grace, the number of precisely matched divisions was 169. 30 divisions differed either in time or location, and a precision of 0.853 and recall 0.849, although some of these were again due to differences in cells tracked around the edges.

In both manual cell tracking and identification of cell divisions, the overall trends in the data annotated by the two researchers remain the same.

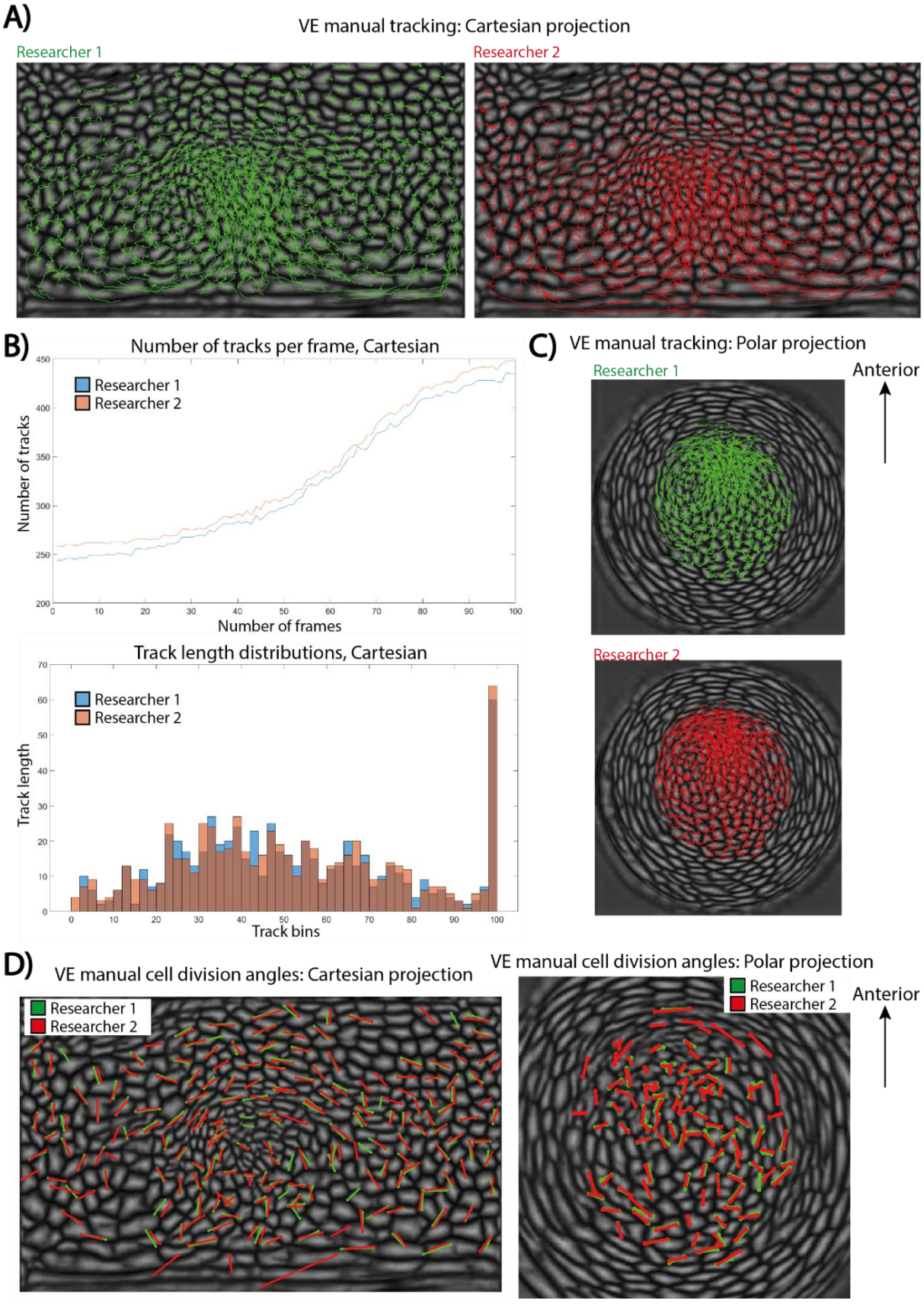
A)
VE manual tracking: Cartesian projection
Researcher 1
Researcher 2
B)
Number of tracks per frame, Cartesian
Researcher 1
Researcher 2
Number of tracks
Number of frames
Track length distributions, Cartesian
Researcher 1
Researcher 2
Track length
Track bins
C)
VE manual tracking: Polar projection
Researcher 1
Anterior
Researcher 2
D)
VE manual cell division angles: Cartesian projection
Researcher 1
Researcher 2
VE manual cell division angles: Polar projection
Researcher 1
Researcher 2
Anterior

Figure 3-22

Figure 3-22: Ground truth manual cell tracking in the VE. A) Manual tracking was carried out by myself and Dr Matthew Stower on the Cartesian projection. B) The number of tracks per frame and track length distributions found for each set of Cartesian annotations in A). C) The manual tracking on the Epi-VE in the polar projection. D) The manually identified division angles in the Cartesian and polar projections, shown with a line joining the two daughter cell centroids. In Cartesian projections, the anterior is central; in polar it is central and upwards. Images and metrics were prepared by Siu Lun Yeung.

3.5.5 Supplementing automatic tracking with manual corrections

At the time of writing, work is continuing using the automated approach outlined above, paired with manual curation. Using this approach, we hope to acquire quantitative information such as changing cell area and shape factors over time, numbers of neighbour exchange events and rosette formations, cell divisions and cell division angles. Being able to extract these features with a 5min time resolution will give us the first truly dynamic and complete description of AVE migration in the context of the epithelial sheet.

3.6 Discussion

MOSES superpixel tracking has enabled the extraction of motion patterns without the need for single cell analysis on every embryo. It has also expanded the dataset available for analysis to include the *mTmG ; Hex-GFP* and *mTmG ; Ttr-Cre* lines, in which individual cells in the VE cannot be delineated.

The classifier trained on the *Hex-GFP* dataset enabled comparison of the migratory movement across embryos in different mouse lines, and helped identify AVE cells in embryos which did not have a specific AVE marker based on their motion signatures. AVE migration was characterised by persistent directional movement, but it was not a steady process as migrating cells would pause and also underwent rapid movement. The average time for the AVE to reach the boundary varied

substantially, and is likely longer than the 4-5 hours suggested (Srinivas et al., 2004). This discontinuous movement is indicative of active migration by cellular protrusions (Isabelle Migeotte et al., 2010; Omelchenko et al., 2014; Srinivas et al., 2004), as opposed to a passive movement.

Using the *Lifeact* data, I was able to view cellular protrusions in the basal layer latching onto the epiblast boundary, displacing the cells proximal to them into the ExE-VE and pulling the AVE upwards in what appears to be an active migration. The cellular projections and apparent attachment to the boundary were also coincident with greater F-actin intensity. I suspect the latching and pulling behaviour may explain the irregular motion signature identified by the AVE classifier, but observations of greater numbers of protrusions over the full AVE cell population would need to show temporal correlation with the instantaneous velocities of the AVE cells to demonstrate a clear cause and effect.

The cells proximal to the AVE showed similar patterns of motion, but otherwise the AVE showed migratory movement distinct from the rest of the VE. It is not known whether the cells proximal to the AVE also send out protrusions, although their extensive deformation at the boundary sets them apart in behaviour to the AVE, which largely maintains a smaller apical surface.

The 2D projection of the VE allows the cells to be manually tracked more easily than in 3D. This has enabled me to follow all the cells in the VE for the first time. The superpixel and manual tracking both confirmed that AVE cells move as a coordinated group (Isabelle Migeotte et al., 2010; Trichas et al., 2011). It has been reported that some *Hex-GFP* positive cells did not migrate from the distal tip (Stuckey et al., 2011), but I saw no evidence of that in our dataset, in line with Shioi et al., 2017. One possibility is that the authors have mistaken newly induced GFP fluorescence at the distal tip for a stationary cell, as it is difficult to delineate *Hex-GFP* positive cells.

Both the individual cell tracking and MOSES superpixel tracking showed that migration leads to bilateral ‘whirls’ of cells over time throughout the Epi-VE, while the ExE-VE remains largely static.

Cells in the lateral Epi-VE contribute to the future anterior, as do cells beginning in the lower posterior Epi-VE.

While largely symmetrical, these whirls showed imbalances over time in accordance with the unsteadiness of AVE migration, and there was a clear right or left bias in the majority of embryos during post-migration. While the cause of migration remains unconfirmed, we are left to speculate as to what might be causing this: Stuckey et al., 2011 found asymmetric proliferation in the lateral sides of the embryo at E5.5, and Hiroshi et al., 2013 between the anterior and posterior; protrusions have also been shown to reach at a range of proximal angles (Omelchenko et al., 2014).

Recent nuclear tracking has also suggested larger scale, coordinated movement across the anterior Epi-VE (Shioi et al., 2017). Our data supports this and also indicates there are contributions to the future anterior from both the lateral and posterior regions. The observed rotational movements are reminiscent of those seen in the chick epiblast dependent on PCP-signalling (Rozbicki et al., 2015; Voiculescu et al., 2007) and in the later PCP-dependent hair follicle formation in mice (Cetera et al., 2018). However, the actual single-cell behaviours were quite different, with movement in the chick caused by medio-lateral cell-cell intercalation events absent in the mouse VE. Investigating the role of PCP signalling would require independent molecular confirmation.

Cell intercalation is known to drive many morphological changes during embryogenesis (reviewed in Walck-Shannon and Hardin 2014). Imaging and modelling experiments have shown that the AVE moves through the Epi-VE via extensive cell intercalation events (Isabelle Migeotte et al., 2010; Trichas et al., 2011, 2012). However, these studies have only been able to examine small planes of view of the embryo using time lapse confocal imaging.

Here, the MOSES deformation meshes showed that the AVE migration causes large scale tissue deformation of the epithelial sheet. Data from *Lifeact* and *Hex-GFP* embryos has shown cells which begin in the Epi-VE proximal to the anterior often move past the boundary into the anatomical ExE-VE region. This is accompanied by extreme deformation of the cell morphology, with the

appearance they are squashed between the ExE-VE and the AVE, and can be accompanied by buckling at the surface in later timepoints. The extreme elongation of some these cells is suggestive of coming up against an impassable physical barrier, has previously described by Trichas et al. 2011, and supports their notion of impermissibility, with much less deformation and movement seen in the ExE-VE region.

After using the *Lifeact* line to manual delineate individual cells across the entire VE, it is clear that although the cells undergo junctional rearrangements, they have a strong preference for keeping connections to existing neighbours, even when under great normal and sheer stresses. This was evident in the shape changes of the cells, with the most extreme elongation shown in cells between the AVE and the boundary. The monolayer maintains integrity, and very few cells showed 'loose connections' with others and moving independently of their neighbours. Cell divisions appear to be a tension-breaking event that allow cells to intercalate between neighbours.

How shortening junctions participate in neighbour exchange and rosette formation, and whether they contribute to overall coordination of migration (Trichas et al., 2012) remains to be seen, as instances of dramatic neighbour exchanges exhibiting 'loose connections' were only found in a minority of embryos. In agreement with Trichas et al., 2012, sequential contractions such as those seen in *Drosophila* (Blankenship et al., 2006) have not been identified here, but a more detailed study of rosette formation should confirm this. Due to the lack of coordination, it is more likely that junctional rearrangements and cell intercalation events are a consequence of the deformation caused by AVE migration rather than contributing to it. Overall, the behaviour of the VE was one of a tissue with stronger cell-cell adhesion than adhesion to the basal membrane below.

The 2D geometric projections have also allowed the movement of the epiblast cells at the Epi/VE interface to be observed in the entire sheet at E5.5. Previously, limited epiblast movement has been shown only as early as E6.5 with a limited view of the posterior in confocal stacks (Williams et al., 2012). As Williams et al. reported for later stages, the epiblast did not show bilateral whirls

like the VE. Instead, cells moved in localised flows with no global symmetry or direction. In our dataset the cells remained motile throughout the captured timelapses, suggesting they become less mobile some time between E5.75 and E6.5.

Chapter 4: Asymmetries in the E5.5 embryo

4.1 Introduction

4.1.1 Asymmetries in morphological shape

AVE migration defines the A-P axis in post implantation embryos. However it is contentious whether A-P polarity is only established during AVE migration or already exists prior to this. Nor is it known if the A-P axis can be established on any side of the embryo. There is some evidence to suggest that the A-P axis is specified prior to AVE migration, and that the AVE may be migrating in response to existing cues, as opposed to a random symmetry breaking event.

One suggested demonstration of this asymmetry is in the tilt of the ectoplacental cone (EPC). Smith (Smith, 1985) recorded asymmetry of the mouse blastocyst at implantation, with the ICM-polar trophectoderm complex tilted at an angle relative to the proximal-distal axis. Smith suggested this was the first breaking of radial symmetry, and that the axis persisted as the A-P axis to later stages, manifesting as the tilt of the EPC, towards the posterior, and away from the anterior.

Gardner, Meredith and Altman, 1992 investigated this hypothesis during primitive streak formation, taking measurements of EPC angle in fixed embryos at E6.5. They marked the surface towards which the EPC was tilted, identifying a conspicuous tilt in 2/3rds of the embryos. Out of these embryos, they identified 14/29 in which the EPC was tilted towards the posterior, denoted by the primitive streak, and 15/29 for which it was tilted towards the anterior, with no embryos showing a perpendicular tilt. They also noted a leftwards tilt in their embryos, which they suggested could be due to a curved A-P axis (Figure 4-1D).

Another suggested asymmetry is in the eccentricity of the epiblast cross-section. Although eccentricity is a technical term, I use it here to describe general elliptical nature denoted by an aspect ratio >1 (ratio of long to short axis). The pre-gastrulation embryo is highly elliptical, and at

E6.5 the primitive streak marking the embryo posterior lies along the long axis (Gardner et al., 1992). However, at E6.0 the A-P axis as marked by the AVE cells is aligned with the short axis of the embryo cross-section, not the long axis as it is half a day later (Mesnard et al., 2004; Aitana Perea-Gomez et al., 2004).

Mesnard *et al.*, 2004 found that the eccentricity in the embryo was more pronounced at E5.0, with an average aspect ratio of 1.22 compared to being almost radially symmetrical with aspect ratio (AR)=1.05 at E5.5, due to a lengthening of the short axis. By E5.75 this had increased again to 1.14, after cavitation occurs, and by E6.5 the aspect ratio had increased to 1.49. They checked the orientation of the embryonic axis with the uterine axis, finding them almost parallel at E5.0, but randomly oriented at E5.75-E6.0, before the long axis aligned perpendicular to the uterine long axis at E6.5 (Figure 4-1Ai and B). They noted that AVE migration aligned with the period of random orientation, and used Cer1 expression to check the orientation of AVE with respect to the uterine and embryonic aspect ratios. They found no connection between Cer1 expression and the uterine long axis, but found it was preferentially (although not absolutely) aligned to the short axis of the embryo (Figure 4-1Aii).

Perea-Gomez et al. looked later, between E6.2 and E6.5. Although 100% of the embryos were elliptical, the AVE as marked by *Hex* varied, and was found along the short axis in only 18/49 embryos (Aitana Perea-Gomez et al., 2004). Similar to Mesnard et al., the average aspect ratio at E6.2-E6.5 was 1.58 ±0.632. The younger embryos, as determined by embryo size, had an A-P axis closer to the short axis of the embryo whereas the A-P axis of older embryos was closer to the long axis (Figure 4-1Ci).

DiI labelling experiments from both groups also showed this shift of A-P from short to long axis between E6.0 and E6.5 was not due to cell movement, but more likely through tissue remodelling as the short axis and long axis changed lengths (Mesnard et al., 2004; Aitana Perea-Gomez et al., 2004) (Figure 4-1Cii). Mesnard et al. speculated this was due to preferential growth along the short

axis, and Perea-Gomez et al. additionally suggested that the shape of epiblast cells could be effecting the rotation of the cavity and this in turn could affect the axis.

Mesnard et al. and Perea-Gomez et al. both measured transverse sections of the whole egg cylinder in the embryonic region i.e. the epi-VE surface. Rivera-Perez et al. (Rivera-Pérez et al., 2003) also found that the short axis of the epiblast aligned with the AVE, and additionally noted the squashing of epiblast cells in response to the AVE's characteristic VE Thickening (VET). This resulted in the epiblast resembling a 'flattened sac-like structure'. Measuring the diameters of the epiblast and outer VE at the halfway point, at 0° and then with a 90° rotation, they showed the VET was positioned at the minor axis of the epiblast (average AR of 0.97), and the major axis of the VE (1.02) (Figure 4-1D). They found the embryo was more radially symmetrical in later embryos where the VET was less pronounced (Rivera-Pérez et al., 2003). However, Rivera-Perez at al. used fixed samples, and none of the eccentricity studies were able to discern whether the AVE caused the changing eccentricity or was choosing its migration direction in response to it (Mesnard et al., 2004).

4.1.2 Regional differences in cell division

It has also been suggested that regional differences in the rate of cell division could provide a directional nudge initiating the movement of the AVE to the future anterior (Yamamoto et al., 2004). Yamamoto et al. found BrdU incorporation was uniform in the VE prior to migration, but was reduced in the anterior of migrating embryos corresponding to the Lefty1 and Cer1 expression domains. The asymmetry persisted until E6.5. Yamamoto et al. concluded that Nodal stimulated the proliferation of cells in the VE, and that lower levels of Nodal caused decreased proliferation in the AVE region, antagonised by Lefty1 and Cer1, and suggested this directional imbalance could combine with active migration.

However, no such regional difference was seen in an additional BrdU study, which used higher resolution confocal imaging and accurate cell counting (Stuckey et al., 2011), or through nuclei

tracking (Shioi et al., 2017). Stuckey et al. found the mean BrdU incorporation index to be 76%, in all regions, at both E5.5 and E6.25. From the 15 embryos examined, 8 had slightly higher proliferation in the anterior VE compared to the posterior, whereas for the remaining 7 the converse occurred. The percentage of mitotic cells, as shown by an anti-PHOSPHO-HISTONE-H3 antibody, also showed no difference between the anterior and posterior. However, they did notice a statistically significant increase in the percentage of dividing cells on the right side of the epiblast compared with the left, at E5.5, and a similar trend in the VE (N=5 embryos). Stuckey et al. also found that *Nodal* driven proliferation in the epiblast was essential for AVE migration, showing a marked reduction in the percentage of mitotic cells in the epiblasts of embryos mutant for the Nodal co-receptor Cripto, which induces the AVE but does not migrate (Ding et al., 1998). There was no effect on proliferation in the VE. The result was confirmed with Nodal inhibitors just after the initiation of migration, with no difference in AVE or VE marker expression, and three different cell cycle inhibitors which resulted in migration arrest in a majority of the embryos. There was indication migration could be partially rescued by Dkk1, and Stuckey et al. suggested that epiblast proliferation served to move the AVE region away from signals that would inhibit its migration.

The timelapse nuclei tracking of Shioi et al. 2017 concurred with Stuckey et al. Although Shioi et al. did not capture pre-migration, they found no significant differences in cell cycle between spatial regions between E5.5 and E6.5, with an average cell cycle across the VE of approximately 11hours (N=3). They also noted spatial and temporal clustering in the daughter cells, half of which divided within 30mins of each other (average 2.0 ± 2.4hours, n=110), and continued to localise close together.

Antonica *et al.*, 2019 used timelapse confocal imaging to study proliferation using a line with the AVE marker Cer1 and cell cycle reporter R26Fucci2a, which expresses mCherry in G1 and mVenus in S/G2/M phases. However, they struggled to detect any mCherry labelled cells before E6.5. They instead counted the number of mVenus-positive cells and compared it in the anterior and posterior

regions across 5 embryos. They found a decrease in the number of mVenus-positive cells of 49.9% in the anterior, compared with only 19.6% in the posterior, over around 4 hours at E5.5. Additionally, perturbing the cell cycle progression using an FGF inhibitor in pre-implantation embryos affected migration while maintaining the appearance of cellular protrusions, suggesting active migration might still be possible. However, the specificity of FGF inhibition was not clear, and the lack of detection of mCherry cells meant they were unable to give cell divisions in terms of the number of cells in a region, as Stuckey et al. had, failing to account for changing regional densities as cells migrate. Antonica et al. also chose to stage their N=5 embryos according to the highest number of mVenus-positive cells seen, instead of the proportion of distance migrated.

In this chapter I look for embryo and cell asymmetries in the VE in pre-migration and migratory phases to see if there are any indications of a pre-existing A-P axis and spatial heterogeneity in cell proliferation. Specifically, I investigated 1) the angle of the EPC vs the direction of migration; 2) whether there is asymmetry in the global shape of the embryos (eccentricity); 3) if there are spatially regional differences in proliferation during pre-migration. If asymmetries are present before the onset of migration, this would indicate the AVE cells are responding to this pre-existing asymmetry; if no asymmetries are present, it suggests the AVE creates the first asymmetry through its migration.

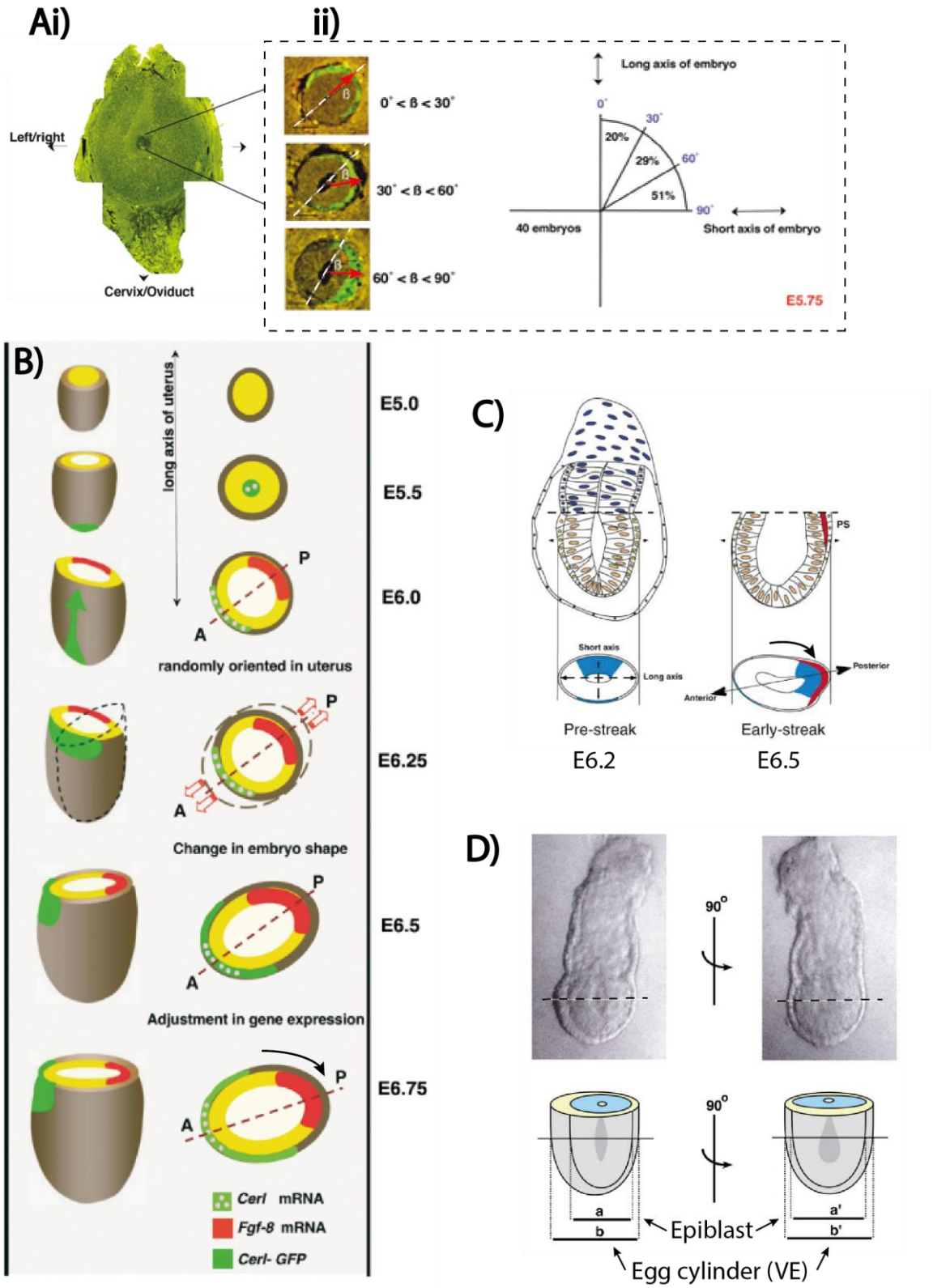
Ai)
ii)
Left/right
Cervix/Oviduct
0° < ß < 30°
30° < ß < 60°
60° < ß < 90°
Long axis of embryo
0°
30°
20%
29%
60°
51%
90°
40 embryos
Short axis of embryo
E5.75
B)
long axis of uterus
E5.0
E5.5
E6.0
P
A
randomly oriented in uterus
E6.25
Change in embryo shape
E6.5
Adjustment in gene expression
E6.75
Cerl mRNA
Fgf-8 mRNA
Cerl- GFP
C)
PS
Short axis
Long axis
Anterior
Posterior
Pre-streak
E6.2
Early-streak
E6.5
D)
90°
a
b
a'
b'
Epiblast
Egg cylinder (VE)

Figure 4-1

Figure 4-1: Evidence suggests the A-P axis may exist prior to AVE migration. Ai) Mesnard et al. investigated the orientation the egg cylinder cross-section with the uterus. B) At E5.0 the embryo long axis was aligned with the long axis of the uterus, before being randomly oriented during the period of AVE migration. It elongated after AVE migration, and by E6.5 the A-P axis was aligned with the embryonic long axis, perpendicular to the uterine long axis. Ci) Perea-Gomez et al. also found the A-P axis shifted from the short axis in earlier embryos to the long axis in E6.5 embryos. D) Rivera-Perez et al. measured the change in width of the egg cylinder and epiblast and found a flattening of the epiblast coinciding with VET. Adapted from Mesnard et al., 2004; Perea-Gomez et al., 2004; and Rivera-Pérez, Mager and Magnuson, 2003, respectively.

4.2 The ectoplacental cone tilt relative to the A-P axis clusters into two groups at E5.5

Many of our embryos show an asymmetric cone. In order to understand whether there was a relationship between the angle of the tilt and the direction of migration at E5.5, I measured the EPC tilt relative to the migrating AVE. At this stage the embryo is not as elliptical as during streak formation. The cone angle was defined as in Gardner, Meredith, and Altman 1992, with a line drawn through the cone from its lowest point into the ExE-VE (assumed posterior in Smith 1985 through to the highest point (see example embryo in Figure 4-2A).

First, I established if there was an asymmetric tilt of the EPC, and if this changed over time. I used ImageJ 3D Viewer to analyse timelapses of the 3D embryo. There was very little change in the angle of the cone over time, and no discernible difference pre- or post-migration; thus an angle measured at any timepoint is representative (Figure 4-2A). However, a minority of embryos did straighten and appear to lose any asymmetry over the timelapse – it is not clear whether this would happen *in vivo*, or is a result of the embryo no longer being connected to the uterine lining (Figure 4-2B). The embryos for which this occurred or which did not show a conspicuous tilt, were counted as 'central' so as not to introduce embryos for which there was significant uncertainty in the

measurements. Embryos with an unclear cone due to damage, or with no cone attached, were excluded from the analysis.

If the embryos showed a conspicuous tilt, I moved onto the next stage of analysis. I digitally divided the embryos into embryonic and ab-embryonic halves, saving each using an assigned random number (a different number for each half). Next, I aligned the EPCs and AVEs independently to the front view using 3D Viewer (ImageJ: Schmid et al. 2010), in ascending order according to the randomly assigned number. I then calculated the relative angles between the two recorded angles for each embryo. I repeated a second time using the entire embryo and recorded relative angles between the EPC and the AVE. The plotted results were an average of the two measurements, which had an average difference of 7.6° (2%), standard deviation (stdev) of 2.5° and a range of 4-12°. Measurements are reported to a precision of 2°.

The results are shown in Table 4-1 and Figure 4-2C. Out of 22 embryos, 6 had no discernible EPC tilt (described as 'central'), 1 had no cone (close dissection) and 1 had a tilt which was unclear due to debris or damage. The latter 2 are discounted, giving N=20. Of the 14 embryos which do show an EPC tilt, 8 were biased with the cone roughly towards the posterior at 180°, and the remaining 6 at some distance to the right of the anterior, if viewing the embryo with the anterior front. The mean values of the two clusters differ by 143°, and this departure from a defined axis presents difficulties finding significance in both groups using global binning. Despite this, the clustering is significant if divided into 8 quadrants around the mean angle of the more posterior group (p=0.042: $\alpha<0.05$, $\chi 2$ test), and if divided into 6 quadrants using the mean of the more anterior group (p=0.0277: $\alpha<0.05$, χ^2 test).

As Gardner et al. found at E6.5, and compared in Figure 4-2D, the results do seem to show two groupings of angles, slightly off the A-P axis defined by the direction of AVE migration. However, my results on the anterior side of the embryo showed a more marked tilt towards the perpendicular, with an average shift from the A-P axis of 46° compared to Gardner et al.'s 3.6°.

My measurement were taken as angles as described, assuming a roughly circular transverse section; Gardner et al. measured the location of the EPC tilt based on a percentage distance around the perimeter of the VE in transverse section. As the embryos are more elliptical at E6.5, with the A-P axis along the long axis, their results would likely show narrower clustering had angles been used.

The clustering of the EPC angle relative to the AVE-defined anterior indicates a pre-existing axis to which the EPC is also aligned.

Embryo	1	2	Average
401	156	164	160
455_E2	central	central	central
455_E3	NC	NC	NC
491	112	104	108
505	central	central	central
864	148	144	146
871_E1	126	132	129
871_E2	central	central	central
917	296	292	294
921	118	108	113
922	272	266	269
924	152	148	150
926	282	274	278
927	172	180	176
928_E1	central	central	central
928_E2	326	314	320
930	206	216	211
932	292	300	296
848	central	central	central
860	unclear	unclear	unclear
905	central	central	central
910	296	306	301

Table 4-1: Results of measurements from the AVE to the EPC. Measurement 1 is the from a blind test, with the embryo split into halves and the AVE and EPC angle each measured relative to the front of the stack. Measurement 2 is from the whole embryo. The result given is the average, with the error ± difference between the two measurements.

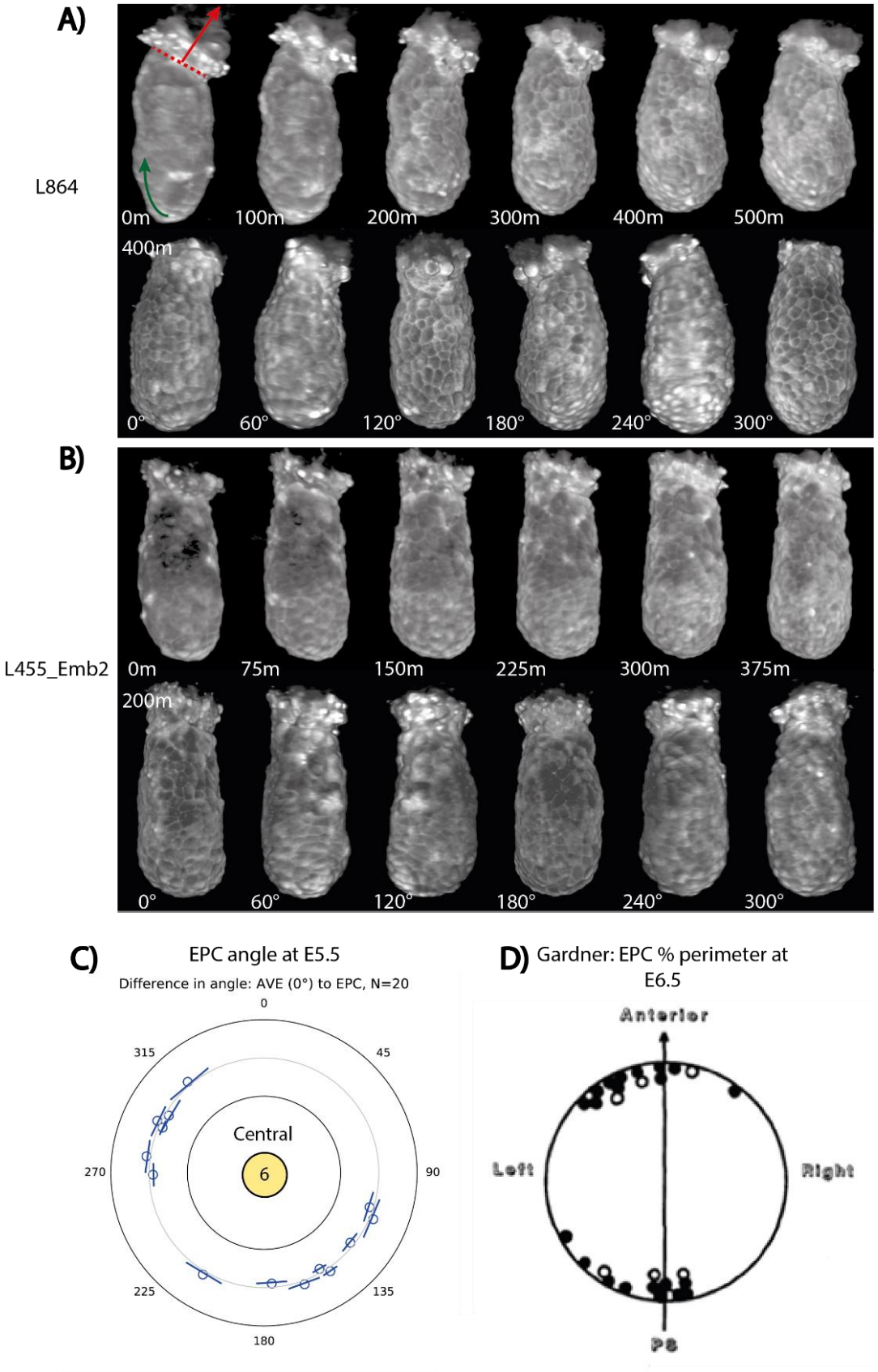
A)
L864
0m
100m
200m
300m
400m
500m
400m
0°
60°
120°
180°
240°
300°
B)
L455_Emb2
0m
75m
150m
225m
300m
375m
200m
0°
60°
120°
180°
240°
300°
C)
EPC angle at E5.5
Difference in angle: AVE (0°) to EPC, N=20
0
45
90
135
180
225
270
315
Central
6
D)
Gardner: EPC % perimeter at E6.5
Anterior
Left
Right
PS

Figure 4-2

Figure 4-2: Measuring the EPC tilt relative to the A-P axis. A) Embryo L864 is shown to demonstrate an overt tilt of the EPC (red arrow), which does not change over the timelapse (top row). The bottom row rotates the embryo at 400mins, where the image shown in top row corresponds to an angle between 60° and 120° in the bottom. The AVE movement is marked by the green arrow. B) Six of the embryos had EPCs with no overt discernible tilt. Embryo L455_Emb2 is shown as an example where the EPC appears to straighten over the timelapse and was labelled as 'central' for the analysis. C) Results from N=20 embryos, show EPC locations (blue) relative to the AVE (fixed at 0°, posterior opposite at 180°) clustering into two groups, an average of 46° off the A-P axis. Error bars show the twice the difference of the two measurements, with the circular marker at the average. D) Results at E6.5 show a similar clustering, adapted from Gardner, Meredith, and Altman 1992; with measurements as percentages of the VE perimeter. The orientation of left and right is of looking down at an embryo cross-section from the proximal view. The anterior was discerned by the shape and movement of AVE cells, or by Hex-GFP fluorescence. Perspective is from above.

4.3 Eccentricity of the embryonic half of the embryo

It has previously been shown that the embryonic half of the embryo is more eccentric at E5.0 (average aspect ratio = 1.22), before becoming roughly circular at E5.5 (AR=1.05), and becoming more eccentric again by E5.75 (AR=1.14) (Mesnard et al., 2004). There is also evidence that the migrating AVE cells may be responsible for some of this change, the more columnar cells (also known as Visceral Endoderm Thickening or VET), compressing the epiblast below (Rivera-Pérez et al., 2003).

The previous studies into transverse eccentricity in the egg cylinder used histological sections, or in the case of Rivera-Perez et al., Differential Interference Contrast (DIC) with a single timepoint. Using the lightsheet data, I was able to observe shape changes over time in both sagittal and transverse sections. I analysed the shape of the epiblast throughout the timelapse in the 8 embryos which captured both pre-migration and migration phases.

With this analysis, I hoped to answer two main questions. The first: does the global shape of the embryo predict the direction of migration? If this were the case, it would be evident in consistent alignment of the long-axis of the embryo with the A-P axis (as shown by the later migrating AVE cells) and would indicate a pre-existing A-P axis. The second question is whether or not a shape change occurs in the embryo during migration. If this were the case, it would be evident in the changing eccentricity of the epiblast during migration. Furthermore, if this could potentially be attributed to the morphology of the more columnar AVE cells, as opposed to a global change in the shape of the egg cylinder, the changes in eccentricity would not occur in the VE.

In order to answer these questions, I first aligned each embryo with the AVE migration to the left using the locations found to investigate the EPC tilt. To measure the eccentricity, I took the transverse sections every 50mins, at two locations along the proximal-distal axis: the midpoint of the ExE and the midpoint of the epiblast. For the embryonic half, I drew a polygon around the VE, epiblast, and cavity cross-sections in ImageJ, and used the Ellipse Fitting tool to measure the aspect ratio and angle of the long axis for each. The aspect ratio was defined as the major/minor axis, thus will always be ≥1, 1 being exactly circular. Additionally, I annotated the cavity and epiblast for the same frames in sagittal sections at the centre of the embryo, to outline the edge of these tissues during migration. The raw data can be seen in Supplementary Table 6-1, and the transverse and sagittal sections can be seen in Supplementary Figure 6-1 to 6-4.

Both the angle of the major axis and the aspect ratio are important to understand the deformation of an ellipse: two ellipses may have the same aspect ratio, but be very elliptical in different directions, another two may be at the same angle but with different aspect ratios. Additionally, near circular cross-sections can give highly variable corresponding angles, as a small change in eccentricity can result in a large change in angle disproportionate to any biological effect. For this reason, angle values were only considered when the corresponding aspect ratio >1.05, and discounted for cross-sections with AR≤1.05 (referred to as ‘circular’). Angles were measured from

the horizontal at 0° (A-P axis as denoted by the AVE location at 180°), with vertical at 90° (perpendicular to the A-P axis), as shown in the diagram in Figure 4-3A. By definition, if the long-axis is perpendicular to the A-P axis, the short axis is aligned with the A-P axis.

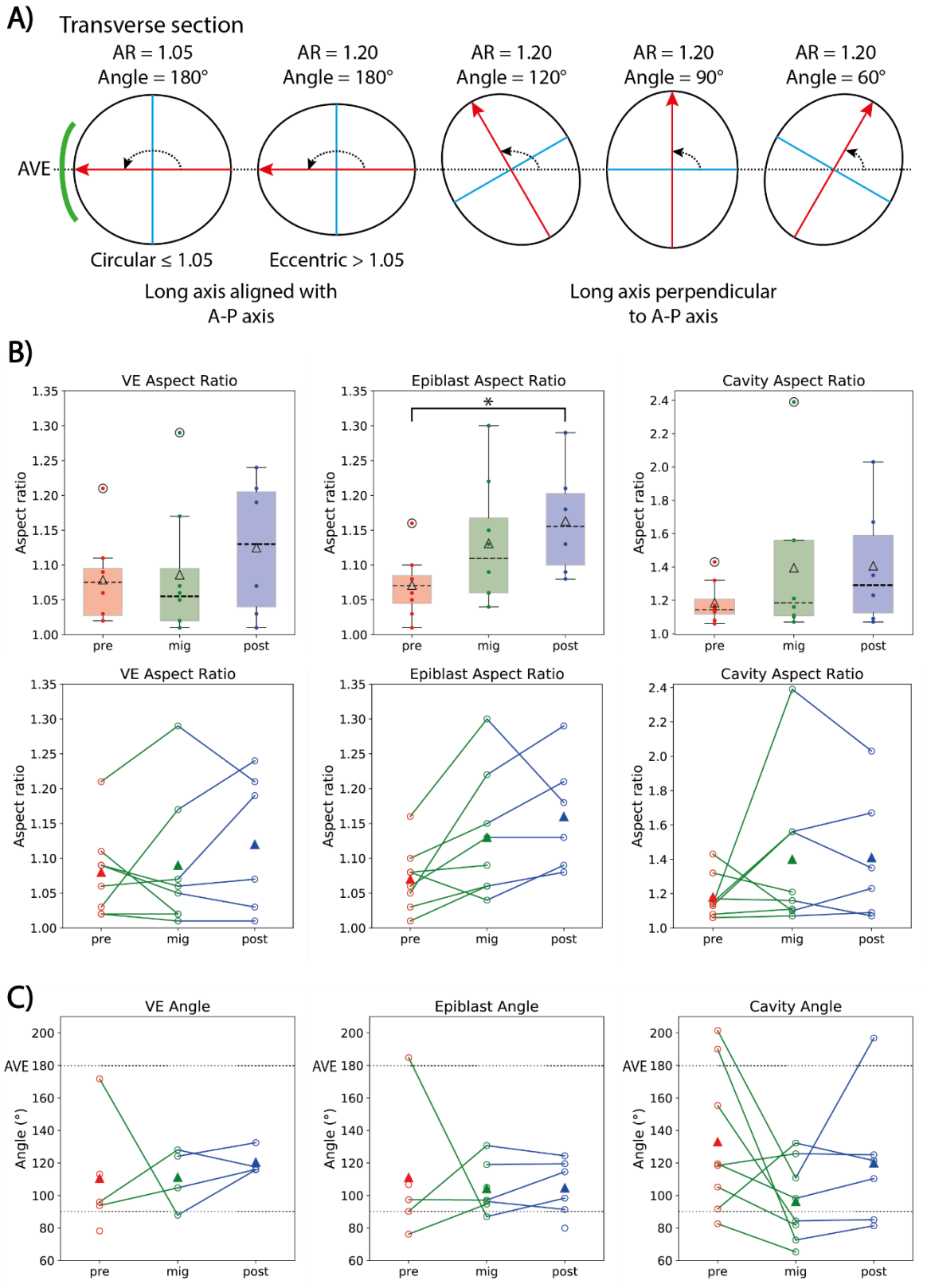
A)
Transverse section
AR = 1.05
Angle = 180°
AR = 1.20
Angle = 180°
AR = 1.20
Angle = 120°
AR = 1.20
Angle = 90°
AR = 1.20
Angle = 60°
AVE
Circular ≤ 1.05
Eccentric > 1.05
Long axis aligned with A-P axis
Long axis perpendicular to A-P axis
B)
VE Aspect Ratio
Epiblast Aspect Ratio
Cavity Aspect Ratio
Aspect ratio
pre
mig
post
C)
VE Angle
Epiblast Angle
Cavity Angle
Angle (°)
AVE

Figure 4-3

Figure 4-3: Changes in shape of the transverse cross-section during migration. A) The transverse section was measured using an Ellipse Fitting Tool (ImageJ). N=8 embryos with both pre-migration and migration phases were aligned such that the AVE was left of the embryo (180°), with the A-P axis (dotted line) on the horizontal (0-180°). The long axis is shown in red, and short axis in blue. An aspect ratio of ≤1.05 is considered circular, and angle values are discounted for these embryos. B) Comparison of the aspect ratios of the transverse section, and angle of the long axis for the VE, epiblast, and cavity. Values were taken from the last timepoint in each phase: pre-migration (red), migration (green), and post-migration (blue), shown in Table 4-2. There is significant increase in the epiblast aspect ratio between pre and post-migration ($p=0.01933$: $*p<0.05$, two-tailed T-test with equal variances). The line plot additionally links the embryos longitudinally where the data is available. C) The line plot for angle data, with dotted lines indicating the AVE at 180° and perpendicular to the AVE at 90°. Averages in B) and C) are indicated with triangular markers.

Epiblast	Pre		Mig		Post	
Embryo	Angle (°)	AR	Angle (°)	AR	Angle (°)	AR
L455_Emb2	90.22	1.10	130.70	1.15	124.40	1.21
L455_Emb3	NA	1.01	96.32	1.06	91.38	1.08
L505	97.40	1.16	97.12	1.30	114.58	1.18
L864	184.81	1.06	86.99	1.13	98.36	1.13
L871_Emb1	76.18	1.08	94.73	1.09	NA	NA
L924	106.71	1.08	NA	1.04	79.92	1.09
L928_Emb2	NA	1.05	119.02	1.22	119.51	1.29
L930	NA	1.03	104.92	1.06	NA	NA
Average	**111.06**	**1.07**	**104.26**	**1.13**	**104.69**	**1.16**
stdev	**38.20**	**0.044**	**14.25**	**0.086**	**16.00**	**0.071**

VE	Pre		Mig		Post	
Embryo	Angle (°)	AR	Angle (°)	AR	Angle (°)	AR
L455_Emb2	96.00	1.06	128.07	1.07	117.56	1.19
L455_Emb3	NA	1.02	NA	1.01	NA	1.01
L505	93.78	1.21	104.69	1.29	116.02	1.21
L864	171.74	1.09	87.88	1.06	115.81	1.07
L871_Emb1	78.16	1.11	NA	1.02	NA	NA
L924	113.09	1.09	NA	1.05	NA	1.03
L928_Emb2	NA	1.03	124.11	1.17	132.47	1.24
L930	NA	1.02	NA	1.02	NA	NA
Average	**110.55**	**1.08**	**111.19**	**1.09**	**120.47**	**1.12**
stdev	**32.54**	**0.058**	**16.10**	**0.091**	**6.96**	**0.091**

Cavity	Pre		Mig		Post	
Embryo	Angle (°)	AR	Angle (°)	AR	Angle (°)	AR
L455_Emb2	91.68	1.13	132.25	1.56	121.43	1.67
L455_Emb3	201.48	1.17	110.76	1.16	196.85	1.07
L505	119.43	1.15	98.19	1.56	110.39	1.35
L864	190.04	1.43	72.59	1.10	81.36	1.23
L871_Emb1	82.60	1.32	65.28	1.21	NA	NA
L924	155.35	1.06	84.35	1.07	85.11	1.09
L928_Emb2	118.45	1.14	125.67	2.39	125.03	2.03
L930	105.17	1.08	81.83	1.11	NA	NA
Average	**133.03**	**1.18**	**96.37**	**1.40**	**120.03**	**1.41**
stdev	**41.62**	**0.118**	**23.03**	**0.420**	**38.16**	**0.343**

Table 4-2: Angle and aspect ratio (AR) measurements at the last timepoint of each phase. Raw angle measurements are restricted to 0-180°, thus to average the data appropriately values in red have been rotated to their equivalent values outside this range. 'NA' values denote either a discounted angle due to the AR≤0.5, or values missing as the embryo did not capture that phase of AVE migration. The averages are an approximate comparison as not all embryos have the same number of timepoints in the post-migration phase.

4.3.1 The global shape of the embryo does not predict the direction of migration

In order to see if there was a pre-existing asymmetry which predicted the direction of migration, I measured the aspect ratio and angle of the long axis of the transverse sections of the embryos prior to migration, and compared them to the direction of migration. The measurements for the last timepoint of each phase are shown in Table 4-2, with the aspect ratio shown as a boxplot in Figure 4-3B. Although useful to summarise, average analysis does not show temporal evolution, particularly for the angle data of an ellipse. The angle data is therefore shown as a line plot where longitudinal data is available (Figure 4-3C), and full temporal plots can be seen in Supplementary Figure 6-5.

Both the VE and epiblast cross-sections showed a range of aspect ratios pre-migration. Additionally 2/8 embryos had a circular VE, with AR ≤ 1.05, and 3/8 embryos had an epiblast AR ≤ 1.05. For the embryos whose cross-sections (6/8 VE, 5/8 epiblast) did show eccentricity with AR>1.05, the average direction of the long-axis appeared random, (VE = 110.55° ± 32.54, Epi = 111.06° ± 38.20), with examples of the long-axis aligned both parallel and perpendicular to the future anterior. This indicates there is no consistent asymmetry in the transverse plane of the embryo prior to migration, and suggests eccentricity does not predict the direction of migration.

4.3.2 The AVE aligns with the epiblast short axis during migration

Given that it has been shown that E5.5 embryos have a characteristic shape at later stages (Mesnard et al., 2004; Aitana Perea-Gomez et al., 2004), I next assessed the shape and position of the embryos during migration (plotted in Figure 4-3B and C). Comparing the pre-migration values to the same analysis for the last migration timepoint (i.e. when the leading AVE cells reach the boundary), there is evidence to suggest that AVE migration changes the shape of the epiblast. By the time the AVE cells have reached the boundary, 8/8 embryos have shown a change in shape of the epiblast transverse cross-section. In 7/8 embryos the long-axis of the epiblast ends up perpendicular to the anterior (Figure 4-3C and Supplementary Figure 6-5).

On average, the epiblast aspect ratio increased from 1.07 ± 0.044 in pre-migration to 1.13 ± 0.086 by the end of migration. The long-axis angle also trended more perpendicular to the AVE at 180°, decreasing from 111.06° ± 38.20 pre-migration to 104.26° ± 14.25. Neither of these shifts were significant individually, but together the changes indicate a gradual morphological shape change is occurring. By post-migration there is a significant increase the average epiblast aspect ratio from 1.07 ± 0.044 in pre-migration to 1.16 ± 0.071 (Figure 4-3B).

Given that there was a significant change in the shape of the epiblast between pre-migration and post-migration stages, I next explored precisely how the shape and angle of the embryos changed over time with measurements taken every 50mins (Supplementary Table 6-1 and Supplementary Figure 6-1 to 6-5). Plotting the aspect ratio and angle longitudinally, there is some variation across embryos in how the morphological change of the epiblast manifests (Supplementary Figure 6-5). In the 3/7 embryos beginning either with the long-axis roughly parallel to the A-P axis (≈180°), or with a more circular cross-section (AR≤1.05), this shape change is shown by a prominent shift in angle to roughly the perpendicular ≈90° (L455_Emb3, L864, L930). In the case of L864 (Figure 4-4A), this shift is 97.82° as the long-axis goes from 184.81° pre-migration to 86.99° by the end of the migration phase. In 1/7 embryos (L505, shown in Figure 4-4B), the shape change is characterised by an increase in aspect ratio of 1.16 to 1.30, as the long axis begins with the axis already perpendicular to the AVE. In the remaining 3/7 embryos the shape change was seen changes to both aspect ratio and angle (L928_Emb2, L924 and L871_Emb1).

The behaviour of embryo L871_Emb1 was slightly more nuanced, beginning perpendicular and shifting parallel to the A-P axis during the first 150mins of migration, before demonstrating the characteristic return to perpendicular and increase in aspect ratio (Supplementary Figure 6-3 and 6-5). However, the cavity of the embryo underwent a dramatic expansion during the migration phase, which peaked in terms of cross-sectional area at 150mins. The long axis of the cavity and

epiblast appeared closely linked during this expansion, and strongly suggesting that in such cases the cavity expansion affects the eccentricity of the epiblast.

Finally, 1/8 embryos (L455_Emb2, Supplementary Figure 6-1 and 6-5) also underwent a shape change, but it is not clear that it follows the trend of aligning the short-axis to the direction of migration, and the long-axis perpendicular to it. The epiblast did show an increase in aspect ratio during migration, but the angle of the long axis aligns began perpendicular at 90.22° and shifted to 130.7° during migration, contrary to the directional shift seen in the other embryos. Examining the data, the only sign of VET is in the 0th transverse frame during the very short migration, but it is important to note the thickest point appears to be about 40° off the horizontal, which could explain the difference, and is likely also responsible for a degree of variation in the other embryos. The epiblast in the sagittal section also appears to tilt directionally downwards and to the right in response to the AVE migration, a shape change also particularly apparent in L864 and L924.

In summary, shape changes occur in the epiblast concurrent with VET during AVE migration. These shape changes manifest in a range of specific shifts in angle and aspect ratio of the transverse section as the short axis aligns to the AVE cells, and flattening of the sagittal section.

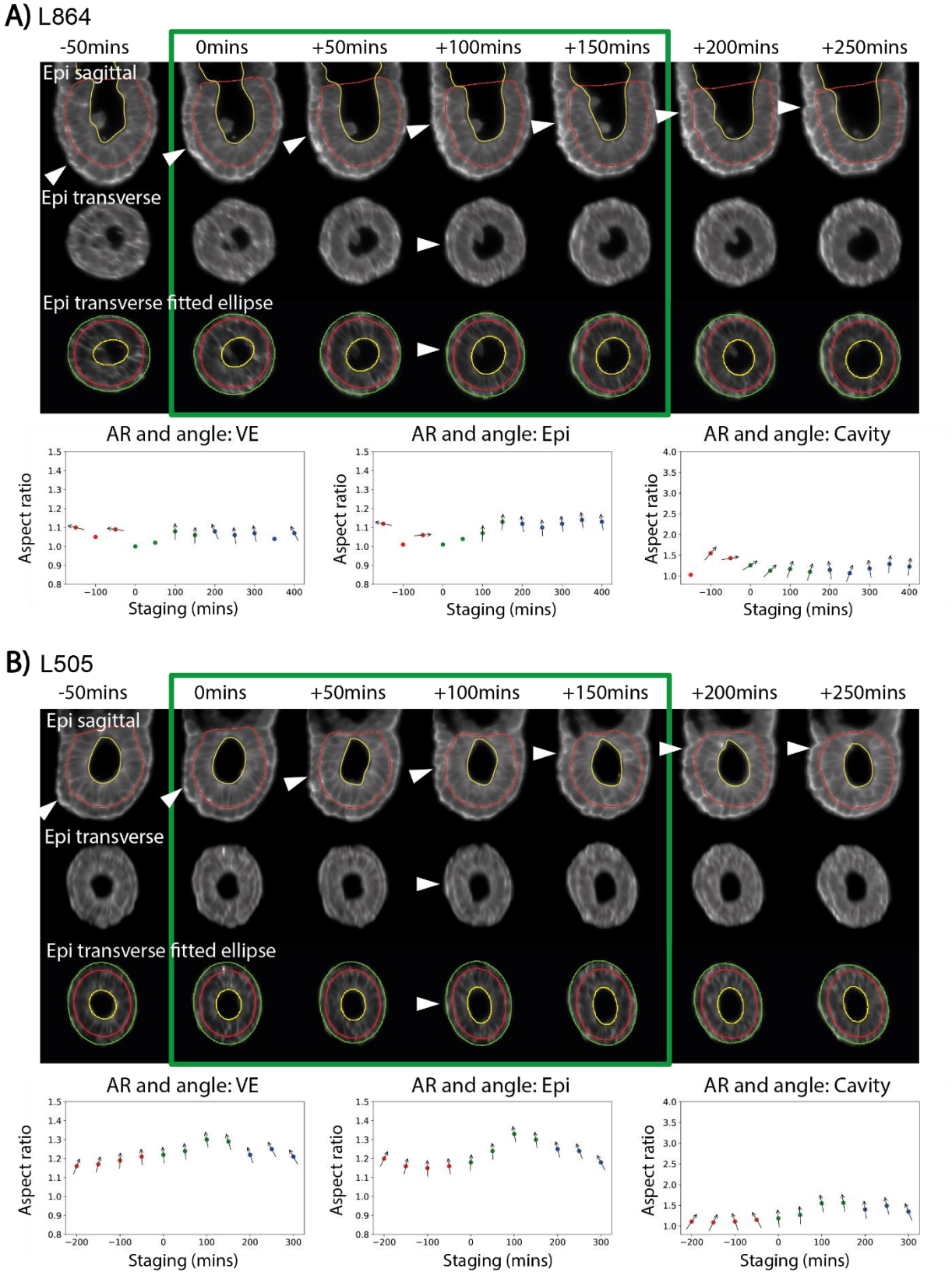
A) L864
-50mins
0mins
+50mins
+100mins
+150mins
+200mins
+250mins
Epi sagittal
Epi transverse
Epi transverse fitted ellipse
AR and angle: VE
AR and angle: Epi
AR and angle: Cavity
Aspect ratio
Staging (mins)
B) L505
-50mins
0mins
+50mins
+100mins
+150mins
+200mins
+250mins
Epi sagittal
Epi transverse
Epi transverse fitted ellipse
AR and angle: VE
AR and angle: Epi
AR and angle: Cavity
Aspect ratio
Staging (mins)

Figure 4-4

Figure 4-4: The long-axis aligns perpendicular to VET. A) An example of embryo L864, which demonstrates the shift in eccentricity by a shift in angle of the long axis from horizontal (aligned with the A-P axis) to vertical (perpendicular to the A-P axis) during the course of migration. B) L505 began with the long-axis already oriented roughly perpendicular to the A-P axis prior to migration. Instead of a change in this angle, the shape change manifested in an increase in aspect ratio as the AVE migrated. The leading edge of the AVE is denoted by a white arrowhead in sections, and the green box indicates frames in the migration phase, which begins at the staged time of 0mins.

4.3.3 The shape changes in the epiblast are concurrent with VET

The analysis of the shape and angle of the embryo between pre- and post-migration revealed that the only significant change occurred in the epiblast, which became more elliptical (Figure 4-3B). Although the VE showed a slight increase in average aspect ratio between pre-migration and migration, the spread of values in migration is larger (Figure 4-3B). Additionally, as 4/8 of the embryos show a more circular transverse cross-section during the migration, this is not a significant trend (Figure 4-3B). The aspect ratio did notably shift between migration and post-migration, but this is not a trend which extends to the longitudinal data available for 6/8 embryos, with 2/6 showing a large increase in AR, 1 showing a large decrease, and 3 staying roughly the same (Figure 4-3B and Supplementary Figure 6-5).

That the shape changes in the transverse epiblast during AVE migration did not occur concurrently in the VE suggests they could be due to more columnar AVE cells migrating on the anterior side. The timelapse data enabled the interaction between the cell layers to be viewed over time in the sagittal sections. In the sagittal sections, the effect of the columnar AVE cells becomes more obvious, as it is possible to follow flattening in the epiblast and cavity concurrent with the migration of the AVE cells. This is particularly evident in embryo L928_Emb2, which has a small cavity, and the advantage of *Hex-GFP* positive cells to give a precise location for the AVE (Supplementary Figure 6-4). The coincidental movement suggests that the significant change in shape of the epiblast might be due to the AVE cell population.

4.3.4 The expanding cavity reduces the aspect ratio *in-vitro*

During the analysis of the shape of embryos I also noted that many of the embryos in the dataset showed an abnormally large cavity expansion. The cavity in E5.5-6.5 embryos *in vivo* is very narrow, as can be seen in Mesnard et al.'s histological sections in Figure 4-1Aii. It is a reported artefact of culturing embryos *in vitro* that the cavity expands significantly as the egg cylinder is no longer protected by the decidua and is vulnerable to differences in osmolarity. To see the impact this could be having on the dataset, I determined the frame number at which the cavity began to rapidly expand in each embryo (Table 4-3).

The effect was prevalent, with all but two embryos (L455_Emb2 and L928_Emb2) undergoing abnormal cavity expansion in the epiblast at some point in the timelapse (Table 4-3). There did not appear to be any correlation between the time of epiblast cavity expansion and AVE migration. Instead, 21/24 embryos expanded within the first half of the timelapse, and 15/24 before the first 50mins of the timelapse (10 or 5 frames), supporting increased cavitation as a culturing artefact. Additionally, I noted that cavitation of the ExE was not expected until much later, but a large cavity expansion is seen in the ExE 16/24 embryos, usually after the expansion had occurred in the epiblast. Ectopic cavities could also form in the ExE, an example of which can be seen in Supplementary Figure 6-2.

In order to discern the effect this abnormal cavity expansion was having on both the sagittal and transverse eccentricity, isolated from the dynamic influence of VET during migration, I examined the effect of cavity expansion on an embryo imaged from late migration stages. In Figure 4-5 I show the abnormally expanding cavity of embryo L926, at around 240mins into the post-migration timelapse.

This embryo undergoes a cavity expansion after 220mins of imaging (Figure 4-5) so I compared the aspect ratio of the VE and Epiblast prior to and post cavity expansion. This showed a decrease from 1.42 to 1.14 for the epiblast and 1.27 to 1.10 for the VE. It also reduces the effect of VET, lessening

the difference between the aspect ratios as the area of the cavity increases from 0.28 to 0.04 (Figure 4-5B).

As with L928_Emb2, a migrating embryo for which the cavity does not expand, the *Hex-GFP* positive AVE cells in L926 can clearly be seen to migrate up the anterior of embryo in the sagittal section, concurrent with notable flattening in the epiblast. This is also reflected in the shape of the cavity in the epiblast prior to expansion, with a distinct but short-lived asymmetric 'L' shape visible by 220mins, the asymmetry disappearing as the cavity expansion occurs soon afterwards. This can also be seen in Supplementary Video 9.

In addition to the reduction in aspect ratio post-cavitation, significantly larger epiblast aspect ratios were seen in the two migrating embryos with no cavity (L455_Emb2: AR=1.24, L928_Emb2: AR=1.32, p=0.0036: **p<0.01 Single Factor ANOVA). L505 (AR=1.33) was excluded from this test because the shape change manifests predominately as a change in aspect ratio, contrary to the other embryos (Supplementary Figure 6-5). Combining these observations, it is likely that the expanding cavity is having a dampening effect on the aspect ratios of epiblast and the VE compared to what one could expect to see *in vivo*, and this may include reducing the difference between them due to VET.

In summary, the short axis of the embryo transverse cross-section consistently changes angle to align with the AVE during migration, coincident with the appearance of VET. This alignment is not seen prior to migration. Asymmetric flattening of the epiblast concurrent with VET is apparent in the difference between the VE and epiblast, in both average measurements of aspect ratio and qualitative observations of the temporal data. However, the pro-amniotic cavity abnormally expands during *in vitro* culturing in the majority of the embryos, which measurements suggest may be dampening the observed effect, and reducing the overall eccentricity of the egg cylinder.

Embryo	Epi Cavity begins expanding (mins)	ExE Cavity begins expanding (mins)	Manual staging (mins)		
			Pre-migration	Migration to Boundary	Post-Boundary
401	150	295		0-180	185-495
455_E2	NA	NA	0-220	225-290	260-290
455_E3	<0	145	0-200	205-505	510-550
491	35	155		0-245	250-495
505	5	45	0-190	195-365	370_545
864	80	80	0-150	155-345	350-570
871_E1	25	195	0-45	50-325	
871_E2	<0	55		0-325	
917	0	560		0-180	185-595
921	0	140		0-320	
922	170	NA		0-490	500-690
924	20	400	0-120	130-700	710-960
926	220	210			0-440
927	<0	NA		0-290	300-410
928_E1	20	NA		0-450	460-930
928_E2	NA	240	0-90	100-360	370-520
930	150	440	0-260	270-590	
932	<0	NA		0-390	400-760
848	<0	0		0-230	240-290
860	<0	60		0-290	300-340
905	30	NA			0-290
910	110	150		0-210	220-350
945	110	NA	0-260		

Table 4-3: Measurements of abnormal Epi and ExE cavity expansion. Only two embryos did not show abnormal cavity expansion in the epiblast: L455_Emb2 and L928_Emb2. The epiblast cavity expanded within the first half of the timelapse in 21/24 embryos before the first 50mins of the timelapse in 15/24 embryos. Many embryos also showed abnormal and occasionally ectopic cavity formation in the ExE.

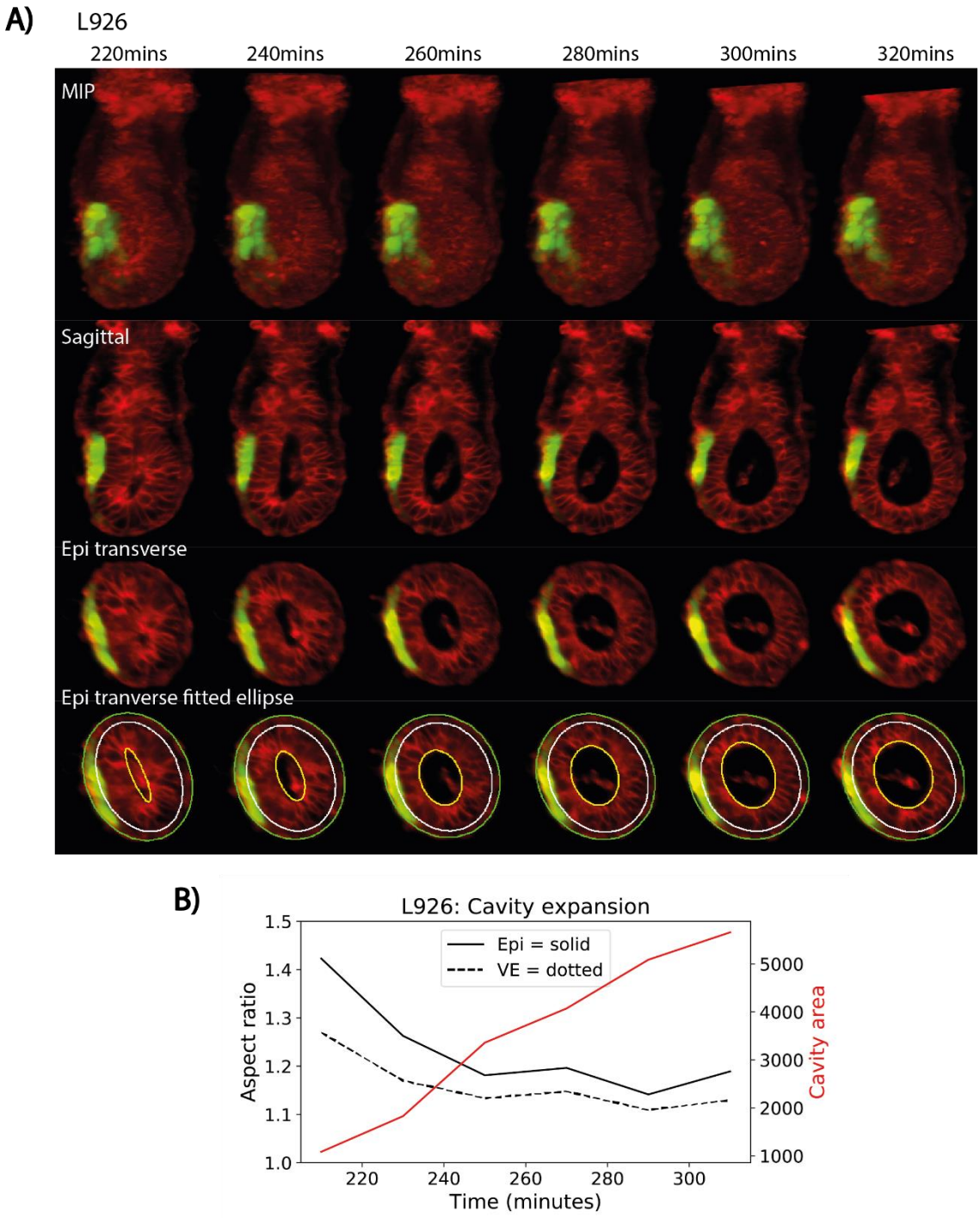

Figure 4-5: Measuring the effect of the expanding cavity of L926 on aspect ratio of the epiblast. A) Shows the maximum intensity projection, sagittal, and transverse sections of L926, a later embryo which undergoes cavity expansion in the post-migration phase. Ellipses are fitted to the transverse section to measure the aspect ratio and angles of each cell layer. B) The aspect ratios in the epiblast (solid black) and VE (dotted black) decrease as the cavity expands becoming more circular, as shown by its increase in cross-sectional area (right axis, red line – units are not real values, but pixels^2 relative to the data registration). Data plotted is shown in Supplementary Table 6-1.

4.4 Analysis of cell division events in the VE during AVE migration

One theory proposed by previous studies is that an elevated rate of proliferation in the posterior may nudge the AVE cells to the future anterior. Studies in fixed samples and under timelapse imaging, have shown evidence for reduced proliferation in the AVE region (Antonica et al., 2019; Yamamoto et al., 2004) and against this hypothesis (Shioi et al., 2017; Stuckey et al., 2011), with a variety of methods.

In order to determine if there are asymmetries in division prior to or during migration, I carried out manual analysis of the cell divisions in four *Lifeact* embryos during pre-migration and migratory phases as defined by the manual staging. The 2D surface projections with the *Lifeact* membrane marker enable the visualisation of cell divisions at a 5min time resolution, and permit observations of the dynamic behaviour with an unambiguous biological marker. Using the Cartesian 2D projections and VGG Image Annotator (Dutta & Zisserman, 2019), I manually identified the locations of the cell divisions across the timelapses. The embryos were staged such that AVE migration begins at 0mins, and negative frames relate to pre-migration. For the purpose of the cell division analysis, I did not make distinction between migratory and post-migratory phases, and simply refer to anything after pre-migration as 'migration'. I divided the VE into equal quadrants, and split the Epi-VE and ExE-VE around the average boundary position across the timelapse, as denoted by the average height of the geometrically matched epiblast. The numbering of the quadrants can be seen in in Figure 4-6, with the AVE region in the centre of quadrant 3 (red).

By recording the coordinates and timepoint of each cell division, I was able to look for elevated rates of proliferation in each quadrant. As the quadrants contain different numbers of cells, it is important to use a measure of division rate which takes this into account. Previously, the number has been given as a percentage of the total cells (Shioi et al., 2017; Stuckey et al., 2011). However, as our dataset has been acquired with higher temporal resolution, following all cells in the VE manually for every frame was impractical. Instead, I counted the number of cells in the first frame

of the timelapse (pre-migration), the start of migration, and the last timepoint of the timelapse, in order to normalise the rate of proliferation by the average number of cells in a quadrant. This can be also seen in Figure 4-6. The static quadrant scheme does not take into account movement of cells between quadrants over time, but this should be of little consequence for the static pre-migration phase, and gives a reasonable measure for the migration phase.

The uncertainties in manual cell counting and spotted cell divisions can be found in *Table 4-4*, which were used to draw uncertainty bars in the following figures. The error in division count was estimated using the difference from the total expected from division by the difference in cells counted. The cell count itself contains intrinsic errors, as not all cells in the epithelium can be clearly delineated. It was (likely over-estimated at) 5% per frame, giving a percentage error of 10% for the average number cells per quadrant over the timelapse. The cell numbers are likely underestimated in the AVE region, and near the boundary, as cells become highly compacted and difficult to discern. This will result in a lower average cell number, and thus a slightly higher normalised number of cell divisions per quadrant towards the end of the timelapse.

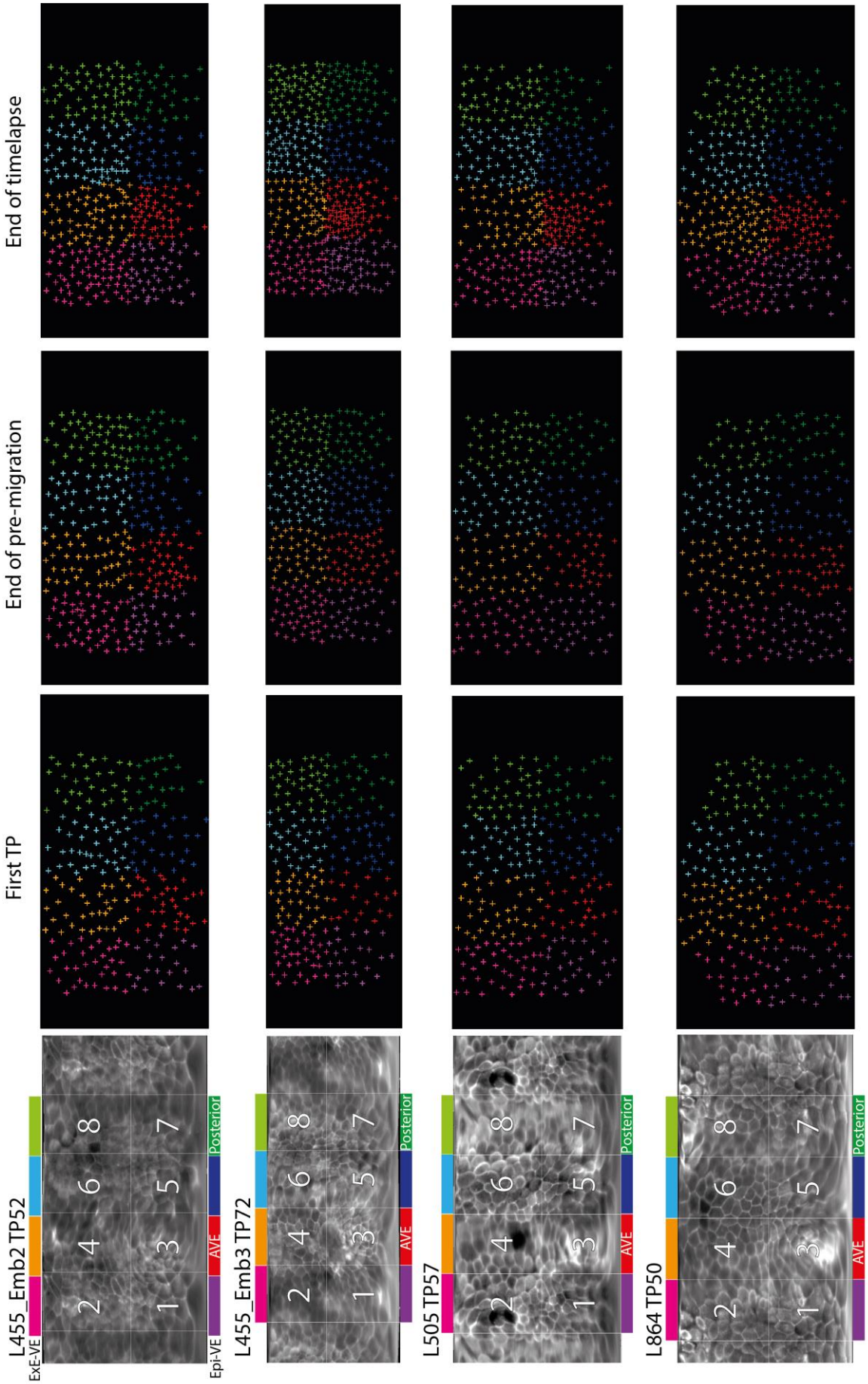
First TP
End of pre-migration
End of timelapse
L455_Emb2 TP52
L455_Emb3 TP72
L505 TP57
L864 TP50
ExE-VE
Epi-VE
AVE
Posterior
1
2
3
4
5
6
7
8

Figure 4-6: The number of cells in each quadrant was counted in the first frame, last frame of pre-migration, and end of the timelapse. Each coloured cross represents a cell centroid. The quadrants are numbered according to the overlays on the left, with corresponding colours which can be seen in the plots and later in the graphs in this section. The frames were wrapped around and repeated to as to fully capture the cells in the posterior, hence why the frame is longer than the quadrant section. Note quadrant 8 in L505 and quadrants 2 and 8 in L864 contain uncounted cells from the EPC.

Stage	Embryo	Difference in cells counted (last-first TP)	Total cell divisions	Error in division count	Error in division count per quadrant	% Error division count per quadrant	Estimated % error in cells counted x2	Total % error
All	L455_Emb2	136	145	-9	-1.125	-6.21	10	16.21
	L455_Emb3	179	155	24	3	15.48	10	25.48
	L505	130	117	13	1.625	11.11	10	21.11
	L864	137	145	-8	-1	-5.52	10	15.52
					Avg % error	**9.58**	**10**	**19.58**
Pre	L455_Emb2	60	71	-11	-1.375	-15.49	10	25.49
	L455_Emb3	77	63	14	1.75	22.22	10	32.22
	L505	30	17	13	1.625	76.47	10	86.47
	L864	36	21	15	1.875	71.43	10	81.43
					Avg % error	**46.40**	**10**	**56.40**
Mig	L455_Emb2	76	74	2	0.25	2.70	10	12.70
	L455_Emb3	102	92	10	1.25	10.87	10	20.87
	L505	100	100	0	0	0.00	10	10.00
	L864	101	124	-23	-2.875	-18.55	10	28.55
					Avg % error	**8.03**	**10**	**18.03**

Table 4-4: Estimated errors in counting the number of cells and cell divisions. Errors in the number of divisions were estimated by giving the difference between the number of divisions seen and the difference in the number of cells counted (for every cell division there should be an additional cell). The cell counting errors were estimated at 5% per frame.

4.4.1 There are no regional asymmetries in VE cell density prior to AVE migration

I first looked at the change in cell density of each quadrant. This accurate measure uses density change as a proxy for cell proliferation and has smaller errors due only to errors in the cell counting. It is available by reversing the 2D surface projection to provide accurate 3D quadrant areas (done by Dr Felix Zhou), and accounts for changes in growth and shape of the embryo. If a nudge were being given from the posterior to the anterior through proliferation in the VE, one would expect to see a higher change in cell density in the posterior compared to the anterior.

Using the cell counts from Figure 4-6, I plotted the cell densities of each quadrant (Supplementary Figure 6-6) for the first timepoint of the timelapse (TP1, in pre-migration), the last timepoint of pre-migration, and the end of the timelapse. Density units are given in the intuitive measure of cells per $(10\mu m)^2$ or $c/(10\mu m)^2$ i.e. how many cells fit in a $100\mu m^2$ or a 10µm x 10µm area. This cell density data is summarised in Figure 4-7A, and the corresponding cell density change rate is given in Figure 4-7B, which accounts for the temporal variation between embryos.

There were no significant differences in cell density between quadrants, either at the earliest pre-migration timepoint, or at the start of migration (Figure 4-7A). Only one embryo has a higher cell density in the posterior Epi-VE at the start of the timelapse (L455_Emb3). By the start of migration, all 4 embryos have a more densely packed anterior Epi-VE quadrant (red, 3) compared to the posterior Epi-VE quadrant (dark green, 7), with an average density of $0.44c/(10\mu m)^2$ compared to $0.36c/(10\mu m)^2$. For reference, this gives cells in the anterior Epi-VE an average area of $227\mu m^2$ compared to $278\mu m^2$ in the posterior Epi-VE.

However, this density is a reflection of differently shaped cells – it is known that AVE cells constrict their apical surface, and thus one would expect the AVE region to be more densely packed. The change in cell density therefore gives a clearer picture of where pressure in the sheet is coming from, which is shown in full in Supplementary Figure 6-7, and summarised in Figure 4-7B. This data

showed that, as well the AVE being denser in embryo at the start of migration, there were no significant differences in the rate of cell density change during pre-migration (Figure 4-7A).

Looking at the embryos individually, 2/4 showed a greater posterior Epi-VE density change compared with the anterior Epi-VE pre-migration (Supplementary Figure 6-7). However, these differences were very small, amounting to approximately 1 in 26 cells in increased density. Additionally, in one of these (L505) both the anterior Epi-VE and posterior Epi-VE quadrants had a negative density change rate over pre-migration, suggesting growth was accounting for a greater change than cell division, and that proliferation could not be contributing to increasing pressure.

During migration, the density change rate was significantly lower in the posterior Epi-VE compared to the anterior Epi-VE (Figure 4-7B). This density decrease in the posterior Epi-VE occurred in 4/4 embryos and is inconsistent with the notion of a driving force due to asymmetric rates of proliferation (Supplementary Figure 6-7).

By the end of migration, there are regional differences in cell density across the VE. The cell density in the posterior Epi-VE quadrant (7) was significantly lower than the anterior Epi-VE (quadrant 3) as well as several ExE-VE quadrants (4 and 6) (Figure 4-7B), as the AVE cells overflow into the neighbouring ExE-VE regions. Interestingly, there were pronounced differences in density change between the two lateral Epi-VE quadrants (1 and 5) during migration which, although not significant, were present in 3/4 embryos (Supplementary Figure 6-7). This difference is reflected in the significantly lower density of one lateral Epi-VE quadrant (5) compared to the anterior quadrants (3 and 4), and may indicate the presence of a left-right asymmetry.

Overall, the change in cell density reflects the observations of relatively smaller apical cells, and elongating posterior Epi-VE cells which flatten and extend in the anterior direction as the AVE migrates.

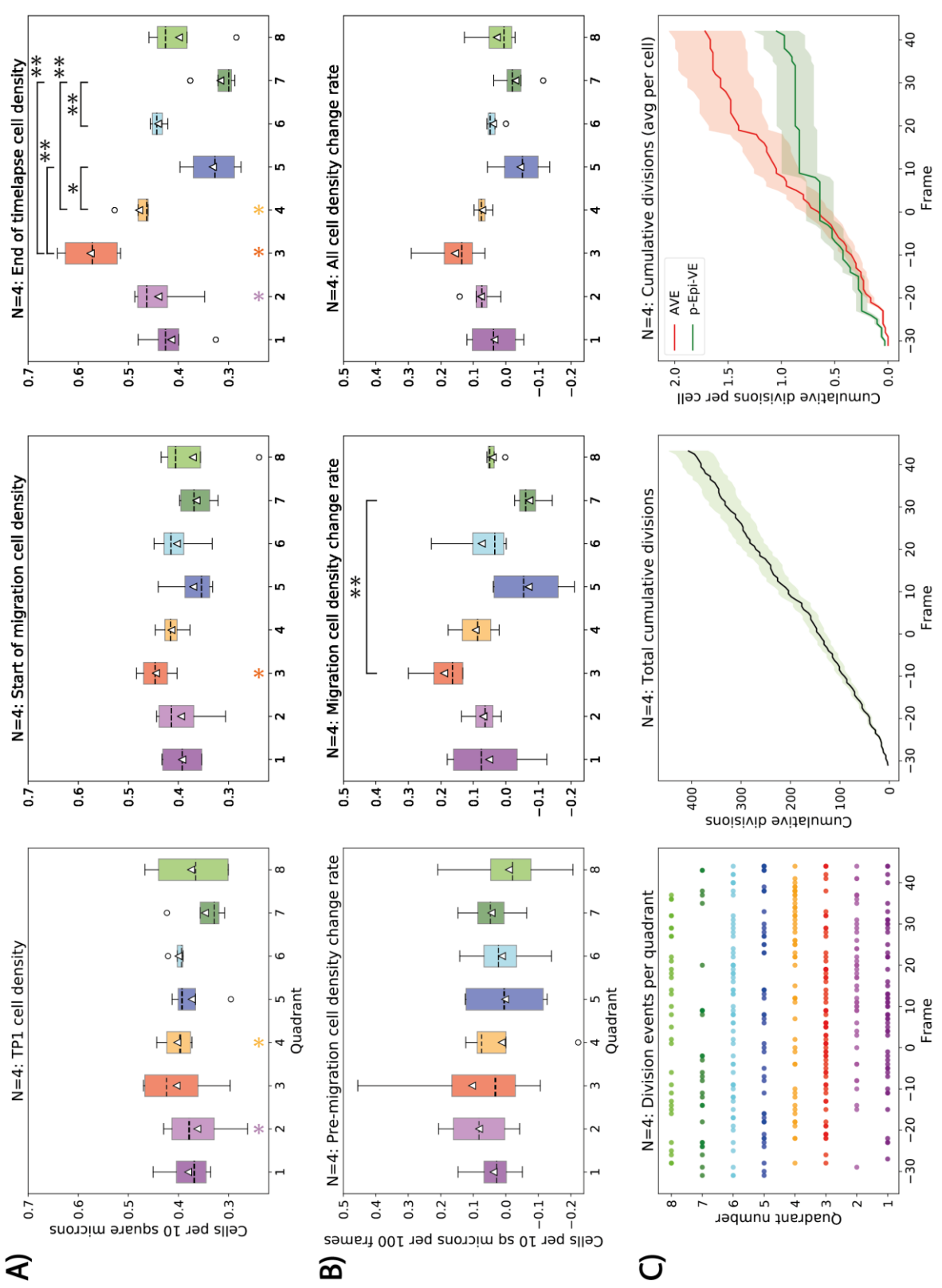
A)
N=4: TP1 cell density
Cells per 10 square microns
Quadrant
N=4: Start of migration cell density
N=4: End of timelapse cell density
B)
N=4: Pre-migration cell density change rate
Cells per 10 sq microns per 100 frames
Quadrant
N=4: Migration cell density change rate
N=4: All cell density change rate
C)
N=4: Division events per quadrant
Quadrant number
Frame
N=4: Total cumulative divisions
Cumulative divisions
Frame
N=4: Cumulative divisions (avg per cell)
AVE
p-Epi-VE
Cumulative divisions per cell
Frame

Figure 4-7: Average changes in cell density and proliferation, from N=4 embryos.

*A) There were no significant differences in cell density in at the start of the timelapse or start of migration: single factor ANOVA ($p=0.93$, $\alpha<0.05$) or non-parametric Friedman $\chi 2$ rank test ($p=0.4936$, $\alpha<0.05$). Values are given in cells per $(10\mu m)^2$. By the end of the timelapse, significant differences in quadrant density emerged (ANOVA, followed by two-tailed T-test with equal variances and Bonferroni correction for multiple comparisons: black *$p<0.00714$, **$p<0.00142$). Coloured * show significant differences between the same quadrant in different timepoints (paired T-test, *$p<0.05$).*

*B) The more temporally accurate cell density change showed no significant differences between quadrants in pre-migration, but significantly higher cell desnity change in the anterior Epi-VE (red, 3), compared to the posterior Epi-VE (dark green, 7) during migration (ANOVA followed by two-tailed T-test with equal variances and Bonferroni correction, $p=0.00136$, *$p<0.00714$, **$p<0.00142$). Units are in cells per $(10\mu m)^2$ per 100 frames. No individual quadrant showed a significant difference in the rate of cell density change between pre- and migration phases (ANOVA: Two-Factor With Replication, $p=0.66$, $\alpha<0.05$).*

C) Division events are temporally and spatially stochastic, appearing in bursts of close cells. Plotting divisions cumulatively over the 4 embryos, a steady rate of division emerges, alough this diverges between anterior and posterior Epi-VE quadrants during migration. Cumulative divisions in the right plot are normalised by the average number of cells in a quadrant. The staging is reflected in the Frame number on the x-axis, with 0 marking the start of migration and negative frames pre-migration. Shading gives the uncertainty in the cumulative measurements according to Table 4-4. Frames are acquired every 5mins.

4.4.2 There are no regional differences in the rate of proliferation between the anterior and posterior Epi-VE

Changes in cell density could be caused by either greater proliferation compared to embryonic growth or, particularly during migration, cells moving between quadrants. Therefore, in addition to changing cell density, I also manually annotated cell divisions across the 4 embryos, providing greater temporal detail, and accounting for cell movement where necessary by normalising cell divisions by the average number of cell in each quadrant.

Plotting the cell divisions over time divided into quadrants in Supplementary Figure 6-8 and with the average data summarised in Figure 4-7C, a stochastic picture of cell divisions emerges, with cells clustering in bursts of spatially and temporally regionalised divisions. While identifying cell divisions events I noticed that many appeared in bursts, with neighbouring cells often dividing within 5/10 minutes of one another.

In the second column of Figure 4-7C, I have plotted the cumulative cell divisions for the N=4 embryos, irrespective of quadrant (shown for individual embryos in Supplementary Figure 6-8). The rates of proliferation were very similar both between embryos and throughout the timelapse. Furthermore, the approximately linear rate, suggests that there is a steady rate of proliferation E5.5-E5.75, with variation in the individual rates caused by temporally stochastic divisions balancing out over multiple embryos.

To see if there were regional differences in the VE which could be responsible for pushing the AVE cells towards the anterior, I then looked at the proliferation rates within each quadrant, normalised by the average number of cells in the quadrant (Figure 4-7C and Supplementary Figure 6-8 last column). The theory that Nodal is required for proliferation in the VE suggests Nodal antagonists Lefty1 and Cer1 would decrease the relative rate of proliferation in the AVE region during migration. This means that there would be less division events per cell in the anterior Epi-VE, than in the posterior Epi-VE.

I statistically tested for difference in the normalised proliferation rate between the anterior (quadrant 3) and posterior (quadrant 7) (Figure 4-7C). This was done using linear squares regression fit using the normalised cumulative division rate curves with quadrant 3 (x-axis) and quadrant 7 (y-axis). The result is a fitted line with equation y = slope * x + intercept. If the proliferation rate between quadrants was equal, the resulting fitted slope = 1; if < 1, the posterior (y-axis) is only a fraction of the anterior (x-axis) which is undergoing higher division; if > 1, the posterior undergoes higher division. In all embryos, the fitted slopes in pre-migration and migration gave a slope < 1 indicating higher division rate in anterior quadrant, consistent with the density change data.

I additionally tested if this relationship changed between pre-migration and migration. Applying single factor ANOVA test on the fitted regression slopes, there was no significant difference between anterior Epi-VE and posterior Epi-VE proliferation between pre-migration and migration (average slope = 0.636 in pre-migration, average slope = 0.402 in migration). Discounting L455_Emb3, which showed distinctly different behaviour to the other three embryos in the migration phase (average slope in migration for L455_Emb3 = 0.857), the same test using the remaining 3/4 embryos showed a significant difference between the slope of the two quadrants between pre-migration and migration (ANOVA: Single Factor, p=0.0145, α<0.05). The slope was thus significantly decreased showing that the increased rate of anterior Epi-VE proliferation compared to posterior Epi-VE is significantly even greater than it was during pre-migration (average migration slope with 3/4 embryos = 0.250).

In summary, the anterior Epi-VE proliferation rate across each phase is always higher than that of the posterior Epi-VE and becomes significantly more so during migration, contrary to the theory that Nodal antagonists decrease relative proliferation in the anterior compared to the posterior. The number of cell divisions per quadrant also supports this conclusion (Supplementary Figure 6-8). By the start of migration, 3/4 embryos have had more divisions in absolute numbers in the anterior

Epi-VE than the posterior Epi-VE (a-Epi-VE: p-Epi-VE = 9:5, 13:10, 4:3), while 1/4, which had 3 divisions in each region.

As with the study of cell density change, this data also indicates proliferation is unlikely to sustain AVE migration. In 4/4 embryos, there are fewer absolute cell divisions in the posterior Epi-VE during migration, and in 3/4 fewer normalised divisions per cell in the posterior Epi-VE during migration. L455_Emb3 is the exceptional embryo as revealed in the linear regression analysis, which has 11 cell divisions in the anterior Epi-VE and 10 in the posterior Epi-VE, which does give an increased number of normalised divisions per cell in the posterior Epi-VE. However, this difference only equates to an increase of ≈0.1 divisions per cell over 61 frames (6hours).

Combined with the decrease in density in the posterior Epi-VE as the embryo grows, this indicates that proliferation is unlikely to act as either a passive directional 'nudge' or as driving force to actively sustain migration.

4.4.3 There are regional differences in the angle of cell division between the anterior and posterior Epi-VE

Although there were no differences in the rate of cell divisions in different regions of the VE, manual analysis does suggest that the angle of cell division could be regionally biased.

For each cell division, I also measured the angle between a line joining the centroids of the daughter cells, and the horizontal, and these were translated by Dr Felix Zhou back into 3D coordinate space. As with the eccentricity measurements, an angle of 0° (horizontal) means the daughters are aligned perpendicular to the proximal-distal axis, and an angle of 90° (vertical) means daughters lie parallel to the proximal-distal axis. In Figure 4-8 I have plotted the angles for each region onto the space of the embryo projection. It is striking that the angles do not appear randomly oriented, but instead appear to follow the deformation of the epithelial sheet as seen by comparison to the MOSES deformation meshes introduced in Chapter 3, and appear symmetrical along the direction of AVE

migration. Somewhat surprisingly, this is also discernible in the pre-migration phase for the two embryos with a higher number of per-migration cell divisions, thus enabling a pattern to emerge (L455_Emb2 and L455_Emb3) (Figure 4-8).

Combining the angle data from the 4 embryos, I compared pre-migration and migration phase angles (Figure 4-9). The radial pattern deformation surrounding the AVE migration does not lend itself easily to horizontal/vertical analysis in box-plots, particularly as I have shown cells near the anterior boundary move from the Epi-VE into the ExE-VE quadrants. However, in the lateral quadrants (1,2,5,6), the distribution of angles became more symmetrical around the anterior (quadrants 3 and 4) during migration, reflecting the deformation centred on these quadrants (Figure 4-9). The anterior quadrants also shifted to more vertical angles in the direction of AVE migration. Following this pattern, the average angle in the posterior-ExE (quadrant 8) increased from a median of 26° in pre-migration to 48° in the migration phase, showing the posterior divisions occurring more vertically. These shifts between pre-migration and migration angles in the anterior quadrants (3,4) and the posterior ExE-VE are significant (Figure 4-9).

There is a degree of warping present in the Cartesian projection which makes the plotted angles harder to interpret around the distal tip. Therefore, to confirm the lack of 'nudge' from the posterior quadrant, and make the true angles around the distal tip clearer, I also measured and plotted the angles in the polar tip projection of L455_Emb2 shown in Figure 4-10A, with the AVE migrating towards the right.

If the 'nudge' theory is correct, one would expect to see either reduced anterior divisions relative to the posterior, or division angles oriented towards the direction of migration (Figure 4-10B). In the zoomed in sections of Figure 4-10A, neither of these is apparent. We can see more cell divisions occurring in the anterior Epi-VE region, and the analysis of this embryo in the previous section confirmed the divisions per cell was nearly identical between the anterior Epi-VE and posterior Epi-VE. The posterior Epi-VE divisions also fail to show directionality along the A-P axis, suggesting that

a change in cell division angle pre-migration does not contribute to 'nudging' the AVE towards the anterior.

Based on the analysis above, there is no evidence to support the theory that asymmetric proliferation in the VE layer nudges the AVE towards the anterior direction.

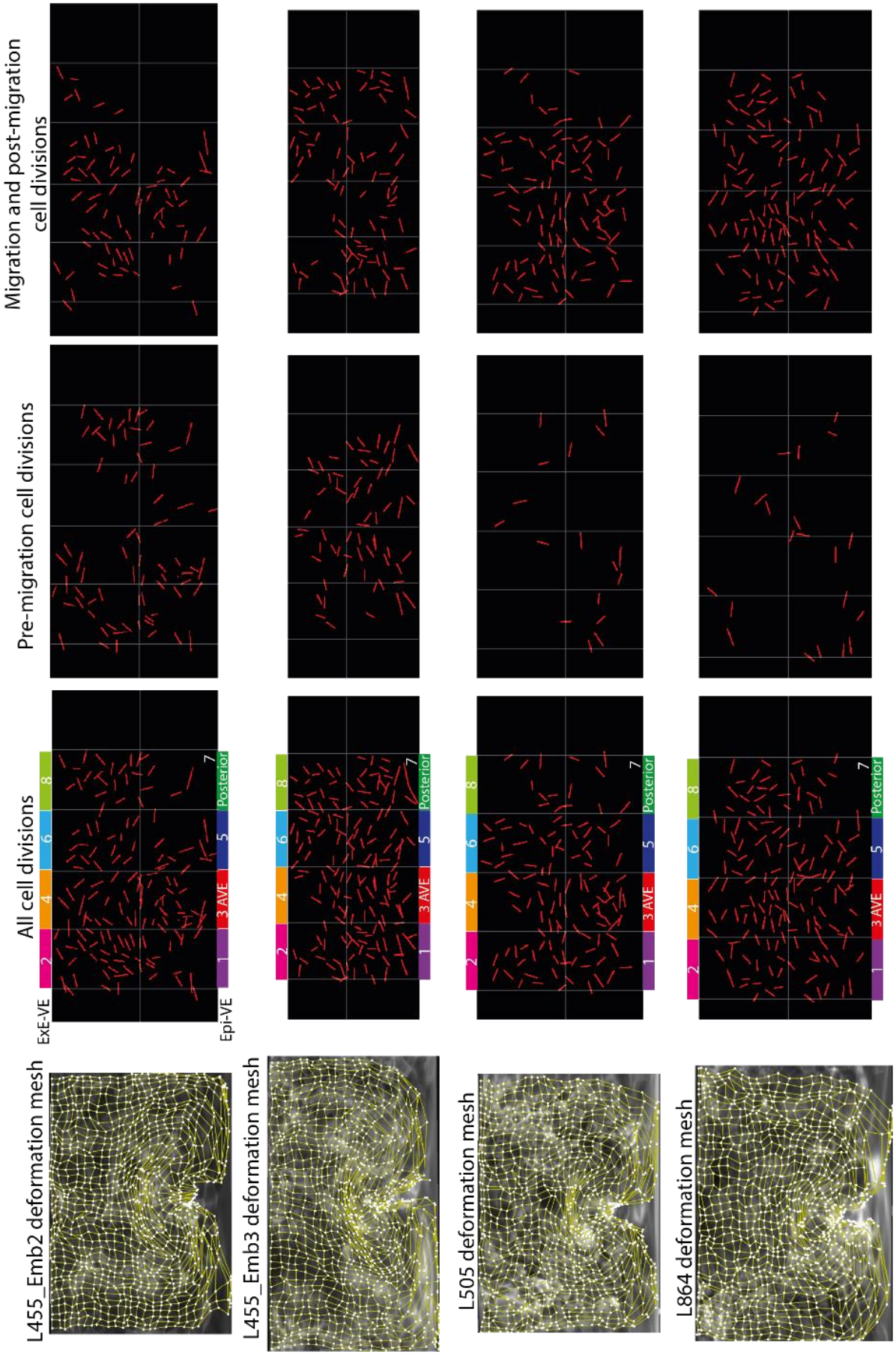
Migration and post-migration cell divisions
Pre-migration cell divisions
All cell divisions
ExE-VE
Epi-VE
1
2
3 AVE
4
5
6
7
8
Posterior
L455_Emb2 deformation mesh
L455_Emb3 deformation mesh
L505 deformation mesh
L864 deformation mesh

Figure 4-8: Plotting the cell angles over the 2D Cartesian projection shows a non-random orientation that bears a resemblance to the deformation meshes created using the MOSES superpixel tracking. This is also apparent in the pre-migration phases of L455_Emb2 and L455_Emb3.

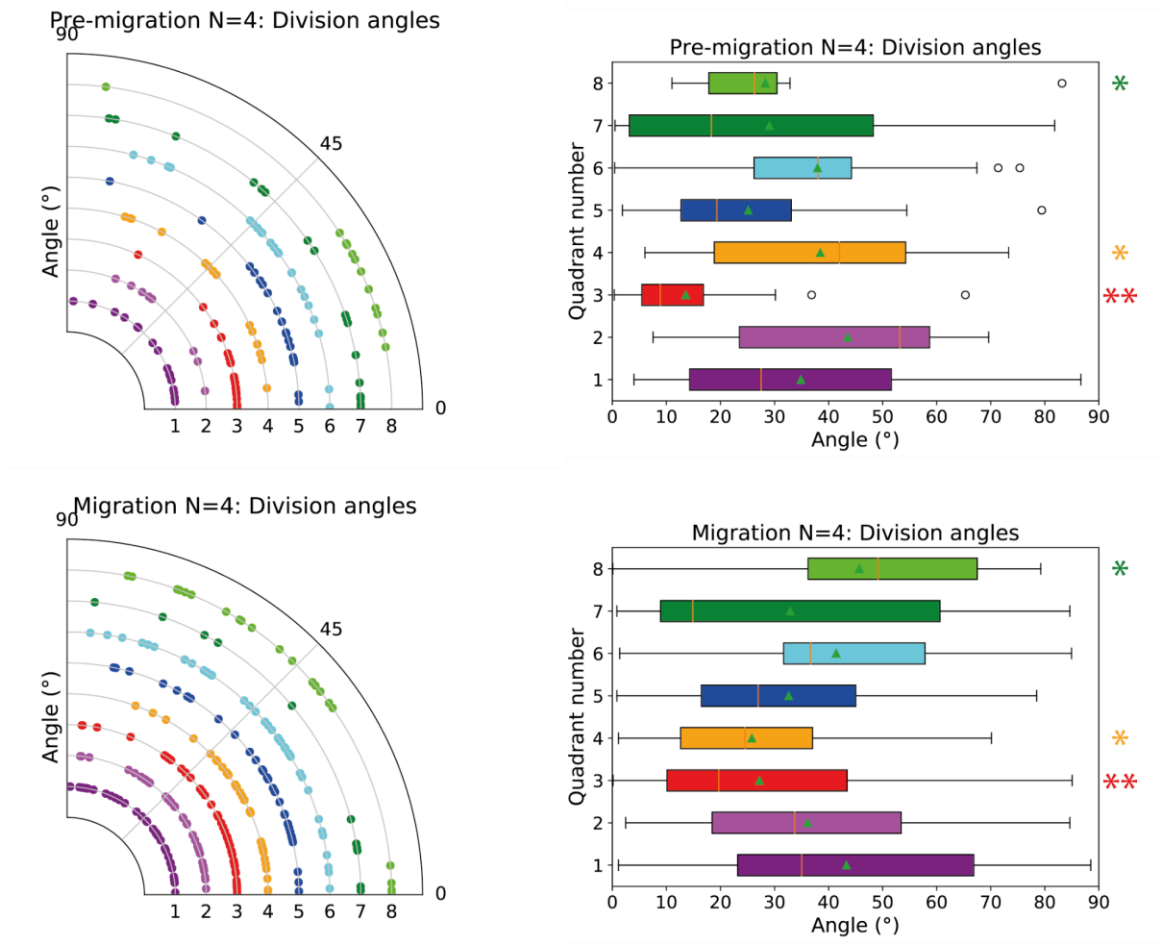

*Figure 4-9: Rose and boxplots of the division angles combined from the N=4 embryos, during pre-migration, and migration. The symmetry emerging around the AVE is apparent in the changing angles of cell division in quadrants 1-6 between pre-migration and migration phases. The anterior quadrants show significant changes in cell division angle: as cells in the anterior ExE-VE (quadrant 4) undergo more horizontal divisions and cells in the anterior Epi-VE (quadrant 3) shift more vertically. The posterior-ExE-VE (quadrant 8, light green) also shows a significant shift to more vertical divisions during migration. Asterisks (*) show a significant shift in angle of the same quadrant between pre-migration and migration, according to the Mann Whitney U rank test (*p<0.05, **p<0.01, q3: p=0.0058, q4: p=0.041, q8: p=0.024).*

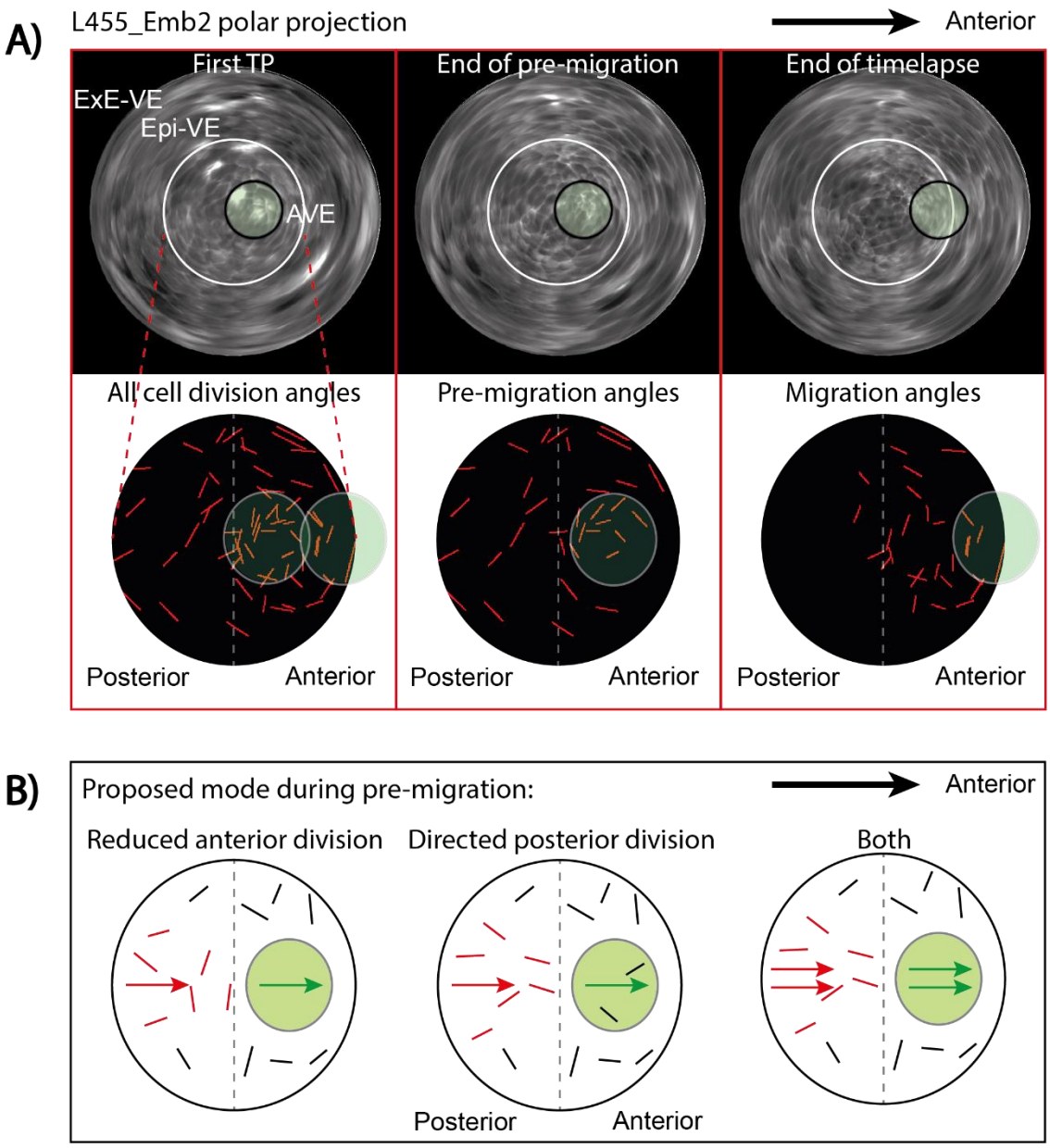

Figure 4-10: Angle divisions in the Epi-VE shown for L455_Emb2 in the polar projection. A) The angles are plotted on zoomed in sections, with posterior to the left and anterior to the right. B) If divisions were 'nudging' the AVE towards the anterior, you would expect either reduced anterior division pre-migration, more direction posterior divisions in pre-migration, or a combination of the two. Neither of these is seen in A). The AVE is denoted by a green circle.

4.4.4 Cells in the VE monolayer can divide along their apical-basal axis

The high proportion of cell divisions missed, as shown in the estimated errors in *Table 4-4*, particularly in embryos L455_Emb3 and L505, was concerning. During manual annotations, I noticed cases where cells showed characteristic rounding and burst of actin intensity, but no division. Additionally, a number of cells appeared to divide asymmetrically, with daughter cells showing different apical surface areas. However, upon close examination of the 3D z-sections, it became clear that small numbers of cells were dividing perpendicular to the VE epithelium, with a cell forming above or below another, in both the Epi-VE and ExE-VE. Such cells are missed when counting from the surface projection as it covers only a single depth level.

In these cases, both daughter cells can be lost partially or entirely from the single depth projection, a phenomena I had previously attributed to cell death or blebbing. I identified this as a cause of rosette formation, as the cells previously surrounding the mother meet at the joining point between the two daughters. It is not known how long these cells remain out of frame, as they are difficult to follow, but theoretically they should appear in later frames as they settle back into the monolayer, and still be included in the overall cell count.

The similarity in manual counts between two researchers shown in Chapter 3 suggests the out of plane divisions account for a large degree of the difference between cells and divisions counted. The out of plane divisions will however have little to no effect on the measurement of cell density, which is independent of cell division count, relying only on the cell count. While cells may be out of plane for the timepoints chosen, a maximum of a few such cells could be expected over the whole embryo, making it unlikely to affect the results of the regional, VE proliferation analysis in Section 4.4.

4.5 Discussion

It has been theorised that the A-P axis and manifest asymmetries may exist prior to AVE migration (Smith, 1985; Yamamoto et al., 2004). I have analysed timelapse datasets of E5.5 embryos and investigated whether there are asymmetries in the tilt of the EPC, proliferation rates and angles pre and during migration, the effect of the migrating cells on the morphology of the epiblast beneath, and at the overall embryo shape. The emerging picture is of an active migration, with directed AVE movement, and widespread deformation across the epithelial sheet.

By measuring the angle of the EPC relative to A-P axis, I found clustering suggestive of a curved axis existing prior to migration. I found no indication that cell proliferation in the VE gives rise to the specific direction of AVE migration, and in two cases: the angle of cell division and the eccentricity of the epiblast, analysis suggests it is the AVE migration causing asymmetries, not being directed by them.

I have shown that the tilt of the EPC at E5.5 demonstrates similar bi-angle clustering relative to the AVE migration direction to that observed at E6.5 (Gardner et al., 1992). However, the clusters are more divergent than demonstrated in Gardner et al.'s study, with an average of 46° from the A-P axis.

As the embryo cultures normally between E5.5 and E6.5 without attachment to the uterine wall, the AVE migration is not reliant on signals from the uterine wall to initiate a direction. However, the cone angle at E6.5 and now at E5.5-E5.75 has shown bilateral clustering, and the earlier prerequisite for developing blastocysts *in vitro* to be attached to a culture substrate (reviewed in Tam, 2004) supports the notion that these orientations may have been imparted to the embryo earlier, and carried through from the asymmetric ICM as Smith suggested (Smith, 1985). There is no evidence in these timelapse studies to suggest this is not the case.

There was no indication eccentricity in the transverse section could predict the direction of AVE migration at E5.5. The measurements of eccentricity E5.5-E5.75 did show that the AVE aligns with the short axis of the epiblast over the course of migration. That this dynamic change in orientation coincides with AVE migration when the embryo is cultured unconstrained *in vitro* confirms the shift is not reliant on uterine signals.

This resulting alignment is coincident with flattening in the epiblast moving as the AVE migrates and suggests that the more columnar AVE cells compress the epiblast below. This would occur if the tension across the apical VE is greater than that at the basal membrane, which would be dependent on epiblast proliferation and cell compressibility. The lack of any consistent change in the epiblast shape nor any sign of VE asymmetry prior to migration also indicates the asymmetry in the epiblast is not acting as a directional cue to the AVE cells, but as no embryos in the dataset capture a perfectly symmetric AVE at the distal tip, I cannot rule this out.

However, any causal relationship between migration and changes in eccentricity in the epiblast cannot be definitively proved without intervention experiments. The role of biomechanical forces is difficult to address, without a way to measure the forces on and exerted by the epiblast and how this is affected by cavity frequent abnormal cavity expansion. It is likely that the embryos without abnormally expanded cavities are the best representation of *in vivo* behaviour, but that only applies to 2/8 embryos here which were imaged pre-migration.

The overall picture of proliferation given using high time resolution data is one of highly stochastic divisions, clustering spatial and temporally, in agreement with Stuckey *et al.*, 2011; Shioi *et al.*, 2017. Around 50-70% of the cells in the embryo divide across the timelapse, but this still leaves room for differences to arise naturally in the timing of proliferation between the quadrants, particularly as cells from the same mother will have a similar cell cycle and likely to be located close to each other, leading to clusters of divisions regionalised both spatially and temporally. This clustering observation is in line with that of Shioi *et al.*, 2017, who noted half of all daughter cells

divided with 30mins of each other (average 2.0 ± 2.4hours, N=110), and continued to localise close together. They did not capture pre-migration, but found no significant differences in cell cycle between regions between E5.5 and E6.5, with an average length across the VE of approximately 11hours.

The 2D projection had distinct advantages in terms of ease of annotation and measuring in-plane cell division angles. The cell divisions were easy to identify with a single frame time resolution, exhibiting characteristic shape changes and bursts of bright actin. However the number of cells also needs to be counted for each frame in order to give an accurate rate of cell division to allow comparison between quadrants with different numbers of cells which is impractical to do manually. The ability to combine this process with automated tracking would be a major improvement over using the average number of cells to normalise the migration phase.

The presence of out of plane cell divisions is contrary to the assumption the VE maintains an intact monolayer throughout AVE migration. Out-of-plane or near out-of-plane divisions perpendicular to the can be mistaken on the projection as a cell death, or apical actin. One could assume out of plane divisions are equally likely to occur in any region. However, the VE is not homogeneous during AVE induction and migration. I have shown both that cells in the posterior get very thinly stretched, which suggests out-of-plane divisions are unlikely in that region. Whereas I noted the out of plane divisions can cause rosette formation, I would suggest this is not consequential in regions around the AVE undergoing deformation, but for example, could cause one in the posterior or ExE-VE.

Overall, the differences between the cell counts and division counts are only a small proportion of the total divisions identified, and that number also includes any human error. By using the additional measure of cell density to show decreasing density in the posterior overall, and lower relative density compared to the anterior, I can conclude the effects of out of plane divisions are unlikely to have an effect on the conclusions drawn. With these caveats, I have found no evidence

to support the notion that AVE migration is initiated or driven by asymmetric proliferation in the VE between the anterior and posterior quadrants.

As with analysis by Stuckey et al., 2011, a left or right bias was identified in proliferation data for the later Epi-VE quadrants of 3/4 embryos. However, it was neither statistically significant between quadrants, nor consistent to one side of the embryo, thus a larger sample would be needed to test this. Stuckey speculated the corresponding bias also seen in the epiblast could contribute to the change in long axis of the embryo between E5.5 and E6.5, which would not require a consistent left or right increase: an increase in a single side would potentially cause the shift if it continued after the end of migration. There is also the possibility that asymmetric lateral proliferation causes a left-right bias in post-migration AVE movement, as identified in the previous chapter. This could be investigation further by checking the individual correlations within each embryo, but would require a larger dataset including more migration and post-migration frames, whereas the focus here was more towards pre-migration.

Being able to observe cell shape changes with the *Lifeact* line allowed me to accurately measure the angle of cell divisions for the first time. I found an absence of cells in the posterior Epi-VE dividing concertedly along the anterior-posterior axis prior to migration, suggesting this also plays no role in initiating or sustaining migration. However, the angles of cell division do appear non-random, and shift towards the sheet deformation over time, which warrants further investigation.

Although this relationship with sheet deformation does emerge in pre-migration in the two embryos with more pre-migration cell divisions, viewing them in the epithelial sheet gives no indication they are ordered enough to provide a cue for any anterior movement: the numbers of cell divisions are so small the presence of asymmetric cell divisions would account for a very limited nudge even if they were all directing the AVE to the anterior in a temporally coordinated manner.

Chapter 5: General Discussion

This interdisciplinary study has allowed the most thorough characterisation of AVE migration in the mouse to date. Through the development of a novel data processing framework, and utilisation of both manual single cell and automatic superpixel analysis, a much clearer picture of AVE migration has emerged. In the following sections, I revisit and discuss some of the questions identified in my Introduction, in light of the conclusions from my results chapters, and explore future opportunities for continuing work.

5.1 Is the A-P axis defined prior to AVE migration?

In Chapter 4 I showed that the tilt of the ectoplacental cone (EPC) exhibits bi-angular clustering 46° off the A-P axis, which is approximately aligned with the A-P axis a day later (Gardner et al., 1992). I also showed the short axis of the epiblast transverse section rotates to align with the AVE over the course of migration, where it is known to remain until around E6.2, before shifting to the long axis (Mesnard et al., 2004; Aitana Perea-Gomez et al., 2004).

A shift was seen in the tilt of the EPC between my embryos dissected at around E5.5 and those E6.5 in Gardner's study. Although I have shown the EPC tilt does not change over the course of AVE migration, there is no indication it would not alter *in vivo*. It is tempting to speculate a mechanism exists *in vivo* which results in a shift in the EPC tilt concurrent with the changing eccentricity of the epiblast, which has not yet occurred in embryos dissected before migration. Such a mechanism would explain the systematic shift in alignment of the EPC with the A-P axis, and suggest the AVE is migrating to a previously specified anterior. However, not enough is currently known about the angle of the EPC *in utero*. At both E5.5 and E6.5, there are also embryos without an obvious EPC tilt, and the tilt of the EPC may be indicative of the asymmetry laid out in the Inner Cell Mass at the blastocyst stage, not consequential to it (Smith, 1985).

While compression of the anterior epiblast during migration is apparent, concurrent with the AVE aligning with the short-axis during migration, I cannot show a causative relationship between movement and surface shape without measurements of cell movement in the epiblast. It is also possible long axis lengthening is related to differing rates of proliferation in the lateral epiblast, as identified by Stuckey at E5.5, or cell sorting in the epiblast, as cells preferentially move towards those with similar nodal expression (Lu & Robertson, 2004). This may also be the case prior to migration, as Mesnard et al., 2004 show the embryo is more elliptical at E5.0. Perea-Gomez et al. found eccentricity existed in homozygous Nodal mutants in which the AVE failed to migrate (Perea-Gomez2004). However, as Mesnard et al. noted the embryo already shows asymmetry before AVE induction at E5.5, this may be leftover from the alignment with the uterine long axis. Viewing the changes in the Nodal mutant with timelapse data would indicate whether the changes in eccentricity occurred without migration, or if they were linked.

5.2 Do AVE cells migrate actively?

The MOSES superpixel tracking has shown in the cumulative distance graphs (Figure 3-2 and Figure 3-3) that AVE migration is not a steady process, but rather irregular, undergoing periods of little or very rapid movement. I have also been able to observe cellular protrusions extending from the leading edge of the AVE, which support and add to previous studies (I. Migeotte et al., 2011; Omelchenko et al., 2014; Srinivas et al., 2004; Trichas et al., 2011). The 'latching and pulling' behaviour of these protrusions, combined with the irregular migration, indicates an active migration.

Although further study of the projections is required to confirm this relationship, it is interesting to review the current literature for theories of how the active migration of a subset of cells can cause the tissue-wide deformation I have shown across the VE. The *in vivo* study of collective movement in a continuous epithelium, is less understood than the mechanisms of single cell or *in vitro* cell

motion, which are more easily studied (reviewed in Campàs 2016). Thus, a number of inferences must be drawn from the behaviour of monolayer epithelial cells in culture.

One model of epithelial migration proposes a few leading edge cells exhibit structural and functional differences which specialise them for pulling, such as exhibiting cellular protrusions, but this has fallen out of favour. Instead of this individual model cell movement, there is building evidence for collective migration involving cooperative transmission of forces between cells through intercellular junctions, which seems more relevant to the tissue-wide deformation seen here (reviewed in Trepat and Fredberg 2011). Migeotte et al., 2010 showed cells in the posterior of the AVE group exhibit smaller protrusions, also a feature of the coherent migration shown in epithelial would healing (Farooqui & Fenteany, 2005). Traction Force Microscopy has shown that the same 'sub-marginal' cells behind the leading edge exhibit strong, but heterogeneous tractional forces (Trepat et al., 2009).

Although chemotaxis has been suggested as a guidance mechanism, and gradients in adhesion molecules have not been observed (Trichas et al., 2011), little attention has been given to the investigation of a stress gradient (durotaxis), which can require force transmission between cells (plithotaxis). Plithotaxis relies on cells being connected to others, in order for cells to migrate in the direction of principle stress, and seems a good candidate for the passive collective movement seemingly exhibited across the VE. Fibroblast cells in culture are known to generate stronger traction than those on softer substrates, and they will not migrate from a harder to a softer boundary (Lo, Wang, Dembo, & Wang, 2000). Lo et al. also showed this movement could be guided towards localised tension in the substrate.

Laser ablation experiments would provide insight into the mechanics of the epithelial sheet, as it can be used to infer the ratio of cell forces via the speed of the displacing vertex when paired with confocal microscopy (Rauzi & Lenne, 2011). Ablating cells proximal to the AVE, such that they might move laterally and make way for the migrating cells may have implications for the speed of

migration. Additional ablation between the leading edge cells and the second wave behind may indicate the degree of active migration involved in the second wave, independent of pulling from the leading edge.

Calcium chelation or anti-CADHERIN antibodies could also be candidates to show whether the AVE requires strong adhesion to surrounding cells in order to migrate (Tambe et al., 2011). Measurements of the stiffness of the proximal vs distal epiblast, and ExE vs proximal epiblast may indicate whether the AVE is moving up a stiffness gradient as opposed to, or in concert with, a chemoattractant, but these are difficult to obtain for the basal membrane. Recent advances in hydrogels of known elastic modulus and fluorescent beads have extended Traction Force Microscopy to 3D, allowing direct mapping of mechanical stress during convergent-extension in *Xenopus* (J. Zhou, Pal, Maiti, & Davidson, 2015). A highly elastic gel could potentially be used to measure changing stresses due to growth during migration in different regions of the embryo, without causing deformation (Leonavicius et al., 2018).

5.3 Is migration driven by asymmetric proliferation in the VE?

By manually identifying cell division events in the VE 2D projections, I have shown that AVE migration is not initiated or driven passively by relatively increased rates of cell division in the posterior. The 2D projected datasets have enabled the assessment of accurate position, timing, and angle of cell division across the entire epithelial sheet, and also precise staging of the datasets.

The cell proliferation analysis could be repeated with *Nodal* or *Cripto* mutants (crossed into a *Lifeact* background) which fail to migrate, or with a *Nodal* inhibitor to halt migration. Additionally, a novel mouse line has recently been reported which can inhibit cell divisions through inducible over-expression of P21 (Pu et al., 2020). If this were used in conjunction with novel *Cre*-reporter lines to restrict expression to the posterior or anterior VE then the role of cell division could be assessed. The alternative method for carrying out this experiment would be to use moving quadrants which

deform and follow the same starting cells over the timelapse. This would have the benefit of maintaining cells in their original quadrants, which I would expect to show clearer distinctions in behaviour between regions, particularly between the Epi-VE and ExE-VE.

The task of manually identifying and following out-of-plane divisions in the 3D embryo timelapse is cumbersome, as they can only be seen in the middle of the stack. Even in BigDataViewer, this is impractical due to the rendering time required between frames. An added difficulty is identifying which of the potential candidates found in the stack is then missing from the projection. Such a task would be more suited to an automated 3D segmentation method, which would also be required for tracking the epiblast as they undergo interkinetic nuclear-like migration.

The alignment of cell division angle with the MOSES mesh deformations is striking during migration, but needs further study in polar projections to correlate the orientations with AVE movement before definitive conclusions can be drawn.

Regional alignment of cell division axes is an infrequently studied phenomena in mice *in vivo*, but oriented division is known to play an important role in morphogenesis, wound healing, and tumorigenesis (reviewed in Yang et al. 2015), particularly in response to mechanical forces (reviewed in Nestor-Bergmann, Goddard, and Woolner 2014).

The division axis strongly aligns with directed flow in epithelial sheets *in vitro* (Marel, Podewitz, Zorn, Rädler, & Elgeti, 2014), although this correlation may be aligned with the long axis and indirectly aligned with stress in the absence of neighbour exchange (Wyatt et al., 2015). Oriented cell division along lines of maximal tension has also been shown in plants (Louveaux, Julien, Mirabet, Boudaoud, & Hamant, 2016). The orientation of the mitotic spindle in the *Drosophila* wing imaginal disc, an embryonic epithelial structure, is correlated with morphology in the corresponding adult organs (Baena-López, Baonza, & García-Bellido, 2005). The orientation is parallel to lines of stress (LeGoff, Rouault, & Lecuit, 2013; Y. Mao et al., 2011), but not required for the normal organogenesis, as additional cell behaviours compensate (Z. Zhou, Alégot, & Irvine,

2019). Oriented division is necessary for tissue elongation in the *Drosophila* germband, but does not require the PCP-pathway component Dishevelled (Silva & Vincent, 2007), as in the case in *Xenopus* neural tube closure (Kieserman & Wallingford, 2009). In Zebrafish, it requires *Frizzled-7* components of the non-canonical Wnt/PCP signalling pathway (Quesada-Hernández et al., 2010).

This tendency for the orientation of cell division to be aligned with the long axis of a cell is known as Hertwig's Rule, and has been applied to great effect in the automatic tracking algorithm to identify cell divisions, suggesting it may be generally followed during AVE migration. However, it is difficult to decouple causative effects of cell shape on division orientation, and the possibility both cell shape and division orientation are aligning to the same tension forces. Tissue tension and not cell shape has been shown to determine the division angle in *Drosophila* follicular epithelium, which suggested the planar positioning was dependent on apical cortical tension (Finegan et al., 2019), and HeLa cells have been shown to divide along the axis of applied stretch, not the long axis of the cell (Fink et al., 2011).

It is tempting to suggest that the mitotic spindles of the cells are aligning along axes of stress as the sheet is placed under tension during the AVE migration. The radial pattern of the angles suggests they are not responding to a chemoattractant. The posterior cells are very flat in section, which combined with the angle of cell division, would explain the ability of the epithelial sheet to allow collective cell movement and to cope with the deformation during AVE migration. Laser ablation experiments or studies of the orientation angles in embryos mutant for *Dvl2* or *Frizzled* could help to ascertain the involvement of PCP signalling.

The non-random pattern of division angles was also apparent in two embryos which showed a high number of cell divisions pre-migration, which may have been a response to the columnarity of the inducing AVE cells. Embryo manipulation experiments such as micropipette aspiration could also show whether cells orient around induced stretch (Chaigne et al., 2013), although an easier starting point could involve *in vitro* studies of plated embryonic stem cells.

It is not clear from this dataset whether the AVE cell population is induced asymmetrically or symmetrically at the distal tip. In all embryos with pre-migration captured, the AVE was already leaning towards the prospective anterior, giving the possibility a directional cue has already occurred, either by epiblast shape change, cell proliferation, or transmigration. While we now have the tools to investigate whether AVE cells are induced asymmetrically, an earlier dataset would help to determine these points.

5.4 Do cells in the epiblast coordinate movement with those in the VE or AVE?

Using this pipeline it was possible to visualise the entire epiblast at the Epi/VE interface for the first time. While I have shown that the epiblast cells do not exhibit the bilateral whirls of the VE or the similar movements of the chick epiblast during migration, they do show localised directional motion. The motion of the epiblast cells during migration could be a manifestation of dynamic heterogeneity, wherein faster and slower cells group into cooperative clusters, and reduce their movement once they reach a certain density (Garrahan, 2011). Such a model could explain the reduction in movement seen later in E6.5 (Williams et al., 2012).

The possibility of non-random epiblast movement in response to a NODAL gradient has been suggested (Lu and Robertson 2004), and it would interesting to see whether or not this movement occurs in embryos cultured in a *Nodal* inhibitor such as SB-431542, or the embryos mutant for *Nodal* co-receptor *Cripto* (Stuckey et al. 2011). The lack of coordinated movement between the AVE and epiblast during migration, or of similar patterns between embryos, suggests the movement of epiblast cells does not play a direct part during AVE migration.

5.5 Does epiblast to VE transmigration occur?

It has been suggested that the AVE at least partially consists of epiblast cells transmigrating into the VE at the distal tip, due to the greater mechanical constraints there (Hiramatsu et al., 2013;

Matsuo & Hiramatsu, 2017). Despite a dataset of 23 embryos with 5 and 10min time resolution, no cells were observed transmigrating from the epiblast to the VE, or vice versa. If this was a regular occurrence as reported in the *Sox2-Cre* studies, I would expect to have seen at least some instances of it, particularly as extensive analysis has taken place in 5 *Lifeact* embryos. Following epiblast cells in section, cells moving out of the plane of view can have the appearance of an intercalation event, but in each instance further investigation found the cell in its original tissue. This is especially true when cells divide perpendicular to the basal lamina and take several frames to settle back into the monolayer structure.

This is the second timelapse study which has not seen evidence of transmigration, the first being Shioi et al., 2017. As the dataset does not capture inducing AVE cells, the possibility that transmigration does causes the induction of AVE cells as Hiramatsu et al., 2013 suggested cannot be excluded. Imaging earlier *Lifeact* embryos with a similar time resolution could clarify this, but such as experiment would have to examine cells using full 3D approach to avoid mistaking out-of-plane cell divisions in the VE for transmigrating epiblast cells.

5.6 Automating segmentation and cell tracking

In collaboration with Dr Felix Zhou and Siu Lun Yeung, we are developing automated approaches to segment and track cells in the Cartesian 2D VE projection. Both the automated segmentation and tracking have shown considerable success on a challenging dataset. The convolutional neural network approach used for cell segmentation provides an alternative to better quality imaging, in place of timelapse acquisition with more angles or with higher laser power, which would sacrifice the health of the embryo at this delicate stage due to an increased phototoxic load. Use of a Multi-View Light Sheet would help increase image quality, but would still require registration, automatic segmentation and tracking for large scale quantitative analysis.

The ongoing work to automate the segmentation and tracking of cells could potentially carry out the equivalent of thousands of hours of manual annotations in a matter of minutes. Combined with the 2D surface projections, they would give us the ability to extract quantitative measures such as shape, surface area, neighbour interactions, and migratory movements from individual cells. Once trained, the CNN can be applied to unseen datasets with similar fluorescence, and has already shown success in picking up epiblast cells, and those in the polar projection that it has not been specifically trained on. I would expect this data-driven approach to work well on any dataset with membrane fluorescence and sufficient signal-to-noise ratio. Additionally, I have shown that a CNN trained on datasets from two researchers independently is more robust than either one when dealing with these difficult datasets, reducing variability in addition to saving time.

Although the CNN works well with the epiblast fluorescence, we cannot track epiblast cells in 2D surface projections for more than a few frames using the current method. The heuristics are very different for a highly motile body of cells which undergoes INM-like divisions, causing large numbers of cells to leave the plane of view. A more practical solution would be to extend the CNN to 3D by applying it to the stacks of the embryo, and then building up cell volumes. The 3D segmentation could then potentially be tracked using nearest neighbour assignment and manual curation. This would also require more computing power, as projecting the embryo surface in 2D dramatically reduced the size of a timelapse dataset.

5.7 Implications of methods development for future experiments

The option of using the commercially available Ziess Z1 lightsheet microscope, combined with robust registration software and artificial image enhancement approach using a carefully trained CNN, makes high resolution timelapse imaging more accessible to groups without the resources to build their own SiMView microscopes. However, all aspects of the data processing framework and analysis can also be applied to higher quality SiMView datasets.

While the *mTmG ; Ttr-Cre* line was initially used for the prospect of digitally separating the VE and epiblast layers, the 2D projection of both surface layers has rendered this unnecessary. We were still able to employ the dataset in many aspects of the analysis, including MOSES superpixel tracking and measurements of embryonic shape change. The *mTmG ; Hex-GFP* line has been additionally useful for investigating the behaviour of *Hex-GFP* positive AVE cells compared to the rest of the VE, using both the classifier and viewing the migration of cells past the boundary. The *Lifeact* line has perhaps proved the most useful, providing the ability to delineate individual cells for manual cell tracking and shape observations, and regional analysis of cell divisions and division angles.

An ideal imaging set up would employ simultaneous multiview imaging, with a novel *Lifeact-GFP x Hex-CFP* mouse line to both delineate cells and identify the AVE, with the ability to identify protrusions in both lines. Being able to image multiple angles simultaneously would reduce the phototoxic load by half, allowing a higher resolution temporal or spatial acquisition for more detailed investigations of cellular protrusions using both lines. There is also potential to include a HISTONE-2B-RFP nuclei marker (Abe et al., 2011), but the success of the automatic segmentation has shown this is not necessary for automatic segmentation and tracking, and combining three markers will come at a cost of time resolution or reduced exposure.

5.8 Conclusion

The development of a new data processing framework to spatially and temporally register data has enabled a close and detailed analysis of the E5.5 embryo, including dynamic shape changes which occur during migration. The ability to remove the drift and rotation of the samples has made a larger pool of embryos available which may previously have been discarded due to the difficulty involved in analysing such a timelapse. Normalising the growth of the embryo has also allowed the most accurate depiction of relative cell movement to date, without losing the original measures such as real cell density over time. The ability to spatially register angles has also allowed for

analysis of the full embryo, not restricting it to a single angle or plane of view. Analysis of the VE monolayer has been made vastly easier by Cartesian and polar projections of the VE surface and has helped facilitate the first comprehensive tracking of cells in the entire sheet. Projecting the epiblast has also allowed the cellular movement at the interface to be analysed at E5.5 for the first time.

Together, these approaches have led to the most complete picture of AVE migration so far: one of active migration and large-scale tissue deformation, with indications of a pre-defined A-P axis, specified independent of cell proliferation.

The majority of the temporal analysis (Chapters 3 and 4) were only possible with registered data, and manual annotations were made quicker and simpler by using the 2D Cartesian and polar projections. However, many questions still remain.

The ongoing work on automated cell segmentation and tracking in 2D would allow the time resolution of the dataset to be fully taken advantage of, and give a truly dynamic picture of AVE migration in a greater number of embryos including extensive cellular properties such as shape change and neighbour exchange. The further extension to 3D would allow additional volumetric measures to be incorporated into the analysis, such as cellular volume asymmetries, and the rate of proliferation in the epiblast, enabling a complete 4D atlas of the motion and behaviours of cells in both tissues during epithelial morphogenesis.

References

Abe, T., Kiyonari, H., Shioi, G., Inoue, K. I., Nakao, K., Aizawa, S., & Fujimori, T. (2011). Establishment of conditional reporter mouse lines at ROSA26 locus for live cell imaging. *Genesis*, *49*(7), 579–590. https://doi.org/10.1002/dvg.20753

Amat, F., Lemon, W., Mossing, D. P., McDole, K., Wan, Y., Branson, K., … Keller, P. J. (2014). Fast, accurate reconstruction of cell lineages from large-scale fluorescence microscopy data. *Nature Methods*, *11*(9), 951–958. https://doi.org/10.1038/nmeth.3036

Antonica, F., Orietti, L. C., Mort, R. L., & Zernicka-Goetz, M. (2019). Concerted cell divisions in embryonic visceral endoderm guide anterior visceral endoderm migration. *Developmental Biology*, *450*(2), 132–140. https://doi.org/10.1016/j.ydbio.2019.03.016

Avilion, A. A., Nicolis, S. K., Pevny, L. H., Perez, L., Vivian, N., & Lovell-Badge, R. (2003). Multipotent cell lineages in early mouse development depend on SOX2 function. *Genes and Development*, *17*(1), 126–140. https://doi.org/10.1101/gad.224503

Baena-López, L. A., Baonza, A., & García-Bellido, A. (2005). The orientation of cell divisions determines the shape of Drosophila organs. *Current Biology*, *15*(18), 1640–1644. https://doi.org/10.1016/j.cub.2005.07.062

Bai, M., & Urtasun, R. (2017). Deep watershed transform for instance segmentation. In *Proceedings - 30th IEEE Conference on Computer Vision and Pattern Recognition, CVPR 2017* (Vol. 2017-Janua, pp. 2858–2866). IEEE. https://doi.org/10.1109/CVPR.2017.305

Bar-Shalom, Y., Daum, F., & Huang, J. (2009). The Probabilistic Data Association Filter: Estimation in the presence of measurement origin uncertainty. *IEEE Control Systems*, *29*(6), 82–100. https://doi.org/10.1109/MCS.2009.934469

Bar-Shalom, Y., Li, X.-R., & Kirubarajan, T. (2002). *Estimation with Applications to Tracking and Navigation*. New York, USA: John Wiley & Sons, Inc. https://doi.org/10.1002/0471221279

Bartschat, A., Hübner, E., Reischl, M., Mikut, R., & Stegmaier, J. (2016). XPIWIT-an XML pipeline wrapper for the Insight Toolkit. *Bioinformatics (Oxford, England)*, *32*(2), 315–317. https://doi.org/10.1093/bioinformatics/btv559

Bassalert, C., Valverde-Estrella, L., & Chazaud, C. (2018). Primitive Endoderm Differentiation: From Specification to Epithelialization. *Current Topics in Developmental Biology*, *128*, 81–104. https://doi.org/10.1016/BS.CTDB.2017.12.001

Batten, B. E., & Haar, J. L. (1979). Fine structural differentiation of germ layers in the mouse at the time of mesoderm formation. *The Anatomical Record*, *194*(1), 125–141. https://doi.org/10.1002/ar.1091940109

Beck, S., Le Good, J. A., Guzman, M., Haim, N. Ben, Roy, K., Beermann, F., & Constam, D. B. (2002). Extraembryonic proteases regulate Nodal signalling during gastrulation. *Nature Cell Biology*, *4*(12), 981–985. https://doi.org/10.1038/ncb890

Bedzhov, I., Bialecka, M., Zielinska, A., Kosalka, J., Antonica, F., Thompson, A. J., … Zernicka-Goetz, M. (2015, December). Development of the anterior-posterior axis is a self-organizing process in the absence of maternal cues in the mouse embryo. *Cell Research*. Nature Publishing Group. https://doi.org/10.1038/cr.2015.104

Belo, J. A., Bachiller, D., Agius, E., Kemp, C., Borges, A. C., Marques, S., … De Robertis, E. M. (2000). Cerberus-like is a secreted BMP and nodal antagonist not essential for mouse development. *Genesis*, *26*(4), 265–270. https://doi.org/10.1002/(SICI)1526-968X(200004)26:4<265::AID-GENE80>3.0.CO;2-4

Belo, J. A., Bouwmeester, T., Leyns, L., Kertesz, N., Gallo, M., Follettie, M., & De Robertis, E. M. (1997). Cerberus-like is a secreted factor with neuralizing activity expressed in the anterior primitive endoderm of the mouse gastrula. *Mechanisms of Development*, *68*(1–2), 45–57. https://doi.org/10.1016/S0925-4773(97)00125-1

Blankenship, J. T., Backovic, S. T., Sanny, J. S. S. P., Weitz, O., & Zallen, J. A. (2006). Multicellular Rosette Formation Links Planar Cell Polarity to Tissue Morphogenesis. *Developmental Cell*, *11*(4), 459–470. https://doi.org/10.1016/j.devcel.2006.09.007

Bloomekatz, J., Grego-Bessa, J., Migeotte, I., & Anderson, K. V. (2012). Pten regulates collective cell migration during specification of the anterior-posterior axis of the mouse embryo. *Developmental Biology*, *364*(2), 192–201. https://doi.org/10.1016/j.ydbio.2012.02.005

Bompard, G., & Caron, E. (2004). Regulation of WASP/WAVE proteins: Making a long story short. *Journal of Cell Biology*, *166*(7), 957–962. https://doi.org/10.1083/jcb.200403127

Bouwmeester, T., Kim, S. H., Sasai, Y., Lu, B., & De Robertis, E. M. (1996). Cerberus is a head-inducing secreted factor expressed in the anterior endoderm of Spemann's organizer. *Nature*, *382*(6592), 595–601. https://doi.org/10.1038/382595a0

Brennan, J., Lu, C. C., Norris, D. P., Rodriguez, T. A., Beddington, R. S. P., & Robertson, E. J. (2001). Nodal signalling in the epiblast patterns the early mouse embryo. *Nature*, *411*(6840), 965–969. https://doi.org/10.1038/35082103

Brennan, J., Norris, D. P., & Robertson, E. J. (2002). Nodal activity in the node governs left-right asymmetry. *Genes and Development*, *16*(18), 2339–2344. https://doi.org/10.1101/gad.1016202

Cai, H., & Devreotes, P. N. (2011). Moving in the right direction: how eukaryotic cells migrate along chemical gradients. *Seminars in Cell & Developmental Biology*, *22*(8), 834–841. https://doi.org/10.1016/j.semcdb.2011.07.020

Campàs, O. (2016). A toolbox to explore the mechanics of living embryonic tissues. *Seminars in Cell & Developmental Biology*, *55*, 119. https://doi.org/10.1016/J.SEMCDB.2016.03.011

Carreira-Barbosa, F., Kajita, M., Kajita, M., Morel, V., Wada, H., Okamoto, H., … Tada, M. (2009). Flamingo regulates epiboly and convergence/extension movements through cell cohesive and signalling functions during zebrafish gastrulation. *Development (Cambridge, England)*, *136*(3), 383–392. https://doi.org/10.1242/dev.026542

Cetera, M., Leybova, L., Joyce, B., & Devenport, D. (2018). Counter-rotational cell flows drive morphological and cell fate asymmetries in mammalian hair follicles. *Nature Cell Biology*, *20*(5), 541–552. https://doi.org/10.1038/s41556-018-0082-7

Chaigne, A., Campillo, C., Gov, N. S., Voituriez, R., Azoury, J., Umaña-Diaz, C., … Terret, M.-E. (2013). A soft cortex is essential for asymmetric spindle positioning in mouse oocytes. *Nature Cell Biology*, *15*(8), 958–966. https://doi.org/10.1038/ncb2799

Chazaud, C., & Rossant, J. (2006). Disruption of early proximodistal patterning and AVE formation in Apc mutants. *Development*, *133*(17), 3379–3387. https://doi.org/10.1242/dev.02523

Chen, C., & Shen, M. M. (2004). Two modes by which lefty proteins inhibit nodal signaling. *Current*

Biology, *14*(7), 618–624. https://doi.org/10.1016/j.cub.2004.02.042

Chu, G. C., Dunn, N. R., Anderson, D. C., Oxburgh, L., & Robertson, E. J. (2004). Differential requirements for Smad4 in TGFβ-dependent patterning of the early mouse embryo. *Development*, *131*(15), 3501–3512. https://doi.org/10.1242/dev.01248

Ciregan, D., Meier, U., & Schmidhuber, J. (2012). Multi-column deep neural networks for image classification. In *Proceedings of the IEEE Computer Society Conference on Computer Vision and Pattern Recognition* (pp. 3642–3649). IEEE. https://doi.org/10.1109/CVPR.2012.6248110

Clements, M., Pernaute, B., Vella, F., & Rodriguez, T. A. (2011). Crosstalk between Nodal/activin and MAPK p38 signaling is essential for anterior-posterior axis specification. *Current Biology*, *21*(15), 1289–1295. https://doi.org/10.1016/j.cub.2011.06.048

Conlon, F. L., Lyons, K. M., Takaesu, N., Barth, K. S., Kispert, A., Herrmann, B., & Robertson, E. J. (1994). A primary requirement for nodal in the formation and maintenance of the primitive streak in the mouse. *Development*, *120*(7), 1919–1928. https://doi.org/10.1016/0168-9525(94)90026-4

Constam, D. B., & Robertson, E. J. (1999). Regulation of bone morphogenetic protein activity by pro domains and proprotein convertases. *Journal of Cell Biology*, *144*(1), 139–149. https://doi.org/10.1083/jcb.144.1.139

Cordelières, F. (2005). Manual Tracking, a plug-in for ImageJ software. Institut Curie, Orsay, France.

Cortes, C., & Vapnik, V. (1995). Support-vector networks. *Machine Learning*, *20*(3), 273–297. https://doi.org/10.1007/bf00994018

Crompton, L. A., Du Roure, C., & Rodriguez, T. A. (2007). Early embryonic expression patterns of the mouse Flamingo and Prickle orthologues. *Developmental Dynamics*, *236*(11), 3137–3143. https://doi.org/10.1002/dvdy.21338

Dattani, M. T., Martinez-Barbera, J. P., Thomas, P. Q., Brickman, J. M., Gupta, R., Mårtensson, I. L., … Robinson, I. C. A. F. (1998). Mutations in the homeobox gene HESX1/Hesx1 associated with septo-optic dysplasia in human and mouse. *Nature Genetics*, *19*(2), 125–133. https://doi.org/10.1038/477

Desai, R., Sarpal, R., Ishiyama, N., Pellikka, M., Ikura, M., & Tepass, U. (2013). Monomeric α-catenin links cadherin to the actin cytoskeleton. *Nature Cell Biology*, *15*(3), 261–273. https://doi.org/10.1038/ncb2685

Ding, J., Yang, L., Yan, Y. T., Chen, A., Desai, N., Wynshaw-Boris, A., & Shen, M. M. (1998). Cripto is required for correct orientation of the anterior-posterior axis in the mouse embryo. *Nature*, *395*(6703), 702–707. https://doi.org/10.1038/27215

Dutta, A., & Zisserman, A. (2019). The VIA Annotation Software for Images, Audio and Video. In *Proceedings of the 27th ACM International Conference on Multimedia* (pp. 2276–2279). New York, NY, USA: ACM. https://doi.org/10.1145/3343031.3350535

Farooqui, R., & Fenteany, G. (2005). Multiple rows of cells behind an epithelial wound edge extend cryptic lamellipodia to collectively drive cell-sheet movement. *Journal of Cell Science*, *118*(1), 51–63. https://doi.org/10.1242/JCS.01577

Faure, E., Savy, T., Rizzi, B., Melani, C., Stašová, O., Fabrèges, D., … Bourgine, P. (2016). A workflow to process 3D+time microscopy images of developing organisms and reconstruct their cell lineage. *Nature Communications*, *7*(1), 8674. https://doi.org/10.1038/ncomms9674

Fernandez, R., Das, P., Mirabet, V., Moscardi, E., Traas, J., Verdeil, J. L., … Godin, C. (2010). Imaging

plant growth in 4D: Robust tissue reconstruction and lineaging at cell resolution. *Nature Methods*, *7*(7), 547–553. https://doi.org/10.1038/nmeth.1472

Ferrer-Vaquer, A., Piliszek, A., Tian, G., Aho, R. J., Dufort, D., & Hadjantonakis, A. K. (2010). A sensitive and bright single-cell resolution live imaging reporter of Wnt/-catenin signaling in the mouse. *BMC Developmental Biology*, *10*. https://doi.org/10.1186/1471-213X-10-121

Finegan, T. M., Na, D., Cammarota, C., Skeeters, A. V, Nádasi, T. J., Dawney, N. S., … Bergstralh, D. T. (2019). Tissue tension and not interphase cell shape determines cell division orientation in the Drosophila follicular epithelium. *The EMBO Journal*, *38*(3). https://doi.org/10.15252/embj.2018100072

Fink, J., Carpi, N., Betz, T., Bétard, A., Chebah, M., Azioune, A., … Piel, M. (2011). External forces control mitotic spindle positioning. *Nature Cell Biology*, *13*(7), 771–778. https://doi.org/10.1038/ncb2269

Fleming, T. P. (1987). A quantitative analysis of cell allocation to trophectoderm and inner cell mass in the mouse blastocyst. *Developmental Biology*, *119*(2), 520–531. https://doi.org/10.1016/0012-1606(87)90055-8

Foley, A. C., Skromne, I., & Stern, C. D. (2000). Reconciling different models of forebrain induction and patterning: A dual role for the hypoblast. *Development*, *127*(17), 3839–3854. Retrieved from http://www.ncbi.nlm.nih.gov/pubmed/10934028

Gardner, R. L., Meredith, M. R., & Altman, D. G. (1992). Is the anterior-posterior axis of the fetus specified before implantation in the mouse? *Journal of Experimental Zoology*, *264*(4), 437–443. https://doi.org/10.1002/jez.1402640409

Gardner, R. L., & Rossant, J. (1979). Investigation of the fate of 4.5 day post-coitum mouse inner cell mass cells by blastocyst injection. *Journal of Embryology and Experimental Morphology*, *Vol 52*(1), 141–152.

Garrahan, J. P. (2011). Dynamic heterogeneity comes to life. *Proceedings of the National Academy of Sciences*, *108*(12), 4701–4702. https://doi.org/10.1073/pnas.1101436108

Goldin, S. N., & Papaioannou, V. E. (2003). Paracrine action of FGF4 during periimplantation development maintains trophectoderm and primitive endoderm. *Genesis*, *36*(1), 40–47. https://doi.org/10.1002/gene.10192

Gräper, L. (1929). Die Primitiventwicklung des Hünchens nach stereokinematographischen Untersuchungen, kontrolliert durch vitale Farbmarkierung und verglichen mit der Entwicklung anderer Wirbeltiere. *Arch. EntwMech. Org.*, *116*, 382–429.

Harrison, S. M., Dunwoodie, S. L., Arkell, R. M., Lehrach, H., & Beddington, R. S. P. (1995). Isolation of novel tissue-specific genes from cDNA libraries representing the individual tissue constituents of the gastrulating mouse embryo. *Development*, *121*(8), 2479–2489.

Heemskerk, I., & Streichan, S. J. (2015). Tissue cartography: Compressing bio-image data by dimensional reduction. *Nature Methods*, *12*(12), 1139–1142. https://doi.org/10.1038/nmeth.3648

Hiramatsu, R., Matsuoka, T., Kimura-Yoshida, C., Han, S. W., Mochida, K., Adachi, T., … Matsuo, I. (2013). External mechanical cues trigger the establishment of the anterior-posterior axis in early mouse embryos. *Developmental Cell*, *27*(2), 131–144. https://doi.org/10.1016/j.devcel.2013.09.026

Hoshino, H., Shioi, G., & Aizawa, S. (2015). AVE protein expression and visceral endoderm cell

behavior during anterior-posterior axis formation in mouse embryos: Asymmetry in OTX2 and DKK1 expression. *Developmental Biology*, *402*(2), 175–191. https://doi.org/10.1016/j.ydbio.2015.03.023

Huelsken, J., Vogel, R., Brinkmann, V., Erdmann, B., Birchmeier, C., & Birchmeier, W. (2000). Requirement for β-catenin in anterior-posterior axis formation in mice. *Journal of Cell Biology*, *148*(3), 567–578. https://doi.org/10.1083/jcb.148.3.567

Ichikawa, T., Nakazato, K., Keller, P. J., Kajiura-Kobayashi, H., Stelzer, E. H. K., Mochizuki, A., & Nonaka, S. (2013). Live Imaging of Whole Mouse Embryos during Gastrulation: Migration Analyses of Epiblast and Mesodermal Cells. *PLoS ONE*, *8*(7), e64506. https://doi.org/10.1371/journal.pone.0064506

Iizuka, R., Yamagishi-Shirasaki, M., & Funatsu, T. (2011). Kinetic study of de novo chromophore maturation of fluorescent proteins. *Analytical Biochemistry*, *414*(2), 173–178. https://doi.org/10.1016/j.ab.2011.03.036

Johnson, M. H., & Ziomek, C. A. (1981). The foundation of two distinct cell lineages within the mouse morula. *Cell*, *24*(1), 71–80. https://doi.org/10.1016/0092-8674(81)90502-X

Keller, P. J., Schmidt, A. D., Wittbrodt, J., & Stelzer, E. H. K. (2008). Reconstruction of zebrafish early embryonic development by scanned light sheet microscopy. *Science (New York, N.Y.)*, *322*(5904), 1065–1069. https://doi.org/10.1126/science.1162493

Keller, P. J., & Stelzer, E. H. (2008). Quantitative in vivo imaging of entire embryos with Digital Scanned Laser Light Sheet Fluorescence Microscopy. *Current Opinion in Neurobiology*, *18*(6), 624–632. https://doi.org/10.1016/j.conb.2009.03.008

Kendall, A., Gal, Y., & Cipolla, R. (2018). Multi-task Learning Using Uncertainty to Weigh Losses for Scene Geometry and Semantics. In *Proceedings of the IEEE Computer Society Conference on Computer Vision and Pattern Recognition* (pp. 7482–7491). IEEE. https://doi.org/10.1109/CVPR.2018.00781

Khan, Z., Wang, Y. C., Wieschaus, E. F., & Kaschube, M. (2014). Quantitative 4D analyses of epithelial folding during Drosophila gastrulation. *Development (Cambridge)*, *141*(14), 2895–2900. https://doi.org/10.1242/dev.107730

Kieserman, E. K., & Wallingford, J. B. (2009). In vivo imaging reveals a role for Cdc42 in spindle positioning and planar orientation of cell divisions during vertebrate neural tube closure. *Journal of Cell Science*, *122*(14), 2481–2490. https://doi.org/10.1242/JCS.042135

Kimura-Yoshida, C., Nakano, H., Okamura, D., Nakao, K., Yonemura, S., Belo, J. A., … Matsuo, I. (2005). Canonical Wnt signaling and its antagonist regulate anterior-posterior axis polarization by guiding cell migration in mouse visceral endoderm. *Developmental Cell*, *9*(5), 639–650. https://doi.org/10.1016/j.devcel.2005.09.011

Kimura, C., Yoshinaga, K., Tian, E., Suzuki, M., Aizawa, S., & Matsuo, I. (2000). Visceral endoderm mediates forebrain development by suppressing posteriorizing signals. *Developmental Biology*, *225*(2), 304–321. https://doi.org/10.1006/dbio.2000.9835

Krndija, D., Marjou, F. El, Guirao, B., Richon, S., Leroy, O., Bellaiche, Y., … Vignjevic, D. M. (2019). Active cell migration is critical for steady-state epithelial turnover in the gut. *Science*, *365*(6454), 705–710. https://doi.org/10.1126/science.aau3429

Krzic, U., Gunther, S., Saunders, T. E., Streichan, S. J., & Hufnagel, L. (2012). Multiview light-sheet microscope for rapid in toto imaging. *Nature Methods*, *9*(7), 730–733. https://doi.org/10.1038/nmeth.2064

Kwon, G. S., & Hadjantonakis, A.-K. (2009). Transthyretin mouse transgenes direct RFP expression or Cre-mediated recombination throughout the visceral endoderm. *Genesis*, *47*(7), 447–455. https://doi.org/10.1002/dvg.20522

Kwon, G. S., Viotti, M., & Hadjantonakis, A. K. (2008). The Endoderm of the Mouse Embryo Arises by Dynamic Widespread Intercalation of Embryonic and Extraembryonic Lineages. *Developmental Cell*, *15*(4), 509–520. https://doi.org/10.1016/j.devcel.2008.07.017

Lawrence, S., Giles, C. L., Tsoi, A. C., & Back, A. D. (1997). Face recognition: A convolutional neural-network approach. *IEEE Transactions on Neural Networks*, *8*(1), 98–113. https://doi.org/10.1109/72.554195

LeCun, Y., Bottou, L., Bengio, Y., & Haffner, P. (1998). Gradient-based learning applied to document recognition. *Proceedings of the IEEE*, *86*(11), 2278–2323. https://doi.org/10.1109/5.726791

LeGoff, L., Rouault, H., & Lecuit, T. (2013). A global pattern of mechanical stress polarizes cell divisions and cell shape in the growing Drosophila wing disc. *Development (Cambridge)*, *140*(19), 4051–4059. https://doi.org/10.1242/dev.090878

Leonavicius, K., Royer, C., Preece, C., Davies, B., Biggins, J. S., & Srinivas, S. (2018). Mechanics of mouse blastocyst hatching revealed by a hydrogel-based microdeformation assay. *Proceedings of the National Academy of Sciences*, *115*(41), 10375–10380. https://doi.org/10.1073/PNAS.1719930115

Li, L., Zheng, P., & Dean, J. (2010). Maternal control of early mouse development. *Development*, *137*(6), 859–870. https://doi.org/10.1242/dev.039487

Lienkamp, S. S., Liu, K., Karner, C. M., Carroll, T. J., Ronneberger, O., Wallingford, J. B., & Walz, G. (2012). Vertebrate kidney tubules elongate using a planar cell polarity-dependent, rosette-based mechanism of convergent extension. *Nature Genetics*, *44*(12), 1382–1387. https://doi.org/10.1038/ng.2452

Lo, C. M., Wang, H. B., Dembo, M., & Wang, Y. L. (2000). Cell movement is guided by the rigidity of the substrate. *Biophysical Journal*, *79*(1), 144–152. https://doi.org/10.1016/S0006-3495(00)76279-5

Logan, C. Y., & Nusse, R. (2004). THE WNT SIGNALING PATHWAY IN DEVELOPMENT AND DISEASE. *Annual Review of Cell and Developmental Biology*, *20*(1), 781–810. https://doi.org/10.1146/annurev.cellbio.20.010403.113126

Long, J., Shelhamer, E., & Darrell, T. (2015). Fully convolutional networks for semantic segmentation. In *Proceedings of the IEEE Computer Society Conference on Computer Vision and Pattern Recognition* (Vol. 07-12-June, pp. 3431–3440). IEEE. https://doi.org/10.1109/CVPR.2015.7298965

Lou, X., Kang, M., Xenopoulos, P., Muñoz-Descalzo, S., & Hadjantonakis, A. K. (2014). A rapid and efficient 2D/3D nuclear segmentation method for analysis of early mouse embryo and stem cell image data. *Stem Cell Reports*, *2*(3), 382–397. https://doi.org/10.1016/j.stemcr.2014.01.010

Louveaux, M., Julien, J. D., Mirabet, V., Boudaoud, A., & Hamant, O. (2016). Cell division plane orientation based on tensile stress in Arabidopsis thaliana. *Proceedings of the National Academy of Sciences of the United States of America*, *113*(30), E4294–E4303. https://doi.org/10.1073/pnas.1600677113

Lu, C. C., & Robertson, E. J. (2004). Multiple roles for Nodal in the epiblast of the mouse embryo in the establishment of anterior-posterior patterning. *Developmental Biology*, *273*(1), 149–159.

https://doi.org/10.1016/j.ydbio.2004.06.004

Manning, B. D., & Cantley, L. C. (2007). AKT/PKB Signaling: Navigating Downstream. *Cell*, *129*(7), 1261–1274. https://doi.org/10.1016/j.cell.2007.06.009

Mao, B., Wu, W., Davidson, G., Marhold, J., Li, M., Mechler, B. M., … Niehrs, C. (2002). Kremen proteins are Dickkopf receptors that regulate Wnt/β-catenin signalling. *Nature*, *417*(6889), 664–667. https://doi.org/10.1038/nature756

Mao, Y., Tournier, A. L., Bates, P. A., Gale, J. E., Tapon, N., & Thompson, B. J. (2011). Planar polarization of the atypical myosin Dachs orients cell divisions in Drosophila. *Genes and Development*, *25*(2), 131–136. https://doi.org/10.1101/gad.610511

Marel, A. K., Podewitz, N., Zorn, M., Rädler, J. O., & Elgeti, J. (2014). Alignment of cell division axes in directed epithelial cell migration. *New Journal of Physics*, *16*(11), 115005. https://doi.org/10.1088/1367-2630/16/11/115005

Martin, A. C. (2010). Pulsation and stabilization: Contractile forces that underlie morphogenesis. *Developmental Biology*, *341*(1), 114–125. https://doi.org/10.1016/j.ydbio.2009.10.031

Martinez-Barbera, J P, & Beddington, R. S. P. (2001). Getting your head around Hex and Hesx1: Forebrain formation in mouse. *International Journal of Developmental Biology*, *45*(1), 327–336. https://doi.org/10.1387/ijdb.11291863

Martinez-Barbera, Juan Pedro, Rodriguez, T. A., & Beddington, R. S. P. (2000). The homeobox gene Hesx1 is required in the anterior neural ectoderm for normal forebrain formation. *Developmental Biology*, *223*(2), 422–430. https://doi.org/10.1006/dbio.2000.9757

Masuzzo, P., Van Troys, M., Ampe, C., & Martens, L. (2016). Taking Aim at Moving Targets in Computational Cell Migration. *Trends in Cell Biology*, *26*(2), 88–110. https://doi.org/10.1016/j.tcb.2015.09.003

Matsuo, I., & Hiramatsu, R. (2017). Mechanical perspectives on the anterior-posterior axis polarization of mouse implanted embryos. *Mechanisms of Development*. https://doi.org/10.1016/j.mod.2016.09.002

Mattes, D., Haynor, D. R., Vesselle, H., Lewellyn, T. K., & Eubank, W. (2001). Nonrigid multimodality image registration. In M. Sonka & K. M. Hanson (Eds.), *Medical Imaging 2001: Image Processing* (Vol. 4322, pp. 1609–1620). International Society for Optics and Photonics. https://doi.org/10.1117/12.431046

McCormick, M., Liu, X., Jomier, J., Marion, C., & Ibanez, L. (2014). ITK: enabling reproducible research and open science. *Frontiers in Neuroinformatics*, *8*, 13. https://doi.org/10.3389/fninf.2014.00013

McDole, K., Guignard, L., Amat, F., Berger, A., Malandain, G., Royer, L. A., … Keller, P. J. (2018). In Toto Imaging and Reconstruction of Post-Implantation Mouse Development at the Single-Cell Level. *Cell*, *175*(3), 859-876.e33. https://doi.org/10.1016/j.cell.2018.09.031

McDole, K., Xiong, Y., Iglesias, P. A., & Zheng, Y. (2011). Lineage mapping the pre-implantation mouse embryo by two-photon microscopy, new insights into the segregation of cell fates. *Developmental Biology*, *355*(2), 239–249. https://doi.org/10.1016/j.ydbio.2011.04.024

Meijering, E., Dzyubachyk, O., & Smal, I. (2012). Methods for cell and particle tracking. *Methods in Enzymology*, *504*, 183–200. https://doi.org/10.1016/B978-0-12-391857-4.00009-4

Meng, W., Mushika, Y., Ichii, T., & Takeichi, M. (2008). Anchorage of Microtubule Minus Ends to Adherens Junctions Regulates Epithelial Cell-Cell Contacts. *Cell*, *135*(5), 948–959.

https://doi.org/10.1016/j.cell.2008.09.040

Meno, C., Saijoh, Y., Fujii, H., Ikeda, M., Yokoyama, T., Yokoyama, M., … Hamada, H. (1996). Left-right asymmetric expression of the TGFβ-family member lefty in mouse embryos. *Nature*, *381*(6578), 151–155. https://doi.org/10.1038/381151a0

Meno, C., Shimono, A., Saijoh, Y., Yashiro, K., Mochida, K., Ohishi, S., … Hamada, H. (1998). lefty-1 is required for left-right determination as a regulator of lefty-2 and nodal. *Cell*, *94*(3), 287–297. https://doi.org/10.1016/S0092-8674(00)81472-5

Mesnard, D., Filipe, M., Belo, J. A., & Zernicka-Goetz, M. (2004). The Anterior-Posterior Axis Emerges Respecting the Morphology of the Mouse Embryo that Changes and Aligns with the Uterus before Gastrulation. *Current Biology*, *14*(3), 184–196. https://doi.org/10.1016/S0960-9822(04)00010-7

Mesnard, D., Guzman-Ayala, M., & Constam, D. B. (2006). Nodal specifies embryonic visceral endoderm and sustains pluripotent cells in the epiblast before overt axial patterning. *Development*, *133*(13), 2497–2505. https://doi.org/10.1242/dev.02413

Migeotte, I., Grego-Bessa, J., & Anderson, K. V. (2011). Rac1 mediates morphogenetic responses to intercellular signals in the gastrulating mouse embryo. *Development*. https://doi.org/10.1242/dev.059766

Migeotte, Isabelle, Omelchenko, T., Hall, A., & Anderson, K. V. (2010). Rac1-dependent collective cell migration is required for specification of the anterior-posterior body axis of the mouse. *PLoS Biology*, *8*(8), 37–38. https://doi.org/10.1371/journal.pbio.1000442

Mitsui, K., Tokuzawa, Y., Itoh, H., Segawa, K., Murakami, M., Takahashi, K., … Yamanaka, S. (2003). The homeoprotein nanog is required for maintenance of pluripotency in mouse epiblast and ES cells. *Cell*, *113*(5), 631–642. https://doi.org/10.1016/S0092-8674(03)00393-3

Mosaliganti, K. R., Noche, R. R., Xiong, F., Swinburne, I. A., & Megason, S. G. (2012). ACME: automated cell morphology extractor for comprehensive reconstruction of cell membranes. *PLoS Computational Biology*, *8*(12), e1002780. https://doi.org/10.1371/journal.pcbi.1002780

Mukhopadhyay, M., Shtrom, S., Rodriguez-Esteban, C., Chen, L., Tsukui, T., Gomer, L., … Westphal, H. (2001). Dickkopf1 Is Required for Embryonic Head Induction and Limb Morphogenesis in the Mouse. *Developmental Cell*, *1*(3), 423–434. https://doi.org/10.1016/S1534-5807(01)00041-7

Muzumdar, M. D., Tasic, B., Miyamichi, K., Li, N., & Luo, L. (2007). A global double-fluorescent cre reporter mouse. *Genesis*, *45*(9), 593–605. https://doi.org/10.1002/dvg.20335

Nestor-Bergmann, A., Goddard, G., & Woolner, S. (2014). Force and the spindle: Mechanical cues in mitotic spindle orientation. *Seminars in Cell & Developmental Biology*, *34*, 133. https://doi.org/10.1016/J.SEMCDB.2014.07.008

Niwa, H., Toyooka, Y., Shimosato, D., Strumpf, D., Takahashi, K., Yagi, R., & Rossant, J. (2005). Interaction between Oct3/4 and Cdx2 determines trophectoderm differentiation. *Cell*, *123*(5), 917–929. https://doi.org/10.1016/j.cell.2005.08.040

Nomura, Y., Tanaka, H., Poellinger, L., Higashino, F., & Kinjo, M. (2001). Monitoring of in vitro and in vivo translation of green fluorescent protein and its fusion proteins by fluorescence correlation spectroscopy. *Cytometry*, *44*(1), 1–6. https://doi.org/10.1002/1097-0320(20010501)44:1<1::AID-CYTO1075>3.0.CO;2-0

Norris, D. P., Brennan, J., Bikoff, E. K., & Robertson, E. J. (2002). The Foxh1-dependent

autoregulatory enhancer controls the level of Nodal signals in the mouse embryo. *Development*, *129*(14), 3455–3468. Retrieved from thesis; nodal; foxh1; induction

Oliveira, F. P. M., & Tavares, J. M. R. S. (2014). Medical image registration: A review. *Computer Methods in Biomechanics and Biomedical Engineering*, *17*(2), 73–93. https://doi.org/10.1080/10255842.2012.670855

Omelchenko, T., Rabadan, M. A., Hernáandez-Martínez, R., Grego-Bessa, J., Anderson, K. V, & Hall, A. (2014). β-pix directs collective migration of anterior visceral endoderm cells in the early mouse embryo. *Genes and Development*, *28*(24), 2764–2777. https://doi.org/10.1101/gad.251371.114

Perea-Gomez, A., Lawson, K. A., Rhinn, M., Zakin, L., Brûlet, P., Mazan, S., & Ang, S. L. (2001). Otx2 is required for visceral endoderm movement and for the restriction of posterior signals in the epiblast of the mouse embryo. *Development*, *128*(5), 753–765.

Perea-Gomez, Aitana, Camus, A., Moreau, A., Grieve, K., Moneron, G., Dubois, A., … Collignon, J. (2004). Initiation of Gastrulation in the Mouse Embryo Is Preceded by an Apparent Shift in the Orientation of the Anterior-Posterior Axis. *Current Biology*, *14*(3), 197–207. https://doi.org/10.1016/S0960-9822(04)00044-2

Perea-Gomez, Aitana, Meilhac, S. M., Piotrowska-Nitsche, K., Gray, D., Collignon, J., & Zernicka-Goetz, M. (2007). Regionalisation of the mouse visceral endoderm as the blastocyst transforms into the egg cylinder. *BMC Developmental Biology*, *7*, 96. https://doi.org/10.1186/1471-213X-7-96

Perea-Gomez, Aitana, Vella, F. D. J., Shawlot, W., Oulad-Abdelghani, M., Chazaud, C., Meno, C., … Ang, S. L. (2002). Nodal antaginists in the anterior visceral endoderm prevent the formation of multiple primitive streaks. *Developmental Cell*, *3*(5), 745–756. https://doi.org/10.1016/S1534-5807(02)00321-0

Pietzsch, T., Saalfeld, S., Preibisch, S., & Tomancak, P. (2015). BigDataViewer: Visualization and processing for large image data sets. *Nature Methods*, *12*(6), 481–483. https://doi.org/10.1038/nmeth.3392

Plusa, B., Piliszek, A., Frankenberg, S., Artus, J., & Hadjantonakis, A. K. (2008). Distinct sequential cell behaviours direct primitive endoderm formation in the mouse blastocyst. *Development*, *135*(18), 3081–3091. https://doi.org/10.1242/dev.021519

Preibisch, S., Amat, F., Stamataki, E., Sarov, M., Singer, R. H., Myers, E., & Tomancak, P. (2014). Efficient Bayesian-based multiview deconvolution. *Nature Methods*, *11*(6), 645–648. https://doi.org/10.1038/nmeth.2929

Preibisch, S., Saalfeld, S., Schindelin, J., & Tomancak, P. (2010). Software for bead-based registration of selective plane illumination microscopy data. *Nature Methods*, *7*(6), 418–419. https://doi.org/10.1038/nmeth0610-418

Pu, W., Han, X., He, L., Li, Y., Huang, X., Zhang, M., … Zhou, B. (2020). A genetic system for tissue-specific inhibition of cell proliferation. *Development*, *147*(4). https://doi.org/10.1242/DEV.183830

Quesada-Hernández, E., Caneparo, L., Schneider, S., Winkler, S., Liebling, M., Fraser, S. E., & Heisenberg, C.-P. (2010). Stereotypical Cell Division Orientation Controls Neural Rod Midline Formation in Zebrafish. *Current Biology*, *20*(21), 1966–1972. https://doi.org/10.1016/J.CUB.2010.10.009

Rahunathan, S., Stredney, D., Schmalbrock, P., & Clymer, B. D. (2005). Image Registration Using

Rigid Registration and Maximization of Mutual Information. In *MMVR13. The 13th Annual Medicine Meets Virtual Reality Conference*. Retrieved from https://www.osc.edu/files/research/Biomed/vtbone/updates/image_registration.pdf

Rakeman, A. S., & Anderson, K. V. (2006). Axis specification and morphogenesis in the mouse embryo require Nap1, a regulator of WAVE-mediated actin branching. *Development*, *133*(16), 3075–3083. https://doi.org/10.1242/dev.02473

Rauzi, M., Krzic, U., Saunders, T. E., Krajnc, M., Ziherl, P., Hufnagel, L., & Leptin, M. (2015). Embryo-scale tissue mechanics during Drosophila gastrulation movements. *Nature Communications*, *6*, 8677. https://doi.org/10.1038/ncomms9677

Rauzi, M., & Lenne, P. F. (2011). *Cortical Forces in Cell Shape Changes and Tissue Morphogenesis*. *Current Topics in Developmental Biology*. https://doi.org/10.1016/B978-0-12-385065-2.00004-9

Riedl, J., Flynn, K. C., Raducanu, A., Gärtner, F., Beck, G., Bösl, M., … Wedlich-Söldner, R. (2010). Lifeact mice for studying F-actin dynamics. *Nature Methods*, *7*(3), 168–169. https://doi.org/10.1038/nmeth0310-168

Rivera-Pérez, J. A., & Hadjantonakis, A. K. (2015). The dynamics of morphogenesis in the early mouse embryo. *Cold Spring Harbor Perspectives in Biology*, *7*(11). https://doi.org/10.1101/cshperspect.a015867

Rivera-Pérez, J. A., Mager, J., & Magnuson, T. (2003). Dynamic morphogenetic events characterize the mouse visceral endoderm. *Developmental Biology*, *261*(2), 470–487. https://doi.org/10.1016/S0012-1606(03)00302-6

Rodriguez, T. A., Casey, E. S., Harland, R. M., Smith, J. C., & Beddington, R. S. . (2001). Distinct enhancer elements control hex expression during gastrulation and early organogenesis. *Developmental Biology*, *234*(2), 304–316. https://doi.org/10.1006/dbio.2001.0265

Rodriguez, T. A., Srinivas, S., Clements, M. P., Smith, J. C., & Beddington, R. S. P. (2005). Induction and migration of the anterior visceral endoderm is regulated by the extra-embryonic ectoderm. *Development*, *132*(11), 2513–2520. https://doi.org/10.1242/dev.01847

Ronneberger, O., Fischer, P., & Brox, T. (2015). U-net: Convolutional networks for biomedical image segmentation. In *Lecture Notes in Computer Science (including subseries Lecture Notes in Artificial Intelligence and Lecture Notes in Bioinformatics)* (Vol. 9351, pp. 234–241). Springer, Cham. https://doi.org/10.1007/978-3-319-24574-4_28

Rossant, J., & Tam, P. P. L. (2009). Blastocyst lineage formation, early embryonic asymmetries and axis patterning in the mouse. *Development*, *136*(5), 701–713. https://doi.org/10.1242/dev.017178

Royer, L. A., Lemon, W. C., Chhetri, R. K., Wan, Y., Coleman, M., Myers, E. W., & Keller, P. J. (2016). Adaptive light-sheet microscopy for long-term, high-resolution imaging in living organisms. *Nature Biotechnology*, *34*(12), 1267–1278. https://doi.org/10.1038/nbt.3708

Rozbicki, E., Chuai, M., Karjalainen, A. I., Song, F., Sang, H. M., Martin, R., … Weijer, C. J. (2015). Myosin-II-mediated cell shape changes and cell intercalation contribute to primitive streak formation. *Nature Cell Biology*, *17*(4), 397–408. https://doi.org/10.1038/ncb3138

Saijoh, Y., Adachi, H., Sakuma, R., Yeo, C. Y., Yashiro, K., Watanabe, M., … Hamada, H. (2000). Left-right asymmetric expression of lefty2 and nodal is induced by a signaling pathway that includes the transcription factor FAST2. *Molecular Cell*, *5*(1), 35–47. https://doi.org/10.1016/S1097-2765(00)80401-3

Sakuma, R., Ohnishi, Y. I., Meno, C., Fujii, H., Juan, H., Takeuchi, J., … Hamada, H. (2002). Inhibition of Nodal signalling by Lefty mediated through interaction with common receptors and efficient diffusion. *Genes to Cells*, *7*(4), 401–412. https://doi.org/10.1046/j.1365-2443.2002.00528.x

Schmid, B., Schindelin, J., Cardona, A., Longair, M., & Heisenberg, M. (2010). A high-level 3D visualization API for Java and ImageJ. *BMC Bioinformatics*, *11*(1), 274. https://doi.org/10.1186/1471-2105-11-274

Seifert, J. R. K., & Mlodzik, M. (2007). Frizzled/PCP signalling: A conserved mechanism regulating cell polarity and directed motility. *Nature Reviews Genetics*, *8*(2), 126–138. https://doi.org/10.1038/nrg2042

Selchow, O., & Huisken, J. (2013). Light sheet fluorescence microscopy and revolutionary 3D analyses of live specimens. *Photonik International*, 44–47.

Shioi, G., Hoshino, H., Abe, T., Kiyonari, H., Nakao, K., Meng, W., … Aizawa, S. (2017). Apical constriction in distal visceral endoderm cells initiates global, collective cell rearrangement in embryonic visceral endoderm to form anterior visceral endoderm. *Developmental Biology*, *429*(1), 20–30. https://doi.org/10.1016/j.ydbio.2017.07.004

Silva, S. M. da, & Vincent, J.-P. (2007). Oriented cell divisions in the extending germband ofDrosophila. *Development*, *134*(17), 3049–3054. https://doi.org/10.1242/DEV.004911

Smith, L. J. (1985). Embryonic axis orientation in the mouse and its correlation with blastocyst relationships to the uterus. II. Relationships from 4 1/4 to 9 1/2 days. *Journal of Embryology and Experimental Morphology*, *VOL. 89*, 15–35.

Sommer, C., Straehle, C., Kothe, U., & Hamprecht, F. A. (2011). Ilastik: Interactive learning and segmentation toolkit. In *2011 IEEE International Symposium on Biomedical Imaging: From Nano to Macro* (pp. 230–233). IEEE. https://doi.org/10.1109/ISBI.2011.5872394

Srinivas, S. (2006). The anterior visceral endoderm - Turning heads. *Genesis*, *44*(11), 565–572. https://doi.org/10.1002/dvg.20249

Srinivas, S., Rodriguez, T., Clements, M., Smith, J. C., & Beddington, R. S. P. (2004). Active cell migration drives the unilateral movements of the anterior visceral endoderm. *Development*, *131*(5), 1157–1164. https://doi.org/10.1242/dev.01005

Stegmaier, J., Amat, F., Lemon, W., McDole, K., Wan, Y., Teodoro, G., … Keller, P. (2016). Real-time three-dimensional cell segmentation in large-scale microscopy data of developing embryos. | Janelia Research Campus. *Developmental Cell*, *36*(2), 225–240. Retrieved from https://www.janelia.org/publication/real-time-three-dimensional-cell-segmentation-large-scale-microscopy-data-developing

Stower, M. J., & Srinivas, S. (2014). Heading forwards: anterior visceral endoderm migration in patterning the mouse embryo. *Philosophical Transactions of the Royal Society of London. Series B, Biological Sciences*, *369*(1657), 20130546-. https://doi.org/10.1098/rstb.2013.0546

Stower, M. J., & Srinivas, S. (2018). The Head's Tale: Anterior-Posterior Axis Formation in the Mouse Embryo. In A.-K. H. Berenika Plusa (Ed.), *Current Topics in Developmental Biology* (1st ed., Vol. 128, pp. 365–390). Academic Press. https://doi.org/10.1016/bs.ctdb.2017.11.003

Strnad, P., Gunther, S., Reichmann, J., Krzic, U., Balazs, B., De Medeiros, G., … Ellenberg, J. (2016). Inverted light-sheet microscope for imaging mouse pre-implantation development. *Nature Methods*, *13*(2), 139–142. https://doi.org/10.1038/nmeth.3690

Stuckey, D. W., Clements, M., Di-Gregorio, A., Senner, C. E., le Tissier, P., Srinivas, S., & Rodriguez, T. A. (2011). Coordination of cell proliferation and anterior-posterior axis establishment in the mouse embryo. *Development*, *138*(8), 1521–1530. https://doi.org/10.1242/dev.063537

Sutherland, A. E., Speed, T. P., & Calarco, P. G. (1990). Inner cell allocation in the mouse morula: The role of oriented division during fourth cleavage. *Developmental Biology*, *137*(1), 13–25. https://doi.org/10.1016/0012-1606(90)90003-2

Takaoka, K., & Hamada, H. (2012). Cell fate decisions and axis determination in the early mouse embryo. *Development*, *139*(1), 3–14. https://doi.org/10.1242/dev.060095

Takaoka, K., Yamamoto, M., & Hamada, H. (2011). Origin and role of distal visceral endoderm, a group of cells that determines anterior-posterior polarity of the mouse embryo. *Nature Cell Biology*, *13*(7), 743–752. https://doi.org/10.1038/ncb2251

Tam, P. P. L. (2004). Embryonic axes: The long and short of it in the mouse. *Current Biology*, *14*(6), R239–R241. https://doi.org/10.1016/j.cub.2004.02.056

Tam, P. P. L., & Loebel, D. A. F. (2007). Gene function in mouse embryogenesis: get set for gastrulation. *Nature Reviews Genetics*, *8*(5), 368–381. https://doi.org/10.1038/nrg2084

Tambe, D. T., Corey Hardin, C., Angelini, T. E., Rajendran, K., Park, C. Y., Serra-Picamal, X., … Trepat, X. (2011). Collective cell guidance by cooperative intercellular forces. *Nature Materials*, *10*(6), 469–475. https://doi.org/10.1038/nmat3025

Tanaka, S., Kunath, T., Hadjantonakis, A. K., Nagy, A., & Rossant, J. (1998). Promotion to trophoblast stem cell proliferation by FGF4. *Science*, *282*(5396), 2072–2075. https://doi.org/10.1126/science.282.5396.2072

Tao, H., Suzuki, M., Kiyonari, H., Abe, T., Sasaoka, T., & Ueno, N. (2009). Mouse prickle1, the homolog of a PCP gene, is essential for epiblast apical-basal polarity. *Proceedings of the National Academy of Sciences of the United States of America*, *106*(34), 14426–14431. https://doi.org/10.1073/pnas.0901332106

Thirion, J. P. (1998). Image matching as a diffusion process: An analogy with Maxwell's demons. *Medical Image Analysis*, *2*(3), 243–260. https://doi.org/10.1016/S1361-8415(98)80022-4

Thomas, P., & Beddington, R. (1996). Anterior primitive endoderm may be responsible for patterning the anterior neural plate in the mouse embryo. *Current Biology*, *6*(11), 1487–1496. https://doi.org/10.1016/S0960-9822(96)00753-1

Thomas, P. Q., Brown, A., & Beddington, R. S. P. (1998). Hex: A homeobox gene revealing peri-implantation asymmetry in the mouse embryo and an early transient marker of endothelial cell precursors. *Development*, *125*(1), 85–94.

Tinevez, J.-Y., Perry, N., Schindelin, J., Hoopes, G. M., Reynolds, G. D., Laplantine, E., … Eliceiri, K. W. (2017). TrackMate: An open and extensible platform for single-particle tracking. *Methods*, *115*, 80–90. https://doi.org/10.1016/J.YMETH.2016.09.016

Tomer, R., Khairy, K., Amat, F., & Keller, P. J. (2012). Quantitative high-speed imaging of entire developing embryos with simultaneous multiview light-sheet microscopy. *Nature Methods*, *9*(7), 755–763. https://doi.org/10.1038/nmeth.2062

Tran, D., Bourdev, L., Fergus, R., Torresani, L., & Paluri, M. (2015). Learning Spatiotemporal Features with 3D Convolutional Networks. In *2015 IEEE International Conference on Computer Vision (ICCV)* (pp. 4489–4497). IEEE. https://doi.org/10.1109/ICCV.2015.510

Trepat, X., & Fredberg, J. J. (2011). Plithotaxis and emergent dynamics in collective cellular

migration. *Trends in Cell Biology*, *21*(11), 638–646. https://doi.org/10.1016/j.tcb.2011.06.006

Trepat, X., Wasserman, M. R., Angelini, T. E., Millet, E., Weitz, D. A., Butler, J. P., & Fredberg, J. J. (2009). Physical forces during collective cell migration. *Nature Physics*, *5*(6), 426–430. https://doi.org/10.1038/nphys1269

Trichas, G., Begbie, J., & Srinivas, S. (2008). Use of the viral 2A peptide for bicistronic expression in transgenic mice. *BMC Biology*. https://doi.org/10.1186/1741-7007-6-40

Trichas, G., Joyce, B., Crompton, L. A., Wilkins, V., Clements, M., Tada, M., … Srinivas, S. (2011). Nodal dependent differential localisation of dishevelled-2 demarcates regions of differing cell behaviour in the visceral endoderm. *PLoS Biology*, *9*(2), e1001019. https://doi.org/10.1371/journal.pbio.1001019

Trichas, G., Smith, A. M., White, N., Wilkins, V., Watanabe, T., Moore, A., … Srinivas, S. (2012). Multi-cellular rosettes in the mouse visceral endoderm facilitate the ordered migration of anterior visceral endoderm cells. *PLoS Biology*, *10*(2), e1001256. https://doi.org/10.1371/journal.pbio.1001256

Udan, R. S., Piazza, V. G., Hsu, C. W., Hadjantonakis, A. K., & Dickinson, M. E. (2014). Quantitative imaging of cell dynamics in mouse embryos using light-sheet microscopy. *Development (Cambridge)*, *141*(22), 4406–4414. https://doi.org/10.1242/dev.111021

Varlet, I., Collignon, J., & Robertson, E. J. (1997). Nodal expression in the primitive endoderm is required for specification of the anterior axis during mouse gastrulation. *Development*, *124*(5), 1033–1044.

Vercauteren, T., Pennec, X., Perchant, A., & Ayache, N. (2009). Diffeomorphic demons: efficient non-parametric image registration. *NeuroImage*, *45*(1 Suppl), S61–S72. https://doi.org/10.1016/j.neuroimage.2008.10.040

Voiculescu, O., Bertocchini, F., Wolpert, L., Keller, R. E., & Stern, C. D. (2007). The amniote primitive streak is defined by epithelial cell intercalation before gastrulation. *Nature*, *449*(7165), 1049–1052. https://doi.org/10.1038/nature06211

Walck-Shannon, E., & Hardin, J. (2014). Cell intercalation from top to bottom. *Nature Reviews Molecular Cell Biology*, *15*(1), 34–48. https://doi.org/10.1038/nrm3723

Waldrip, W. R., Bikoff, E. K., Hoodless, P. A., Wrana, J. L., & Robertson, E. J. (1998). Smad2 signaling in extraembryonic tissues determines anterior-posterior polarity of the early mouse embryo. *Cell*, *92*(6), 797–808. https://doi.org/10.1016/S0092-8674(00)81407-5

Wan, Y., McDole, K., & Keller, P. J. (2019). Light-Sheet Microscopy and Its Potential for Understanding Developmental Processes. *Annual Review of Cell and Developmental Biology*, *35*(1), 655–681. https://doi.org/10.1146/annurev-cellbio-100818-125311

Watanabe, T., Biggins, J. S., Tannan, N. B., & Srinivas, S. (2014). Limited predictive value of blastomere angle of division in trophectoderm and inner cell mass specification. *Development (Cambridge)*, *141*(11), 2279–2288. https://doi.org/10.1242/dev.103267

Weber, M., & Huisken, J. (2015). In vivo imaging of cardiac development and function in zebrafish using light sheet microscopy. *Swiss Medical Weekly*, *145*(5152). https://doi.org/10.4414/smw.2015.14227

Weinzaepfel, P., Revaud, J., Harchaoui, Z., & Schmid, C. (2013). DeepFlow: Large displacement optical flow with deep matching. In *Proceedings of the IEEE International Conference on Computer Vision* (pp. 1385–1392). IEEE. https://doi.org/10.1109/ICCV.2013.175

Wetzel, R. (1929). Untersuchungen am Huhnchen. Die Entwicklung des Keims wahrend der erste beiden Bruttage. *Archiv. Der Entwicklungmechanik Der Organismen*, *119*, 188–321.

Wilkinson, D. G., Bhatt, S., & Herrmann, B. G. (1990). Expression pattern of the mouse T gene and its role in mesoderm formation. *Nature*, *343*(6259), 657–659. https://doi.org/10.1038/343657a0

Williams, M., Burdsal, C., Periasamy, A., Lewandoski, M., & Sutherland, A. (2012). Mouse primitive streak forms in situ by initiation of epithelial to mesenchymal transition without migration of a cell population. *Developmental Dynamics*, *241*(2), 270–283. https://doi.org/10.1002/dvdy.23711

Wolff, C., Tinevez, J. Y., Pietzsch, T., Stamataki, E., Harich, B., Guignard, L., … Pavlopoulos, A. (2018). Multi-view light-sheet imaging and tracking with the MaMuT software reveals the cell lineage of a direct developing arthropod limb. *ELife*, *7*. https://doi.org/10.7554/eLife.34410

Wolpert, L., & Tickle, C. (2011). *Principles of Development. 4th ed. Oxford University Press*.

Wu, Y., Ghitani, A., Christensen, R., Santella, A., Du, Z., Rondeau, G., … Shroff, H. (2011). Inverted selective plane illumination microscopy (iSPIM) enables coupled cell identity lineaging and neurodevelopmental imaging in Caenorhabditis elegans. *Proceedings of the National Academy of Sciences of the United States of America*, *108*(43), 17708–17713. https://doi.org/10.1073/pnas.1108494108

Wyatt, T. P. J., Harris, A. R., Lam, M., Cheng, Q., Bellis, J., Dimitracopoulos, A., … Baum, B. (2015). Emergence of homeostatic epithelial packing and stress dissipation through divisions oriented along the long cell axis. *Proceedings of the National Academy of Sciences of the United States of America*, *112*(18), 5726–5731. https://doi.org/10.1073/pnas.1420585112

Yagi, R., Kohn, M. J., Karavanova, I., Kaneko, K. J., Vullhorst, D., DePamphilis, M. L., & Buonanno, A. (2007). Transcription factor TEAD4 specifies the trophectoderm lineage at the beginning of mammalian development. *Development (Cambridge, England)*, *134*(21), 3827–3836. https://doi.org/10.1242/dev.010223

Yamamoto, M., Beppu, H., Takaoka, K., Meno, C., Li, E., Miyazono, K., & Hamada, H. (2009). Antagonism between Smad1 and Smad2 signaling determines the site of distal visceral endoderm formation in the mouse embryo. *Journal of Cell Biology*, *184*(2), 323–334. https://doi.org/10.1083/jcb.200808044

Yamamoto, M., Saijoh, Y., Perea-Gomez, A., Shawiot, W., Behringer, R. R., Ang, S. L., … Meno, C. (2004). Nodal antagonists regulate formation of the anteroposterior axis of the mouse embryo. *Nature*, *428*(6981), 387–392. https://doi.org/10.1038/nature02418

Yang, S., Ma, K., Geng, Z., Sun, X., & Fu, X. (2015). Oriented cell division: new roles in guiding skin wound repair and regeneration. *Bioscience Reports*, *35*(6). https://doi.org/10.1042/BSR20150225

Yoo, T. S., Ackerman, M. J., Lorensen, W. E., Schroeder, W., Chalana, V., Aylward, S., … Whitaker, R. (2002). Engineering and algorithm design for an image processing API: A technical report on ITK - The Insight Toolkit. In *Studies in Health Technology and Informatics* (Vol. 85, pp. 586–592). https://doi.org/10.3233/978-1-60750-929-5-586

Zallen, J. A., & Wieschaus, E. (2004). Patterned gene expression directs bipolar planar polarity in Drosophila. *Developmental Cell*, *6*(3), 343–355. https://doi.org/10.1016/s1534-5807(04)00060-7

Zanella, C., Campana, M., Rizzi, B., Melani, C., Sanguinetti, G., Bourgine, P., … Sarti, A. (2010). Cells

segmentation from 3-D confocal images of early zebrafish embryogenesis. *IEEE Transactions on Image Processing*, *19*(3), 770–781. https://doi.org/10.1109/TIP.2009.2033629

Zhang, J., Tam, W. L., Tong, G. Q., Wu, Q., Chan, H. Y., Soh, B. S., … Lim, B. (2006). Sall4 modulates embryonic stem cell pluripotency and early embryonic development by the transcriptional regulation of Pou5f1. *Nature Cell Biology*, *8*(10), 1114–1123. https://doi.org/10.1038/ncb1481

Zhou, F. Y., Ruiz-Puig, C., Owen, R. P., White, M. J., Rittscher, J., & Lu, X. (2019). Motion sensing superpixels (MOSES) is a systematic computational framework to quantify and discover cellular motion phenotypes. *ELife*, *8*. https://doi.org/10.7554/eLife.40162

Zhou, J., Pal, S., Maiti, S., & Davidson, L. A. (2015). Force production and mechanical accommodation during convergent extension. *Development (Cambridge, England)*, *142*(4), 692. https://doi.org/10.1242/DEV.116533

Zhou, Z., Alégot, H., & Irvine, K. D. (2019). Oriented Cell Divisions Are Not Required for Drosophila Wing Shape. *Current Biology*, *29*(5), 856-864.e3. https://doi.org/10.1016/j.cub.2019.01.044

Chapter 6: Appendix

6.1 Supplementary video descriptions

6.1.1 Chapter 2

SV1A-4B show different stages of the data processing framework detailed in Chapter 2 for embryo L871_Emb1, using maximum intensity projections (MIP) from either the x-y or y-z view. This embryo has 66 timepoints, with a 5min resolution.

SV1A and B show the raw timelapse data, after preprocessing (.czi to .tif, with voxel interpolation and intensity rescaling).

SV1A: The raw timelapse of angles 1 and 2 in x-y, prior to any registration.

SV1B: The raw timelapse of angles 1 and 2 in y-z, prior to any registration.

In **SV1A** and **B**, the embryo drifts, rotates and grows during timelapse acquisition. The voxel anisotropy is clear in the difference in resolution between the x-y and y-z views. The data quality also reduced in SV1B and D (the y-z views) due to light scatter through the embryo.

SV2 shows the rigid registration process (angle and timepoint). The description for SV2 is ordered A-D for the images left to right.

SV2A: Two good quality halves of the two registered angles (y-z view). Only angle registration has occurred here, so the embryo still grows and drifts over time. The angles are not fused yet, but the join point is clear, and shows a good spatial registration of the two angles.

SV2B: The timepoint from SV2A have now been registered, in addition to the angles. The embryo no long drifts, rotates, or grows over time (y-z view)

SV2C: The two angles of each timepoint are now fused, using a subtle blending at the join point (y-z view).

SV2D: The fused embryo from the x-y view.

SV3 shows the non-rigid registration.

SV3A: The embryo now undergoes non-rigid registration, matching the apical surface across timepoints (x-y view). The image on the left is without the non-rigid registration (the same as SV2D), and the image on the right is with non-rigid registration applied. This particular embryo was registered using the middle timepoint as the reference point, instead of the moving average implemented for later embryos with longer timelapses.

SV3B: The same non-rigid registration as SV3A from the y-z view. The image on the left is the same as SV2C.

SV4A and B show the projected layers of the embryo, prepared by Dr Felix Zhou.

SV4A: The Cartesian projection of the VE on the left, and the corresponding geometrically matched epiblast projection on the right, with the anterior located centrally. This embryo was imaged with AVE migration lateral to the microscope objective, and so has the lowest resolution. The layers can be directly compared.

SV4B: The corresponding polar projections of the VE and epiblast, with the anterior located centrally and upwards.

6.1.2 Chapter 3

SV5-8 show timelapses corresponding to embryo L491 as detailed in Chapter 3. This embryo has 100 timepoints, with a 5min resolution. L491 was imaged with the anterior towards the microscope objective, and so has higher resolution than the cells image laterally. Projections and deformation maps were prepared by Dr Felix Zhou.

SV5: The polar projection of embryo L491 was used for manual tracking of the cells in the Epi-VE. Those tracks are shown here, every 10 frames (50mins), with a track length of 10 frames. The anterior is located centrally and upwards.

SV6A: The raw Cartesian projection of the VE embryo L491, with timepoints every 5mins. The anterior is located centrally.

SV6B: The corresponding deformation map (right) for the Cartesian projection of L491 shown in SV6A (left).

SV6C: The deformation map for the polar projection of L491.

SV6D: The radial grid deformation for the polar projection of L491.

SV7: The image on the left is the Cartesian projection of the VE of embryo L491 (SV6A). The image on the right shows the corresponding geometrically mapped epiblast projection, which can be used to compare movement between the cell layers.

SV8: The left image shows SV6A, the raw Cartesian projection of the VE of L491. The right image shows the corresponding membrane probability prediction output of the CNN. 'Fuzzier' areas correspond to areas where the segmentation is less certain. The prediction output was created by Dr Felix Zhou.

6.1.3 Chapter 4

SV9 shows the cavity expansion corresponding to the eccentricity analysis in Figure 4-5A, Chapter 4.

SV9: Embryo L926 captures post-migration, beginning after the leading AVE cells (Hex-GFP green fluorescence) have reached the boundary between the Epi-VE and the ExE-VE, but are still migrating. The sagittal section was taken through the centre of the z-stack of the spatiotemporally registered embryo, without non-rigid shape matching. Frames are every 10mins. Before cavity expansion begins at 210mins, an 'L' shape is visible, as the epiblast flattening moves concurrent with the AVE. After expansion, the cavity appears asymmetric, with signs of flattening no longer visible.

6.2 Supplementary figures and tables

Embryo	Stage (mins)	VE		Epiblast		Cavity	
		Angle	AR	Angle	AR	Angle	AR
L455_Emb2	-250	87.52	1.09	74.87	1.08	105.71	1.23
	-200	87.96	1.13	79.31	1.18	66.64	1.57
	-150	95.63	1.1	92.58	1.11	95.94	1.15
	-100	99.85	1.08	84.32	1.07	32.73	1.17
	-50	96	1.06	90.22	1.1	91.68	1.13
	0	128.07	1.07	130.7	1.15	132.25	1.56
	50	123.34	1.1	132.17	1.15	111.97	1.63
	100	127.4	1.14	128.71	1.24	119.3	1.82
	150	117.56	1.19	124.4	1.21	121.43	1.67
L455_Emb3	-250	34.18	1	16.54	1.07	122.5	1.05
	-200	109.12	1.01	2.7	1.02	125.36	1.05
	-150	108.93	1.02	135.09	1.02	122.92	1.06
	-100	18.32	1.02	48.23	1.05	11.14	1.13
	-50	33.26	1.02	13.33	1.01	21.48	1.17
	0	58.57	1.05	29.97	1.07	17.89	1.15
	50	54.39	1.1	50.89	1.1	36.18	1.08
	100	40.54	1.05	12.58	1.06	10.53	1.11
	150	85.66	1.01	92.8	1.06	176.58	1.1
	200	47.04	1.02	76.93	1.07	113.64	1.08
	250	4.81	1.01	96.32	1.06	110.76	1.16
	300	38.54	1.01	91.38	1.08	16.85	1.07
L505	-200	70.76	1.16	66.74	1.2	56.9	1.11
	-150	77.08	1.17	79.61	1.16	63.69	1.09
	-100	87.33	1.19	91.09	1.15	108.21	1.11
	-50	93.78	1.21	97.4	1.16	119.43	1.15
	0	94.87	1.22	86.7	1.18	94.78	1.19
	50	95.79	1.24	92.66	1.24	93.55	1.27
	100	99.02	1.3	99.52	1.33	100.03	1.55
	150	104.69	1.29	97.12	1.3	98.19	1.56
	200	107.02	1.22	102.71	1.25	96.78	1.4
	250	115.01	1.25	108.84	1.24	102.51	1.49
	300	116.02	1.21	114.58	1.18	110.39	1.35
L864	-150	165.94	1.1	167.83	1.12	94.29	1.03
	-100	176.1	1.05	150.63	1.01	48.27	1.55
	-50	171.74	1.09	4.81	1.06	10.04	1.43
	0	46.47	1	29.77	1.01	31.53	1.26
	50	100.45	1.02	129.21	1.04	42.56	1.13
	100	90.29	1.08	88.83	1.07	70.69	1.17
	150	87.88	1.06	86.99	1.13	72.59	1.1
	200	111.43	1.08	98.33	1.12	99.63	1.15
	250	97.92	1.06	92.72	1.1	68.74	1.07
	300	99.29	1.07	96.76	1.12	99.15	1.18
	350	116.28	1.04	97.67	1.14	83.35	1.29
	400	115.81	1.07	98.36	1.13	81.36	1.23

Embryo	Stage (mins)	VE		Epiblast		Cavity	
		Angle	AR	Angle	AR	Angle	AR
L871_Emb1	-50	78.16	1.11	76.18	1.08	82.6	1.32
	0	53.51	1.09	57.21	1.08	60.84	1.14
	50	49.13	1.07	43.11	1.08	35.33	1.07
	100	46.06	1.07	4.16	1.07	16.65	1.12
	150	49.56	1.05	64.35	1.03	26.96	1.18
	200	69.59	1.01	76.03	1.05	126.49	1.05
	250	99.75	1.02	94.73	1.09	65.28	1.21
L924	-150	117	1.06	123.1	1.14	117.6	1.2
	-100	113.43	1.08	118.89	1.1	36.33	1.04
	-50	113.09	1.09	106.71	1.08	155.35	1.06
	0	107.9	1.05	125.59	1.08	65.23	1.06
	50	139.57	1.03	126.22	1.06	155.55	1.03
	100	131.7	1.12	143.71	1.07	141.3	1.05
	150	127.3	1.08	126.51	1.06	114.8	1.08
	200	126.36	1.06	129.95	1.1	124.13	1.14
	250	131.35	1.08	137.09	1.09	132.57	1.24
	300	130.63	1.1	127.31	1.15	131.43	1.25
	350	130.83	1.06	124.99	1.06	112.36	1.24
	400	128.29	1.02	106.03	1.1	117.52	1.11
	450	158.83	1.04	108.95	1.05	66.05	1.07
	500	133.61	1.05	100.79	1.04	84.35	1.07
	550	87.92	1.04	64.07	1.07	67.1	1.15
	600	97.27	1.03	87.02	1.04	109.04	1.03
	650	95.49	1.04	78.26	1.06	67.89	1.09
	700	100.76	1.04	89.99	1.05	50.14	1.1
	750	104.13	1.05	92.06	1.07	57.82	1.12
	800	106.59	1.03	79.92	1.09	85.11	1.09
L928_Emb2	-100	22.16	1.05	22.75	1.09	171.08	1.28
	-50	22.39	1.03	8.85	1.05	118.45	1.14
	0	172.62	1.02	15.31	1.02	101.83	1.34
	50	119.29	1.06	92.34	1.09	106.18	1.86
	100	128.87	1.08	120.19	1.09	116.57	1.99
	150	140.93	1.13	122.14	1.11	106.59	1.96
	200	138.07	1.15	123.15	1.18	116.88	1.96
	250	124.11	1.17	119.02	1.22	125.67	2.39
	300	124.27	1.2	110.21	1.24	121.7	3.66
	350	125.6	1.23	110.53	1.32	106.04	2.22
	400	132.47	1.24	119.51	1.29	125.03	2.03
L930	-300	167.31	1.07	175.07	1.09	0	0
	-250	142.85	1.02	170.01	1.02	0	0
	-200	126.42	1.06	157.9	1.02	0	0
	-150	134.82	1.07	142.68	1.04	69.68	1.5
	-100	143.61	1.07	140.05	1.06	108.49	1.08
	-50	23.38	1.02	163.01	1.03	105.17	1.08
	0	113.7	1.03	6.57	1.03	68.21	1.11
	50	111.58	1.06	127.23	1.04	55.23	1.03
	100	145.33	1.04	132.82	1.07	104.28	1.06
	150	132.78	1.08	118.89	1.06	73.74	1.06
	200	138.67	1.07	118.59	1.03	99.92	1.06
	250	157.44	1.02	104.92	1.06	81.83	1.11

Embryo	Time (mins)	VE			Epiblast			Cav		
		Area	Angle	AR	Area	Angle	AR	Area	Angle	AR
L926	210	20150	114.65	1.27	13476	114.06	1.42	1085	112.90	4.54
	230	19865	110.76	1.17	13564	111.30	1.26	1828	110.67	2.13
	250	20720	121.19	1.13	15240	114.11	1.18	3359	110.63	1.40
	270	21763	123.37	1.15	15924	118.93	1.20	4073	109.03	1.33
	290	21868	125.44	1.11	15541	118.96	1.14	5088	112.11	1.32
	310	22541	126.24	1.13	16387	124.59	1.19	5659	112.83	1.21

Table 6-1

Table 6-1: Measurements of the aspect ratio and major axis angle of the transverse cross-sections for embryos with pre-migration and migration phases, and measurements of the aspect ratio (AR), angle and transverse cross-sectional area of embryo L926. The staging is aligned across embryos so that 0mins is the start of migration, as defined by the manual staging. An aspect ratio <1.05 denotes a more circular cross-section, whereas AR much greater than 1 denotes a more eccentric cross-section. An angle of 90° denotes the long axis is perpendicular to the A-P axis (the AVE is located at 180°).

Figure 6-1 to 6-4: (Next pages) In 7/8 embryos the long axis of the epiblast aligns perpendicular to the A-P axis during migration, and the short axis lies under the thickened AVE. Transverse sections are the view from looking down on the epiblast from the proximal above. White arrows denote the leading edge of the AVE, and in both transverse and sagittal sections, the anterior is on the left of the image. The green box indicates the migration phase as defined by the manual staging. Flattening of the epiblast can be seen in sagittal sections concurrent with AVE migration, and eccentricity measurements were taken of the transverse 'Epi' sections.

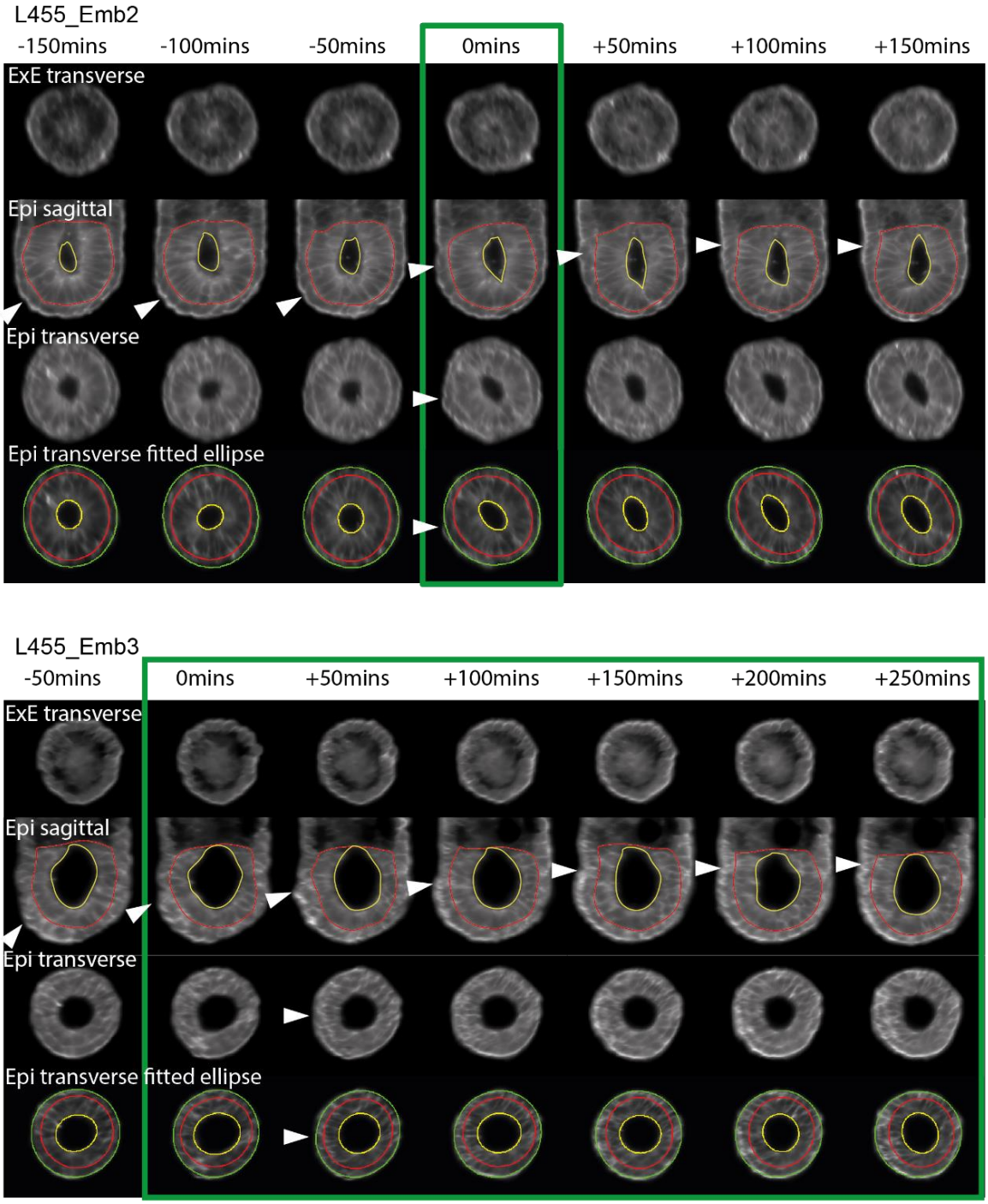

Figure 6-1: Embryo L455_Emb2 is the only embryo where the long axis of of the transverse section begins perpendicular to the A-P axis, but ends less so. It undergoes a very short migration phase. The only sign of VET is in the 0th transverse frame during migration, but it is important to note it also appears to be about 40° off the horizontal. The epiblast in the sagittal section also appears to tilt directionally right in response to the AVE migration.

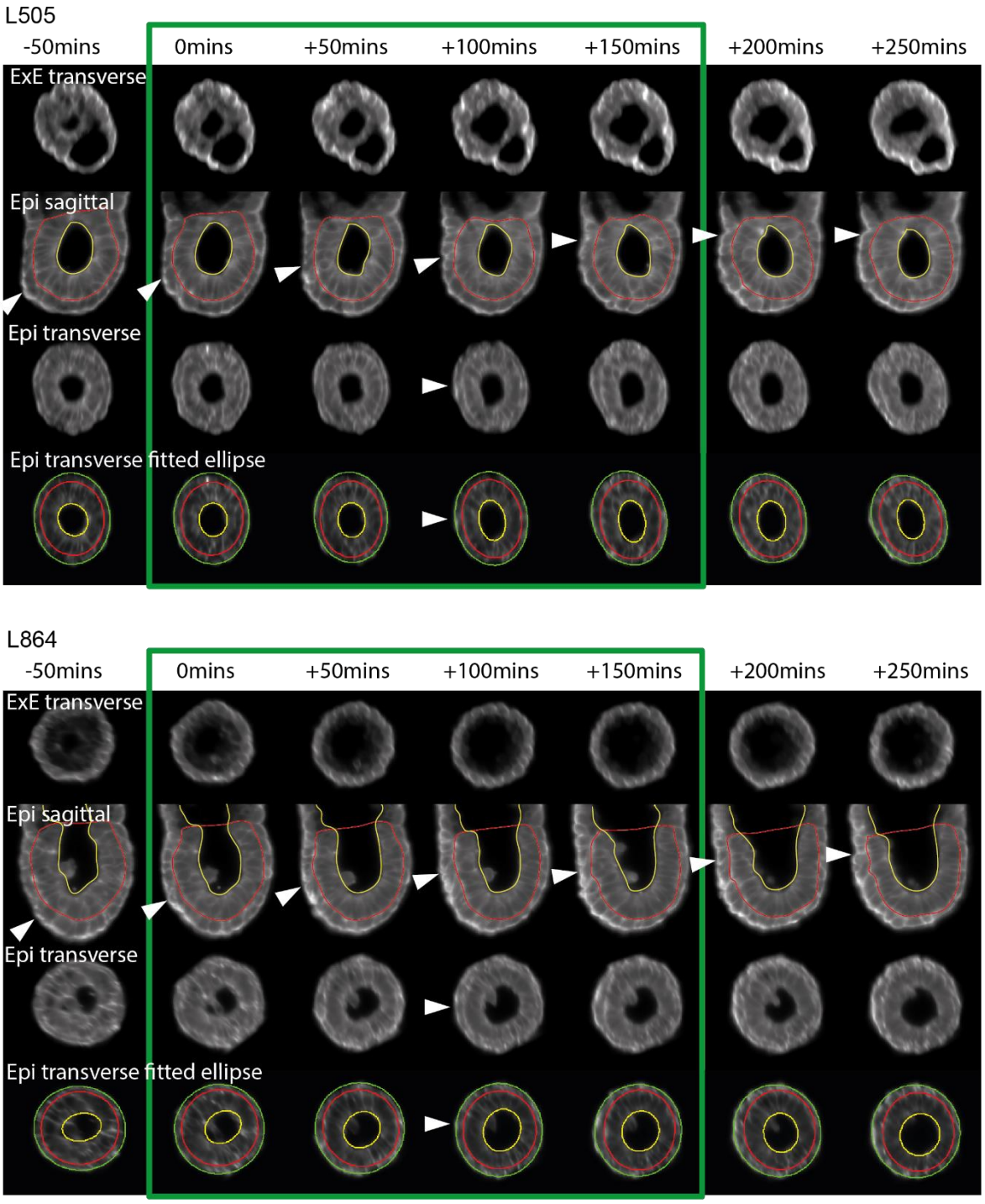

Figure 6-2: Continuation of Figure 6-1. L505 had an ectopic cavity, visible in the ExE transverse section.

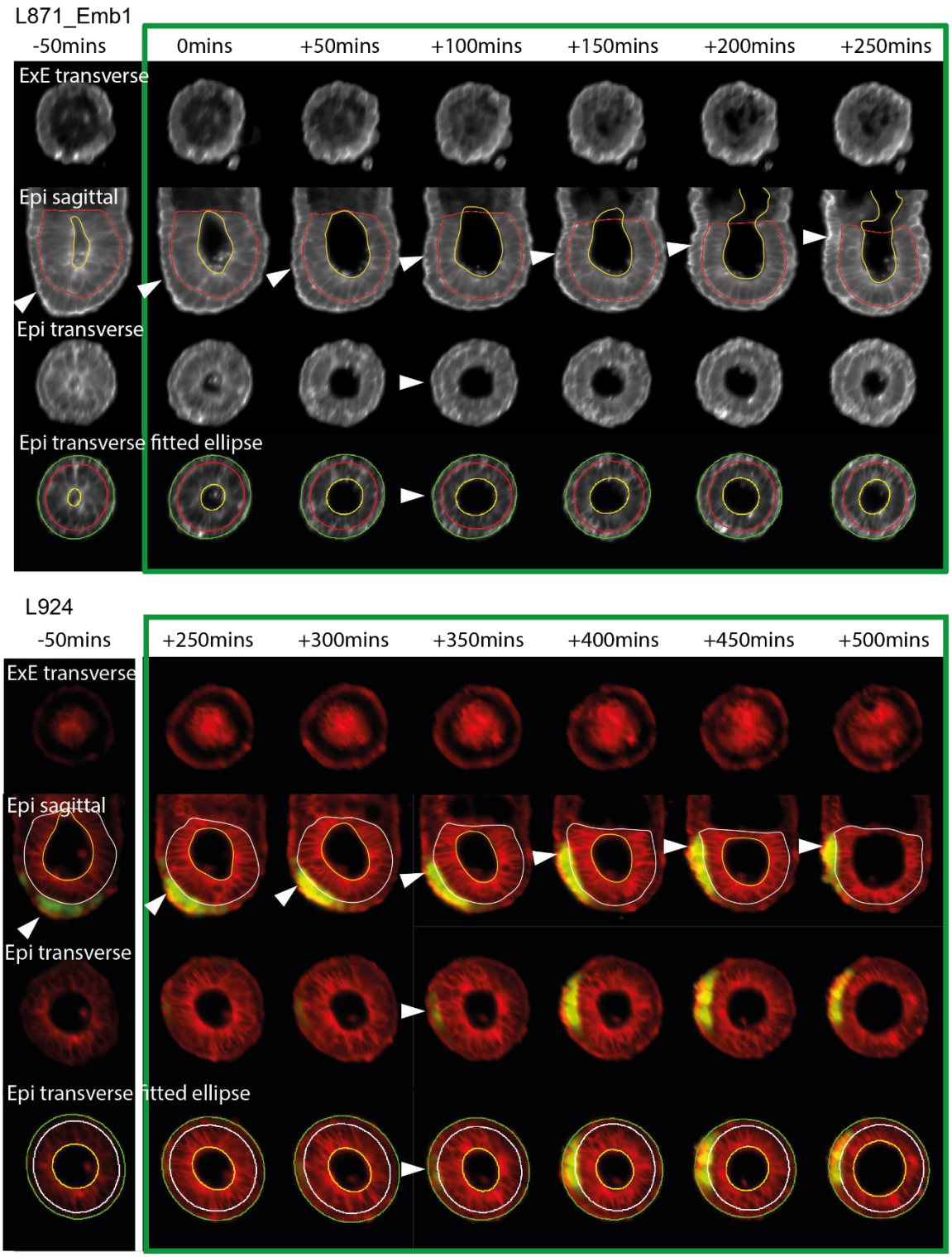

Figure 6-3: Continuation of Figure 6-1. The cavity of embryo L871_Emb1 cavity expands horizontally during the first timepoints of migration, which may be affecting the epiblast eccentricity. Embryo L924 undergoes a particularly long migratory phase (note the gap between frames), and the sagittal section shows distinct rightwards tilting.

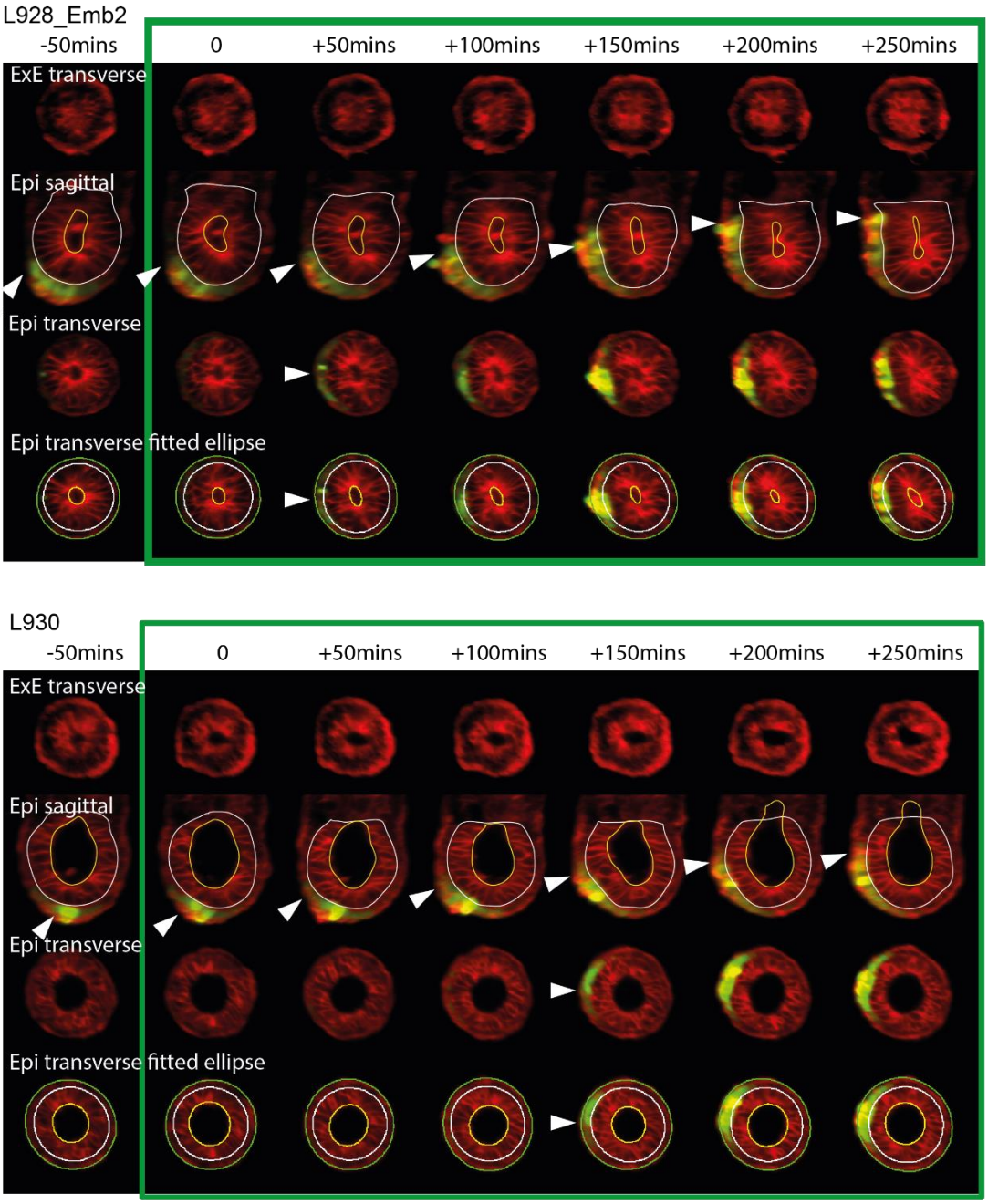

Figure 6-4: Continuation of Figure 6-1. Embryo L928_Emb2 did not undergo abnormal cavity expansion, and the flattening as the AVE migrate is more pronounced in the sagittal section.

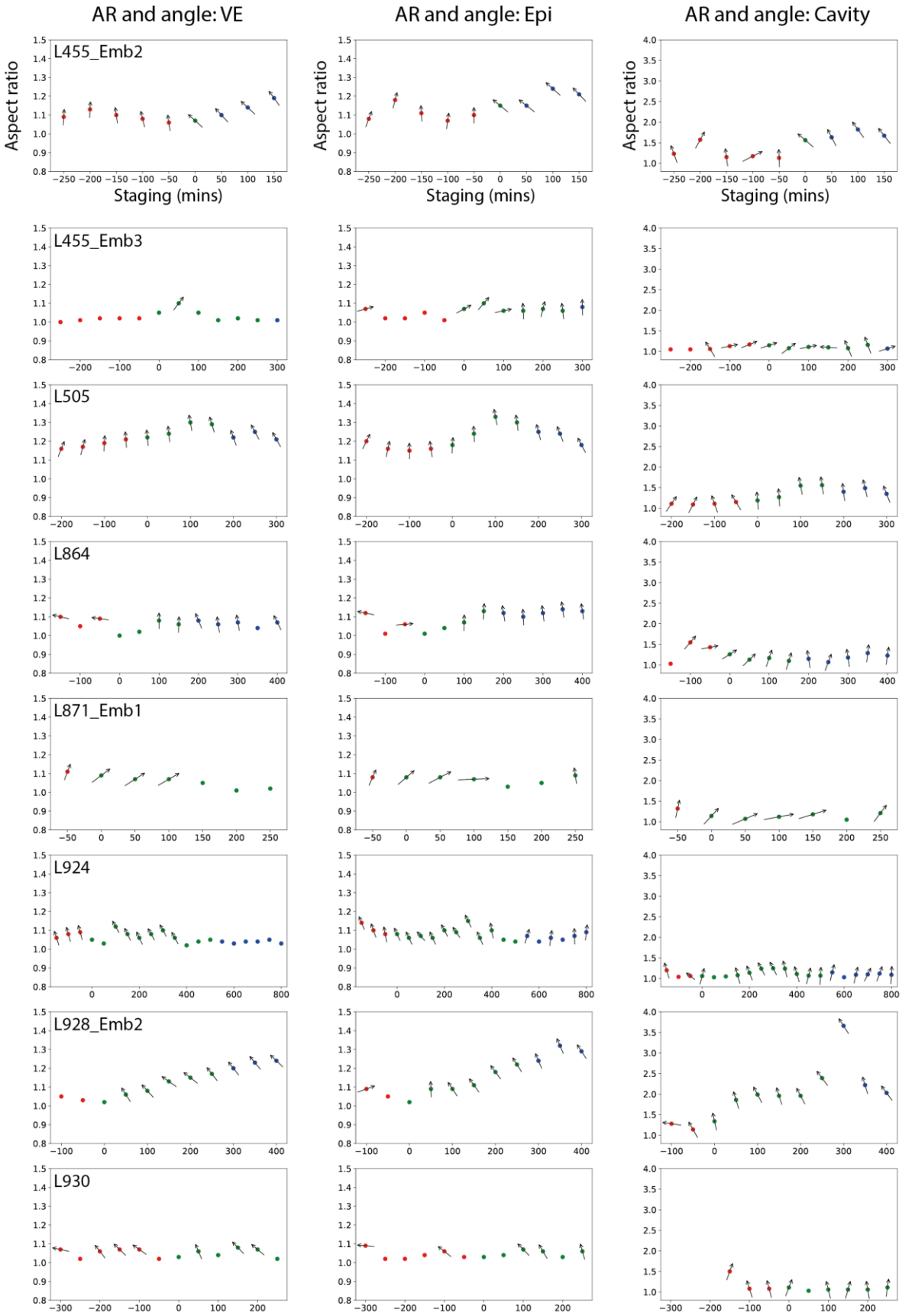
AR and angle: VE
AR and angle: Epi
AR and angle: Cavity
Aspect ratio
Staging (mins)
L455_Emb2
L455_Emb3
L505
L864
L871_Emb1
L924
L928_Emb2
L930

Figure 6-5

Figure 6-5: Plots of the aspect ratio and angles of the transverse section. A) shows the aspect ratio of the VE, B) of the epiblast, and C) of the cavity. Arrows denote the direction of the long axis of the ellipse, and have only been plotted where the aspect ratio >1.05. The A-P axis is oriented to the left in each embryo, and in plots. Pre-migration phases are shown with red markers, migratory in green and post-migration in blue.

In 7/8 embryos the long axis of the epiblast aligns perpendicular to the A-P axis during migration, and the short axis lies under the thickened AVE. In 3/7 embryos (L455_Emb3, L864, L930), this is shown by a shift in long-axis angle from horizontal (aligned with A-P axis) to vertical (perpendicular to the A-P axis). In L505, the shape change is characterised by an increase in aspect ratio, as the long axis begins with the axis already perpendicular to the AVE. In the remaining 3/7 embryos the shape change was seen changes to both aspect ratio and angle (L928_Emb2, L924 and L871_Emb1). L871_Emb1 shows a slight lag as the cavity expands horizontally during the first timepoints of migration, with a corresponding change in the epiblast and VE long axis angles.

L455_Emb2 is the only embryo where the long axis begins vertically, but ends up more horizontal. The largest aspect ratios are seen in the two embryos with no abnormal cavity expansion (L455_Emb2 and L928_Emb2), and also in L505.

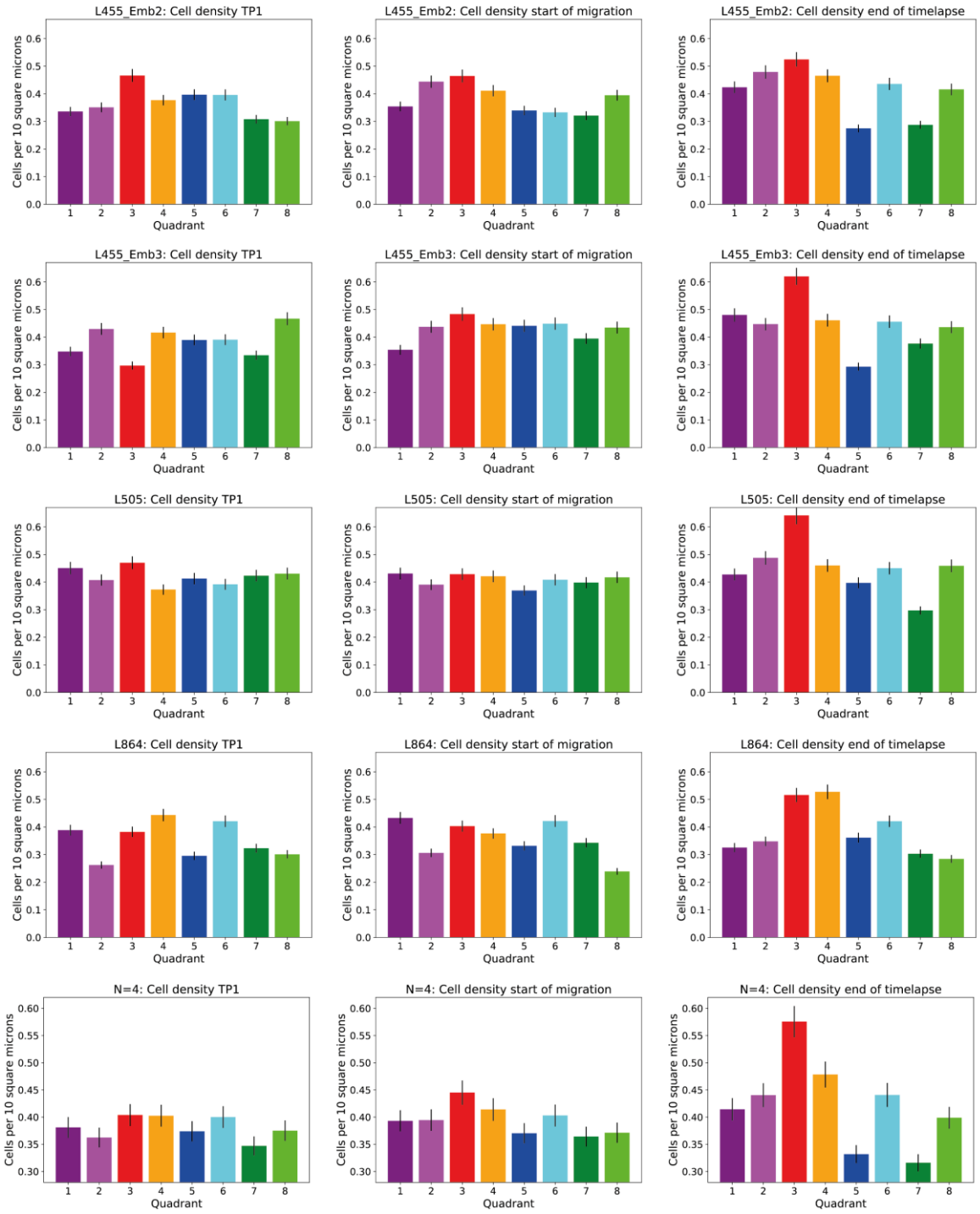

Figure 6-6: Cell density for each quadrant at the start of the timelapse, start of migration, and end of the timelapse. The average of the 4 embryos is given in the bottom row, with a zoomed in y-axis to make differences clearer. By the start of migration (central column), all embryos have denser anterior Epi-VE regions (quadrant 3, red) than posterior Epi-VE regions (quadrant 7, dark green). Density is given in units of cells per (10μm)^2. Note that these are lower than they should be for L505 quadrant 8 and L864 in quadrants 2 and 8, as these contain part of the EPC where cells were not counted.

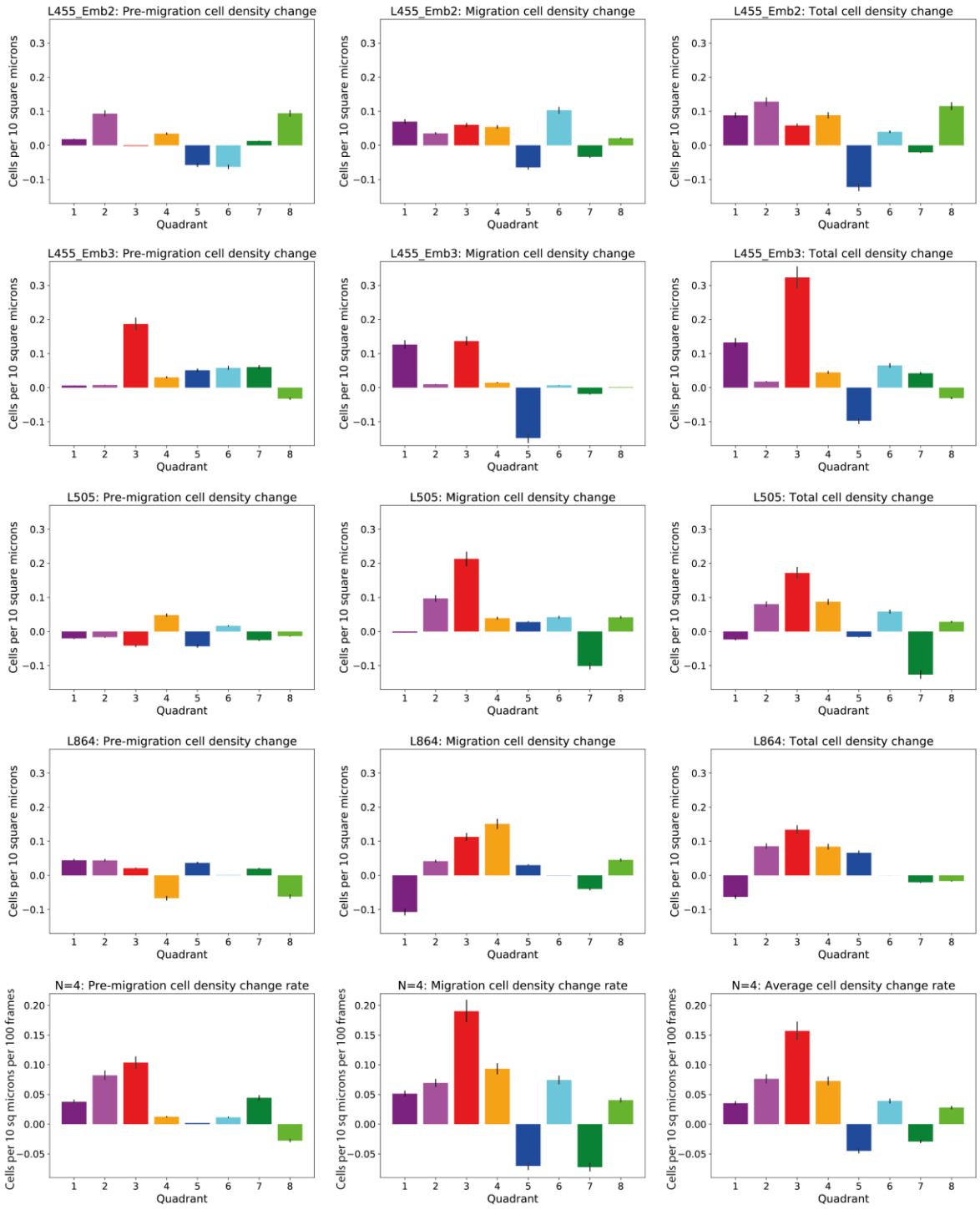
L455_Emb2: Pre-migration cell density change
L455_Emb2: Migration cell density change
L455_Emb2: Total cell density change
L455_Emb3: Pre-migration cell density change
L455_Emb3: Migration cell density change
L455_Emb3: Total cell density change
L505: Pre-migration cell density change
L505: Migration cell density change
L505: Total cell density change
L864: Pre-migration cell density change
L864: Migration cell density change
L864: Total cell density change
N=4: Pre-migration cell density change rate
N=4: Migration cell density change rate
N=4: Average cell density change rate
Cells per 10 square microns
Cells per 10 sq microns per 100 frames
Quadrant

Figure 6-7

Figure 6-7: The change in cell density for each quadrant during pre-migration, and migration phases, and the change of the total timelapse. The average of the 4 embryos is given in the bottom row, using the comparative density change rate (change in density for 100 frames). Only 2/4 (L455_Emb2 and L505) showed a greater cell density change in the posterior Epi-VE density (quadrant 7, dark green) than anterior Epi-VE (quadrant 3, red) in pre-migration. Additionally, in L505 both the anterior Epi-VE and posterior Epi-VE quadrants had a negative density change during pre-migration. The posterior Epi-VE quadrants in 4/4 embryos became less dense during migration. There are pronounced differences in lateral Epi-VE quadrants (1,5) of 3/4 embryos during migration, but these are not consistent to one side of the embryo and not statistically significant.

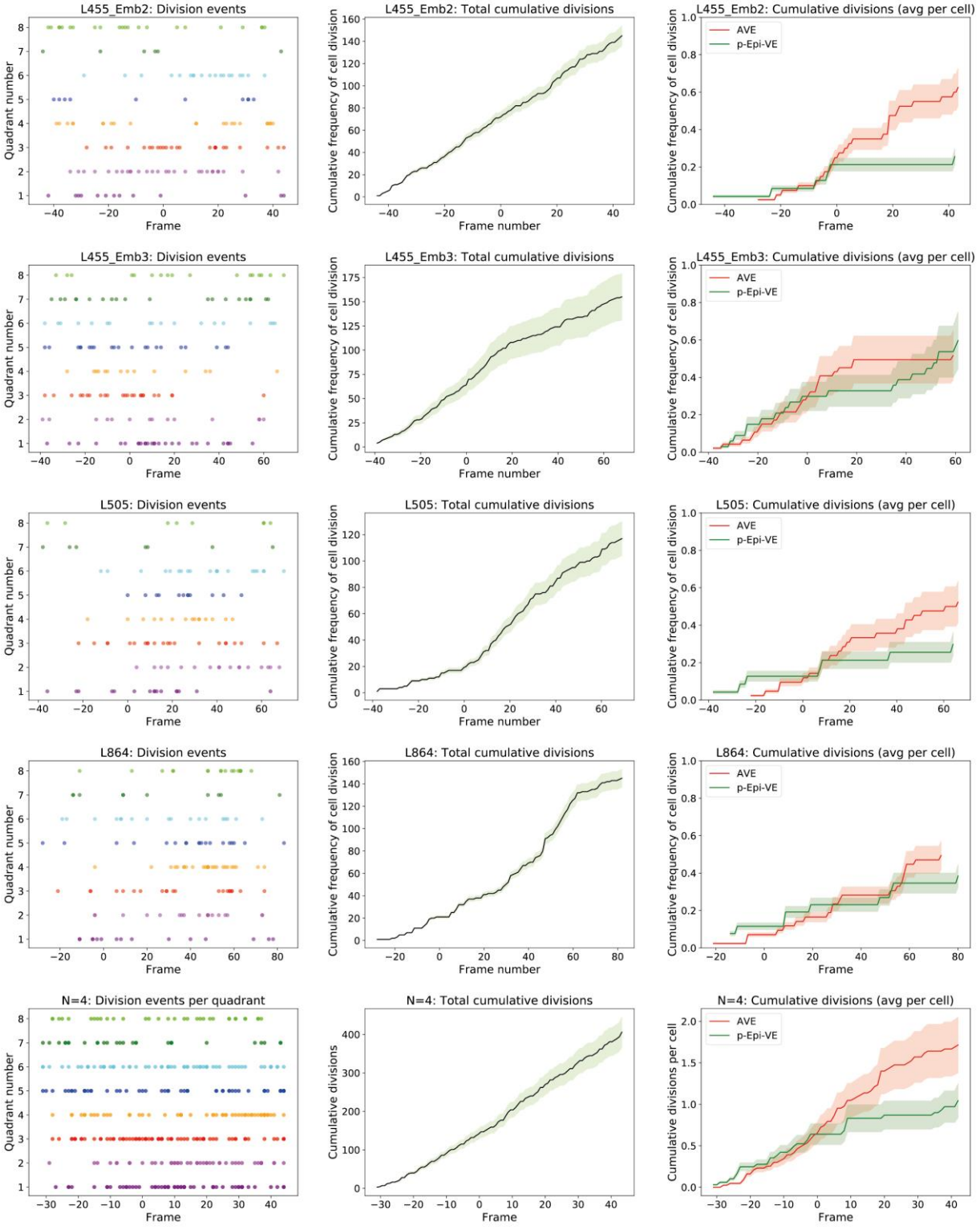
L455_Emb2: Division events
Quadrant number
Frame
L455_Emb2: Total cumulative divisions
Cumulative frequency of cell division
Frame number
L455_Emb2: Cumulative divisions (avg per cell)
AVE
p-Epi-VE
Cumulative frequency of cell division
Frame
L455_Emb3: Division events
Quadrant number
Frame
L455_Emb3: Total cumulative divisions
Cumulative frequency of cell division
Frame number
L455_Emb3: Cumulative divisions (avg per cell)
AVE
p-Epi-VE
Cumulative frequency of cell division
Frame
L505: Division events
Quadrant number
Frame
L505: Total cumulative divisions
Cumulative frequency of cell division
Frame number
L505: Cumulative divisions (avg per cell)
AVE
p-Epi-VE
Cumulative frequency of cell division
Frame
L864: Division events
Quadrant number
Frame
L864: Total cumulative divisions
Cumulative frequency of cell division
Frame number
L864: Cumulative divisions (avg per cell)
AVE
p-Epi-VE
Cumulative frequency of cell division
Frame
N=4: Division events per quadrant
Quadrant number
Frame
N=4: Total cumulative divisions
Cumulative divisions
Frame
N=4: Cumulative divisions (avg per cell)
AVE
p-Epi-VE
Cumulative divisions per cell
Frame

Figure 6-8

Figure 6-8: Division events in the embryo over time. The first column shows the stochastic individual division events. The middle column shows the cumulative cell divisions for all the quadrants. The right column shows the cumulative divisions events in the AVE (red, 3) and posterior Epi-VE quadrants (dark green, 7), normalised to the average number of cells in the quadrant. The staging is reflected in the Frame number on the x-axis, with 0 marking the start of migration and negative frames pre-migration. Shading gives the uncertainty in the cumulative measurements according to Table 4-4. Frames are acquired every 5mins. A linear trend emerges for divisions across the embryo, but the anterior and posterior Epi-VE quadrants diverge during migration.